The Electric Field System of an Excitable Cell

by

Colin Hales

Submitted to the University of Melbourne in total fulfilment of the requirements for the degree of

DOCTOR OF PHILOSOPHY

May, 2011

Department of Electrical and Electronic Engineering
University of Melbourne
Victoria, 3010
Australia

ABSTRACT

The specific microscopic origins of electromagnetic (EM) fields in excitable cell tissue have been underdetermined for a long time. A better understanding of the microscopic EM field origins directly facilitates an understanding of the origins of EEG and MEG signals, along with the role of EM coupling in cell excitability, developmental cues, regulatory processes underlying learning, and the general brain dynamics involved in all of these and of cognition generally. With the aim of isolating and describing the most plausible originating mechanism, the fundamental laws of electromagnetism, as applied to excitable cell tissue, were subjected to an extended review. A bridging form of the macroscopic EM volume conduction equations was constructed that was specially adapted to reveal the microscopic origins of the endogenous EM fields. The basis of the specialization was a focus on coherence between regions of transmembrane current activity expressed by a neuron during the passage of an action potential throughout its structure. A computational exploration of the equations, applied to a large, biologically realistic pyramidal cell, demonstrated that the coherent transmembrane current activity of spiking neurons can express a faint, unified, spatially extended, "line-of-sight-active" extra-neural EM field with complex structure and dynamics, all based on the operation of individual dipoles created by single ion channels, small ion channel aggregates, and large aggregates of the kind found in the synaptic cleft and elsewhere. The result is highly suggestive of an additional "line-of-sight" regulatory mechanism implemented as feedback delivered by EM coupling. This is consistent with recent empirical observations suggesting that this mechanism exists and operates in cortical tissue.

DECLARATION

This is to certify that:

(i) The thesis comprises only my original work towards the PhD except where indicated in the Preface.

(ii) Due acknowledgement has been made in the text to all other material used.

(iii) The thesis is less than 100,000 words in length, exclusive of tables, maps, bibliographies and appendices

_____

Colin Hales

To
Sam, Kristen and Jack
and
my long-suffering brothers.

PREFACE

My 'late-onset-scientist' PhD experience has been a wonderful expenditure of a significant chunk of a life. The chapters to come reveal only a small part of a much larger story. Items not apparent in the bulk of the thesis include:

- Attendance at a neuroscience conference in Perth (2004).
- A speaking presentation at an international conference on neuropsychiatry in Sydney (2006)
- A poster presented at a consciousness conference in Tucson (2006).
- I had an opportunity to contribute an ABC Radio National 'Occam's Razor' program (2005) (Hales 2005).
- A review of a book by noted local physiologist Emeritus Professor Derek Denton, one of the founders of the Florey Institute, whom I got to know personally. The review went into the school of graduate research journal TRAFFIC (Hales 2006).
- Aspects of my PhD journey have been captured in the graduate student association publication 'Plane Tree' (Zolin 2009).
- Along with two local professors and one of my student colleagues, I also participated in a two hour science program on local radio station RRR.

I was privileged to spend a large amount of time with a great number of very talented young students, who taught me all sorts of things and tolerated an 'old guy' in a very supportive way. I only hope I was able to be a positive, constructive influence on them in the same way. These things are as important to me as anything else.

I commenced the PhD process with my eye ultimately focussed on commercialisation of my AGI ideas, and no intention to embark on a career as a general researcher. As I complete it, I am no less enthusiastic about my AGI plans. However, I find myself, to some extent, captured by the pure science potential evident in what must be the mere first faltering steps of a much larger area of scientific exploration. At the age of 55, it seems fate may have other intentions for what's left of my future.

Hales, C. (2005) 'Qualia', Ockham's Razor, R. Williams 17 April 2005.
http://www.abc.net.au/rn/ockhamsrazor/stories/2005/1345858.htm

Hales, C. (2006) Physiology Meets Consciousness. A Review of "the Primordial Emotions: The Dawning of Consciousness" by Derek Denton. In M. Smith (ed.). Traffic Eight, University of Melbourne Postgraduate Society, Melbourne.
http://www.gsa.unimelb.edu.au/Traffic8/index.shtml

Zolin, M. (2009). 'In Pursuit of the Goal', Plane Tree (Graduate student association, University of Melbourne Vol. 15, No. 3, 19-21.

ACKNOWLEDGEMENTS

I cannot find words sufficient to express my appreciation of the support of my kids and my brothers. You have helped me on the path to a major change of direction in my life. You have lived through it with me.

Thanks to Professor John Furness and Professor Joel Bornstein for accepting me into the PhD process and letting me find my direction. Thanks to Dr. Peter Kitchener for (a) remaining interested in all my outlandish ideas, (b) assisting greatly in the laborious process of learning how to write about them, and (c) for helping me find NICTA.

My supervisors, A/Prof. David Grayden and A/Prof. Harry Quiney, deserve a medal for both their tolerance for what continues to be a path through a jungle of controversy and for supplying much needed guidance when I needed it. This and my ongoing battle with mathematical dexterity. I will do my best to make sure their patience is justified and that good science results from it.

Thanks must go to NICTA for their support via a scholarship. Thanks go to David Strover, in particular, for helping a middle-age student on a life-changing venture to get sufficient support in the scholarship process. I am eternally grateful. NICTA is funded by the Australian Government as represented by the Department of Broadband, Communications and the Digital Economy and the Australian Research Council through the ICT Centre of Excellence program.

Thanks go to the D151 neuron data assemblers and the originators of the EAPS NEURON model (http://www.neuron.yale.edu), under ModelDB database number 84589.

This research was supported by a Victorian Life Sciences Computation Initiative (VLSCI) grant number VR0003 on its Peak Computing Facility at the University of Melbourne, an initiative of the Victorian Government.

ABBREVIATIONS

Abbreviation	**Meaning**
AGI	Artificial General Intelligence
ALLO-	A prefix denoting a phenomenon related to activity directed at the other
AP	Action potential
AUTO-	A prefix denoting a phenomenon related to activity directed at the self
BBB	Blood Brain Barrier
CSF	Cerebrospinal Fluid
CNS	Central Nervous System
DROMIC	Propagation in the direction down/towards the axon initial segment
ANTI-DROMIC	Propagation in the direction opposite to dromic (over soma and out into dendrites)
ECM	Extracellular Matrix
ECS	Extracellular Space. Same as ECM.
ECoG	Electrocorticogram
EEG	Electroencephalogram
EM	Electromagnetic
HPC	High Performance Computing
ICS	Intracellular Space
MD	Molecular Dynamics
MEG	Magnetoencephalogram
MM	Molecular Mechanics
MmE	Maxwell's Microscopic Equations
MME	Maxwell's Macroscopic Equations
N_A	Avogadro's Number.
NCC	Neural Correlate of Consciousness
PNS	Peripheral Nervous System
QM	Quantum Mechanics
ROI	Region of Interest

CONTENTS

Chapter 1

THE STRUCTURE OF BRAIN TISSUE & THE EXISTING SCIENCE OF ITS ELECTROMAGNETIC FIELDS

"*Colin: if, at the end of a day, you realize that you know less than you did in the morning, you know you have made progress.*"

John 'Mick' Finch, my grandfather

1.1 Introduction

This thesis is an investigation of the origin of the endogenous electromagnetic (EM) field system of excitable cell tissue. Demonstrating the most likely originating mechanism, opens the door to future determination of the extent to which the EM fields can be one of the various mediators of brain tissue dynamics, self-modification and self-regulation. The validity of the science results from its ability to provide a plausible originating mechanism for both the electric and magnetic fields in the brain whilst simultaneously providing a simple physical mechanism consistent with the most recent experimental neuroscience evidence for brain tissue's capacity for microscopic EM field effects to robustly involve themselves in macroscopic tissue dynamics.

In this chapter, to contextualise the process, the detailed physical structure of cortical tissue is presented. This is necessary because the originating mechanism of all functionally relevant EM fields is ion position and motion. Ions are located in specific places and move in stereotypical ways along routes that are only apparent when the full molecular structure of the material is taken into account. The motivation to perform the science is also revealed, along with the history and current state of the science of the endogenous EM fields.

In later chapters the detailed structure is carefully abstracted away in a manner that facilitates tractability while retaining enough expressiveness to be informative about the tissue in general. The mathematical basis for the mechanism is a specialised, hybrid macroscopic/microscopic form of classical electromagnetism constructed and tested for the purpose. The neuroscience is modelling enacted computationally. The results are the output from high performance computing tailored to purpose and, as non-analytic/numeric data, are presented graphically. In the process we get a first glimpse of the hidden electromagnetic life of the neuron and the early beginnings of the final chapter

on brain endogenous electromagnetism. This chapter covers the structure of excitable cell tissue and some of the background of excitable cell electromagnetism, its terminology, its state-of-play, the motivations that resulted in the research and the foundation of the methods used.

1.2 Motivations: Pursuit of a mechanism

We are approaching the 150th anniversary of the first measurement of the endogenous electric field of excitable cell tissue by Caton (Swartz and Goldensohn 1998). We are also approaching the 100th anniversary of Berger's measurement of the same phenomenon in a human brain (Haas 2003). In the intervening period, science has pursued the origins of the field system to ever finer spatial and temporal scales. Now, in the early 21st century, our common knowledge of the endogenous field system reveals it to be a combined electric and magnetic (electromagnetic or EM) field with a three-dimensional, spatiotemporally complex pattern expressed within and measurable slightly beyond the tissue bounds. We know that the originating microscopic electric and magnetic fields vectorially superpose throughout the space occupied by the brain, creating the unified nature of the field system. Spatially, the microscopic detail of the electric field expression has been tracked to sub-cellular (1μm) levels through measurement of the 'local field potential' (LFP), a voltage measurement usually acquired with a microscopic invasive probe. In the empirical exploration of functionally relevant field patterning, the usual explored range of oscillatory (spectral) features spans 0Hz to 300Hz. Recent experimental work at the cellular level typically put the high frequency cut-off at 600Hz e.g. (Frohlich and McCormick 2010). Action potentials have high rise-times and a duration of roughly 1ms. The actual frequency content at short spatial scales (sub-cellular local activity) must therefore extend into the kHz . Sampling frequencies for electrical measurements must be at least twice the expected signal high frequency limit (Nyquist sampling) to capture all the spectrum of the material. While the spectral ranges (alph, beta, gamma etc.) are well defined under 100Hz (Buzsaki and Draguhn 2004), the deep, fine scale, full spectral content of interest here extends far beyond that range into the tens of KHz.

The long history of indirect research into the brain's EM field has delivered a significant part of our sophisticated knowledge of the brain. It has been examined in the developing brain, in the various normal brain modes such as sleeping and awake, and in pathological modes such as disease, injury and anaesthesia. Over the last twenty years, the field system (as revealed by the LFP) is increasingly being found to be a reliable measure of brain function with superior correlative fidelity than, say, any particular intracellular action potential measurement (Anastassiou, Perin *et al.* 2011, Buzsaki and Draguhn 2004, Frohlich and McCormick 2010, Katzner, Nauhaus *et al.* 2009, Niedermeyer and da Silva 2005, Pesaran 2009).

Yet, despite this escalating research interest, advanced level of understanding, and microscopic measurements, it is sobering to realise that the precise origin of the electric and magnetic fields is, formally, undetermined (Pesaran 2009). This fact makes, for example, the ultimate origin of the electroencephalogram (EEG) a mystery older than neuroscience. Its sibling, the magnetic field, is known to exist because scalp level (mm resolution) magnetoencephalograms (MEG) prove it (Cohen 1968). Thus, deep in the tissue, and of far smaller amplitude, the magnetic equivalent to the LFP, called the magnetic vector potential (Jackson 1999), remains in the too-hard basket, with barely a measurement to assist speculations as to its origin. Currently, the origins of the scalp EEG or cortical surface indicators of electric field such as the electro-corticogram (ECoG), tend to be attributed to generic 'electrochemical activity', usually that associated with chemical synapses. Over the decades, LFP measurement has been cautiously interpreted and usually explained in broad terms as the result of excitable cell electrochemical activity of various kinds (Bedard and Destexhe 2009, Bedard, Kroger *et al.* 2006, Frohlich and McCormick 2010, Gold, Girardin *et al.* 2009, Gold, Henze *et al.* 2007, Gold, Henze *et al.* 2006, Holt 1998, Holt and Koch 1999, Katzner, Nauhaus *et al.* 2009, Speckmann and Elgar 2005). At finer spatial scales, *coherent* transmembrane current is claimed to be the original mechanism (Katzner, Nauhaus *et al.* 2009). That said, it is still unclear exactly which of the many kinds of microscopic electrochemical current activities are the prime determinant of the LFP.

1.2.1 Causal mechanism, 'Back-propagation' and the EM field system

Associated with the lack of a specific microscopic/molecular originating cause of the endogenous EM field is a related complication. Brain EM fields, regardless of their origins, have a chronically confused status as an originator of a functional (causal) role in the brain. For example, in 1989 a physiology review paper clearly attributed, with evidence, multiple causal roles to the endogenous fields (Faber and Korn 1989). Yet in spite of this clear result, the 'epiphenomenal' characterisation of the fields persisted elsewhere (Niedermeyer and da Silva 2005). Status as an epiphenomenon necessitates that the EM field itself has no causal impact on the tissue that generated it. Sometimes the existence of a causal role is acknowledged but regarded as speculative (Nunez and Srinivasan 2006). The current view, based on new measurements, aligns itself with the 1989 review (Anastassiou, Perin *et al.* 2011, Frohlich and McCormick 2010).

In supplying an original mechanism for the EM fields, this thesis directly challenges the 'epiphenomenon' status of the endogenous fields. It does this by revealing a mechanism by which the EM fields can, in principle, by simple expression in space and the impact of the simple line-of-sight action of the Lorentz force, feed back onto the originating neuron and its nearby neighbours, thereby modifying the dynamics of the irradiated cells and EM fields produced by all the impacted cells … and so forth. To illustrate the impact of the change in understanding consider Figure 1-1, which is based on (Frohlich and McCormick 2010). Figure 1-1(a) shows, in a general sense, how the traditional epiphenomenal view strips the electric field of any causal impact on the tissue. In respect of the magnetic field, it is simply mute. In Figure 1-1(a), traditional neural connectivity dominates tissue dynamics in a non-line-of-sight mode through the tortuous paths of axons and dendrites. In providing a plausible mechanism for the observed self-sensitivity to the endogenous fields, this thesis supports a claim that Figure 1-1(b) is a more realistic depiction of the situation in brain material. Figure 1-1(b) superimposes an EM field interaction on the existing activity. Under the revised model, the traditional axo-dendritic (action potential) activity and the EM field activity mutually interact to jointly determine the tissue dynamics. The plausibility of the claim rests on revealing (a), an original cause of a unified, structured field that delivers self-feedback while also supplying (b), an original cause for the magnetic field. To complete a case for the 'back-propagation' mechanism, the fields thus delineated must be of sufficient magnitude to have the requisite causal role.

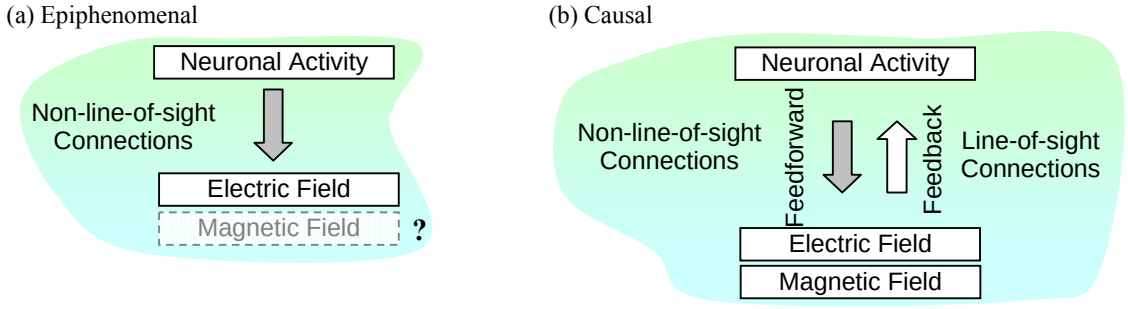

Figure 1-1 The novel back-propagation (feedback) mechanism.

Recent work has delivered evidence that the very weak endogenous electric field system can profoundly influence whole-tissue dynamics. Without specifying an original cause for the fields, the electric field's influence has been empirically pursued from the whole-tissue (Katzner, Nauhaus *et al.* 2009), to cortical layer (Frohlich and McCormick 2010) and to individual neurons (Anastassiou, Perin *et al.* 2011). The result is that far from being an epiphenomenon, the so-called 'extracellular field' expressed at a single neuron level, even when devoid of all synaptic activity (by chemical blocking), can significantly alter the action potential dynamics of a sufficiently proximal neighbouring neuron. From there the influence propagates, quickly extending to tissue-level entrainment.

1.3 The chemical/mechanical structure of brain material

An authoritative claim about EM field origins means we have to deal with the structure of the tissue, fully expressed at an atomic/molecular level. The tissue/cellular microstructure is illustrated in Figure 1-2(a). The tissue sample is grey matter. Note in the top left corner, where a single myelinated axon indicates that the sample is not far from white matter. The Figure 1-2(a) dark blue objects are mitochondria, an intracellular organelle responsible for energy supplies, which has its own, even more negative, resting potential. The crucial information in this diagram is that the tissue is formed by tortuously apposed membranes of neurons and astrocytes of the general kind shown in Figure 1-2(b) and Figure 1-2(c), respectively. Just as important is that the tortuous apposition creates a highly conserved and very narrow (low tens of nm, typically) 'extracellular space' (ECS). This is to be contrasted with the interiors of the cells, which are vastly bigger and create a self-contained 'intracellular space' (ICS) compartment for every cell. Collectively, this gives the ECS the structure of a fine foam (Nicholson and Sykova 1998). The bulk of ECS and ICS material is a water electrolyte. However, in reality, the chemical and structural complexity of these regions is extreme. Figure 1-2(a) has been simplified to that extent. The electrical properties and related details are supplied in Chapter 2.

(a) Tissue cellular microstructure

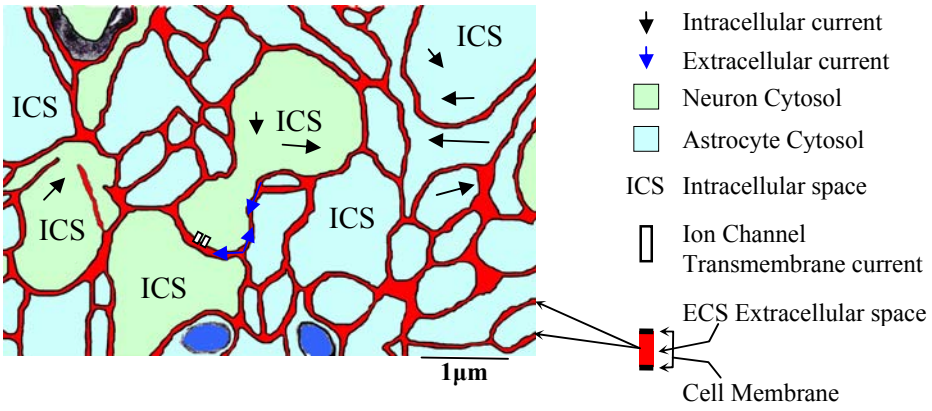

(b) Neuron (pyramidal)

(c) Astrocyte (human)

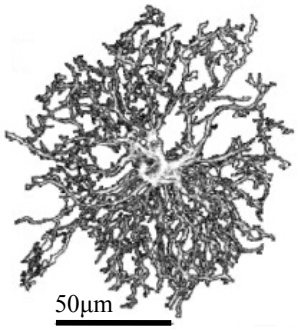

Figure 1-2 (a) is based on (Nicholson and Sykova 1998) and reveals the fine-scale structure of the tissue. It results from the intimate entwining of, for example, (b), pyramidal neuron (Harris, Cruce *et al.* 1980) and (c) astrocytes (Oberheim, Wang *et al.* 2006). Images reproduced with permission.

Note that to date, the ECS gap width is experimentally determined in gray matter to mostly be in the range 20-65nm, although small natural ECS 'lakes' can form (Kandel and Schwartz 2000, p178, Kuffler and Nicholls 1976, p255, Nicholson and Phillips 1981, p227, Nicholson and Sykova 1998). There is a degree of variability in reported gap width. The ECS gap has been found reported to be reduced and controlled to around 20-40nm for the synaptic cleft and 2-4nm in the case of gap

junctions (Hille 2001, p301, Hormuzdi, Filippov *et al.* 2004, Purves 2004). The main constituent material within the ECS is water and electrolytes. While the interstitial gap is very narrow, the ECS has a high tortuosity, leading to its volume fraction being typically cited as between 10% and 20% of cerebral volume (Bach-Y-Rita 2001, Bignami 1991, Geddes and Baker 1967, p273, Nicholson and Phillips 1981, Sykova 1997, Sykova 2004, Sykova and Nicholson 2008, Sykova, Roitbak *et al.* 1999, Van Harrenveld 1968). For example, (McBain, Traynelis *et al.* 1990) cite rat hippocampal CA1 ECS volume at 12%, which tells us that its structures are more tightly interwoven than, say, rat cortex. Within this narrow foam-like structure, proximal to the lipid bilayer, the ECS holds a large collection of various ions in solution. These ions have sister populations, of overall opposite polarity, on the other side of the adjacent sub-membrane ICS (Aidley 1998, Hille 2001). These are considered in more detail in Chapter 2.

One of the important features of astrocytes is that, unlike neurons, astrocyte processes ramify into fine, uniformly distributed branching appendages, which gives them their stellate character. In hippocampal gray matter, these elaborate and dense processes have been found to define a 3D space that is free of processes from other astrocytes (Bushong, Martone *et al.* 2002). This territorial behaviour is a good starting point for understanding their functional influences on the EM field system, although it will not figure in the physics model that is developed later. In terms of Figure 1-2, the territorial nature implies that the revealed astrocyte compartments are likely to all belong to the same astrocyte, whereas the neuron compartments could be those of different neurons. Astrocyte territoriality can reasonably be expected to create some level of electromagnetic unification through the management of the ion stocks in the extra-neuronal medium, along with energy supplies (Nedergaard, Ransom *et al.* 2003).

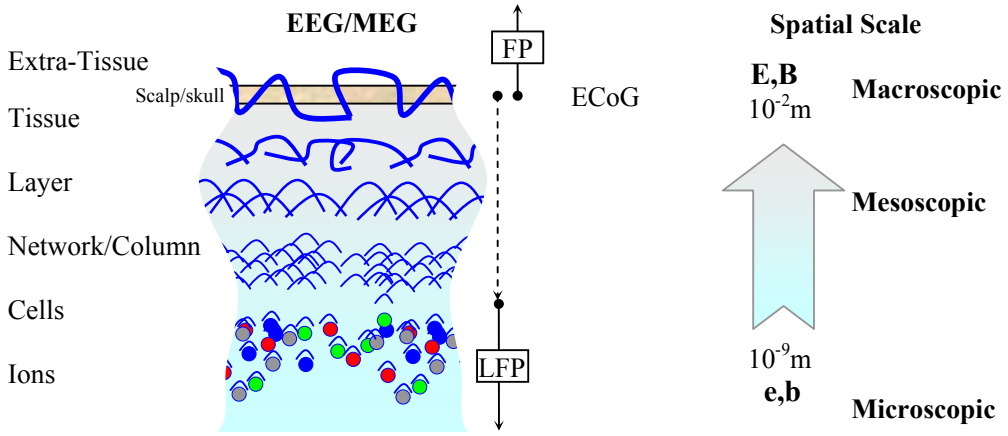

Figure 1-3 The brain's EM field inherits the organisational layering of the tissue matter hierarchy, existing as a unified whole in its own right. The illustration shows a cortical context, where the electric and magnetic field begins microscopically as e and b, respectively. Measurement reveals it as the LFP. Its only possible origins are atoms (ions) as possessors of (net) charge. The microscopic fields e and b vectorially sum, ultimately becoming macroscopic average E and B, respectively. When measured, it is called the FP.

This thesis is concerned with the origin of the electric field, **e**, and the magnetic field, **b**, generated by neurons and expressed outside neurons. Figure 1-3 depicts the accreting layers of organisation that ultimately become the macroscopic spatially averaged electric field, **E**, and magnetic field, **B** that are visible at the level of the scalp. The spatial scale of a measurement is dependent on probe dimension. At a single notional position, the finer the probe, the closer the measurement will be to the microscopic electric field **e**. This is a property of the spatial averaging done by probes with dimensions greater than the spatial resolution of the field it is measuring. This phenomenon has recently been comprehensively verified in an epilepsy context, where both macroscopic and microscopic probes were interspersed and measured simultaneously. The fine probes revealed 'micro-seizures' (evidenced in localised hyper-synchronous LFP behaviour) that were not evident in the macroscopic probes until a later stage in the seizure (Stead, Bower *et al.* 2010). The beginnings of the formal nomenclature have

been revealed here. Lower case refers to microscopic fields, upper case to macroscopic fields. **Bold** is for vector quantities.

1.3.1 Macroscopic/population 'field' terminology

Here we examine the various ways that fields have been characterised in excitable cell tissue. Recent single-cell empirical/modelling interest in the microscopic LFP origins has been explicitly motivated by the need for an explanation of the origins of the scalp EEG and MEG waveforms (Gold, Henze *et al.* 2007, Gold, Henze *et al.* 2006, Holt and Koch 1999, Milstein and Koch 2008). Traditionally, EEG has been understood to be the result of synapse activity (de Munck, Vijn *et al.* 1992, Nunez and Srinivasan 2006, Speckmann and Elgar 2005), although more recent literature acknowledges that the full explanation is actually missing (Pesaran 2009). EEG practitioners measure macroscopic 'field potential' (FP), not LFP (see Figure 1-3). This measurement is made non-invasively at the scalp. With surgery, at the cortical surface, the measurement is made at a spatiotemporally finer resolution, is named Electrocorticogram or ECoG (Niedermeyer and da Silva 2005) and has more high-frequency content. At this level, the naming status of the measurement is ambiguous. It is possible to find it called 'field potential' (FP) and 'local field potential' (LFP) in the literature.

The bottom-up relationship between the microscopic origins of the LFP and its final presentation as FP is unique and is called the 'forward problem' (Hamalainen, Hari *et al.* 1993, Niedermeyer and da Silva 2005, Nunez and Srinivasan 2006). In the absence of the necessary deep originating mechanism, FP measurements relate to the deep microscopic LFP behaviour in a non-unique way called an 'inverse problem'. The inverse problem has been the focus of much work and remains an active, ongoing research effort. This work is variously categorised as 'mean field', 'neural field' and sometimes 'synaptic field' (Coombes 2005, Deco, Jirsa *et al.* 2008, Ermentrout 1998, Ermentrout and Kleinfeld 2001, Jirsa and Haken 1997, Klee and Rall 1977, Liley, Cadusch *et al.* 2002, Nunez and Srinivasan 2006, Robinson, Rennie *et al.* 1997, Vogels, Rajan *et al.* 2005, Wilson and Cowan 1973, Wright, Rennie *et al.* 2004, Wright, Robinson *et al.* 2001). These macroscopic 'fields' are generally held to be a result of the 'mass action' or 'population activity' (Freeman 1975) of accreting layers of nervous tissue organisation of a microscopic originating phenomenon that may or may not be explicitly identified. In the case of the EEG inverse problem called 'source localisation', for example, an abstract dipole source may be used as a solution. In the cases where the original source need not be specified, the mean/neural/synaptic field becomes a 'field' by virtue of its operation within the broad class of field/wave equations, usually driven by noise of some sort. The models are intended to connect the EEG to the behaviour of neural populations, their networked interconnectivity and resultant resonance behaviour. In the abstraction process behind these inverse problem 'solutions', the connection to an originating physical basis creates some explanatory challenges that can limit their usefulness. In contrast, a low level physics explanation of LFP can be used as a substrate upon which to build and constrain mass action field models based on the physical EM fields. This thesis is directed at the ultimate origins of the LFP, so population 'field' activity of this kind is of no further concern here.

1.3.2 Volume transmission

The ECS microenvironment is a recognised short and long-distance intercellular communication 'channel' given the name 'volume transmission' or sometimes 'diffusion transmission'(Agnati and Fuxe 2000, Nicholson, Chen *et al.* 2000, Sykova, Mazel *et al.* 2000). This is a passive mode of chemical transport, also occurring in the Figure 1-2(a) ECS fluid. Volume transmission contrasts with the active electromagnetic convection (electrodiffusion or 'bulk tissue/volume conduction') of ECS ions. The ECS fluid volume is a segregated circulating fluid similar in basic composition to cerebral spinal fluid (CSF). Endocrine and other chemical signalling systems use the ECS as a communication medium supported by ECS fluid circulation. Chemical diffusion (concentration gradient motion) is the major driver of volume transmission. The ECS microenvironment is also subject to mechanical (pressure/volume) dynamics through the vascular system. This activity is part of the overall drive behind volume transmission. Volume transmission is described so that it can be properly excluded from involvement in the origins of the LFP. Note, however, that it is not unreasonable to expect that

volume transmission could, depending on the existence of charged moieties on the transmission molecules, be modulated by 'extracellular' field activity. This modulation is also not considered here.

1.4 Biologically realistic structure, numbers and quantities

Figure 1-4 shows a schematic view of the progressive hierarchical organisational layering from the complete brain down, over eight spatial orders of magnitude (10^{-2}m to 10^{-10}m), to its atomic/molecular basis. Rough generic dimensions and features are representative of cortical gray matter.

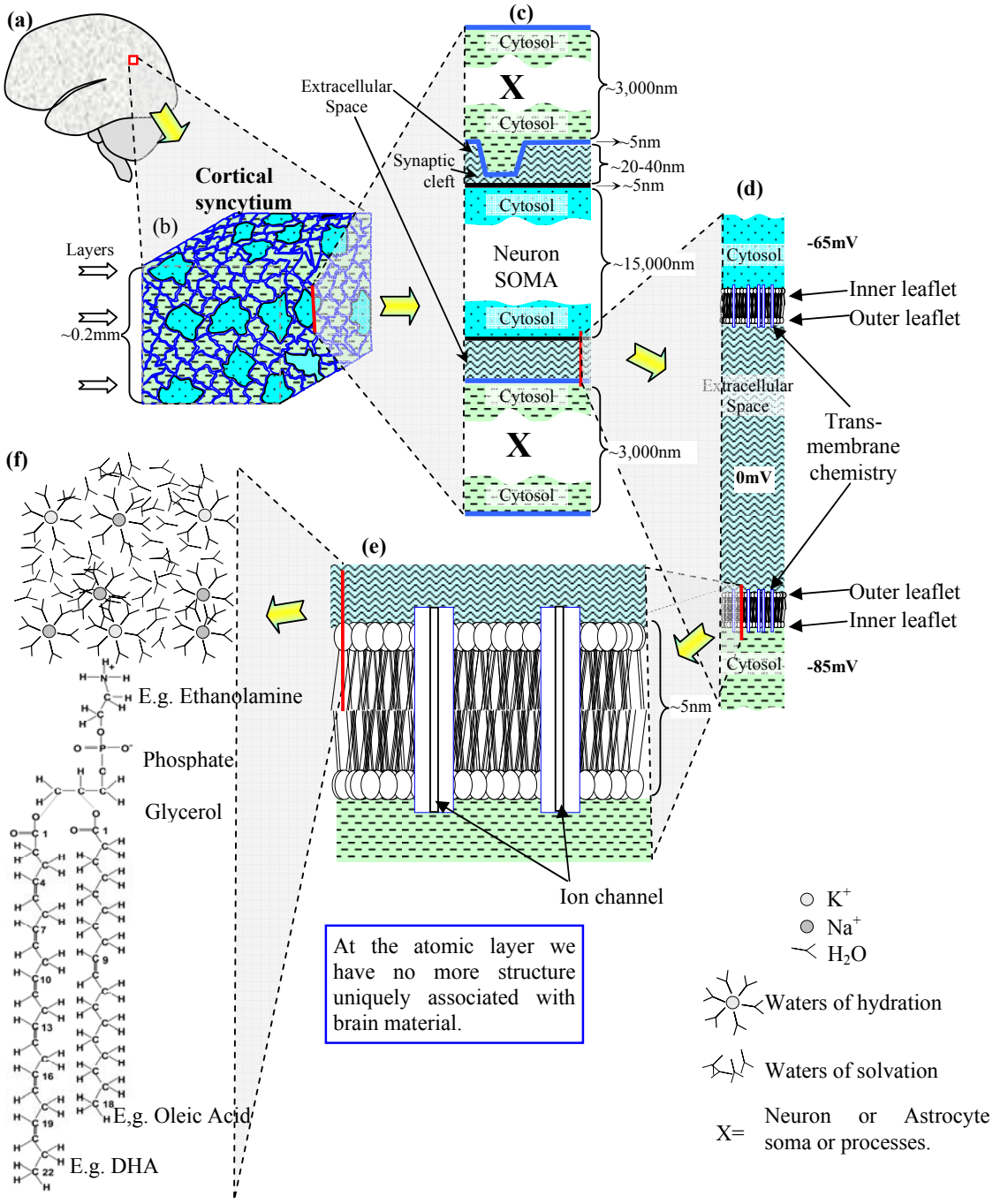

Figure 1-4 Schematic depiction of the matter hierarchy from the whole organ level to the molecular/atomic layers within a typical cell membrane outer leaflet glycerophospholipid molecule. Figures are rough guide only. Not to scale.

Figure 1-4(f) atoms acquire successive layers of nested organisation, eventually appearing as Figure 1-4(a). The material is inhomogenous, anistropic, non-linear, nonstationary and is thermodynamically far from equilibrium. Regularity and departures from regularity operate on multiple interacting timescales, from the subatomic to the whole-organ level (Buzsaki and Draguhn 2004).

1.4.1 The EM syncytium

Here we make a case for the unification of the tissue, at the Figure 1-4(b) level of the matter hierarchy, into a single entity called an electromagnetic syncytium. This is done because it is how cell biologists are taught to view certain kinds of cellular structures. Traditionally a syncytium is considered, by a cell biologist, to be a 'macro-cell' which is a single cell formed by merging the intracellular medium of multiple cells. The resultant structure acts in a role as a single whole cell. The cellular syncytium concept is quite an old one in cell biology, and is routinely applied to various tissues including muscle (smooth and striated, gut and heart) and the eye e.g. (Eisenberg, Barcilon *et al.* 1979). To extend the concept to brain tissue, we now examine the possibility of a neuron-astrocyte functional syncytium formed by the electromagnetic unification of the tissue.

In brain tissue, a certain amount of direct physical (perhaps dynamically switched) cell cytosol merger can be attributed to gap junctions. In this sense, brain tissue might be called a dynamic syncytium for the more familiar reasons. However, here it is suggested that the syncytium concept be expanded to include the operational unity associated with a unified, permeating electromagnetic field structure originating in sub-cellular ion activity. That is, in an excitable cell context, the traditionally understood 'merging' of cells is extended to include a more complex, dynamic electromagnetic 'merging', which acts in addition to the operational merging facilitated by axo-dendritic chemical synapse and gap junction connectivity. Where it is able to, the EM field can become a single entity permeating the tissue. Logically, it is indistinguishable, in a functional sense, from the kind of material unity found in a traditional syncytium. To the extent that regions with sufficient electromagnetic coupling can merge, one can claim that the combined activity is a unified electromagnetic syncytium. Note that this concept plays no direct formal role in later developments. It neither constrains nor influences the analysis. The idea is posed merely so that two similar ideas from different scientific disciplines can find their common descriptive ground in application to a single brain phenomenon: the unity of the EM field system.

1.4.2 Measurement

The common descriptive terminology in electrophysiology has, to a large extent, resulted from the historical use of invasive probes in the measurement process, and invasive probe measurements continue to be the dominant measurement method. When a probe is inserted into $\mathbf{e}(\mathbf{r},t)$ and $\mathbf{b}(\mathbf{r},t)$, the fields interact with the probe, the material and size of the probe modify the fields. In so doing, the probe tip total potential is modified. The modified potential is used as a measurement of LFP at the tip of the probe. It was technically ascertained a long time ago that the electrode acquires a measure of average voltage based on the exposed area of the tip (Hubel 1957, Robinson 1968). The measurement itself is considered to report the average *electric scalar* potential present around the uninsulated tip (Nunez and Srinivasan 2006). The process creates a spatial average of the LFP with respect to a reference potential, and the result has been recently reaffirmed as such for the lower end of the frequency spectrum (Nelson and Pouget 2010, Rosenfalck 1969). A further well described measurement confound is the issue of reference potential itself. The ECS is a poor conductor and has a variable LFP itself, with significant inhomogeneities that can mask important field effects unless care is taken (Faber and Korn 1989). A further issue in measurement is probe asymmetry. Claims that the electrode introduces no directional bias become less supportable at the higher end of the spectrum, and the impact of directional parasitic capacitance, noise and impedance artefacts increasingly become an issue (Nelson and Pouget 2010). Additionally, in combination with the transduction mechanism, including sampling rate and filtration, the probe's interaction with the fields results in temporal averaging.

Note that a penetrating probe (with a typical diameter at least as big as the scale bar) is inserted into the Figure 1-2(a) tissue results in a voltage measurement designated 'extracellular potential' in the literature. This nomenclature seems at odds with the small size of the ECS shown in Figure 1-2. In reality, the probe insertion punctures compartments and/or spreads compartment membranes, increasing the ECS gap width. The 'extracellular potential' is therefore the potential of the ECS and other material that forms around the probe tip and shank. This has been a recognised measurement issue for a very long time (Kuffler and Potter 1964). With careful empirical methods and result interpretation, the measurement process seems, however, to work well.

1.4.3 Brain EM field spectrum issues and related terminology

A useful way to understand the terminology of invasive-probe measurement is to single out spectrum choice. Here we are concerned with the measurement of the 'Local Field Potential' (LFP) for the region of the spectrum that makes action potentials more visible. Broad bandwidth LFP measurements have become a mainstream technique and carefully crafted experiments continue to reveal a cogent picture of the potentials in the regions between neurons. These experiments have directly resulted in the terminology used to describe them. Early, well known explorations of the LFP established the terms 'single unit activity' (SUA) and 'multiple unit activity' (MUA), where the term 'unit' means neuron. The SUA and MUA imply an interest in action potentials and therefore high-frequency content (Hubel and Wiesel 1959, Hubel and Wiesel 1962). This terminology is still used today and techniques for extracting the individual 'units' from a single or multiple site electrode recording, continue to be developed e.g. (Gray, Maldonado *et al.* 1995). The usage of the acronym LFP tends to be used in reference to 'extracellular' low frequency content, generally under 300Hz. In categorizing LFP this way, it is possible to claim that cortical surface (electrocorticogram or ECoG) electrode measurements are a form of LFP, e.g. in '*Decoding Spoken Words Using Local Field Potentials Recorded from the Cortical Surface*' by (Kellis, Miller *et al.* 2010). However, nobody would apply the LFP term to the measurement of scalp EEG. Instead, EEG tends to be called 'field potential' (FP). There is some variability in terms. The phrase 'extracellular potential' or, more recently, 'extracellular field potential' can be seen (Kuokkanen, Wagner *et al.* 2010). Extracellular field potential recorded over a larger frequency range is the 'broad-band LFP' mentioned above. This is depicted in Figure 1-5 (Frohlich and McCormick 2010). Interest in the high end of the spectrum means that the 'broadband LFP' can be treated as a SUA/MUA signal. The SUA/MUA acronyms tend to be found in attempts to assign the origins of LFP action potentials to particular neurons, the intent being to understand the extent of synchrony of the contributing neurons. In contrast, the term LFP tends to be found in a context of an interest in the deeper origins of the total fields **e** and **b** in an explanation of a particular special phenomenon, say the origins of EEG.

Figure 1-5 has been reconstructed based on (Frohlich and McCormick 2010, fig 1). The raw 'extracellular' potential is shown in the top trace as 'broadband LFP' in Figure 1-5(a). It includes *all* frequency content within the limits of the measurement system and includes action potentials (be they of SUA or MUA origins), all contributions by synaptic activity (electrical and chemical), and all other incidental currents. When Figure 1-5(a) is high-pass filtered (>600Hz), the SUA/MUA high frequency components are extracted, and the result is Figure 1-5(b). When Figure 1-5(a) is low pass filtered (<600Hz), it produces the LFP, Figure 1-5(c).

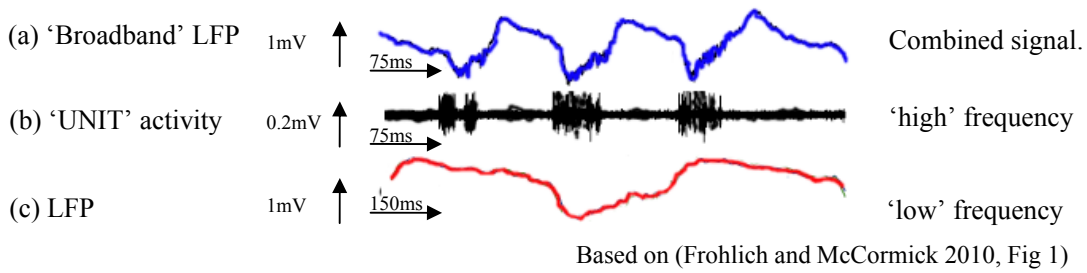

Based on (Frohlich and McCormick 2010, Fig 1)

Figure 1-5 (a) is a raw signal that has (b) high-pass filtered (e.g. > 600 Hz, (David, Malaval *et al.* 2010)) components. In (c) the LFP results by low pass filtering (a) (e.g. < 300Hz, (David, Malaval *et al.* 2010)). Depending in detailed circumstances, the activity in (b) could be bursting

from a single/few 'unit(s)', or the combined effect of many, resulting in 'multiple unit' activity. Note that the displayed signal is ferret visual cortex 'slow wave' activity, and is a simpler wave form than that of the awake, alert, behaving animal.

1.5 Ephapsis

Ephapsis was defined in 1942 in the context of an investigation of axon-axon contact coupling that can be considered qualitatively and quantitatively different to normal synapses (Arvanitaki 1942). At that time they were regarded as 'artificial synapses' (Cowan, Südhof *et al.* 2001, p71). In a neural context, ephapsis originally meant functional connectedness between physically juxtaposed excitable cells that is not mediated by the usual forms of synapse (chemical synapse or electrical/gap junction) (Jefferys 1995). This arose in order to accurately diagnose pathological nerve communications; cytoplasms communicating because of damaged or malformed cellular processes (say a crushed or demyelinated nerve trunk). Synaptic activity is to the synapse as ephaptic activity is to the 'ephapse'. Recent-era usage of the term has expanded to include non-pathological endogenous electromagnetic (line-of-sight) communication between normal excitable cells that are not necessarily apposed, but can be considerable distance apart (Anastassiou, Perin *et al.* 2011, Holt 1998(Ch2), Milstein and Koch 2008). Other literature can report results of examination of precisely the same phenomenon and not use the term ephapsis at all, for example (Frohlich and McCormick 2010).

Electromagnetic coupling is ubiquitous in nature. Even 'touching', in the usual sense, is the entwining of electromagnetic fields. An example is when one picks up a pen. The field origins (the pen-inorganic, the hand-cells) approach each other and when fully engaged, joint behaviour ensues. In contrast, in an excitable cell context, the 'touching' is when the field origin (again cells) remains stationary but the fields extend, interact and mutually influence their cellular originators. The effects is indistinguishable from the mechanical 'touch'. It is merely the mechanism of field interaction that varies. Electromagnetic coupling in other contexts is simply called electromagnetic coupling. The fundamental nature of the coupling is invariant to its context. It is not clear why a neurobiological setting needs to expropriate the term 'ephapsis' originally defined for a medical/pathological context. This terminological issue cannot be resolved here, but was recognised some time ago, with the suggestion that the terms 'field effect' or 'electrical interaction' were adequate in an excitable cell context (Bennett 2000, Faber and Korn 1989). For the purposes of this thesis, the term ephapsis will no longer be used. In terms of a possible future agreement about terminology, ephapsis is taken here to refer to line-of sight EM coupling via the spectral content associated with the excitable cell tissue endogenous EM phenomena that originate and convey the LFP. This confines the spectral range to the tens of kHz and therefore excludes coupling by higher frequency endogenous EM phenomena such as biophotons. Ephaptic transmission therefore refers to the aforementioned syncytial communication mechanism based on EM coupling effects.

1.6 Perspectives on the state of the science of brain EM fields.

An examination of the history reveals that the endogenous EM fields have, for a variety of reasons, been unable to find their appropriate scientific place within the multitude of competing phenomena involved in neural dynamics. It is via the history that we can get an idea of the impact that a change of status will have on the remainder of the science of neural dynamics. There is only one review paper that has examined the sequence of mid twentieth century circumstances in an attempt to explain how field effects remained under-explored to the observed extent. In 1989, Faber and Korn observed that the initial revealing of field-effect interactions occurred during the final stages of a much larger battle over the nature of the physical connection between neurons (Faber and Korn 1989). This was a battle between two options: (a) chemically mediated and (b) electrically mediated interneural communication. MVL Bennett cites that the concept of a distinction between electrical and chemical transmission between excitable cells can be found as far back as the mid nineteenth century (Bennett 1977). The electrical/chemical coupling distinction was being vigorously debated, e.g. Eccles (Eccles 1948, Eccles 1949) (see (Nelson 1966) for a short review in the introduction). To escalate the stakes

even further, the battle was also intimately involved in a second issue that had become known as the 'neuron doctrine' and also dated back into the 19th century.

The neuron doctrine has its beginnings in the 19th century works of the Spanish anatomist Ramon y Cahal, who saw neurons as an anatomically and functionally distinct unit. He saw communication with its surrounds as necessitating an explicit linkage between cell boundaries. To believe this to be the case was to be an advocate of the 'neuron doctrine'. The alternate view, promulgated most famously by Italian physician Camillo Golgi (1843-1926), was one of a cellular syncytium (Jefferys 1995, p690) with reticulation throughout anatomically continuous (joined) neural structures. It was thought that the reticulating cytoplasm of the network could support electrical activity in a manner consistent with observations. Both the 'neuron doctrine' and the issue of the synapse and chemical transmission were not completely resolved until the electron microscope became available and was applied using new fixation techniques. Only then could the chemical synapse and the non-reticular nature of neuron communication be convincingly visualised at the ultra-structure level for the first time (DeRobertis and Bennett 1955). The final confirmation of the chemical synapse meant that Cahal was right. After another half a century, retrospective closure occurred in the 2005 anniversary of the neuron doctrine (Bullock, Bennett *et al.* 2005).

The two issues of electrical/chemical transmission and the neuron doctrine debate were also joined by a third, fourth, fifth and sixth issue. This created a remarkably robust atmosphere conducive to the sidelining of the study of field effects. The third issue is that shortly before the chemical synapse was confirmed, the major breakthroughs of Hodgkin and Huxley occurred (Hodgkin and Huxley 1952a, Hodgkin and Huxley 1952b, Hodgkin and Huxley 1990, Hodgkin, Huxley *et al.* 1952). In accurately characterising the dynamics of membrane permeability, this work explained the fundamental basis of spike propagation. This work led to the establishment of an entire modelling paradigm: compartmental 'transmission-line' modelling that is now within a large body of work that operates under the rubric 'connectionism'. The fourth confound to EM field effect communication is the discovery of the 'electrical synapse'. The first anatomical distinction between the 'electrical' synapse (gap junction) and the 'chemical' synapse possibly occurred around 1953, in an early electron microscopy study by Robertson (Robertson 1953) (see also the early review by Bennett in 1977 (Bennett 1977)). What Robertson called 'polarised' and 'non-polarised' synapses later become chemical and electrical synapses, respectively. A recent personal history/review by Bennett cites the first conclusive evidence for electrical synapses was by (Watanabe 1958) and (Furshpan and Potter 1959). Difficulties in clarifying gap junction anatomical structure were still evident a decade later in 1967, even though gap junctions are prolifically expressed throughout species and throughout anatomical regions. Gap junctions electrically unify cell cytoplasm to some extent, and their functional, if not physical syncytial property is well recognised (Bennett 2000, Fig 3).

The *fifth* confound is that the 'extracellular' electric field magnitudes are small and expressed over short distances. It was relatively easy to make an argument that their functional impact is negligible. If extracellular endogenous electric fields are to be functionally/causally active, then one immediately wonders what the necessary magnitude of such a field must be. This question connects us to the very earliest attempts to quantify the effect using applied exogenous fields by Terzuolo and Bullock in 1956, who concluded two things that empirical evidence continues to support: (i) that the electric field strength necessary to functionally impact an already-active neuron is in the range 1-5 V/m and (ii) that significantly greater electric field magnitude (a whole order of magnitude at least) is needed in order to activate a quiescent neuron (Jefferys 1995, Terzuolo and Bullock 1956). The field magnitudes for a functional role have now been tabulated across some known brain regions, species and circumstances (Weiss and Faber 2010). But that is not all. There is a *sixth* confound. It dates back to the earliest examinations of field effects, where the 'ephapse' was defined as an 'artificial synapse' (Arvanitaki 1942). The beginnings of field-effect communications were thus established as an unnatural condition in PNS constructs.

Moving on forty years from this time of six distracting confounds, we see, in their 1989 retrospective, that Faber and Korn recognised the early rejection of a functional role for field-effects and their relegation to 'epiphenomenon' status. In respect of what is called the 'strong assertions' of the 1930-1950 era, that field effects have a physiological role in CNS tissue, they observe:

> *However, once chemical synaptic transmission in the CNS was clearly demonstrated, with the early intracellular recordings, these strong assertions were quickly abandoned (Brock, Coombs et al. 1952), and the artificial conditions in which electrical interactions had been demonstrated led most investigators to reject the basic concept itself.*
>
> (Faber and Korn 1989)

In 1989 Faber and Korn present, fait accompli, a functional role for endogenous field effect communications, in a manner quite visible to physiologists. This was based on a steady flow of results supporting a physiological role starting in the period from 1963 (Faber and Korn 1989) to 1966 (Jefferys 1995). Further support comes in 1995 in another review in which 'ephaptic coupling' was clearly distinguished from 'field coupling' (Jefferys 1995). Jefferys confirms the (fast-timescale) functional role for endogenous fields and discusses the same kinds of roles in excitability and cell growth cues and other role for EM effects, although he confined the use of the term ephapse to the 'close apposition' situation for which the word ephapsis was originally coined. He also recognized the inconsistency of the terminology usage in the literature.

It appears to be the case that the six original confounds, combined with forty years of development in cable-equation/connectionist neural modelling, have been strangely acculturated, creating a pair of competing science groups. Group (i) finds the evidence for field-effect communication unconvincing. Group (ii) finds the evidence for field-effect communication compelling. The unhelpful nature of this bifurcation became severe enough for one senior researcher to speak out:

> *The dichotomy between two groups of workers on neuroelectrical activity is retarding progress. To study the interrelations between neuronal unit spike activity and compound field potentials of cell populations is both unfashionable and technically challenging. Neither of the mutual disparagements is justified: that spikes are to higher functions as the alphabet is to Shakespeare and that slow field potentials are irrelevant epiphenomena. Spikes are not the basis of the neural code but of multiple codes that coexist with nonspike codes. Field potentials are mainly information-rich signs of underlying processes, but sometimes they are also signals for neighboring cells, that is, they exert influence. This paper concerns opportunities for new research with many channels of wide-band (spike and slow wave) recording. A wealth of structure in time and three-dimensional space is different at each scale-micro-, meso-, and macroactivity.*
>
> (Bullock 1997)

When the literature is inspected it is difficult to find signs of any serious explicit conflict. Instead, what is visible is various researchers 'talking past' each other. Bullock's plea failed to eliminate the behaviour, and it is still easily visible in the first years of the twenty first century. The standard text on EEG phenomena continues to regard the endogenous fields as an epiphenomenon (Niedermeyer and da Silva 2005) or speculative (Nunez and Srinivasan 2006). A 2004 review of electrical coupling and neuronal synchronization focussed almost entirely on gap junctions. The existence of field coupling was mentioned once, in passing, as a 'spillover effect' (Bennett and Zukin 2004). In another review paper on neuronal oscillations in cortical networks, field effect coupling is simply not mentioned, in contrast to synaptic coupling (Buzsaki and Draguhn 2004). Even now, those recognising the validity of field coupling can be regarded as delivering 'hypothesis and theory' (Weiss and Faber 2010). At the same time, EM field effects continue to have regular recognition as a causal agent (Anastassiou, Montgomery *et al.* 2010, Anastassiou, Perin *et al.* 2011, Aronsson and Liljenstrom 2001, Bikson, Inoue *et al.* 2004, Bishop and Oleary 1950, Faber and Korn 1989, Francis, Gluckman *et al.* 2003, Frohlich and McCormick 2010, Jefferys 1981, Jefferys 1995, Jefferys and Haas 1982, McIntyre and Grill 1999, Noebels and Prince 1978, Parra and Bikson 2004, Rall and Shepherd 1968, Reato, Rahman *et al.* 2010, Taylor and Dudek 1982, Terzuolo and Bullock 1956). This literature has now escalated the empirical proof of EM field coupling causal efficacy to the point that continuing to ignore it is becoming a little unreasonable, especially when the new evidence is viewed in light of the decades of support.

The overall view of the process therefore presents as a chronically unreconciled collection of contradictory scientific positions about a single issue. This is hardly new in science. To break the deadlock, we can note that the invariant background issue that has persisted throughout is that there is still no specific mechanism held accountable for the endogenous EM fields. Thus, the above potted history speaks its final word on the motivation behind this thesis: Once the mechanism responsible for the EM fields is delineated, then the science can finally go back over all the contexts and begin to construct and quantify an the role of the EM fields in all the areas in which it has been examined.

1.6.1 The state of recent literature

In the past decade there have been relatively few centres of focused empirical and theoretical activity directed at the elaboration of the causal origins of the brain's endogenous fields. The most active and consistent long term effort has been at the Koch laboratory at Caltech[1], variously engaging with the Buzsaki Laboratory at Rutgers[2]. From the point of view of this thesis, the Koch Lab's literature trail is visible in the lead-author publications of Gary Holt in the late 1990s (Holt and Koch 1999)), Karl Gold in the early-mid 2000s (Gold, Henze *et al.* 2006) and Joshua Milstein (Milstein and Koch 2008). Currently, Costas Anastassiou (Anastassiou, Perin *et al.* 2011) is continuing this line of research by quantifying EM coupling effects. The most significant contribution to the origins of the LFP by this group is the 'Line Source Approximation' (LSA) (Holt 1998, App C), where the transmembrane current is isotropically idealised by projecting it onto the centreline of a compartment in a compartmental model. The LSA method has its origins in work modeling the potentials produced by nerve trunks (Trayanova, Henriquez *et al.* 1990). The LSA method claims to adequately generate LFP values about 1μm from the line source (Holt and Koch 1999). This technique remains the state of the art in source mechanism models for transmembrane currents. It will be seen that this thesis advances the modelling of transmembrane currents to the next level of accuracy and realism, where the LSA might become a far-field version accurate only at mm scales and above, where its actual causal influence may be negligible.

The work of Milstein and Koch uses the same compartmental model neuron (D151) as this thesis and it also targets the spatiotemporal expression of the electric field due to an action potential (Milstein and Koch 2008). Similar to this thesis, (Milstein and Koch 2008) uses volume conduction and a compartmental neuron model generating action potential currents to capture action potential-related LFP spatiotemporal dynamics. The work compares well in these areas. However, their chosen technique contrasts with the upcoming work in two main ways. First, it uses a different expression relating current sources to field potentials. Second, the Milstein paper utilises a harmonic decomposition of the spatiotemporal field.

While apparently offering interesting benchmark result for this thesis, the model neuron is modified in ways that make comparison impossible. The technique described in the paper duplicates dendrite structures, mirroring them and locating them in space in a way that renders the field expression symmetric in the azimuth direction (rotationally around the direction of the axon). Doing this has two effects. (1) The current in each copied compartment adds artificially to the overall field expression. It is not obvious whether this was compensated for in the computations. (2) The harmonic decomposition loses all azimuth terms, which significantly reduces the computational complexity and would be quite acceptable if neurons had no azumuthal complexity in their field expression. In the upcoming work, neurons are shown to be capable of exactly that kind of complexity. The limitations of the approach were recognised by the authors, and their final comment is prophetic:

> *Unfortunately, due to the complexity of the current dynamics displayed by the model neuron we have used for this study, it is difficult to infer how these slower processes would affect the extracellular fields without fully simulating these fields.*
>
> (Milstein and Koch 2008, page 2083)

This thesis sets about establishing and testing a process to do exactly what they suggest.

[1] www.klab.caltech.edu

[2] http://osiris.rutgers.edu/frontmid/indexmid.html

In Europe, a separate, parallel examination of brain tissue EM fields was performed by lead author Claude Bedard through the mid-2000s (Bedard and Destexhe 2009, Bedard, Kroger *et al.* 2004, Bedard, Kroger *et al.* 2006, Bedard, Rodrigues *et al.* 2010). The work is less concerned with originating mechanisms than it is with devising electrical models that account for (in the sense of consistency with prediction) the frequency and temporal content and the spatial scale invariance/variation of the EM field system. The journal editorial of the Journal of Computational Neuroscience (Vol 29, No. 3) provides a useful 'state of play' summary, where the under-determination of the origins of the EM fields (as witnessed in the LFP) remained an issue:

> *Recordings of extracellular potentials have been, and still are, a main workhorse in the quest for understanding how the brain works. The high-frequency part of the signal, the multi-unit activity (MUA), mainly reflects firing of action potentials in the vicinity of the electrode. The low frequency part, the local-field potential (LFP), appears largely to reflect subthreshold activity from a larger group of surrounding neurons. Despite their long history in neuroscience, these extracellular potentials are still not well understood. What can the LFP tell us about the underlying activity in neurons and neuronal networks? Which neurons dominate the MUA?*
>
> ...
>
> *One of the important questions addressed is the biophysical bases of the LFP. While there is an agreement concerning the role of transmembrane currents as sources of the extracellular potentials, the filtering effects of the extracellular medium and its other effects on the recordings, as well as the effect of neuronal morphology, are still highly debated.*
>
> (Einevoll, Wojcik *et al.* 2010, page 367)

The McCormick Lab at Yale recently executed a very thorough empirical analysis of EM coupling in the efforts of Flavio Frohlich (Frohlich and McCormick 2010). This, together with the Anastassiou work (Anastassiou, Montgomery *et al.* 2010, Anastassiou, Perin *et al.* 2011), delivers empirical evidence that supports the historical advocates of active EM coupling, rather than its detractors. At least one of the historical enthusiasts for active EM coupling, Donald Faber, has joined the trail of convergence on active EM field effects in work with Shennan Weiss (Faber and Korn 1989, Korn and Faber 1980, Weiss and Faber 2010). The work reveals the beginnings of a possible future for a system of excitable cell tissue classification based on the extent to which EM coupling plays functional role dependent on field strengths and cell densities throughout the nervous system.

1.7 Chapter summary

This chapter revealed the need to make progress in isolating a specific originating mechanism for the endogenous EM field system of excitable cell tissue. The motivation to pursue this goal is that, despite a very long period of study, no specific mechanism has yet been isolated. The literature reveals a slow convergence on the 'transmembrane current' origin of extracellular potentials. That said, exactly which currents (capacitative, sodium, calcium, etc), which kind (synapse, action potential, gap junction) and which locations (everywhere, initial segment, nodes of Ranvier, post-synaptic density, gap junction plaque, etc.) remains undefined. Interestingly, the recent literature does not address any of these issues, nor does it offer a way to analyse the differences or relative contribution of competing possibilities. This thesis begins the process of addressing this aspect of the science.

A need has been identified for a method to quantify, with biophysics, the origin of the EM fields. This will then facilitate later quantitative analyses of the EM coupling influences and functional roles in specific contexts. To begin, this chapter introduced the molecular and cellular detail of the tissue within which an endogenous EM field is expressed by the position and motion of ions in water and across membranes. We have seen how the tissue is a large collection of tortuously apposed cells whose internal medium is an electrolyte called the 'intracellular space' or ICS. The tortuous cell apposition forms a foam electrolyte bubble complex with a wall thickness of roughly $1/20^{th}$ of a micron. This foam is called the 'extracellular space'. We know that ions are trafficked (1) across the

5nm cell membranes, (2) within the fine ECS fluid (the surface of the ‘bubbles’) and (3) within ICS. The ion density profiles and ion motion define all of the directly functionally relevant currents in the tissue. This stock-take accounts for all of the possible sources of EM field. Therefore, they must originate the EM fields of the tissue. The question is, which of the various charge densities and currents dominate the production of the electric and magnetic field. This requires more investigation of the electrical particulars of the tissue in the context of the application of Maxwell’s equations.

1.8 Chapter bibliography

Agnati, L. F. and Fuxe, K. (2000) Volume Transmission as a Key Feature of Information Handling in the Central Nervous System, Possible New Interpretive Value of the Turing's B-Type Machine. In L. F. Agnati, K. Fuxe, C. Nicholson, and E. Sykova (eds.). *Volume Transmission Revisited*, Elsevier, Amsterdam ; New York.

Aidley, D. J., The Physiology of Excitable Cells, 4th ed., Cambridge University Press, New York, 1998, pp. xii, 477.

Anastassiou, C. A., Montgomery, S. M., Barahona, M., Buzsaki, G. and Koch, C. 'The Effect of Spatially Inhomogeneous Extracellular Electric Fields on Neurons', *Journal of Neuroscience* vol. 30, no. 5, 2010. 1925-1936.

Anastassiou, C. A., Perin, R., Markram, H. and Koch, C. 'Ephaptic Coupling of Cortical Neurons', *Nature Neuroscience* vol. 14, no. 2, 2011. 217-223.

Aronsson, P. and Liljenstrom, H. 'Effects of Non-Synaptic Neuronal Interaction in Cortex on Synchronization and Learning', *Biosystems* vol. 63, no. 1-3, 2001. 43-56.

Arvanitaki, A. 'Effects Evoked in an Axon by the Activity of a Contiguous One', *Journal of Neurophysiology* vol. 5, no. 2, 1942. 89-108.

Bach-Y-Rita, P. 'Nonsynaptic Diffusion Neurotransmission in the Brain: Functional Considerations', *Neurochemical Research* vol. 26, no. 8-9, 2001. 871-873.

Bedard, C. and Destexhe, A. 'Macroscopic Models of Local Field Potentials and the Apparent 1/F Noise in Brain Activity', *Biophysical Journal* vol. 96, no. 7, 2009. 2589-2603.

Bedard, C., Kroger, H. and Destexhe, A. 'Modeling Extracellular Field Potentials and the Frequency-Filtering Properties of Extracellular Space', *Biophysical Journal* vol. 86, no. 3, 2004. 1829-1842.

Bedard, C., Kroger, H. and Destexhe, A. 'Model of Low-Pass Filtering of Local Field Potentials in Brain Tissue', *Physical Review E* vol. 73, no. 5, 2006.

Bedard, C., Rodrigues, S., Roy, N., Contreras, D. and Destexhe, A. 'Evidence for Frequency-Dependent Extracellular Impedance from the Transfer Function between Extracellular and Intracellular Potentials', *Journal of Computational Neuroscience* vol. 29, no. 3, 2010. 389-403.

Bennett, M. V. L. (1977) Electrical Transmission: A Functional Analysis and Comparison with Chemical Transmission. In J. M. Brookhart, V. B. Mountcastle, and E. R. Kandel (eds.). *Handbook of Physiology. Section 1: The Nervous System. Volume 1. Cellular Biology of Neurons, Part 1.*, American Physiological Society Bethesda, Md, Baltimore.

Bennett, M. V. L. 'Electrical Synapses, a Personal Perspective (or History)', *Brain Research Reviews* vol. 32, no. 1, 2000. 16-28.

Bennett, M. V. L. and Zukin, R. S. 'Electrical Coupling and Neuronal Synchronization in the Mammalian Brain', *Neuron* vol. 41, no. 4, 2004. 495-511.

Bignami, A. 'Glial Cells in the Central Nervous System', *Discussions in neuroscience* vol. 8, 1991. 1-45.

Bikson, M., Inoue, M., Akiyama, H., Deans, J. K., Fox, J. E., Miyakawa, H. and Jefferys, J. G. R. 'Effects of Uniform Extracellular Dc Electric Fields on Excitability in Rat Hippocampal Slices in Vitro', *Journal of Physiology-London* vol. 557, no. 1, 2004. 175-190.

Bishop, G. H. and Oleary, J. L. 'Tthe Effects of Polarizing Currents on Cell Potentials and Their Significance in the Interpretation of Central Nervous System Activity', *Electroencephalography and Clinical Neurophysiology* vol. 2, no. 4, 1950. 401-416.

Brock, L. G., Coombs, J. S. and Eccles, J. C. 'The Recording of Potentials from Motoneurones with an Intracellular Electrode', *Journal of Physiology-London* vol. 117, no. 4, 1952. 431-460.

Bullock, T. H. 'Signals and Signs in the Nervous System: The Dynamic Anatomy of Electrical Activity Is Probably Information-Rich', *Proceedings of the National Academy of Sciences of the United States of America* vol. 94, no. 1, 1997. 1-6.

Bullock, T. H., Bennett, M. V. L., Johnston, D., Josephson, R., Marder, E. and Fields, R. D. 'The Neuron Doctrine, Redux', *Science* vol. 310, no. 5749, 2005. 791-793.

Bushong, E. A., Martone, M. E., Jones, Y. Z. and Ellisman, M. H. 'Protoplasmic Astrocytes in Ca1 Stratum Radiatum Occupy Separate Anatomical Domains', *Journal of Neuroscience* vol. 22, no. 1, 2002. 183-192.

Buzsaki, G. and Draguhn, A. 'Neuronal Oscillations in Cortical Networks', *Science* vol. 304, no. 5679, 2004. 1926-1929.

Cohen, D. 'Magnetoencephalography - Evidence of Magnetic Fields Produced by Alpha-Rhythm Currents', *Science* vol. 161, no. 3843, 1968. 784-&.

Coombes, S. 'Waves, Bumps, and Patterns in Neural Field Theories', *Biological Cybernetics* vol. 93, no. 2, 2005. 91-108.

Cowan, W. M., Südhof, T. C., Stevens, C. F. and Howard Hughes Medical Institute., Eds. (2001). Synapses. Baltimore, Johns Hopkins University Press.

David, S. V., Malaval, N. and Shamma, S. A. 'Decoupling Action Potential Bias from Cortical Local Field Potentials', *Computational Intelligence and Neuroscience* vol. 2010, no. ID 393019, 2010. 12.

de Munck, J. C., Vijn, P. C. M. and Da Silva, F. H. L. 'A Random Dipole Model for Spontaneous Brain Activity', *IEEE Transactions on Biomedical Engineering* vol. 39, no. 8, 1992. 791-804.

Deco, G., Jirsa, V. K., Robinson, P. A., Breakspear, M. and Friston, K. 'The Dynamic Brain: From Spiking Neurons to Neural Masses and Cortical Fields', *Plos Computational Biology* vol. 4, no. 8, 2008.

DeRobertis, E. D. P. and Bennett, H. S. 'Some Features of the Submicroscopic Morphology of Synapses in Frog and Earthworm', *Journal of Biophysical and Biochemical Cytology* vol. 1, no. 1, 1955. 47-56.

Eccles, J. C. 'Conduction and Synaptic Transmission in the Nervous System', *Annual Review of Physiology* vol. 10, 1948. 93-116.

Eccles, J. C. 'A Review and Restatement of the Electrical Hypotheses of Synaptic Excitatory and Inhibitory Action', *Archives Des Sciences Physiologiques* vol. 3, no. 4, 1949. 567-584.

Einevoll, G. T., Wojcik, D. K. and Destexhe, A. 'Modeling Extracellular Potentials', *Journal of Computational Neuroscience* vol. 29, no. 3, 2010. 367-369.

Eisenberg, R. S., Barcilon, V. and Mathias, R. T. 'Electrical-Properties of Spherical Syncytia', *Biophysical Journal* vol. 25, no. 1, 1979. 151-180.

Ermentrout, B. 'Neural Networks as Spatio-Temporal Pattern-Forming Systems', *Reports on Progress in Physics* vol. 61, no. 4, 1998. 353-430.

Ermentrout, G. B. and Kleinfeld, D. 'Traveling Electrical Waves in Cortex: Insights from Phase Dynamics and Speculation on a Computational Role', *Neuron* vol. 29, no. 1, 2001. 33-44.

Faber, D. S. and Korn, H. 'Electrical-Field Effects - Their Relevance in Central Neural Networks', *Physiological Reviews* vol. 69, no. 3, 1989. 821-863.

Francis, J. T., Gluckman, B. J. and Schiff, S. J. 'Sensitivity of Neurons to Weak Electric Fields', *Journal of Neuroscience* vol. 23, no. 19, 2003. 7255-7261.

Freeman, A. J., Mass Action in the Nervous System : Examination of the Neurophysiological Basis of Adaptive Behavior through the Eeg, Academic Press, New York, 1975

Frohlich, F. and McCormick, D. A. 'Endogenous Electric Fields May Guide Neocortical Network Activity', *Neuron* vol. 67, no. 1, 2010. 129-143.

Furshpan, E. J. and Potter, D. D. 'Transmission at the Giant Motor Synapses of the Crayfish', *Journal of Physiology-London* vol. 145, no. 2, 1959. 289-&.

Geddes, L. A. and Baker, L. E. 'Specific Resistance of Biological Material-a Compendum of Data for Biomedical Engineer and Physiologist', *Medical & Biological Engineering* vol. 5, no. 3, 1967. 271-&.

Gold, C., Girardin, C. C., Martin, K. A. C. and Koch, C. 'High-Amplitude Positive Spikes Recorded Extracellularly in Cat Visual Cortex', *Journal of Neurophysiology* vol. 102, no. 6, 2009. 3340-3351.

Gold, C., Henze, D. A. and Koch, C. 'Using Extracellular Action Potential Recordings to Constrain Compartmental Models', *Journal of Computational Neuroscience* vol. 23, no. 1, 2007. 39-58.

Gold, C., Henze, D. A., Koch, C. and Buzsaki, G. 'On the Origin of the Extracellular Action Potential Waveform: A Modeling Study', *Journal of Neurophysiology* vol. 95, no. 5, 2006. 3113-3128.

Gray, C. M., Maldonado, P. E., Wilson, M. and McNaughton, B. 'Tetrodes Markedly Improve the Reliability and Yield of Multiple Single-Unit Isolation from Multi-Unit Recordings in Cat Striate Cortex', *Journal of Neuroscience Methods* vol. 63, no. 1-2, 1995. 43-54.

Haas, L. F. 'Hans Berger (1873-1941), Richard Caton (1842-1926), and Electroencephalography. (Neurological Stamp)', *Journal of Neurology, Neurosurgery and Psychiatry* vol. 74, no. 1, 2003. 9(1).

Hamalainen, M., Hari, R., Ilmoniemi, R. J., Knuutila, J. and Lounasmaa, O. V. 'Magnetoencephalography - Theory, Instrumentation, and Applications to Noninvasive Studies of the Working Human Brain', *Reviews of Modern Physics* vol. 65, no. 2, 1993. 413-497.

Harris, K. M., Cruce, W. L. R., Greenough, W. T. and Teyler, T. J. 'A Golgi Impregnation Technique for Thin Brain-Slices Maintained Invitro', *Journal of Neuroscience Methods* vol. 2, no. 4, 1980. 363-371.

Hille, B., Ion Channels of Excitable Membranes, Third ed., Sinauer Associates, Inc., Sunderland, MA., 2001

Hodgkin, A. L. and Huxley, A. F. 'Currents Carried by Sodium and Potassium Ions through the Membrane of the Giant Axon of Loligo', *Journal of Physiology-London* vol. 116, no. 4, 1952a. 449-472.

Hodgkin, A. L. and Huxley, A. F. 'The Dual Effect of Membrane Potential on Sodium Conductance in the Giant Axon of Loligo', *Journal of Physiology-London* vol. 116, no. 4, 1952b. 497-506.

Hodgkin, A. L. and Huxley, A. F. 'A Quantitative Description of Membrane Current and Its Application to Conduction and Excitation in Nerve (Reprinted from Journal of Physiology, Vol 117, Pg 500-544, 1952)', *Bulletin of Mathematical Biology* vol. 52, no. 1-2, 1990. 25-71.

Hodgkin, A. L., Huxley, A. F. and Katz, B. 'Measurement of Current-Voltage Relations in the Membrane of the Giant Axon of Loligo', *Journal of Physiology-London* vol. 116, no. 4, 1952. 424-448.

Holt, G. R. (1998) A Critical Reexamination of Some Assumptions, Implications of Cable Theory in Neurobiology. California Institute of Technology, Pasedena, California.

Holt, G. R. and Koch, C. 'Electrical Interactions Via the Extracellular Potential near Cell Bodies', *Journal of Computational Neuroscience* vol. 6, no. 2, 1999. 169-184.

Hormuzdi, S. G., Filippov, M. A., Mitropoulou, G., Monyer, H. and Bruzzone, R. 'Electrical Synapses: A Dynamic Signaling System That Shapes the Activity of Neuronal Networks', *Biochimica Et Biophysica Acta-Biomembranes* vol. 1662, no. 1-2, 2004. 113-137.

Hubel, D. H. 'Tungsten Microelectrode for Recording from Single Units', *Science* vol. 125, no. 3247, 1957. 549-550.

Hubel, D. H. and Wiesel, T. N. 'Receptive Fields of Single Neurones in the Cat's Striate Cortex', *Journal of Physiology-London* vol. 148, no. 3, 1959. 574-591.

Hubel, D. H. and Wiesel, T. N. 'Receptive Fields, Binocular Interaction and Functional Architecture in Cat's Visual Cortex', *Journal of Physiology-London* vol. 160, no. 1, 1962. 106-&.

Jackson, J. D., Classical Electrodynamics, 3rd ed., Wiley, New York, 1999

Jefferys, J. G. R. 'Influence of Electric-Fields on the Excitability of Granule Cells in Guinea-Pig Hippocampal Slices', *Journal of Physiology-London* vol. 319, no. OCT, 1981. 143-152.

Jefferys, J. G. R. 'Nonsynaptic Modulation of Neuronal-Activity in the Brain - Electric Currents and Extracellular Ions', *Physiological Reviews* vol. 75, no. 4, 1995. 689-723.

Jefferys, J. G. R. and Haas, H. L. 'Synchronized Bursting of Ca1 Hippocampal Pyramidal Cells in the Absence of Synaptic Transmission', *Nature* vol. 300, no. 5891, 1982. 448-450.

Jirsa, V. K. and Haken, H. 'A Derivation of a Macroscopic Field Theory of the Brain from the Quasi-Microscopic Neural Dynamics', *Physica D* vol. 99, no. 4, 1997. 503-526.

Kandel, E. R. and Schwartz, J. H., Principles of Neural Science, 4th , International ed., McGraw-Hill, New York, 2000, pp. xli, 1414.

Katzner, S., Nauhaus, I., Benucci, A., Bonin, V., Ringach, D. L. and Carandini, M. 'Local Origin of Field Potentials in Visual Cortex', *Neuron* vol. 61, no. 1, 2009. 35-41.

Kellis, S., Miller, K., Thomson, K., Brown, R., House, P. and Greger, B. 'Decoding Spoken Words Using Local Field Potentials Recorded from the Cortical Surface', *Journal of Neural Engineering* vol. 7, no. 5, 2010.

Klee, M. and Rall, W. 'Computed Potentials of Cortically Arranged Populations of Neurons', *Journal of Neurophysiology* vol. 40, no. 3, 1977. 647-666.

Korn, H. and Faber, D. S. 'Electrical-Field Effect Interactions in the Vertebrate Brain', *Trends in Neurosciences* vol. 3, no. 1, 1980. 6-9.

Kuffler, S. W. and Nicholls, J. G., From Neuron to Brain : A Cellular Approach to the Function of the Nervous System, Sinauer Associates, Sunderland, Mass., 1976, pp. xiii, 486 p.

Kuffler, S. W. and Potter, D. D. 'Glia in Leech Central Nervous System - Physiological Properties + Neuron-Glia Relationship', *Journal of Neurophysiology* vol. 27, no. 2, 1964. 290-&.

Kuokkanen, P. T., Wagner, H., Ashida, G., Carr, C. E. and Kempter, R. 'On the Origin of the Extracellular Field Potential in the Nucleus Laminaris of the Barn Owl (Tyto Alba)', *Journal of Neurophysiology* vol. 104, no. 4, 2010. 2274-2290.

Liley, D. T. J., Cadusch, P. J. and Dafilis, M. P. 'A Spatially Continuous Mean Field Theory of Electrocortical Activity', *Network-Computation in Neural Systems* vol. 13, no. 1, 2002. 67-113.

McBain, C. J., Traynelis, S. F. and Dingledine, R. 'Regional Variation of Extracellular-Space in the Hippocampus', *Science* vol. 249, no. 4969, 1990. 674-677.

McIntyre, C. C. and Grill, W. M. 'Excitation of Central Nervous System Neurons by Nonuniform Electric Fields', *Biophysical Journal* vol. 76, no. 2, 1999. 878-888.

Milstein, J. N. and Koch, C. 'Dynamic Moment Analysis of the Extracellular Electric Field of a Biologically Realistic Spiking Neuron', *Neural Computation* vol. 20, no. 8, 2008. 2070-2084.

Nedergaard, M., Ransom, B. and Goldman, S. A. 'New Roles for Astrocytes: Redefining the Functional Architecture of the Brain', *Trends in Neurosciences* vol. 26, no. 10, 2003. 523-530.

Nelson, M. J. and Pouget, P. 'Do Electrode Properties Create a Problem in Interpreting Local Field Potential Recordings?', *Journal of Neurophysiology* vol. 103, no. 5, 2010. 2315-2317.

Nelson, P. G. 'Interaction between Spinal Motoneurons of the Cat', *Journal of Neurophysiology* vol. 29, no. 2, 1966. 275-287.

Nicholson, C., Chen, K. C., Hrabetova, S. and Tao, L. (2000) Diffusion of Molecules in Brain Extracellular Space: Theory and Experiment. In L. F. Agnati, K. Fuxe, C. Nicholson, and E. Sykova (eds.). *Progress in Brain Research ; Volume Transmission Revisited*, Elsevier, Amsterdam ; New York.

Nicholson, C. and Phillips, J. M. 'Ion Diffusion Modified by Tortuosity and Volume Fraction in the Extracellular Micro-Environment of the Rat Cerebellum', *Journal of Physiology-London* vol. 321, no. DEC, 1981. 225-257.

Nicholson, C. and Sykova, E. 'Extracellular Space Structure Revealed by Diffusion Analysis', *Trends in Neurosciences* vol. 21, no. 5, 1998. 207-215.

Niedermeyer, E. and da Silva, F. H. L., Electroencephalography : Basic Principles, Clinical Applications, and Related Fields, 5th ed., Lippincott Williams & Wilkins, Philadelphia, 2005, pp. xiii, 1309 p.

Noebels, J. L. and Prince, D. A. 'Excitability Changes in Thalamocortical Relay Neurons During Synchronous Discharges in Cat Neocortex', *Journal of Neurophysiology* vol. 41, no. 5, 1978. 1282-1296.

Nunez, P. L. and Srinivasan, R., Electric Fields of the Brain : The Neurophysics of Eeg, 2nd ed., Oxford University Press, Oxford, New York, 2006

Oberheim, N. A., Wang, X. H., Goldman, S. and Nedergaard, M. 'Astrocytic Complexity Distinguishes the Human Brain', *Trends in Neurosciences* vol. 29, no. 10, 2006. 547-553.

Parra, L. C. and Bikson, M. (2004) Model of the Effect of Extracellular Fields on Spike Time Coherence. *Proceedings of the 26th Annual International Conference of the Ieee Engineering in Medicine and Biology Society, Vols 1-7*

Pesaran, B. 'Uncovering the Mysterious Origins of Local Field Potentials', *Neuron* vol. 61, no. 1, 2009. 1-2.

Purves, D., Neuroscience, 3rd ed., Sinauer Associates, Sunderland, Mass., 2004, pp. xix, 771, [737].

Rall, W. and Shepherd, G. M. 'Theoretical Reconstruction of Field Potentials and Dendrodendritic Synaptic Interactions in Olfactory Bulb', *Journal of Neurophysiology* vol. 31, no. 6, 1968. 884-&.

Reato, D., Rahman, A., Bikson, M. and Parra, L. C. 'Low-Intensity Electrical Stimulation Affects Network Dynamics by Modulating Population Rate and Spike Timing', *Journal of Neuroscience* vol. 30, no. 45, 2010. 15067-15079.

Robertson, J. D. 'Ultrastructure of Two Invertebrate Synapses', *Proceedings of the Society for Experimental Biology and Medicine* vol. 82, no. 2, 1953. 219–223.

Robinson, D. A. 'Electrical Properties of Metal Microelectrodes', *Proceedings of the Institute of Electrical and Electronics Engineers* vol. 56, no. 6, 1968. 1065-&.

Robinson, P. A., Rennie, C. J. and Wright, J. J. 'Propagation and Stability of Waves of Electrical Activity in the Cerebral Cortex', *Physical Review E* vol. 56, no. 1, 1997. 826-840.

Rosenfalck, P. 'Intra- and Extracellular Potential Fields of Active Nerve and Muscle Fibres - a Physico-Mathematical Analysis Af Different Models', *Acta Physiologica Scandinavica* vol. Supplement, 1969. 9-168.

Speckmann, E.-J. and Elgar, C. E. (2005) Introduction to the Neurophysiological Basis of the Eeg and Dc Potentials. In E. Niedermeyer, and F. H. Lopes da Silva (eds.). *Electroencephalography : Basic Principles, Clinical Applications, and Related Fields*, Lippincott Williams & Wilkins, Philadelphia.

Stead, M., Bower, M., Brinkmann, B. H., Lee, K., Marsh, W. R., Meyer, F. B., Litt, B., Gompel, J. and Worrell, G. A. 'Microseizures and the Spatiotemporal Scales of Human Partial Epilepsy', *Brain* vol. 133, 2010. 2789-2797.

Swartz, B. E. and Goldensohn, E. S. 'Timeline of the History of Eeg and Associated Fields', *Electroencephalography and Clinical Neurophysiology* vol. 106, no. 2, 1998. 173-176.

Sykova, E. 'The Extracellular Space in the Cns: Its Regulation, Volume and Geometry in Normal and Pathological Neuronal Function', *Neuroscientist* vol. 3, no. 1, 1997. 28-41.

Sykova, E. 'Extrasynaptic Volume Transmission and Diffusion Parameters of the Extracellular Space', *Neuroscience* vol. 129, no. 4, 2004. 861-876.

Sykova, E., Mazel, T., Vargova, L., Vorisek, I. and Prokopova-Kubinova, S. (2000) Extracellular Space Diffusion and Pathological States. In L. F. Agnati, K. Fuxe, C. Nicholson, and E. Sykova (eds.). *Progress in Brain Research ; Volume Transmission Revisited*, Elsevier, Amsterdam ; New York.

Sykova, E. and Nicholson, C. 'Diffusion in Brain Extracellular Space', *Physiological Reviews* vol. 88, no. 4, 2008. 1277-1340.

Sykova, E., Roitbak, T., Mazel, T., Simonova, Z. and Harvey, A. R. 'Astrocytes, Oligodendroglia, Extracellular Space Volume and Geometry in Rat Fetal Brain Grafts', *Neuroscience* vol. 91, no. 2, 1999. 783-798.

Taylor, C. P. and Dudek, F. E. 'Synchronous Neural after Discharges in Rat Hippocampal Slices without Active-Chemical Synapses', *Science* vol. 218, no. 4574, 1982. 810-812.

Terzuolo, C. A. and Bullock, T. H. 'Measurement If Imposed Voltage Gradient Adequate to Modulate Neuronal Firing', *Proceedings of the National Academy of Sciences of the United States of America* vol. 42, no. 9, 1956. 687-694.

Trayanova, N. A., Henriquez, C. S. and Plonsey, R. 'Limitations of Approximate Solutions for Computing the Extracellular Potential of Single Fibers and Bundle Equivalents', *Ieee Transactions on Biomedical Engineering* vol. 37, no. 1, 1990. 22-35.

Van Harrenveld, A. (1968) The Extracellular Space in the Vertebrate Central Nervous System. In G. H. Bourne (ed.). *The Structure and Function of Nervous Tissue*, Academic Press, New York.

Vogels, T. P., Rajan, K. and Abbott, L. F. 'Neural Network Dynamics', *Annual Review of Neuroscience* vol. 28, 2005. 357-376.

Watanabe, A. 'The Interaction of Electrical Activity among Neurons of Lobster Cardiac Ganglion', *Japanese Jounral of Physiology* vol. 8, 1958. 305-318.

Weiss, S. A. and Faber, D. S. 'Field Effects in the Cns Play Functional Roles', *Frontiers in Neural Circuits* vol. 4, 2010.

Wilson, H. R. and Cowan, J. D. 'Mathematical Theory of Functional Dynamics of Cortical and Thalamic Nervous-Tissue', *Kybernetik* vol. 13, no. 2, 1973. 55-80.

Wright, J. J., Rennie, C. J., Lees, G. J., Robinson, P. A., Bourke, P. D., Chapman, C. L., Gordon, E. and Rowe, D. L. 'Simulated Electrocortical Activity at Microscopic, Mesoscopic and Global Scales', *International Journal of Bifurcation and Chaos* vol. 14, no. 2, 2004. 853-872.

Wright, J. J., Robinson, P. A., Rennie, C. J., Cordon, E., Bourke, P. D., Chapman, C. L., Hawthorn, N., Lees, G. J. and Alexander, D. 'Toward an Integrated Continuum Model of Cerebral Dynamics: The Cerebral Rhythms, Synchronous Oscillation and Cortical Stability', *Biosystems* vol. 63, no. 1-3, 2001. 71-88.

Chapter 2

TISSUE ELECTROCHEMICAL NATURE, CURRENT ANALYSIS, MAXWELL'S EQUATIONS

"*I am as I am not*"
Heraclitis of Ephesus 535–c. 475BCE

2.1 Introduction

Exactly how is the brain's endogenous EM field system originated? Which currents and charges have a prime role? What formalisms are appropriate, at this point in history, to examine them? The previous chapter described 'single-' and 'multi-' unit recordings made in tissue. The mere fact that invasive probes can be used to support claims to have detected single-neuron activity is implicitly a cogent hint that (a) individual neurons express the fields and (b), that their contribution to the overall field system does not extend far into the bulk medium. It suggests that EM coupling effects, as a possible causal agent, are most likely to be found influential on nearest neighbours. However, this does not preclude potential influences over much greater distances by virtue of the level and kind of collaborative activity over any region and over a spatial/temporal scale of interest. With a focus on the elaboration of single-cell originating mechanisms, this chapter isolates and characterises the functionally important charges and currents in brain tissue. To discriminate their contribution to the EM field system, a distinction between coherence and synchrony is defined. With a focus on the paramembrane charge microenvironment, causal relations and relative coherence are used to isolate the charges and currents most responsible for expression of the EM field. This is provided, (a) to develop an appreciation of the complexities of line-of-sight EM communication revealed in the later modelling and (b), because the knowledge important in understanding what is abstracted away by the upcoming modelling choices, thereby facilitating an informed interpretation of results.

With the most likely currents in hand, the chapter then turns to formal electromagnetism with a view to understanding how the tissue has been traditionally treated, and whether this treatment is appropriate to reveal the field system. The traditional approach has been enacted with a view to revealing voltage and currents, not electric and magnetic fields. The traditional formalisms have not been adequately assessed from this latter perspective. With knowledge of the appropriate form of the equations of electromagnetism, the topic then turns to experimental strategy. Overall the process helps tease out an appropriate first step in the eventual full treatment of tissue field expression.

2.2 The paramembrane, ECS and ICS charge microenvironment and its basic dynamics

The relevant regions of cellular microenvironment are shown in Figure 2-1, which shows the same tissue sample shown in Chapter 1, but with compartment resting potentials shown arbitrarily allocated for indicative purposes. Within the narrow foam-like structure, proximal to the lipid bilayer, the ECS holds a large collection of various ions in solution. These ions have sister populations, of overall opposite polarity, on the other side of the adjacent sub-membrane (intracellular/cytosol) ICS (Aidley 1998, Dayan and Abbott 2001, Hille 2001, Johnston and Wu 1995). The charge population segregations are established by transmembrane ion transporters not shown in Figure 2-1.

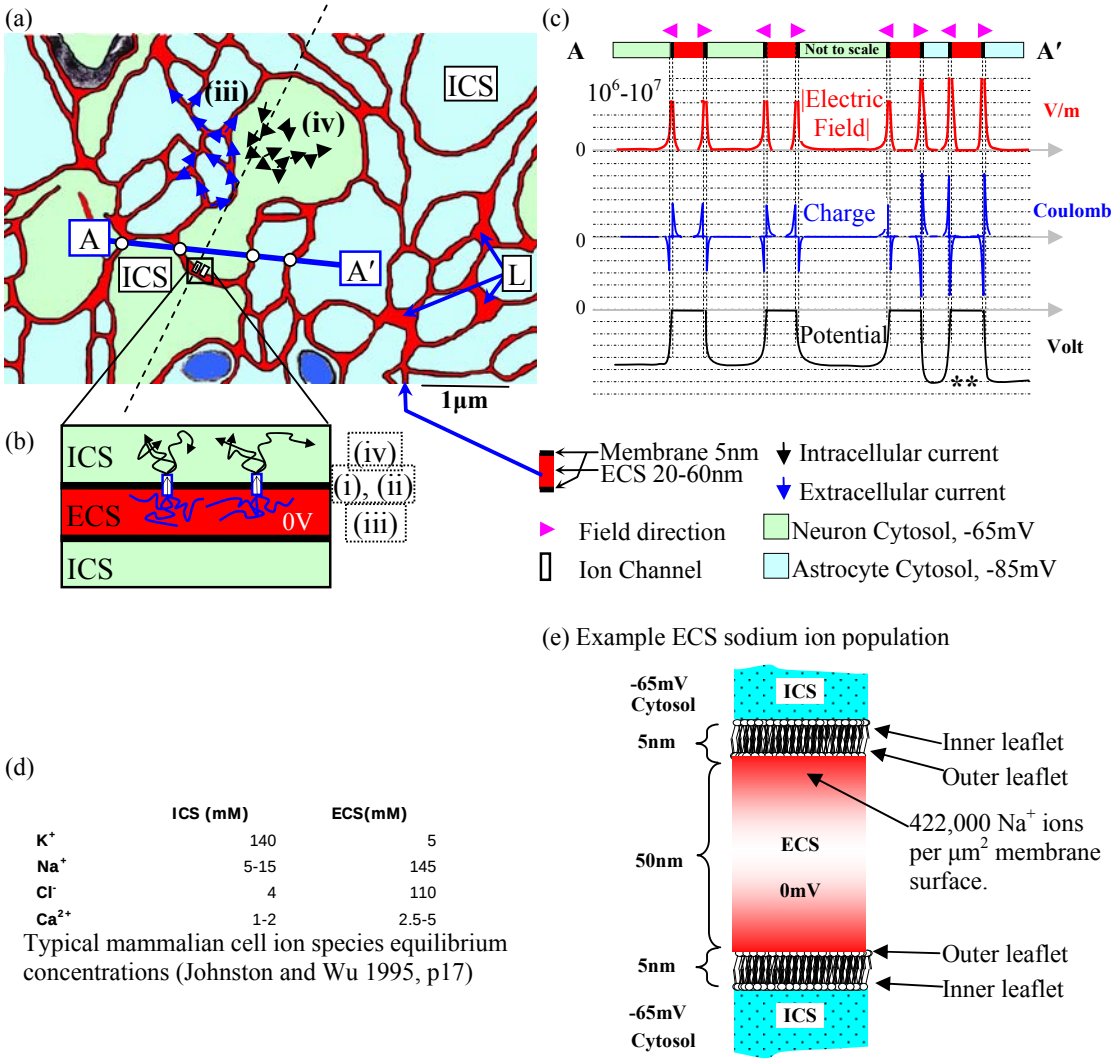

(d)

	ICS (mM)	ECS(mM)
K^+	140	5
Na^+	5-15	145
Cl^-	4	110
Ca^{2+}	1-2	2.5-5

Typical mammalian cell ion species equilibrium concentrations (Johnston and Wu 1995, p17)

Figure 2-1 (a) The equilibrium environment of neural tissue. The blue/black arrows show the general flow of ECS/ICS current resp. The green/blue regions are neuron/astrocyte cytosol that have equilibrium potentials of -65/-85mV resp. (ECS reference potential of 0V). (b) ECS/ICS currents, and their tendency to spatially decorrelate from the transmembrane current and therefore with the overall EM field structure. (c) Along A-A′, the resting potential (V, black), charge populations (Q, blue) and electric field magnitude/direction (|E|, red) are shown. The ►arrow heads indicate the direction of the resting electric field. L signifies an ECS 'lake'. (d) The equilibrium charge concentrations (Aidley 1998, Dayan and Abbott 2001, Hille 2001, Johnston and Wu 1995), and (e) the particulars of the sodium equilibrium concentration ECS profile.

Within the constraint of overall charge neutrality, small aggregate differences in ion species ratios exist across the membrane, creating the resting potential mosaic and the electric field strength and direction shown in Figure 2-1(c). This configuration creates the most energetically dense field system in any tissue: the neuron and astrocyte transmembrane electrical field, which is of the order 10^6-10^7V/m in the direction of the arrow heads (Freeman 1975, Lee, Klingler *et al.* 1994, Maggio, Borioli *et al.* 2008, Peterka, Takahashi *et al.* 2011, Pethig 1986, Romijn 2002). This store of energy is implemented in the polarisation of the membrane molecules in their role as the dielectric of a distributed capacitor. In practical applications of technology, such as fuel delivery to a car, this field, exposed to air, would be treated as a sparking hazard. Tucked away inside our cranium, however, it safely serves as an energy stockpile for field excursions into the tissue.

Discussions of equilibrium paramembrane charge populations can be found in general texts such as (Aidley 1998, Dayan and Abbott 2001, Hille 2001, Johnston and Wu 1995). The potential difference profile in Figure 2-1(c) is created and maintained by small concentration differentials between para-membrane ion species. These are cell-specific. For example, Figure 2-1(c)** shows that the membrane potential of astrocytes is roughly -85mV. This is more negative than the typical neuron resting membrane potential of about -65 mV (Kuffler and Nicholls 1976, Magistretti and Ransom 2002).

> "*Glial cells are interposed between virtually all neurons and axons, with a K^+-dominated resting membrane potential ~20 mV more negative than neurons.*"
>
> (Chen and Nicholson 2000)

Thus, the tortuous foam structured extracellular space (ECS/red) borders regions of high neuron and astrocyte resting potential. Figure 2-1(c) depicts a particular view of the configuration of charge and related phenomena along the line A-A′. From any place in the tissue, A, to any other 'line-of-sight' target, A′, involves multiple encounters with the paramembrane charge microenvironments. Along line A-A′, the resting potential (V, black), charge populations (Q, blue) and electric field magnitude/direction (|E|, red) all vary roughly as shown. Typical charge densities are expressed in Figure 2-1(d) in terms of resting/equilibrium molar concentrations. The charge density situation is shown in Figure 2-1(e) for two apposed neurons and for ECS sodium only. The apposition of two cells means that the actual total amount of charge per unit ECS volume in the Figure 2-1(e) circumstance will be roughly twice the value in the Figure 2-1(d) table. The net charge profile in Figure 2-1(c) can be found in general terms in the literature (Aidley 1998, Bedard, Kroger *et al.* 2006, Hille 2001). Figure 2-1(e) shows a small ECS patch 1μm^2 x 0.05μm across. This has a volume of 5x10^{-20}m^3. The Figure 2-1)(d)) ECS Na^+ ion concentration of 145mM corresponds to roughly 4,366,053 Na^+ ions, assuming a uniform distribution. This represents the source of all sodium ions for a region far larger than any single ion channel. A single ion channel will consume roughly 1000 ions per action potential. In principle, at, say 10Hz, the entire stocks of ion would be gone due to the operation of a single ion channel for 7 minutes. If ion stocks are to be maintained at a level consistent with long term operation at nominal cell potentials, ion stocks must be actively replenished on a continuous basis.

2.2.1 Ion hydration and solvation shells

The ions of the salts used to form the ECS/ICS electrolytes dissociate in water. The dissociated ions are highly attracted to the polarised nature of water molecules. They tend to assemble a collection of 'waters of hydration' around each ion, bonded by hydrogen bonds. This, amongst other effects, slows the mobility of the ions in the electrolyte (Hille 2001, p326-338).

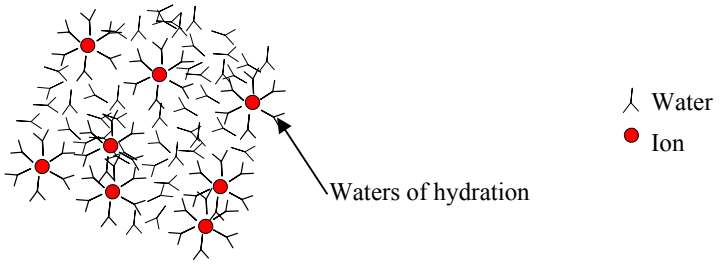

Figure 2-2 The issue of ion mobility and waters of hydration.

The details of solvation states and the dynamics of ion hydration in neural electrolytes remains a work in progress. In reaching an understanding of the processes we are largely reliant on the general principles of physical chemistry. The neural electrolyte has a degree of order that can give it a gel-like property that relates to the ordering of self-solvated water. The modern view of solvation is that water is likely to organise itself into subtle states including 'solvation shells'(Burnham, Petersen *et al.* 2006). In neural electrolytes subject to the endogenous field system, hydrated-ion mobility results from local interactions with water's solvation shells whilst the EM field system is applied to the fluid as a whole. At the atomic/molecular level, this makes the passage of ions through the electrolyte a complex process. The essential idea is that (a) the passage of ions through ECS/ICS water host medium, and (b) the passage of a *dehydrated* ion through the narrow pore of a transmembrane protein structure differ in marked ways that are important in the construction of claims about field production. ECS/ICS free-range ion electrodiffusion involves randomised molecular accelerations and collisions (with water, other ions and other local molecules). It is reasonable to consider that field dominance will depend on (a) the extent to which the ECS/ICS average inter-collision path length is comparable to pore length and (b) the extent to which ECS/ICS trajectory vectors align with the pore's trajectory. Note that unlike the pore, ECS/ICS ion paths will, during the process of pore ingress/egress, (a) have some curvature as a result of the local magnetic field (the Lorentz force) and (b) undergo changes to kinetic energy as a result of being de-/re-hydrated. The present general understanding of the relationship between the pore and its transiting ion(s) is that the pore itself replaces the hydration and solvation shell structures, providing 'virtual' hydration during pore transit (Hille 2001, p326-338). In facilitating control over the direction of motion, and to some extent the ion's velocity profile, an ion's involvement field production becomes differentiated from the free range ion behaviour. The difference is accentuated in Figure 2-1(b), which shows the effect of the reasonable expectation that the ECS/ICS portions of the trajectory of any individual ion will be comparatively randomised.

2.3 The macroscopic field system as depicted in standard texts

The generally held view in neuroscience and electroencephalography is that scalp potentials arise from simple cortical dipole dynamics that can be easily connected to the measured coarse field potential (FP) behaviour. The underlying dipole structure is usually attributed to the synchronous activity of large numbers of firing neurons that cause extended (mm scale) regions of disparate polarity across neural structures that span multiple layers of the cortex. The rationale is that simultaneous synaptic activity in apical dendrites creates one end of a dipole. The other end of the dipole is usually identified as the region of cell soma. The notional dipole results in electric field projections that span the dipole (causing current flows in the surrounding medium) and projecting through the scalp. The tangential component of the electric field then causes the small currents in the scalp that create the potentials recorded by scalp electrodes. A stylised version of the phenomenon is shown in Figure 2-3 and was based on diagrams in (Speckmann and Elgar 2005), (Nunez and Srinivasan 2006, p5) and (Kandel and Schwartz 2000, p914/5). The interesting feature of the diagram is that the endogenous field lines (both electric and magnetic) have to extend over a distance larger than the cortex that generates them. Despite the radical attenuation of the fields, measurements at the scalp are quite practical.

A useful way to calibrate diagrams such as Figure 2-3 in the context of the changes proposed here, is to consider that the physical tissue is actually a conducting foam implemented on the μm scale as shown in Figure 2-1. The actual ECS currents will be spatially decorrelated at the level of the foam. Therefore, despite the existence of an overall macroscopic dipole system in the form of Figure 2-3, the actual microscopic situation cannot be as per Figure 2-3. It is simply impossible for the microscopic currents to flow that way. This identifies a clear expectation that the microscopic field expression cannot be as per Ohm's law (see equation (2.14)). This is because the conductivity (assuming the concept is applicable) is highly inhomogeneous, time varying and anistropic at the level of the generation of the EM fields.

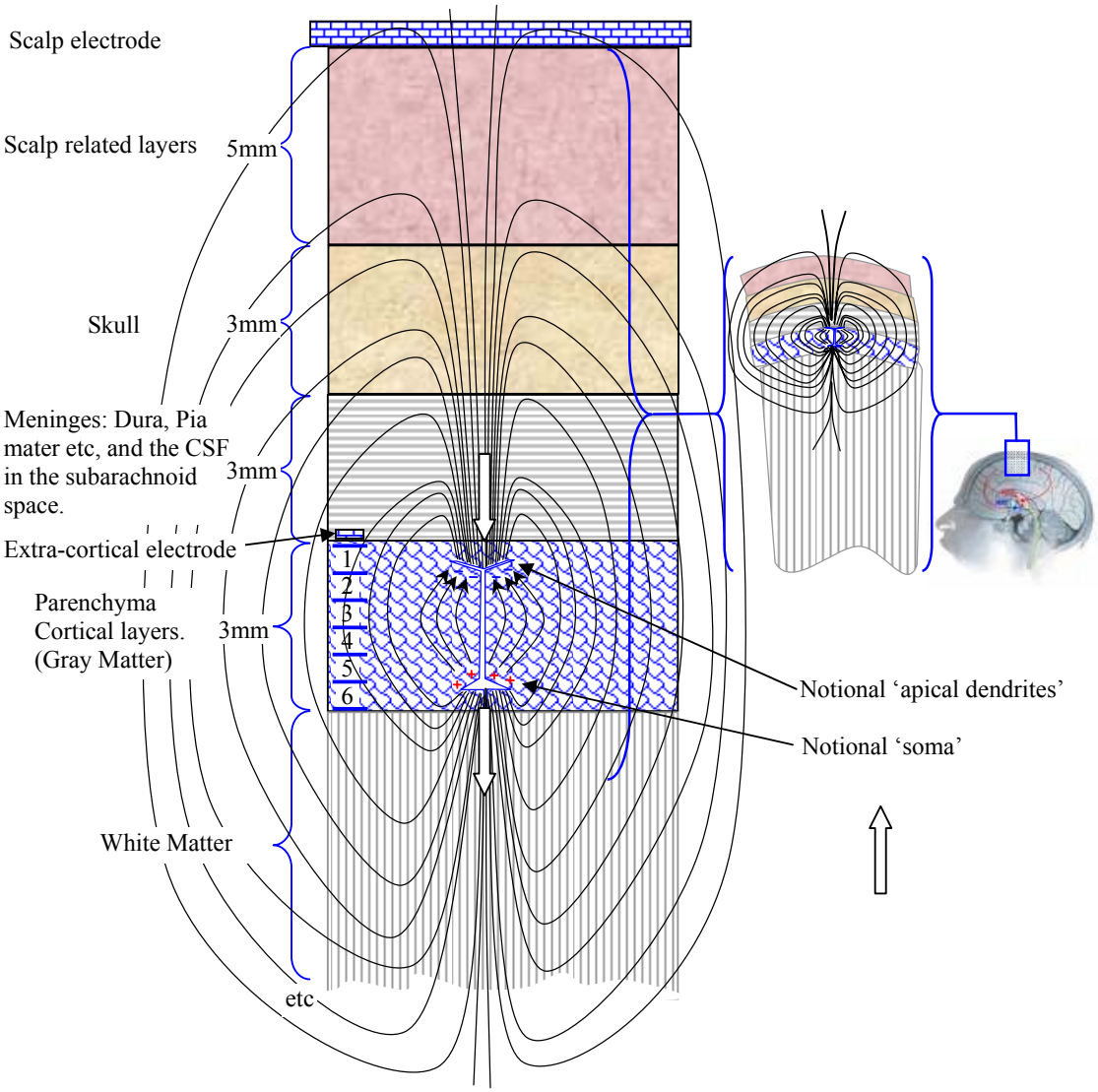

Figure 2-3 The classic explanation of bulk material human EEG field origins. The field lines originate in a dynamic collection of adjacent closely coupled virtual dipoles that relate roughly to charge populations created in cellular anatomical features in the cortical layers. The electric field lines emanate from the scalp, causing tangential currents along the conductivity of the scalp. These are averaged and measured by the coarse EEG surface electrode. Based on (Kandel and Schwartz 2000, Nunez and Srinivasan 2006, Speckmann and Elgar 2005). Not to scale.

2.4 Current: what kinds and where?

2.4.1 Distinguishing one current from another in their EM field expression.

In the neuroscience literature, the words spatial, temporal and spatiotemporal, synchrony, coherence, resonance, oscillation, reciprocation and their relationship with correlation are not always defined or distinguished consistently. There is a level of interchangability in their usage. Here, in a situation where we seek the dominant original cause of an electromagnetic field, we need to exercise appropriate care. To distinguish the contribution of currents to an electromagnetic field is conceptually very simple. We need only concentrate on a common sense view of coherence. In that view, here, coherence has a slightly stronger meaning than synchrony. Coherence is taken to include causal

relations in a way that synchrony does not. Two synchronous phenomena, A and B, need not be causally related. If A and B are partly coherent, then if A is observed, there is an increased expectation of B because A is, to some extent, necessary before B can occur. If A is sufficient to cause B then there is certainty in B if A occurs. If A is necessary and sufficient, then (i) without A, B can never occur and (ii) if A occurs then B will occur. These ideas can be applied to sort out the various current types and the chain of causality that is involved in the charge microenvironment of section 2.2.

It has already been observed here that without the paramembrane charge atmospheres, there will be no electromagnetism. In the absence of transmembrane ion trafficking, the charge atmospheres would express an electrostatic field and otherwise be functionally inert. We know ion channel permeability originates all cell electrical dynamics. This fact enable us to locate transmembrane ion traffic at the top of a set of causal relations behind the expression of a dynamic EM field. First we assume an event E_1 occurs, resulting in a change of (ion channel related) membrane permeability, thereby permitting transmembrane ion flow (however it arises). This results in two subsequent paramembrane charge motion events E_2 and E_3. This chain of causality is circular; some kind of antecedent event (paramembrane charge disturbance), say E_0, is needed to trigger E_1. In this simple chain of events, from typical membrane equivalent circuit models used in neural modelling (Aidley 1998, Dayan and Abbott 2001, Hille 2001, Johnston and Wu 1995, Koch 1999, Koch and Segev 1998), we know the functionally important currents (can be seen numbered in Figure 2-1(b)) are:

(i) transmembrane ion currents.
(ii) transmembrane capacitative (molecular polarisation change) current.
(iii) 'extracellular'/ECS current.
(iv) 'intracellular'/ICS current.

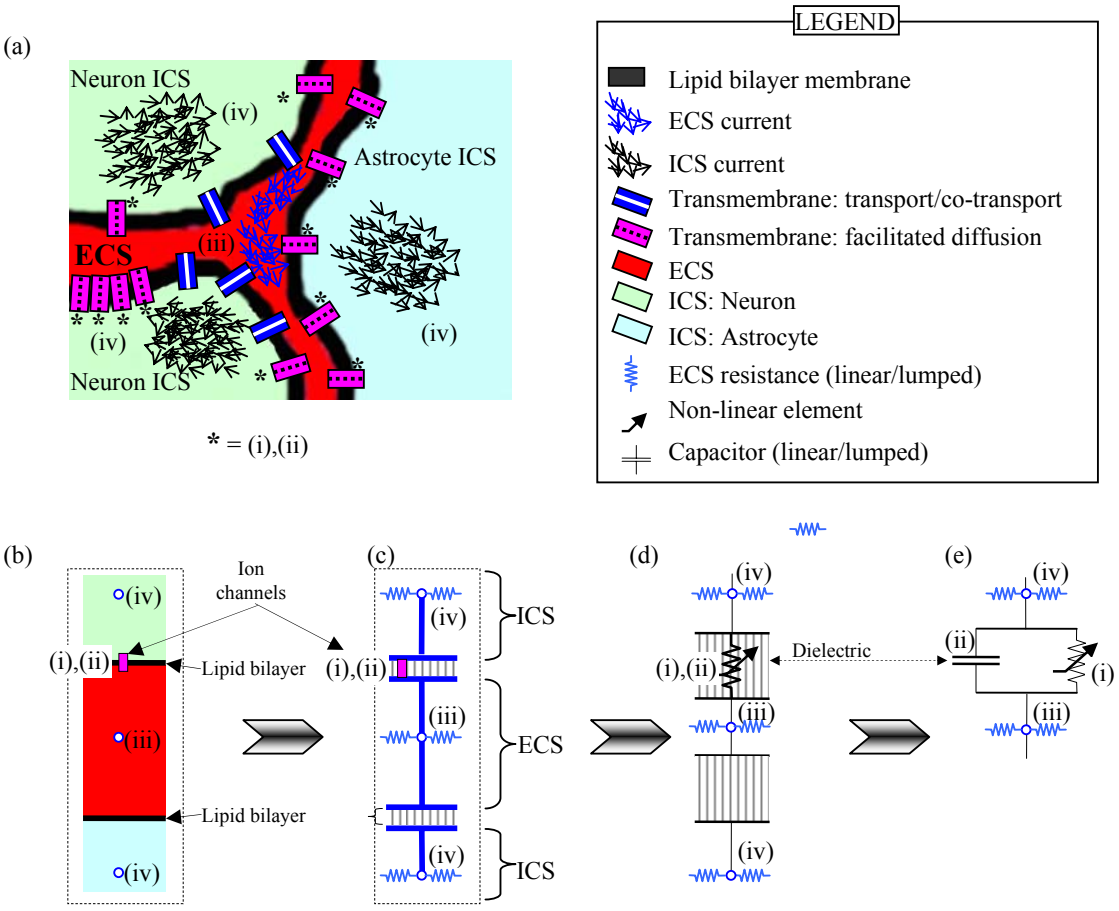

Figure 2-4 Distinguishing coherent and incoherent currents at the ion channel level. (a)…(e) depicts the abstraction of the biological current flows (responsible for the fields) into their equivalent circuit, where the fields are gone/irrelevant. See the text for further details.

Current (i)…(iv) are shown, interpreted physically and in terms of models, in Figure 2-4. The currents are numbered consistently throughout. Figure 2-4(a) shows the microscopic situation of transmembrane ion channels and charge transporters. The former operate functionally in action potentials and other normal functions. The latter operate in the background to replenish the paramembrane ion charge atmosphere. Non-transmembrane currents are shown as non-specific free ion movement usually modelled as resistive flow as shown in Figure 2-4. Figure 2-4(c), (d) and (e) show the usual rationale of the transition to an equivalent circuit. The Figure 2-4(b) lipid bilayer and local charge atmosphere become Figure 2-4(c) capacitor dielectric and plates, respectively. It is long established that, high frequency nonlinearity effects aside, the lipid bilayer has an effective capacitance of roughly $1\mu F/cm^2$ or $10^{-2}F/m^2$ (Aidley 1998, Dayan and Abbott 2001, Hille 2001, Nunez and Srinivasan 2006). In reality, the ion channels are nonlinear elements that collapse the transmembrane electric field (capacitor dielectric). This is shown specifically in Figure 2-4(d). Note that the adjacent cell (astrocyte) is usually completely absent from the model. This absence is depicted in Figure 2-4(e), which also shows the externalisation of the circuit elements that results in the familiar form. The only omission is the battery element that is involved in the threshold levels for the various current types. This can be regarded as part of the non-linear element. The capacitive current, (ii), is eventually segregated out into a separate circuit element. In a full simulation, many equivalent circuits are daisy chained. At this point it is easy to see how the currents in the equivalent circuit have lost their relationship with the production of a field system in space.

2.4.2 Transmembrane current: ion channel

Based on the above discussion it is a reasonable expectation that the fields based on transmembrane current will stand out over the others because, unlike the others, it has spatial coherence they lack. Transmembrane current is (a) a causal predecessor and (b) relatively highly localised, single-file and has a distinct velocity profile. This is unlike the unconstrained and therefore relatively diffuse ECS or ICS current, even though it will have the same overall magnitude. Therefore, even though the transmembrane currents and the ECS/ICS currents all share a well established causal/temporal relationship and satisfy charge conservation laws (as expressed by Norton's theorem), their role in electric and magnetic field production contributions is different.

Transmembrane ion activity has four major types. (1) action-potential, (2) chemical synapse, (3) electrical synapse and (4) co-transportation. In terms of their coherence and capacity to produce a field contribution, only (4) co-transportation is different. Current (4) is there to replenish ion stocks in the background, and is relatively loosely related to currents (1)…(3). Its field contribution will be asynchronous, inconsistently located and slow-acting. Current (2) is (mostly) ligand-gated. Current (3) is voltage gated. In (1)…(3), relatively coherent transmembrane current is the reasonable expectation. As a result they will all generate fields that are highly correlated with each other. Differences will be manifest in their time-course and relative magnitude.

2.4.3 Transmembrane current: capacitative

A capacitative jolt (of local charge polarisation redistribution) is, by necessity, a natural causal descendent of the process of allowing transmembrane current to flow. It, too, will therefore contribute coherent field production. A related current is the ion channel gating current. This has not been mentioned before. It is a small capacitative effect that occurs with sudden changes in transmembrane channel protein conformation associated with pore permeability control. It is a relatively small effect and is not often discussed in the literature (Hille 2001). It is mentioned here for completeness. It will be spatially and temporally coherent with the main transmembrane current. It will form no part in the later modelling. Its absence is not expected to have a significant impact on the overall results.

2.4.4 ECS/ICS current

ECS/ICS current is comprised of ion motions that are depicted in Figure 2-4(a) as a cloud of arrows to reinforce the diffuseness of the charge motions. They have no enforced path through space. The motions involve the ion and its hydration shells in myriad collisions with a huge mass of ICS chemistry including intracellular organelles and cytoskeletal infrastructure of all kinds (golgi

apparatus, nucleus, lysosomes, microfilaments, vesicles, microtubules and so forth) (Alberts 2002). ECS obstacles include the ECS-born chemistry involved in passive volume transmission and intercellular structural elements. This randomisation of ion trajectory makes the same current express a more spatially diffuse, and temporally sporadic field system. The expected field pattern will superpose on the more coherent field systems as field-noise.

2.4.5 Ion species issues

There is a large and growing taxonomy of transmembrane ion channel proteins expressed in excitable cells in different combinations and spatial dispositions in different nervous tissue regions in different species (Hille 2001). In typical brain tissue compartmental models, the functionally relevant ion species may include ionised Na, K, Ca and Cl. These may transit the pores of multiple different channel proteins. In terms of field production it is clear that their relative co-location is important. Multiple ion channel types can be involved in a single action potential. If Na channels are mixed with K in a particular part of a neuron, then their field pattern will be different to that expressed by the same channels, but spatially grouped with all Na channels in one place and all K channels in another. Even though the total current in both cases is identical, the field systems will differ in their microscopic structure.

2.5 The general nature of the field system produced by ion channel transmembrane charge motion

What do the ion channel current fields look like? Basic expectations are shown in Figure 2-5, where we see an abstracted transmembrane protein structure that provides a pore for ion transit, and directs a moving system of electric field lines along its axis. Basic electromagnetism tells us a transmembrane current, regardless of how it is physically originated, will direct electric field force lines along the dashed line in Figure 2-5, impacting the surrounding medium in a ‘line-of-sight’ fashion. The motion is, in effect, a current flowing along a notional conducting wire connecting ECS and ICS. Elementary electromagnetics of thin wires also tells us that the magnetic field will be in the plane of the membrane as shown in Figure 2-5. It will be faint, but will emanate at the speed of light, superpose and spatiotemporally locked with the electric field because they share the same origin.

Knowledge of the time-course of transmembrane current tells us that the neuron transmembrane field system, **e**, undergoes profound dynamic changes, including localised complete collapse and field reversal, as an action potential makes its way longitudinally, along the plane of the membrane. A basic knowledge of electrodynamics is all that is needed to predict this outcome. In addition, we know that the field collapse is a membrane-transverse phenomenon that coexists with the direction of travel of the action potential, which is membrane-longitudinal. It has been shown (above) how this transverse field collapse and reestablishment involves charge motions that originate all functionally relevant currents in the tissue.

The magnitude of the extra-cranial expression of the brain’s endogenous magnetic field, **b**, is typically cited in the range pT to fT (Hamalainen, Hari *et al.* 1993). These tiny fields are increasingly accessible as measurement technology improves. The MEG source reconstruction literature, as in EEG, attributes the magnetic fields to deep macroscopic ‘mean-field’ theory currents that lose their obvious connection to a deep microscopic origin. In the analysis to come, the magnetic field is a natural by-product of the mathematics involved in ion channel currents. Although the details of the magnetic field are not examined in this thesis, it is worth examining the expected nature of these fields. Note that we are discussing only coherent facilitated diffusion currents – neuron ion channel operation in synapses and in action potentials. Figure 2-5 is provided to illustrate how ion channel coherence creates a magnetic field, and supports coherence in the process, through a mechanism within the membrane.
It is a reasonable expectation that **b** and **e** will jointly superpose in accordance with Maxwell’s equations and network synchrony, finally emerging at the scalp.

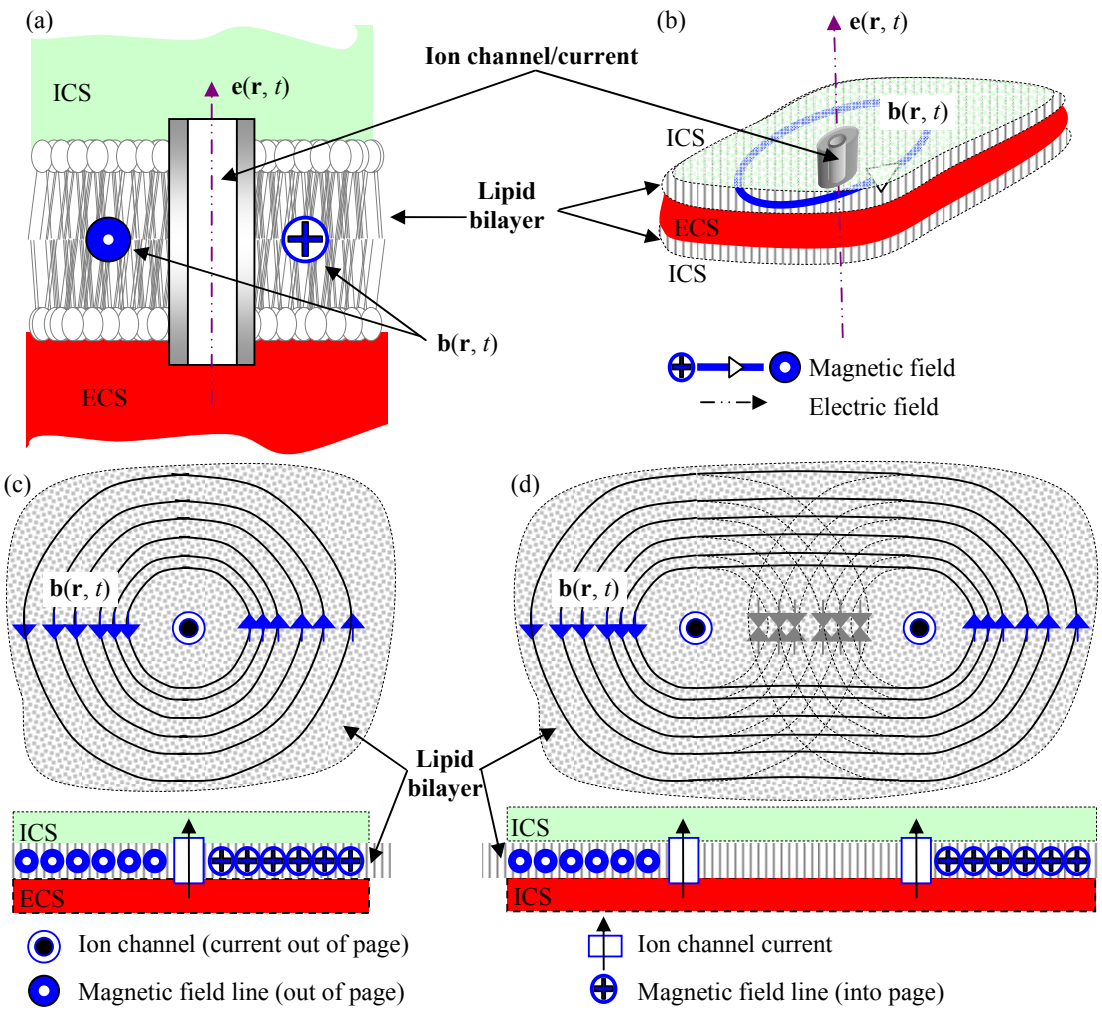

Figure 2-5 The electric (e) and magnetic field (b) due to a transmembrane current filament. (a) shows the membrane-transverse electric field arrangement. (b) shows an isometric view of the magnetic field expected from the dynamics of the membrane-transverse electric field. (c) shows a view of (b) directed orthogonally to view (a). (d) shows how multiple magnetic fields are expected to superpose in (and outside) the plane of the membrane.

2.6 The EM field: mathematics housekeeping

It is time to more formally establish the basics of nomenclature used in the discussion of Maxwell's equations.

2.6.1 MmE and MME

Table 2-1 shows the differential form of Maxwell's macroscopic equations (MME) contrasted with the microscopic version (called MmE) (Jackson 1999, Page 248). For conversion between SI and other units systems (Electrostatic (esu), Electromagnetic (emu), Gaussian, Heavyside-Lorentz) see (Jackson 1999, Page 781).

Microscopic	Macroscopic	Meaning	
Differential MmE	Differential MME		
$\nabla \cdot \mathbf{e} = \frac{\eta}{\varepsilon_0}$	$\nabla \cdot \mathbf{D} = \rho$	Coulomb's Law: The spatial (divergence) rate of change of field is proportional to	**(2.1)**

		spatial charge density.	
$\nabla \times \mathbf{e} + \frac{\partial \mathbf{b}}{\partial t} = 0$	$\nabla \times \mathbf{E} + \frac{\partial \mathbf{B}}{\partial t} = 0$	Faraday's Law: The spatial (curl) rate of change of electric field results in a temporal rate of change of the magnetic field.	(2.2)
$\nabla \cdot \mathbf{b} = 0$	$\nabla \cdot \mathbf{B} = 0$	The non-existence of magnetic monopoles: The spatial (divergence) rate of change of the magnetic field is zero.	(2.3)
$\nabla \times \mathbf{b} - \frac{1}{c^2}\frac{\partial \mathbf{e}}{\partial t} = \mu_0 \mathbf{j}$	$\nabla \times \mathbf{H} - \frac{\partial \mathbf{D}}{\partial t} = \mathbf{J}$	Ampere's Law: The spatial (curl) rate of change of magnetic field combined with the temporal rate of change of the electric field determines the spatial current density. Maxwell added the displacement current term.	(2.4)
N/A	$\mathbf{D} = \varepsilon_0 \mathbf{E} + \mathbf{P}$	**P** is the polarisation of the macroscopic material medium.	(2.5)
N/A	$\mathbf{H} = \frac{1}{\mu_0}\mathbf{B} - \mathbf{M}$	**M** is the magnetisation of the macroscopic material medium.	(2.6)

Table 2-1 Microscopic and Macroscopic (differential) Electrodynamics Equations.

Notes and SI units:

η, ρ	= volume charge density	(Coulomb/meter^3)
ε_0	= free space permittivity	(Farad/meter) or (Coulomb/(Volt meter))
μ_0	= free space permeability	(Henry/meter) or (Volt second/(Amp meter))
c	= free space speed of light	(Meter/sec)
j,**J**	= vector electrical current density	(Amp/meter^2)
e, **E**	= vector electric field	(Volts/ meter)
b, **B**	= vector magnetic flux	(Weber/meter^2) or (Volt second/meter^2)
H	= vector magnetic field	(Amp/meter)
M	= vector magnetisation	(Amp/meter)
D	= vector displacement	(Coulomb/meter^2)
P	= vector polarisation	(Coulomb/meter^2)

For completeness and future reference,

$$c^2 = 1/\mu_0\varepsilon_0 \,. \tag{2.7}$$

2.6.2 General EM field formalisms

Using the above vector field equations and nomenclature, the *microscopic* electric field at point **r** at time *t* is signified as

$$\mathbf{e}(\mathbf{r},t) \tag{2.8}$$

and the magnetic field is

$$\mathbf{b}(\mathbf{r},t). \tag{2.9}$$

The spectral content of **e** and **b** in brain tissue ranges from 0Hz (DC) to sub-visible light. The very high end of the spectrum results from the brain's (39DegC) thermal activity, and other specialised molecular behaviours, resulting in ultraweak biophotons being continuously emitted by all living cells (and their mitochondria), without any excitation (Bokkon 2009, Bokkon, Salari *et al.* 2010, Kobayashi, Takeda *et al.* 1999a, Kobayashi, Takeda *et al.* 1999b). This thesis excludes such phenomena by restricting **e**(**r**,*t*) and **b**(**r**,*t*) to the frequency range 0Hz to the tens of kHz. This choice confines **e**(**r**,*t*) and **b**(**r**,*t*) to activity related to action potentials, audition and the slower processes involved in neuron and astrocyte behaviour. Fields **e**(**r**,*t*) and **b**(**r**,*t*) are vector fields and can therefore be expressed, via Helmholtz decomposition, in terms of a scalar potential and a vector potential as

$$\mathbf{e}(\mathbf{r},t) = -\nabla\phi_e(\mathbf{r},t) + \nabla\times\mathbf{a}_e(\mathbf{r},t) \quad \textbf{(2.10)}$$

and

$$\mathbf{b}(\mathbf{r},t) = -\nabla\phi_m(\mathbf{r},t) + \nabla\times\mathbf{a}_b(\mathbf{r},t). \quad \textbf{(2.11)}$$

The units of both electric scalar and electric vector potentials are Volts (V). Because 'magnetic charge' remains undetected (Jackson 1999), the magnetic scalar potential is zero and the pair of equations (2.10) and (2.11) can be written in the more familiar form (Jackson 1999)

$$\mathbf{e}(\mathbf{r},t) = -\nabla\phi(\mathbf{r},t) - \frac{\partial\mathbf{a}(\mathbf{r},t)}{\partial t} \quad \textbf{(2.12)}$$

and

$$\mathbf{b}(\mathbf{r},t) = \nabla\times\mathbf{a}(\mathbf{r},t). \quad \textbf{(2.13)}$$

In this form, the units are (V) for the scalar potential and (V·s/m) for the vector potential. In electromagnetism, when the term 'vector potential' is used, the convention assumes equations (2.12) and (2.13) quantity **a** is being referenced, not $\mathbf{a}_e$ or $\mathbf{a}_b$. In this way, the equations are coupled by a single vector potential. There is a measure of flexibility in the form of these potential functions, because there are many different vector and scalar potentials that express identical EM fields **e** and **b**. The specific form of equations (2.10) and (2.11) is determined by a choice of electromagnetic gauge, and the gauge is determined by the choice of the divergence of the vector potential **a**, which is otherwise unspecified by Maxwell's equations (Jackson 2002, Jackson and Okun 2001).

In experimental excitable cell biophysics, the magnetic field, and the related vector potential has received no attention since it was determined, in the 1960s, that its relative magnitude and slow dynamics render its relative overall contribution in brain tissue negligible (Plonsey and Heppner 1967). The vector potential has been neglected because our instruments cannot measure it or separate it from the much larger scalar potential. For this reason, empirical research has been entirely confined to the measurement and expression of the electric scalar potential. In the neuroscience literature, there is rarely, if ever, any attention paid to the existence of the vector potential. Both **e** and **b** are visible experimentally outside the brain at the level of the scalp in EEG and MEG, respectively. This thesis aims to demonstrate the dominant contributor to the origins of both fields **e** and **b** and their central and important functional role, even if **b** is small.

2.7 Brain tissue as a convector

> "*Convection current, as distinct from conduction current, does not involve conductors and consequently does not satisfy Ohm's law. It occurs when current flows through an insulating medium such as liquid, rarefied gas, or a vacuum. A beam of electrons in a vacuum tube, for example, is a convection current.*"
>
> Matthew Sadiku
> 'Elements of Electromagnetics' (Sadiku 2001, p163)

Conduction concepts based on Ohm's law have been used successfully to model brain tissue voltages and currents ever since excitable cells were first studied. Entire systems of compartmental modelling, based on various forms of linear and nonlinear conduction, successfully capture much of the essence of excitable cell operation. Yet, the reality is that, in a formal sense, in the circumstances of all the functionally relevant electrical activity, the material is a convector not a conductor. Using conduction as a material metaphor in a convection circumstance is a very productive and useful way to quantify electrodiffusion processes in terms of voltages and currents. But the usage of a conduction metaphor does not make the material conductor. If the brain is a convector and we have been using conduction metaphors without question, what has been missed? A justification of the use of conduction metaphors is, strangely, absent from the literature. If we are to fully characterise EM phenomena (in contrast to voltages and currents) in brains, then its formal intrinsic nature seems a good place to start. The fields are degenerately related to currents and voltages and are also highly dependent on geometry. The

brain's native charge densities and current density behaviours, realistically located in space, must be our starting point. To raise the awareness of the issue, a technical contrast of conduction and convection is in order.

2.7.1 Convection vs. Conduction

The equations of electromagnetism, considered under 'quasi-magnetostatic' conditions, make it is possible to establish an additional equation that relates the electric field in a specific kind of material to the resultant current density that the field establishes (Jackson 1999). If **J** is the (macroscopic) current density vector in $A \cdot m^{-2}$, σ is a material conductivity in $(\Omega \cdot m)^{-1}$, and **E** is the electric field vector in $V \cdot m^{-1}$, then in a conductor, Ohm's law operates as the additional constraint,

$$\mathbf{J}(\mathbf{r},t) = \sigma \mathbf{E}(\mathbf{r},t). \qquad \textbf{(2.14)}$$

In this form the assumed material is anisotropic, homogeneous, linear, stationary conductivity. In brains, a convector, Ohm's law does not strictly apply. However, equation (2.14) may apply as a carefully used approximation. If **J** and **E** are empirically known at a point in space, then it is possible to calculate a *virtual* conductivity σ. This is quite valid except when one begins to examine the details of the **J** vs. **E** relations during dynamic events. This is when the difference makes itself felt. Equation (2.14) also implicitly enforces a view of causal relations that has been discussed above. All else being equal, equation (2.14) says that the current density **J** completely defines the electric field. In the reality of brain material at microscopic scales this has been demonstrated to be an inaccurate depiction of the material behaviour. The relation offers no connection to the original cause of the field or the current.

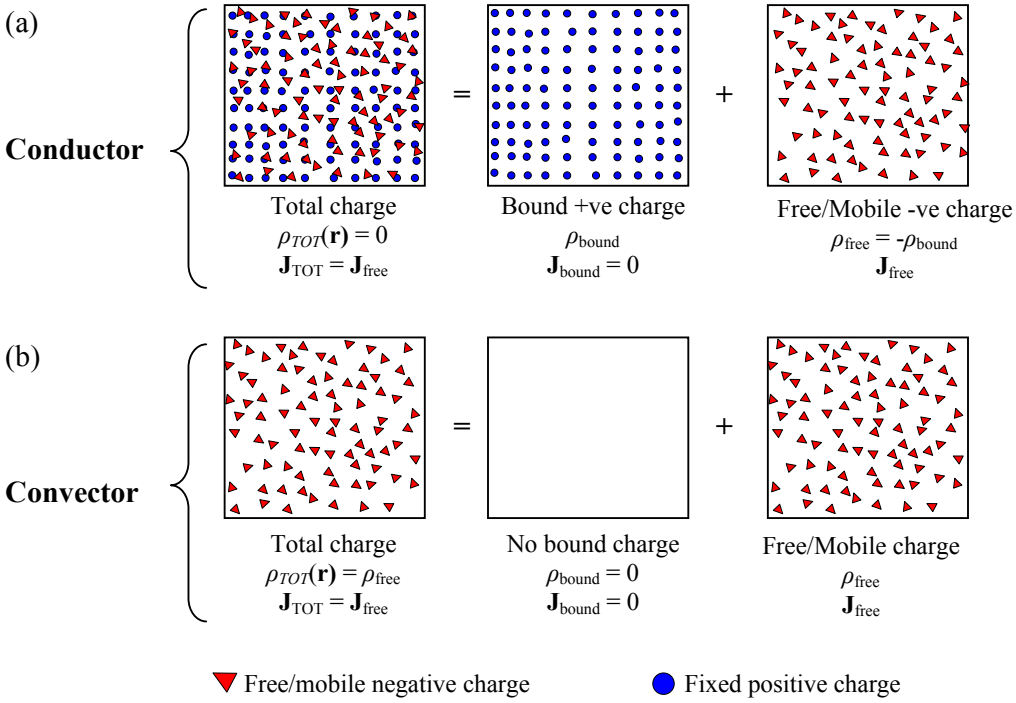

Figure 2-6 Traditional conduction contrasted to convection. (a) In conduction, the bound positive charge density (locked in the crystalline framework of the material) supports a current density while maintaining zero net charge density at a very fine level of granularity. See Jackson (Jackson 1999, p706). In contrast, convection has no such background charge density. Charge transport exists in a form that permanently has both a net charge density and a current density.

Formally, conduction conditions can only be said to be present in a region where the net charge density is vanishingly small (Jackson 1999, p706). To see this, we apply Sadiku's terms to brain material. Here we find ions moving (a current) in an extremely good liquid insulator (water). We also have ions moving (a current) through ion channel pores that behave like water by mimicry of water

hydration shells, reducing the range of possible motions. The walls of the pore are, in effect, a kind of insulator. The channel's surrounding medium, the apposed leaflets of the glycerophospholipid bilayer, is also a very good insulator. On top of this, immediately astride the channels, are massive ECS/ICS populations of isolated charge density. This kind of electrically motivated ion movement is convection, not conduction. Diffusion-motivated ion movement, in the same circumstances, is also convection.

Figure 2-6 more formally contrasts conduction and convection. The difference relates to the spatial scale at which charge neutrality exists. Conduction formalisms of the Ohm's law kind become physically expressed only when charge neutrality is maintained at the scale at which current is expressed and measured. In macroscopic electromagnetism, volume charge density (C/m^3) is typically represented, at a position $\mathbf{r}$ and time t, by $\rho(\mathbf{r},t)$. In a conductor, ρ is zero and disturbances settle out on timescales much shorter than the disturbances of interest in the current. Figure 2-6(a) depicts metallic conduction, where the free charge carriers constitute a current density, $\mathbf{J}_{free}$, whilst overall the net charge density, ρ_{TOT}, is much reduced because of a background bound (crystalline) opposite charge density, ρ_{bound} (Jackson 1999, p706). Note that the 'bound' term specifically means spatially fixed with respect to a reference frame. The temporarily co-located charge population on a plate of a capacitor is not 'bound' charge in the sense meant here. Thus it can be seen how the charge density and current density are, on average, at timescales larger than a specific time constant (derived below), decoupled in conductors. In contrast, the Figure 2-6(b) convector has no pervasive ρ_{bound}.

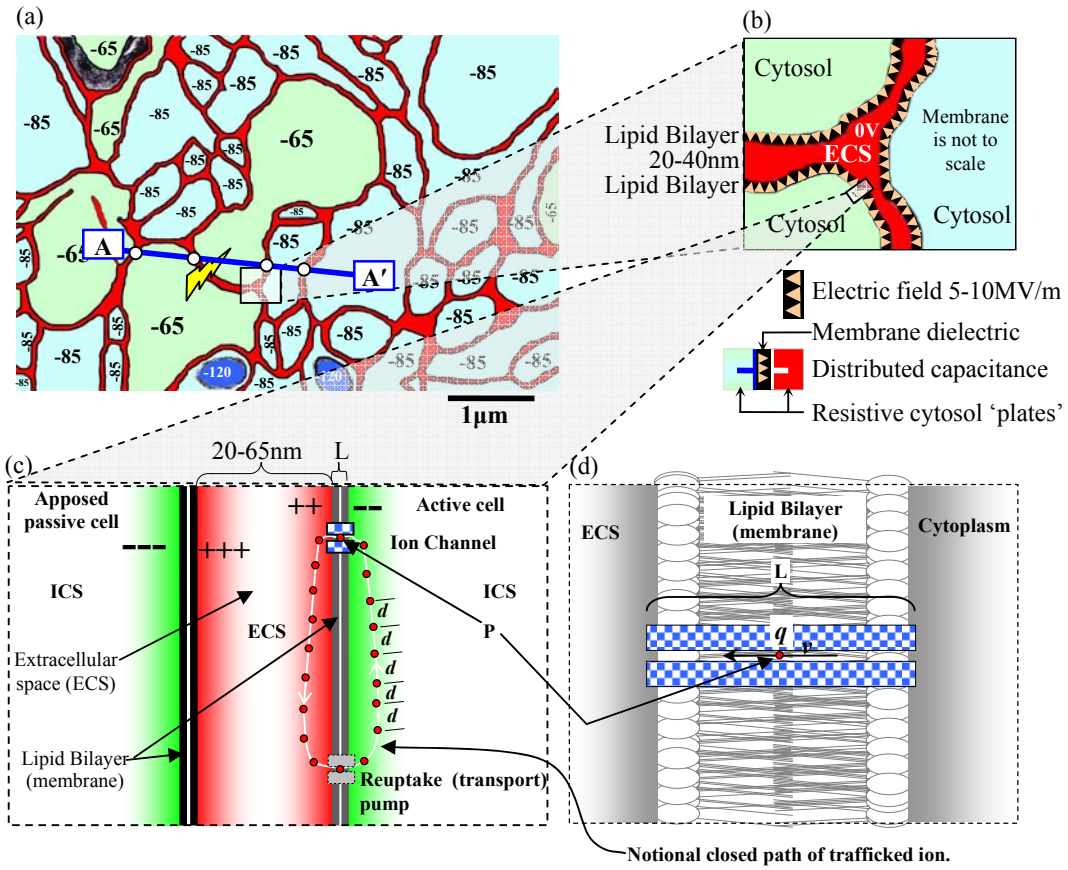

Figure 2-7 The convective life of the transmembrane ion. In (a) is the syncytium stylised and shown expressing the resting potential of the cells. In (b) is a magnified view showing the apposed membrane and their electric field. (c) is an even higher magnification and shows the overall closed path taken by ions. The primary active (field-relevant) component of the path is the 'ion channel' portion. The ICS and ECS portion of the path are relatively incoherent and diffuse, creating field noise (as described elsewhere). Charge reuptake is not highly coherent with the primary transmembrane current could operate at different rates). In (d) we have maximum magnification, showing an individual charge mid-transit through the ion channel pore. Not to scale.

Figure 2-7 further illustrate the conduction/convection distinction. Figure 2-1(a) has been amended to make the resting potentials more obvious. Figure 2-7(b) shows a small region of ECS that is subsequently magnified to reveal local conditions generally. A generic portion of Figure 2-7(b) has, in turn, been magnified further in Figure 2-7(c) and Figure 2-7(d), revealing the large dynamic populations of net ion charge density that are crammed tightly against the membranes by its huge electric field (Bedard, Kroger *et al.* 2006). Figure 2-7(c) shows how a neuron membrane typically services an active ion channel. It shows a charge, say K^+, transiting the membrane, where it joins the local ECS charge population. Figure 2-7(c) also shows, at some later time, and in a different locale, how a charge transporter (these operate with a different mechanism and with very different transit dynamics (Aidley 1998, Hille 2001)) returns the K^+ to the neuron ICS. During the process, the transmembrane potential undergoes a symmetrical shift, first one way, then a reversal the other way (as reflected in the graphs of Figure 2-1(c)). This mechanism for management of overall charge density is very different to that depicted in Figure 2-6(a).

When the ECS is treated as a zero voltage reference in models, the cytoplasm is net negative (Aidley 1998, Bedard and Destexhe 2009, Hille 2001, Johnston and Wu 1995, Kuffler and Nicholls 1976). A model set up to account for the realistic aggregation of paramembrane charge would include the background potential mosaic typified by Figure 2-7(a), a potential profile upon which all LFP activity, however small, is superimposed. This mosaic has not yet been explicitly located in literature in the form of Figure 2-7(a). Instead it seems to be implicit in the depictions of local transmembrane potential variation be found in texts (Aidley 1998, Dayan and Abbott 2001, Hille 2001, Johnston and Wu 1995). With the physical reality of charge density and current density spelled out, we can now attend to how the equations of electromagnetism applicable to brain tissue appear in conduction and convection circumstances. It is straightforward to coerce the four basic Maxwell's microscopic equations (MmE), and their equivalent in Maxwell's macroscopic equations (MME) (see 2.6.1 below), into a form that reveals the relationship between charge density fluctuations and current density. The mathematics, in its better known guise, is called the law of conservation of charge and it is *universal*, i.e. applicable to conduction and convection alike. The MmE form is

$$\frac{d\rho(\mathbf{r},t)}{dt} + \nabla \bullet \mathbf{J}(\mathbf{r},t) = 0 \,. \qquad \textbf{(2.15)}$$

An assertion of the classical conduction circumstances of Figure 2-6(a) is an assertion that the left hand term is zero because η is effectively zero. Because the left term is zero, this forces the right term, divergence of the current density, to be zero. In contrast, in convection, each term is non-zero and their sum is zero. In both cases, we have conserved charge, but the dynamics of the fields produced by each situation are very different. Equation (2.15) is the starting point for assessments of the applicability of conduction formalisms that consider the charge dynamics. In all previous such analyses found to date, formally recognisable circular logic becomes visible. It is relatively straightforward to coerce the macroscopic form of equation (2.15) into

$$\frac{d\rho(\mathbf{r},t)}{dt} + \frac{\sigma}{\varepsilon}\rho(\mathbf{r},t) = 0 \,, \qquad \textbf{(2.16)}$$

where ρ is the macroscopic charge density. Parameters ε and σ are the material permittivity and conductivity, respectively. These are assumed stationary, homogeneous and isotropic. This equation is a simple first order differential equation with the obvious solution

$$\rho(\mathbf{r},t) = \rho(\mathbf{r},0)e^{-\frac{t}{\tau}} \,, \qquad \textbf{(2.17)}$$

where the time constant, in seconds, is

$$\tau = \frac{\varepsilon}{\sigma} \,. \qquad \textbf{(2.18)}$$

In the literature, the procedure is to identify values of typical macroscopic ε and σ , then insert them in (2.18). For the typical quasi-conductivity of bulk brain tissue of roughly $1(\Omega \cdot m)^{-1}$, and with relative permittivity of water, roughly 80, and membrane, roughly the same for our purposes (Joshi, Sridhara *et al.* 2006), this time constant is $\varepsilon_0/\sigma \approx 10^{-11}$ to 10^{-9} second, although 10^{-6}s has been found (Holt 1998, p7). The conclusion is then reached that τ is much shorter than anything happening in the brain (say an action potential), therefore charge disturbances settle out so quickly that the charge density is

effectively zero. Therefore, the argument goes, the applicable form of MME involves an assumption that charge density is zero, e.g. (Lindsay, Rosenberg *et al.* 2004).

The logical problem with this procedure is that it presupposes that conduction exists and that the dynamics of charge density change follow Ohm's Law. Not only is the logic flawed, but the charge density can never actually do this at all scales, and the scale dependence of the assumption is never explicitly qualified. The above discussions of cellular microstructure revealed large, persistent transmembrane charge aggregations that fundamentally underpin all of the activity related to action potentials. At microscopic scales, these populations may, as a result of the transmembrane process, settle back to a previous state after the Figure 2-7(c) translocation has completed. However, this is nothing like the Figure 2-6(a) process of a conductor, where a solid atomic lattice maintains charge neutrality at an atomic scale, uniformly throughout space. This is simply not the case in the material at the scales of relevance to the establishment of the field system.

Yet conduction formalisms work rather well, at least for currents and voltages at certain spatial scales. This apparent contradiction can be resolved by inspecting the situation in more detail. This is done using Figure 2-8, which shows that at any given microscopic point, say A, as we proceed to ever larger spatial scales, the physical charge density profile at the beginning is relatively anisotropic and inhomogeneous. This is a convection zone. Yet overall, if we take an average charge density over an increasing spatial scale (say, of increasing circles as shown in the figure), the overall charge density starts to become relatively stable and approach zero. At spatial scales not much bigger than, say 20-50μm, it can be seen how the material begins to resemble Figure 2-6(a) conduction conditions, albeit on a coarse-grained basis, in which (2.16) applies well enough to be predictive. Coarse measurement probes will measure behaviours consistent with conduction. However useful it may be, that consistency, is actually an artefact of the measurement and of the material behaviour.

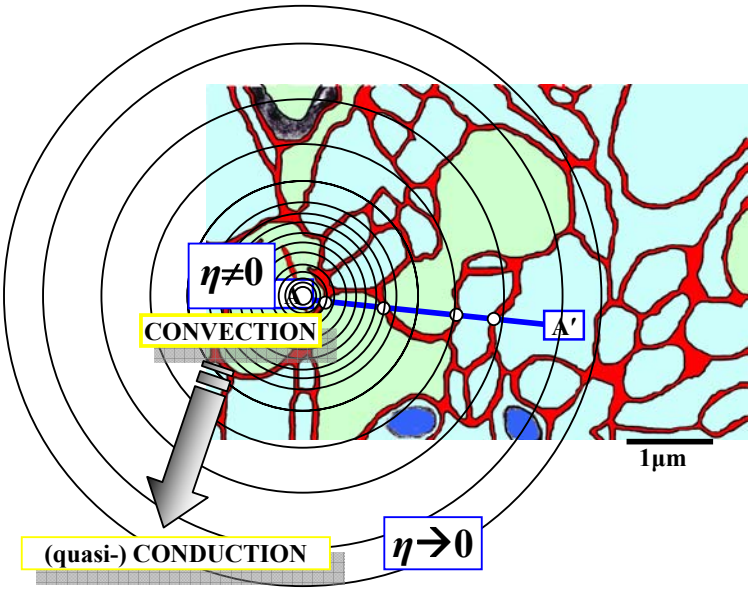

Figure 2-8 Convection becomes quasi-conduction in neural tissue at the right spatial scale.. The process is mediated by an asymptotic approach to overall neutral charge density in a progression from microscopic to macroscopic scales.

This is the suggested mechanism by which a complex material that is intrinsically convective can be validly treated as a conductor in the sense that Ohm's law can be applied. Yet in reality, deep in the material, the actual dynamics of paramembrane charge disturbance and equilibration are vastly different to equation (2.16), in line with Figure 2-7. In terms of basic charge conservation, the difference between conduction and convection can be seen in the way (2.15) works. In conduction we have the equation (2.15) balance via the left-side/right-side *physical* balance of the form 0 = 0. In convection, however, (2.15) *physically* balances in the manner of X-X = 0. The divergence of the current density is non-ohmic (divergence is non-zero) and the rate of change of the charge density is

non-zero. The treatment, in the literature, of conductivity and permittivity as spatially inhomogeneous can be a conceptually useful generalisation (e.g. (Bedard, Kroger *et al.* 2004)). In the case of conductivity, the treatment of non-homogeneous conductivity does not obviously account for the fundamental of Ohm's Law in a situation where its application is a-priori arguably inapplicable (small spatial scales). The proper accounting of realistic charge density - without the enforcement of Ohms Law - is required.

2.7.2 The mathematics of convection & conduction

As part of the exploratory process behind this thesis, the following form of Maxwell's microscopic equations was derived. Unlike the more familiar differential and integral forms, it explicitly expresses the total electric and magnetic fields, and reveals their cross-coupling. Their practical usefulness is limited, but they have proved useful in a pedagogical sense:

$$\mathbf{e}(\mathbf{r},t) = \left. -\frac{1}{4\pi\varepsilon_0}\nabla\int_U \frac{\eta(\mathbf{r}',t)}{|\mathbf{r}-\mathbf{r}'|}d^3r' \right|_A \left. -\frac{1}{4\pi}\nabla\times\int_U \frac{\partial\mathbf{b}(\mathbf{r}',t)}{\partial t}\frac{1}{|\mathbf{r}-\mathbf{r}'|}d^3r' \right|_B \tag{2.19}$$

$$\mathbf{b}(\mathbf{r},t) = \left. \frac{\mu_0}{4\pi}\nabla\times\int_U \frac{\mathbf{j}(\mathbf{r}',t)}{|\mathbf{r}-\mathbf{r}'|}d^3r' \right|_A \left. +\frac{1}{4\pi}\frac{1}{c^2}\nabla\times\int_U \frac{\partial\mathbf{e}(\mathbf{r}',t)}{\partial t}\frac{1}{|\mathbf{r}-\mathbf{r}'|}d^3r' \right|_B . \tag{2.20}$$

This form of the equations was derived through the abovementioned Helmholtz decomposition, combined with the use of a Newtonian potential. I was able to find a form similar and mathematically equivalent to (2.19) and (2.20), except that it is based on the macroscopic equations in the Coulomb gauge, and a longitudinal/transverse decomposition. It is therefore slightly different (Hirose 2000). Otherwise I was unable to find any reference depicting MmE exactly as per the (2.19) and (2.20) form. So the equations are either actually novel, or merely practically novel because of arcanity, to a neuroscientist, in accessing them in the physics literature. To make the proof transparent and accessible to neurobiology, the derivation is included in Appendix B, along with proof that under the appropriate conditions, it results in the usual differential form of the microscopic equations (MmE). Equations (2.19) and (2.20) can be used to reveal conduction, convection, radiation, electrostatics and (quasi-)magnetostatics, constitutive and free-space forms as shown in Figure 2-9.

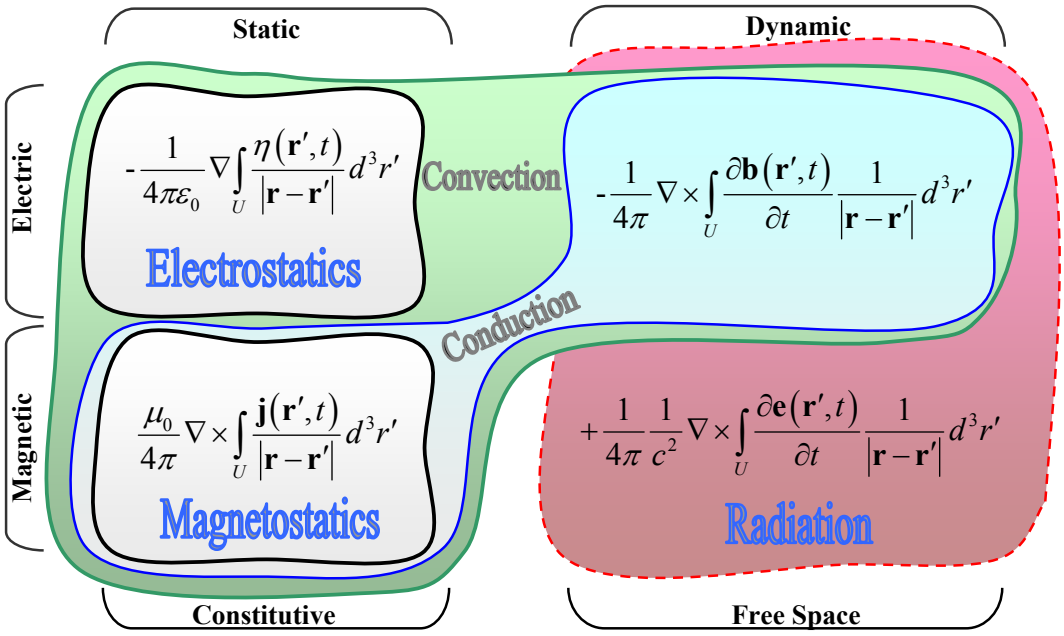

Figure 2-9 The various forms of the classical microscopic equations of electrodynamics.

The equations depict a collection of charge at positions in space, η, and the same collection of charge moving in space so as to create a vector current density, $\mathbf{j}$. If the charges are moving in a situation of

zero net charge density, then conduction is occurring. This makes conduction a special case of convection. The emergence of Ohm's law from equation (2.19), with $\eta = 0$, can only happen when there is an average rate of change of the magnetic field feeding (2.19)*B*. This situation occurs when microscopic charge motions include collision dynamics that dissipate heat. In that condition, an 'average current density' can coexist with a finite (2.19)*B*. This results in Ohm's law whilst maintaining conservation of charge (via (2.15)) simultaneously with the divergence of **j** being zero as discussed above. In brain material, with large regions of non-zero η located in functionally critical zones, the constitutive (macroscopic) form is convection. For this reason, conduction is not strictly a form of magnetostatics, and is called quasi-magnetostatics (Jackson 1999).

Note that in application to the brain, the universally accepted neglect of (2.20)*B* is an acceptance of a the irrelevance of radiative effects in brain material. In brain material the electric fields change, so in reality (2.20)*B* will be non-zero. In brain material, if this does happen, the radiative contribution to (2.20) will be vanishing small, largely because of the $1/c^2$ term. This vanishingly small radiation is expected to be immediately absorbed by the surrounding material. Experimentally, we know the quasi-magnetostatic effects result in no detectable radiation, yet a detectable 'quasi-static' magnetic field (via the MEG).

2.8 Remnant issues in understanding and modelling brain material – the implications of a microscopic approach.

We can also note that in all of the assessments of the appropriate form of electromagnetism in brain material found so far, going back to the 1940s, the single unaddressed presupposition was that the generic macroscopic material form of Maxwell's equations could be applied at all spatiotemporal scales (Holt 1998, Lindsay, Rosenberg *et al.* 2004, Lorente de No 1947a, Lorente de No 1947b, Plonsey 1964, Plonsey and Collin 1961, Plonsey and Fleming 1969, Plonsey and Heppner 1967, Rosenfalck 1969). The only direct reference to the use of microscopic equations found was:

> "*The microscopic equations work very well for a few charges and currents isolated in a near vacuum. However, in a macroscopic medium like tissue, they are of no use except to shed light on the macroscopic version*"
>
> Nunez and Srinivasan
> 'Electric fields of the brain : the neurophysics of EEG'
> (Nunez and Srinivasan 2006, Page 129)

This position is quite apt for the overall macroscopic fields and the general characterisation of fields with coarse spatial dynamics when macroscopic parameters apply. However, when the ultimate origins of the fields are sought, persistence with MME down to its deep atomic origins might become a confounding influence. Therefore, one of the tasks of this thesis has become the goal of construction of a classical-physics bridge from the macroscopic to the microscopic realm suitable for brain specialists. This will become clear in the upcoming chapters.

2.8.1 MmE ⇔ MME, The transition

Jackson has devoted considerable energy to the MME derivation (Jackson 1999, Chapter 6) from the more fundamental MmE. The derivation of MME from MmE involves an assumption of a generic 'free' (isolated mobile charge) cohort and a generic 'bound' (spatially fixed notional molecules of no particular composition) charge/spin cohort. These presupposed abstract cohorts become a material abstraction, and give the equations their 'constitutive' classification. The charge cohorts create microscopic **e** and **b** fields. These are then used to construct spatially averaged 'mean field' expressions for the macroscopic **E** and **B** fields whose properties are, under the assumptions of macroscopic conditions, dominated by the first couple of terms of a series expansion. The results are the MME equations. The MME equations have been used successfully for a well over a century and, in the hands of electrical engineers, have been used to deliver major technologies. However, the MME conditions are a highly abstract simplification of the details of condensed matter.

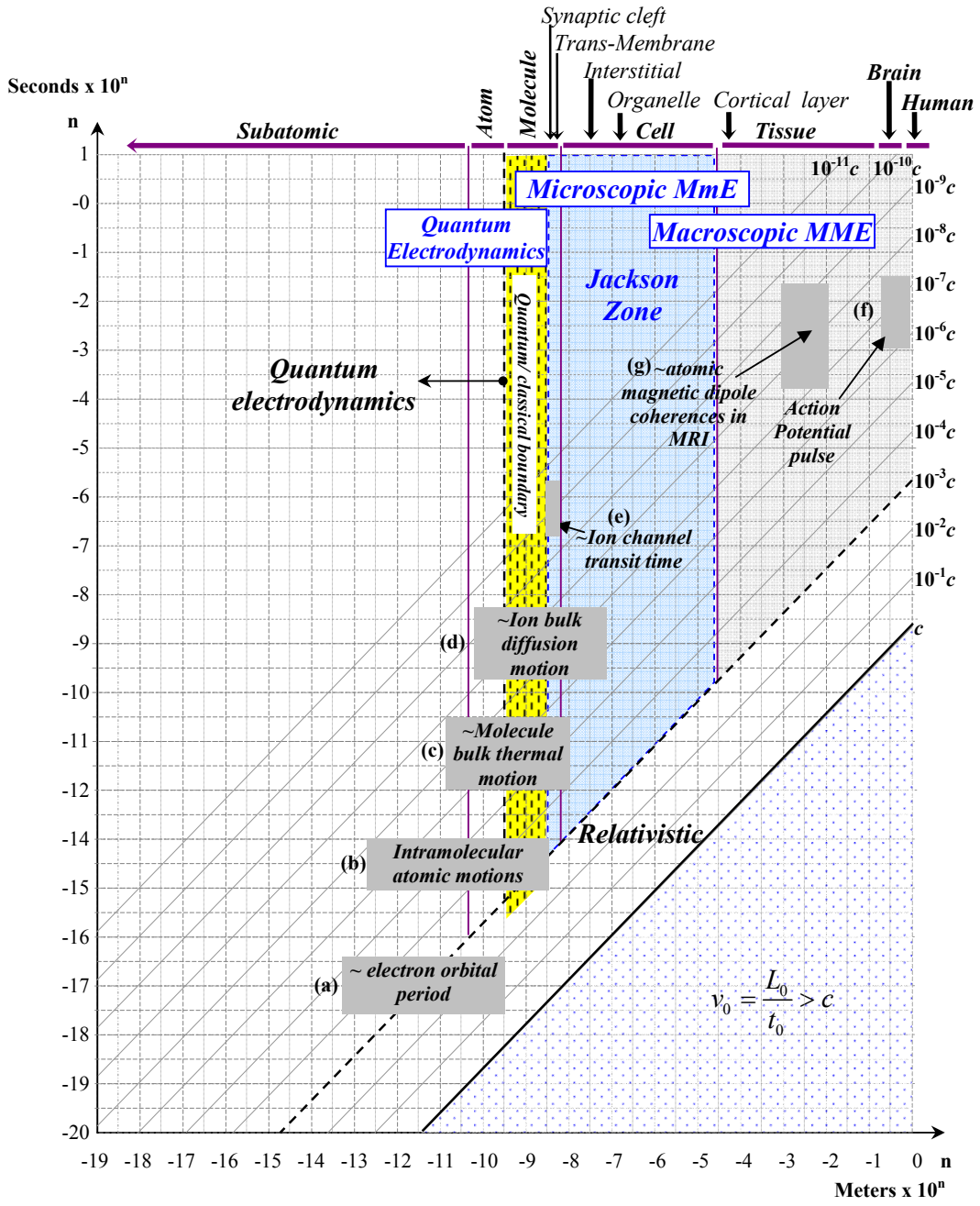

Figure 2-10 Natural phenomena mapped onto their spatiotemporal region, correlated with the brain material matter hierarchy. The 'Jackson Zone' indicates where the microscopic to macroscopic transition becomes debatable.

Here we recognise that the original derivation of MME, the material abstraction was designed for ensemble behaviours that remained homogeneous and isotropic over scales large compared with the range over which the MmE spatial average is computed. Also, temporal correlations between members of a notional material ensemble are supposed to average to zero on short timescales. This can be argued as being in conflict, to some extent, with the reality of brain material, which has important operational features implemented and varying at the level of under 10^{-8}m. Note that in the Jackson MME derivation there is no specification of matter phase (liquid, solid, gas) or matter composition complexity and feature sizes. The MME are thus highly generic and expected to deal with condensed matter and some non-condensed matter circumstances. In doing so, the Jackson derivation has recommended limits in the area of (i) smallest amount of material ($10^{23\pm5}$ electrons and nucleii), (ii) lowest 'length' limit (10^{-8}m) and (iii) lowest time limit (discussed below). Here we concentrate on (i)

and (ii). Meeting these conditions results in the abstract characterisation of the circumstances as a relatively spatially smooth and temporally slowly varying material medium operating according to continuum mathematics.

Figure 2-10 depicts the various spatiotemporal scales involved in the hierarchy of condensed matter. All the data used in Figure 2-10 is available in (Jackson 1999) and other commonly available texts. Relativistic physics puts a boundary on all phenomena operating under the speed of light, *c*. Quantum physics places a lower spatial limit around the level of the 'molecule'. Consider the way we might locate, say, ion channel transit. Individual ion channels allow currents of the order of 10^{-12}A (Coulombs per second). This is what a patch clamp recording of a single open channel typically reveals (Hille 2001, p90). Given the transmembrane pore length of 5nm to 7.5nm, and that a Coulomb consists of roughly 6.241×10^{18} univalent charges, a patch clamp current measurement corresponds to a passage of the order of 10^6 univalent charges per second (a transit time of roughly 1μs). Assuming simple ion channel kinetics with an average 'open' duration of 1ms (a single spike), of the order of 10^3 single-file charges will transit with an average speed of the order of cm/s. This locates Figure 2-10(e). Next we consider the Jackson limit on material amount. For our purposes, we can assume that a brain is mostly water. Each molecule has 3 nucleons and 10 electrons. A mole (6.02×10^{23} molecules) of water is roughly 0.018kg. At physiological conditions, water has a density of roughly 1kg/dm^3. Based on these values, the amount of material specified by (Jackson 1999, Page 249), which ranges between 10^{18} and10^{28} molecules, corresponds to a sphere of water with a diameter ranging between 164μm and 0.35m, respectively. Clearly, the latter limit is inappropriate. More interesting is the lower limit, which falls right in the midst of the dimensions of feature expression in excitable cell material. For example, the diameter of a cell soma ranges between 1μm and 100μm (astrocytes and neurons).

Figure 2-10 portrays the spatiotemporal range of functionally important brain features in such a way that the applicability of MME and MmE can be assessed. In that analysis, the issue of Jackson's spatial and temporal limits is a very subtle one, indeed important enough to spell out verbatim:

> "*It is plausible therefore to take the length $L_0 = 10^{-8}m = 10^2Å$ as the absolute lower limit to the macroscopic domain. The period of oscillation associated with light of this wavelength is $L_0/c \approx 10^{-17}s$. In a volume of $L_0^3=10^{-24}m^3$ there are, in ordinary matter, still of the order of 10^6 nuclei and electrons. Thus in any region of macroscopic interest with $L >> L_0$ there are so many nuclei and electrons that fluctuations will be completely washed out by spatial averaging. On the other hand, because the time scale associated with L is actually in the range of atomic and molecular motions, a time-averaging would not be appropriate. There is, nevertheless, no evidence, after the spatial averaging, of the microscopic time fluctuations of the medium. This is so because, in the absence of special preparation and the establishment of ordering over macroscopic distances, the time variations of the microscopic fields are uncorrelated over macroscopic distances of order L. All that survive are the frequency components corresponding to oscillators driven at the external applied frequencies.*"
>
> J.D.Jackson
> Classical Electrodynamics(Jackson 1999, p249)

In brain material, the process of 'special preparation' has been delivered: *The intricate microstructure of brain material*. It has spatial and temporal correlations of the fields over much larger distances than L_0 and much larger times than apply to Jackson's macroscopic derivation. We are speaking exclusively of the endogenous fields (endogenous EM field coherence) of brain material, which arises due to an organisation of matter on a spatial scale *less* than L_0 (e.g. the membrane). Everything about the situation in brain material suggests that the macroscopic 19th century form is suspect when examining the microscopic origins of the endogenous fields of brain tissue. To highlight the region of doubt, in Figure 2-10 the spatial range spanning 0.01μm to 164μm has been called the *Jackson Zone*, in which the unexamined application of macroscopic electromagnetism seems ill advised.

2.8.2 Further relevant 'continuum' mathematics

A microscopic approach to the origins of the endogenous fields forces the acknowledgement of the punctate nature of the charges involved. In such an approach, continuum material mathematics loses some of its validity, although all derived models should, if properly constructed, approach the behaviour of continuum models (such as passive diffusion) for appropriate spatiotemporal scales and ensemble sizes. Space and time, on the other hand, can remain a continuum. The mathematics thus remains a space and time continuum containing a punctate mass/charge ensemble. Stochastic processes such as molecular and atomic collisions, solvation, hydration and the randomness of protein conformation change, are to be expected. Notwithstanding the local (atomic/molecular) force fields resulting from quantum mechanics (e.g. hydrogen bonds), the motion is Newtonian, driven by the Lorentz force equation. For the record, the Lorentz force is:

$$\mathbf{F}_k\left(\mathbf{r}_k,t\right)=q_k\mathbf{e}\left(\mathbf{r}_k,t\right)+q_k\mathbf{v}_k\left(t\right)\times\mathbf{b}\left(\mathbf{r}_k,t\right), \tag{2.21}$$

where, $\mathbf{F}_k$ signifies the force, experienced by an individual charge k located at a point $\mathbf{r}_k$ at time t, due to the existence of electric and magnetic fields, and

$$\mathbf{v}_k\left(t\right)=\frac{\partial\mathbf{r}_k\left(t\right)}{\partial t} \tag{2.22}$$

is the velocity of charge k. Note that an assumption of negligible endogenous **b** means that the right term of (2.21) is expected not to contribute any significant impact on ion motions. If a dynamic, large exogenous **b** arose, then charge motions can be expected to be affected in accordance with equation (2.21). Newtonian motions and the local atomic force potentials involved in a punctate mass/charge ensemble means that the true detail of the microscopic origins of the endogenous fields must ultimately become a form of computational molecular (electro)dynamics.

2.9 Strategy

Armed with the above information, this section examines the most appropriate way ahead for EM field research.

2.9.1 Bridging the 'Jackson Zone'

The fundamental outcome is that the macroscopic fields (of the order of mm) in which the macroscopic laws of electromagnetism can be applied, originate in a microscopic mechanism (of the order of nm) that is well beneath the appropriate scale of validity of macroscopic electromagnetism. This paradoxical situation tells us that MME equations are to be regarded as suspect in their capacity to accurately reveal the origins of what are observed as macroscopic fields. The alternative, microscopic electromagnetism, turns the neuroscience of the brain's endogenous EM fields into a very onerous form of molecular (electro-)dynamics that, if used, involves a major cultural shift in brain modelling. This raises the question of how best to proceed in the mathematical revealing of the endogenous fields.

To resolve this problem, both sides of this macroscopic/microscopic divide were explored at considerable length, with the result being the identification of the need for a bridging form of macroscopic Maxwell's equations that carefully intrudes into the microscopic realm in a practical and revealing way. The solution is the well-travelled 'volume conduction' equations, a macroscopic electromagnetism formalism (Malmivuo and Plonsey 1995), except driven by *microscopic sources*. The microscopic sources connect the equations to the revealed microscopic origins of the EM fields: ion channels. The volume conduction equations abstract away the syncytium detail of the tissue at macroscopic levels. None of the charge densities revealed above, or their background potentials, will appear in such a formalism. This becomes practical provided the model could be argued to be physically valid, and care is taken to understand how the impact of the presupposition of 'conduction' impacts the resultant predictions of the LFP. That done, descriptive but inexact results and could provide an interim exploratory method for a period of time during which more appropriate forms of electrodynamics equations can be developed. The material abstraction is crude and unrealistic. It

involves the need to develop a special form of the volume conduction equation. This was found to be straightforward (see Chapter 4).

2.9.2 Using computing to overcome the tyranny of numbers

Capturing the microscopic original (ion channel) currents involves the volume conduction formalism in the onerous statistics of ion channels and biologically expressed neuron cell morphology. This latter detail is the route to the need for high performance computing and the presentation of results in purely numerical form. This appears to be the compromise necessary to reveal the microscopic field origins with a mathematical technique based on a macroscopic formalism. The single most difficult aspect of the process of clearly characterising the fields is the oppression of sheer quantity. Every statistic that one cares to use to describe the tissue involves vast quantities of atoms, proteins, cells, synapses and so forth. Add to that the well known situation of the brain as a highly non-linear, non-homogeneous, anisotropic, non-stationary far from equilibrium dissipative system and you have a recipe for perhaps the most difficult-to-describe single entity known to science.

In this thesis, high performance computing (HPC) was found to be well suited to tackle the large numbers involved. HPC was able to tackle the electric field originating at a spatial scale of under 10 nanometres, expressed and examined at mm scales over seconds of real-time. It was able to do this with an entire, biologically realistic pyramidal neuron with close to 20,000 individually located ion channels. In one sense, HPC is a blunt instrument using sheer computational power to overcome the geometric explosiveness intrinsic to the nested hierarchical organisation of the tissue. The chosen context is not amenable to closed-form mathematical solutions. In their loss, what is gained is a view of what is really going on – the emergent properties of large numbers of simple elements arranged in space in complex patterns. In another sense, the use of HPC across multiple scales is a unique kind of science outcome. This latter aspect is addressed in Chapter 8.

2.10 Summary

This chapter completes the literature review covering the fundamental structure of brain tissue from the molecular level to the tissue level and the equations of electromagnetism appropriate to the accurate expression of the EM field system. The list of essential outcomes is as follows:

1) Brain tissue is validly classed as an ‘electromagnetic syncytium’. The syncytium idea acknowledges the operational unity of the material based the electromagnetic enmeshing of electrically active neurons and astrocytes. One of the terms already applied to this ‘enmeshing’ is ephapsis.
2) An analysis of the nature of the functionally relevant known currents was carried out. By examining each current type and its spatiotemporal coherence in the chain of causality, ion channel currents emerged as the most plausible original source because (a) they have both spatial and temporal coherence that other currents lack, (b) they are causally antecedent to all other currents and (c) they simultaneously provide a simple mechanism for the electric and magnetic fields.
3) Based on ion channel transmembrane current behaviour, basic expectations of the nature of the electric and magnetic fields were outlined. The electric field was shown to originate in a membrane-transverse configuration. The magnetic field circulates the (changing) electric field in the plane of the membrane.
4) The brain, as a formal electromagnetic object at microscopic scales, was shown to be a convector that becomes a quasi- or ‘virtual’ conductor above a certain spatial scale.
5) Previous assessments of the appropriate forms of Maxwell’s equations (a) presupposed the macroscopic form of Maxwell’s equations and (b) assumed Ohm’s law applied at all spatiotemporal scales. They focussed on the relative importance of terms *within* the macroscopic form, where the reality of brain material brings into question the applicability of the macroscopic form itself.
6) The change to a microscopic form of Maxwell’s equations was revealed as onerous. A strategy for an interim form of the macroscopic volume conduction formalism was chosen, where it will be driven by microscopic current sources.

As a result of this analysis it is now possible to a formulate specific set of hypotheses and an experimental regime to suit. It is to that task I now turn.

2.11 Chapter bibliography

Aidley, D. J., The Physiology of Excitable Cells, 4th ed., Cambridge University Press, New York, 1998, pp. xii, 477.

Alberts, B., Molecular Biology of the Cell, 4th ed., Garland Science, New York, 2002, pp. xxxiv, 1463, G1436, I1449, T1461.

Bedard, C. and Destexhe, A. 'Macroscopic Models of Local Field Potentials and the Apparent 1/F Noise in Brain Activity', *Biophysical Journal* vol. 96, no. 7, 2009. 2589-2603.

Bedard, C., Kroger, H. and Destexhe, A. 'Modeling Extracellular Field Potentials and the Frequency-Filtering Properties of Extracellular Space', *Biophysical Journal* vol. 86, no. 3, 2004. 1829-1842.

Bedard, C., Kroger, H. and Destexhe, A. 'Model of Low-Pass Filtering of Local Field Potentials in Brain Tissue', *Physical Review E* vol. 73, no. 5, 2006.

Bokkon, I. 'Visual Perception and Imagery: A New Molecular Hypothesis', *Biosystems* vol. 96, no. 2, 2009. 178-184.

Bokkon, I., Salari, V., Tuszynski, J. A. and Antal, I. 'Estimation of the Number of Biophotons Involved in the Visual Perception of a Single-Object Image: Biophoton Intensity Can Be Considerably Higher inside Cells Than Outside', *Journal of Photochemistry and Photobiology B-Biology* vol. 100, no. 3, 2010. 160-166.

Burnham, C. J., Petersen, M. K., Day, T. J. F., Iyengar, S. S. and Voth, G. A. 'The Properties of Ion-Water Clusters. Ii. Solvation Structures of Na+, Cl-, and H+ Clusters as a Function of Temperature', *Journal of Chemical Physics* vol. 124, no. 2, 2006.

Chen, K. C. and Nicholson, C. 'Spatial Buffering of Potassium Ions in Brain Extracellular Space', *Biophysical Journal* vol. 78, no. 6, 2000. 2776-2797.

Dayan, P. and Abbott, L. F., Theoretical Neuroscience : Computational and Mathematical Modeling of Neural Systems, MIT Press, Cambridge, Mass. ; London, 2001, pp. xv, 460.

Freeman, A. J., Mass Action in the Nervous System : Examination of the Neurophysiological Basis of Adaptive Behavior through the Eeg, Academic Press, New York, 1975

Hamalainen, M., Hari, R., Ilmoniemi, R. J., Knuutila, J. and Lounasmaa, O. V. 'Magnetoencephalography - Theory, Instrumentation, and Applications to Noninvasive Studies of the Working Human Brain', *Reviews of Modern Physics* vol. 65, no. 2, 1993. 413-497.

Hille, B., Ion Channels of Excitable Membranes, Third ed., Sinauer Associates, Inc., Sunderland, MA., 2001

Hirose, A. 'Electric Field in the Coulomb Gauge', *Physics Essays* vol. 13, no. 4, 2000. 613-615.

Holt, G. R. (1998) A Critical Reexamination of Some Assumptions, Implications of Cable Theory in Neurobiology. California Institute of Technology, Pasedena, California.

Jackson, J. D., Classical Electrodynamics, 3rd ed., Wiley, New York, 1999

Jackson, J. D. 'From Lorenz to Coulomb and Other Explicit Gauge Transformations', *American Journal of Physics* vol. 70, no. 9, 2002. 917-928.

Jackson, J. D. and Okun, L. B. 'Historical Roots of Gauge Invariance', *Reviews of Modern Physics* vol. 73, no. 3, 2001. 663-680.

Johnston, D. and Wu, S. M.-s., Foundations of Cellular Neurophysiology, MIT Press, Cambridge, Mass., 1995, pp. xxxi, 676 p.

Joshi, R. P., Sridhara, V. and Schoenbach, K. H. 'Microscopic Calculations of Local Lipid Membrane Permittivities and Diffusion Coefficients for Application to Electroporation Analyses', *Biochemical and Biophysical Research Communications* vol. 348, no. 2, 2006. 643-648.

Kandel, E. R. and Schwartz, J. H., Principles of Neural Science, 4th , International ed., McGraw-Hill, New York, 2000, pp. xli, 1414.

Kobayashi, M., Takeda, M., Ito, K. I., Kato, H. and Inaba, H. 'Two-Dimensional Photon Counting Imaging and Spatiotemporal Characterization of Ultraweak Photon Emission from a Rat's Brain in Vivo', *Journal of Neuroscience Methods* vol. 93, no. 2, 1999a. 163-168.

Kobayashi, M., Takeda, M., Sato, T., Yamazaki, Y., Kaneko, K., Ito, K., Kato, H. and Inaba, H. 'In Vivo Imaging of Spontaneous Ultraweak Photon Emission from a Rat's Brain Correlated with Cerebral Energy Metabolism and Oxidative Stress', *Neuroscience Research* vol. 34, no. 2, 1999b. 103-113.

Koch, C., Biophysics of Computation : Information Processing in Single Neurons, Oxford University Press, New York, 1999, pp. xxiii, 562 p.

Koch, C. and Segev, I., Eds. (1998). Methods in Neuronal Modeling : From Ions to Networks. Computational Neuroscience. Cambridge, Mass., MIT Press.

Kuffler, S. W. and Nicholls, J. G., From Neuron to Brain : A Cellular Approach to the Function of the Nervous System, Sinauer Associates, Sunderland, Mass., 1976, pp. xiii, 486 p.

Lee, K. Y. C., Klingler, J. F. and McConnell, H. M. 'Electric-Field-Induced Concentration Gradients in Lipid Monolayers', *Science* vol. 263, no. 5147, 1994. 655-658.

Lindsay, K. A., Rosenberg, J. R. and Tucker, G. 'From Maxwell's Equations to the Cable Equation and Beyond', *Progress in Biophysics & Molecular Biology* vol. 85, no. 1, 2004. 71-116.

Lorente de No, R., A Study of Nerve Physiology, Part I (Vol 131), The Rockefeller Institute for Medical Research, New York, 1947a, p. 496.

Lorente de No, R., A Study of Nerve Physiology, Part Ii (Vol 132), The Rockefeller Institute for Medical Research, New York, 1947b, p. 548.

Maggio, B., Borioli, G. A., Del Boca, M., De Tullio, L., Fanani, M. L., Oliveira, R. G., Rosetti, C. M. and Wilke, N. 'Composition-Driven Surface Domain Structuring Mediated by Sphingolipids and Membrane-Active Proteins', *Cell Biochemistry and Biophysics* vol. 50, no. 2, 2008. 79-109.

Magistretti, P. J. and Ransom , B. R. (2002) Chapter 10: Astrocytes. In K. L. Davis, D. Charney, J. T. Coyle, and C. Nemeroff (eds.). *Neuropsychopharmacology: The Fifth Generation of Progress*, Lippincott Williams & Wilkins

Malmivuo, J. and Plonsey, R., Bioelectromagnetism : Principles and Applications of Bioelectric and Biomagnetic Fields, Oxford University Press, New York, 1995, pp. xxii, 482 p.

Nunez, P. L. and Srinivasan, R., Electric Fields of the Brain : The Neurophysics of EEG, 2nd ed., Oxford University Press, Oxford, New York, 2006

Peterka, D. S., Takahashi, H. and Yuste, R. 'Imaging Voltage in Neurons', *NEURON* vol. 69, no. 1, 2011. 9-21.

Pethig, R. (1986) Ion, Electron, and Proton Transport in Membranes: A Review of the Physical Processes Involved. In F. Gutmann, and H. Keyzer (eds.). *Modern Bioelectrochemistry*, Plenum Press, New York.

Plonsey, R. 'Volume Conductor Fields of Action Currents', *Biophysical Journal* vol. 4, no. 4, 1964. 317-&.

Plonsey, R. and Collin, R., Principles and Applications of Electromagnetic Fields, McGraw Hill, New York, 1961

Plonsey, R. and Fleming, D. G., Bioelectric Phenomena, McGraw-Hill, New York,, 1969, pp. xiv, 380 p.

Plonsey, R. and Heppner, D. B. 'Considerations of Quasi-Stationarity in Electrophysiological Systems', *Bulletin of Mathematical Biophysics* vol. 29, no. 4, 1967. 657-&.

Romijn, H. 'Are Virtual Photons the Elementary Carriers of Consciousness?', *Journal of Consciousness Studies* vol. 9, no. 1, 2002. 61-81.

Rosenfalck, P. 'Intra- and Extracellular Potential Fields of Active Nerve and Muscle Fibres - a Physico-Mathematical Analysis of Different Models', *Acta Physiologica Scandinavica* vol. Supplement, 1969. 9-168.

Sadiku, M. N. O., Elements of Electromagnetics, 3rd ed., Oxford University Press, New York, 2001

Speckmann, E.-J. and Elgar, C. E. (2005) Introduction to the Neurophysiological Basis of the Eeg and Dc Potentials. In E. Niedermeyer, and F. H. Lopes da Silva (eds.). *Electroencephalography : Basic Principles, Clinical Applications, and Related Fields*, Lippincott Williams & Wilkins, Philadelphia.

Chapter 3

EXPERIMENTAL METHOD & HYPOTHESES

"*Empirical evidence derives no necessity for causal relationships…*"

Patterns of Scientific Explanation
Thomas Nagel (Nagel 1961)

3.1 Introduction

In the previous two chapters, a review of brain anatomy and physiology was conducted aimed at the most likely mechanism responsible for the endogenous EM fields in excitable cell tissue. Additionally, a review of the historical use of the equations of electromagnetism by neuroscience was conducted. The equations of electromagnetism were assembled in a way that clearly demonstrated how charges, currents and their dynamics originate the fields. The analysis then involved a detailed look at the way charges and currents are established and behave in brain tissue. Spatiotemporal coherence was isolated as the essential feature of charge and currents that allowed different populations of charge and current to be held more or less accountable for a structured EM field system. The more coherent the current/charge behaviour, the stronger and more regular their resultant field system contribution. Of the range of currents known to dominate the tissue, transmembrane (ion channel) currents were isolated as having the maximum level of spatial and temporal coherence. The circumstances of the coherence demands coordinated behaviour by multiple ion channels. This includes the active channels involved in sub-threshold ion channel dynamics, action potential instigation, action potential propagation, post-synaptic ion channel dynamics, gap junction plaque dynamics and any capacitative currents related to them.

The analysis revealed that the fields originate in a microscopic original cause that is seven or eight spatial orders of magnitude smaller than fields recorded by macroscopic probes. By revealing the hierarchical structure of the material, it was demonstrated how the EM field is unified by vector superposition, into a single system that inherits its structure and dynamics from the entire matter-hierarchy of the material down to its molecular origins. The unity of the field system was characterized under the name 'EM syncytium'. The originating currents were also held accountable for the production of a magnetic field that is equally detailed, although much smaller in terms of its effect on the medium. It was demonstrated how the resultant endogenous field system exerts an influence at the speed of light in a line-of-sight manner via the Lorentz force. The proposed coherent current mechanism was posited as being capable of mutually influencing the neurons that generated it. This mechanism is consistent with recent empirical evidence that is highly suggestive that the field system is self modifying (Anastassiou, Perin *et al.* 2011, Frohlich and McCormick 2010).

With a plausible basic mechanism in hand, it becomes necessary to explore the field system produced by the transmembrane currents. Ultimately, with sufficient tissue detail, it will be possible to consider predicting brain EM fields at a whole-tissue level. At this stage of development, however, the actual EM field produced by a gap junction plaque, post-synaptic plaque or an action potential are not defined for even a single instance of any one of these phenomenon. What is available is a large body of whole-neuron compartmental cable equation models. As a starting point, it seems reasonable to investigate the EM fields produced by all the ion channels during the production of an action potential. The question then becomes one of knowing the relationship between individual ion channels and their contribution to a compartmental current. This provides the launching place for experimental study, which therefore requires testable hypotheses.

3.2 Hypotheses

Two hypotheses were constructed in such a way that testing (simulation) might reveal EM field behaviours consistent with the observed self-modifying behaviour of the field system. The development of EM field originating mechanism is at a very early, tentative stage. As such, the hypotheses have to be aimed at fundamental outcomes. The process is not demonstrating quantitatively accurate fields, but rather, it demonstrates how fields with the properties appropriate to self modification behaviour can be expressed by coherent currents at all.

3.2.1 HYPOTHESIS H1

Ion channel current coherence in a single neuron can project and direct a unified, stable, faint electric field system large enough to bathe itself and its local neural/astrocyte neighbours. **(3.1)**

3.2.2 HYPOTHESIS H2.

The collective dynamics of excitable cell tissue based on neurons is more completely described as a two-axis mutual action-potential/electromagnetic (AP/EM) resonance than the traditional single axis action-potential (AP) description alone. **(3.2)**

3.2.3 Discussion

Successful testing of hypothesis 1 does not require delivery of quantitative accuracy (strength) of the fields. It is now well established that line-of-sight EM field effects, in real tissue, are significant enough to cause the empirically observed self-modification (Anastassiou, Perin *et al.* 2011, Frohlich and McCormick 2010). What is missing from the discourse is a viable specific explanatory mechanism. Hypothesis 1 establishes and scientifically characterizes a plausible possible mechanism. Once established, the mechanism can be deployed (in future work) into more realistic tissue simulations capable of accurately computing the fields observed in the lab. For the same reason, hypothesis 1 does not acquire the production of details of any particular field system for any particular neuron.

Hypothesis 2 is contingent on the successful testing of hypothesis 1. If no unified, consistent field system can be expressed by ion channel coherence, then there is no point in establishing its role in tissue configurability. Hypothesis 2 requires additional behaviour in the form of a demonstration of adaptability. If neurons have some level of EM field adaptability, in which a single neuron action potential (for example) can exhibit more than one EM field system, then the EM field line-of-sight influences have the level of degeneracy necessary for them act as configuration ‘degree of freedom’ that is not currently in any neural modelling system. If sufficient adaptability (degeneracy) can be demonstrated, then the observed EM field self-modification property, and the adaptability involved in axo-dendritic coupling by synapses, together, form a more complete description of the system dynamics.

3.3 Choosing the experimental procedure

3.3.1 Background

The previous chapter showed that the expression of macroscopic fields by microscopic sources requires their application beneath the spatial limits for the valid application of macroscopic electromagnetism. Additionally, within macroscopic EM itself, the use of Ohm's law was found to be formally inaccurate (at the scale of the microscopic sources) due to neural tissue's charge configuration and dynamics being that of a convector. One alternative was to discard macroscopic EM in favour of microscopic electromagnetism. This approach requires an onerous wholesale conversion to molecular electrodynamics. The requisite cultural and technological impact made the approach a very difficult one. Given the state of development of the science, it seemed prudent to implement an interim bridge between the macroscopic and microscopic realm. Despite being inaccurate at some (not fully defined) level, this bridging approach makes maximal use of the large body of knowledge of macroscopic EM, while facilitating the beginnings of a microscopic approach. Provided the shortcomings and scope of applicability is realistically appraised, the bridging approach squeezes the last useful knowledge out of a system of macroscopic formalisms that is reaching the limits of its usefulness. The final determinant of experimental approach recognizes the onerous statistics involved in accounting for realistic neuron morphology and ion channel expression.

The most well travelled form of macroscopic electromagnetism, developed specifically for biology in the middle of the twentieth century, is the 'volume conduction' formulation of macroscopic electromagnetism. This formalism is derived from first principles in the next chapter. It is a macroscopic formalism that presupposes conduction (Ohm's law), and hence attracts the above criticism in its application to microscopic scales. If there is a bridging form of the macroscopic equations of electromagnetism, it suffices to simply make use of macroscopic EM underneath its validity limes and accept that situation. That is, the use of volume conduction must be sanctioned, for our purposes, at spatial scales beneath their limit of valid use. Given macroscopic electromagnetism is presupposed, volume conduction can then be driven by microscopic sources. Given an assumption of Ohm's law, then there is the further caveat that the intricate charge population behaviour will not be captured by the method. Microscopic sources can be established in a manner accounting for realistic neuron morphology and ion channel details. This involves the overall process in a numerical approach requiring high performance computing.

Coherent transmembrane current has been identified as dominant contributor to the EM fields. The largest volume of data capturing transmembrane currents exists within compartmental modelling. The overall 'bridging' approach has thus converged on

- Continued use of macroscopic EM.
- Volume conduction mathematics and driven by microscopic current sources (the acceptance that Ohm's law is applicable).
- Current sources derived from a compartmental neuron model that provides a the classes of transmembrane current. This recognizes that the most common typical use of compartmental models is the accurate production of action potentials.
- Use of 'compartment' current as a source of ion channel current.
- Realistic current sources and computation of fields handled by high performance computing.
- Computation of the LFP (electric field), whilst demonstrating that the magnetic field is produced by the same system of sources.

The experimental process thus reduces to the identification of a suitable compartmental neural model that can deliver the transmembrane currents, the customization of the volume conduction equations to a set of realistic ion-channel-like sources, followed by the implementation of suitable high performance computing to carry out the field calculations. The resultant experimental system will therefore only deliver the electric fields. The contribution of synapses and action potentials will therefore depend on the whether the chosen model includes the associated currents in a realistic way (including their correct temporal instigation). This was regarded as adequate for 'proof-of-mechanism' support for hypothesis 1.

3.3.2 Chosen experimental regime

As it happens there is an ideal candidate compartmental neuron model used in a recent analysis directed at LFP prediction for a single neuron (Milstein and Koch 2008). It produced very different LFP results because it used a simplified system of current sources. It also delivered a computational result. This delivers some evidence of the state of the science involved in the isolation of a mechanism behind the LFP. Milstein used a particular compartmental model that had repeatedly been used in similar contexts for about five years and had been generalized and installed in a public repository. The simulation used the NEURON (Hines and Carnevale 1997) compartmental model of a rat hippocampus CA1 pyramidal neuron. The packaged version is available at http://www.neuron.yale.edu under ModelDB number 84589. The NEURON code had to be modified to report transmembrane (including separated passive, capacitative, sodium, potassium and calcium) currents during the production of an action potential. Note that there were twelve different channel types, with multiple channels for the different ions. The package does not separate the currents by channel type, but summed them over ion type. This is the reason for the particular transmembrane current components. As per the previous two chapters, the ICS and ECS currents are less coherent and therefore expected to contribute only field noise and are ignored for the purposes of hypothesis 1.

The action potential was triggered artificially. As a result there is no useful synaptic current produced by the simulation. As a result, hypothesis testing was confined to the transmembrane currents related to an action potential. This is probably fortuitous because real synapse current will be highly dependent on the timing of action potentials from other neurons in a network of neurons that is not part of the simulation. Confinement to the action potential fields is therefore to be preferred because it will be expressed by the natural dynamics of the model. Synapses can be added in future work. The NEURON model does not account for individual ion channels, but did include a complete biologically realistic 3D model (1128 compartments) of the neuron (called D151). The model included the best known ion channel density variations throughout the D151 structure. This was reflected in variations in transmembrane current for individual compartments.

3.3.3 Ion Channels vs. Current filaments

The NEURON model does not implement ion channels individually. Rather, their collective behaviour is manifest in the equivalent lumped-element circuit for each compartment. The current that is delivered by the package is transmembrane current. To translate the total current into equivalent ion channel activity, the concept of a ‘current filament’ was devised. A current filament takes a portion of the total transmembrane current and considers it to be located as a tiny filament in space. One end of the filament is embedded in the surface of the compartment. In this way the operation of an ion channel pore is approximated.

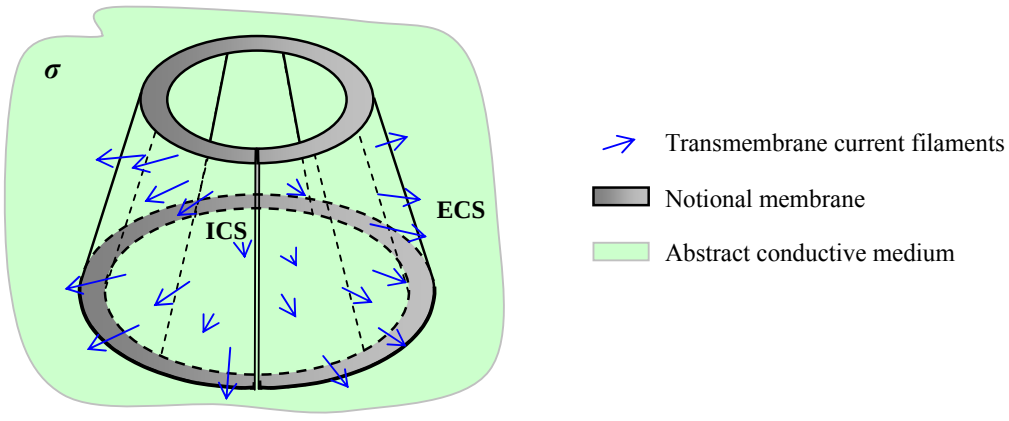

Figure 3-1 An abstract NEURON compartment (a conical frustum) populated with membrane-orthogonal filaments. The filaments are effectively embedded in a uniform conductive medium with conductivity *σ*.

Each compartment is populated with its own set of filaments, which may vary from compartment to compartment. Within a compartment, the filaments may be arranged in a defined pattern. For example, all filaments could be arranged in one small region resembling a 'plaque'. The distribution of filaments may be regular (a grid) and uniform over the surface of the frustum. The distribution may be random. In the working simulation, one filament population strategy was to allocated filaments randomly in space, with the number of filaments per compartment set based on 1 filament per unit μm^2 surface area, with a minimum number of 10 and a maximum number of 25. This strategy resulted in nearly 20,000 filaments. The important implication of this arrangement is that the ion channel is an abstraction that introduces an experimental variable. Artefacts resulting from the abstraction must be adequately analysed and explored in the experimental work. The other complication is that it requires the development of a system location of filaments to the surface on an arbitrarily located conical frustum. This is handled as part of Chapter 6.

3.3.4 Uniform conductive medium

The choice of volume conduction equations invoked an extreme tissue approximation that has two serious drawbacks. The first is that all charge populations are ignored. The equations will produce LFP, but it will not include the huge background cytosol potential mosaic identified in Chapter 2. This means that the LFP produced by the volume conduction formalism can only be said to apply to the dynamics of the LFP. As long as this is properly recognized and acknowledged, this will not alter the basic conclusions of the work. Future more accurate models can account for the realities of the ECS and ICS charge populations. Hypothesis 1 is therefore further qualified to that extent. The rationale is that if it is not possible to get a plausible field system in an abstracted, simplified medium, then the complexities of the medium are not going to add anything useful to the outcome. However, establishing a simple field mechanism an ideal medium is a valuable starting point for future refinements aimed at more tissue realism. Another reason for considering the tissue approximation adequate is the history of studies in the literature that have made the same approximation (for example (Milstein and Koch 2008)).

3.4 Chapter Summary

This chapter developed two hypotheses suited to the initial isolation of a plausible mechanism originating neuron endogenous EM fields. Hypothesis 1 isolates the basic field system expression. Hypothesis 2 investigates the relationship between neuron properties and the field expression, thereby revealing the extent of the adaptability of the field system.

To test the hypotheses based on the most likely original cause, ion channel current coherence, a bridging form of the 'volume conduction' formulation of the macroscopic equations of electromagnetism is to be established in which microscopic current filaments stand in for ion channel operation. The volume conduction equations will reveal the electric field via the LFP. The magnetic field will not be computed. The extreme simplicity of a uniform conductive medium is chosen, thereby eliminating the need for charge population specification and other complexities related to material non-uniformities. The coherent currents will be created by a large biologically realistic cable-equation (NEURON) model. Action potential currents will be allocated to small filaments spatially located orthogonal to the neuron membrane. Each filament creates a small field of its own. Their collective field expression originates the electric field due to the action potential. The details of the particular experiments are covered in Chapter 7.

3.5 Chapter bibliography

Anastassiou, C. A., Perin, R., Markram, H. and Koch, C. 'Ephaptic Coupling of Cortical Neurons', *Nature Neuroscience* vol. 14, no. 2, 2011. 217-223.

Frohlich, F. and McCormick, D. A. 'Endogenous Electric Fields May Guide Neocortical Network Activity', *Neuron* vol. 67, no. 1, 2010. 129-143.

Hines, M. L. and Carnevale, N. T. 'The Neuron Simulation Environment', *Neural Computation* vol. 9, no. 6, 1997. 1179-1209.

Milstein, J. N. and Koch, C. 'Dynamic Moment Analysis of the Extracellular Electric Field of a Biologically Realistic Spiking Neuron', *Neural Computation* vol. 20, no. 8, 2008. 2070-2084.

Nagel, E. (1961) Patterns of Scientific Explanation. *The Structure of Science : Problems in the Logic of Scientific Explanation*, Routledge, London.

Chapter 4

VOLUME CONDUCTION

> "*... that neither beliefs nor acts of belief, nor decisions, nor even preferences, are reasonable or rational except in the sense that they are reached by procedures methods that are reasonable or rational. (The phrase rational belief is rather like the phrase 'fast food'.) ...*"
>
> David Miller, a student of Karl Popper
> In 'Induction: A Problem Solved' (Miller 2005, p111)

This chapter visits the volume conduction formalisms applied to excitable cell tissue in the later chapters. The volume conduction formalism, as applied to bioelectromagnetism is generally attributed to the work of Lorente de Nó (Lorente de No 1947a, Lorente de No 1947b). It was further developed by Plonsey from about 1961 onwards (Plonsey 1964, Plonsey and Collin 1961). Tracking down the original derivation is quite difficult. The literature is also in dated form and has multiple inconsistent threads and some errors. Together these make accessing and internalizing the work a non-trivial process. For this reason I have compiled the various components from the literature trail, updated/corrected it, and present it here in modern terms.

4.1 INTRODUCTION

The classical equations of macroscopic electromagnetism were adapted about fifty years ago for use on the endogenous fields of bulk excitable cell tissue. The first form to appear applied to uniform infinite stationary conductive media. The original volume conduction equations continue to be used in attempts to characterise the 'extracellular' fields of excitable cells during synaptic activity and action potential (Gold, Henze *et al.* 2006, Holt 1998, Holt and Koch 1999, Milstein and Koch 2008). Over the fifty year period, various formulations for non-homogenous media have been constructed. The fundamental conditions common to all volume conduction formalisms are (i) macroscopic electromagnetism, (ii) quasi-static dynamics, (iii) negligible involvement of the magnetic field, (iv) Ohm's law and (v) active current sources embedded inside a conductive media. An authoritative general reference for quasi-static fields is Jackson (Jackson 1999, Chapter 5). The actual form of the applicable equations then depends on further assumptions about material properties and geometry. Where possible, the volume conduction formulation is examined in light of modern neuroscience knowledge. The consolidating and modernising the original derivation revealed a few non-problematic oddities. These are outlined and resolved.

It is important to understand that, in their original construction, there was no spatial minimum beneath which the equations were invalidated. Such a limit has been identified in Chapter 2, and it applies to all macroscopic electromagnetism, not just volume conduction. It is also worth reinforcing that the

volume conduction equations are a *continuum* form with no other predetermined or recommended limits. Temporal limits may be taken to be the decay-times associated with disturbances to the charge density (effective zero divergence of the current density). In their establishment, it will be shown below that a set of arbitrary volume current density sources are defined. In the practical use of the equations, the specific manner by which this set of (non-Ohmic) sources is established in space is not specified. The rationale is, whatever the details of source implementation are, the necessary charge behaviours are sufficiently spatially constrained, far from points of interest, that their impact may be neglected. Provided these constraints are recognised, the formalism functions well. They have been usefully applied in this form for fifty years, and there appears to be useful life left in them.

4.1.1 The Original Volume Conduction Equations

The first and primary form of the volume conduction equations added the assumption of an infinite, linear, isotropic, homogenous, stationary conductivity. Plonsey and Fleming derived a scalar potential function (Plonsey and Fleming 1969, p203),

$$\varphi(\mathbf{r},t)=\frac{1}{4\pi\sigma}\int_V \frac{I_v(\mathbf{r}',t)}{|\mathbf{r}-\mathbf{r}'|}d^3r' \tag{4.1}$$

where

$$I_v(\mathbf{r},t)=-\nabla\bullet\mathbf{J}_s(\mathbf{r},t). \tag{4.2}$$

The scalar potential φ, in Volts, at any point $\mathbf{r}$ (inside and outside V) and time t is thus driven by a distributed source current density vector field $\mathbf{J}_s(\mathbf{r},t)$ embedded in an infinite material of uniform, linear, stationary conductivity σ. $I_v(\mathbf{r},t)$ is a scalar function of a vector position $\mathbf{r}$ and time t that delivers volume current density in units $A\cdot m^{-3}$. The current sources are completely contained by the volume V. The derivation of equations (4.1) and (4.2) is the target here, and has its origins in (Plonsey and Collin 1961, Section 9.9). The equations have been carried through to the most recent version of a book by (Malmivuo and Plonsey 1995). The driver term $I_v(\mathbf{r},t)$ in equation (4.1) is best understood as the current-moment contribution of a current density field, where the current density is regarded as a collection of current dipoles and the units of 'dipole moment' are A·m. The dynamics involved with a current density are therefore the dynamics of 'current dipole moment per unit volume'. A physically plausible and mathematically justified demonstration of the appropriateness of this interpretation is given in (Plonsey and Fleming 1969, p215). Within the quasi-static formulation of MME is Ohm's law, which applies to uniform, stationary conductors as per

$$\mathbf{J}(\mathbf{r},t)=\sigma\mathbf{E}(\mathbf{r},t). \tag{4.3}$$

Current density $\mathbf{J}$ is in $A\cdot m^{-2}$, σ is conductivity in $(\Omega\cdot m)^{-1}$ and $\mathbf{E}$ is the electric field vector in $V\cdot m^{-1}$. A simplistic physical derivation of Ohm's law, and a contrast between conduction and convection, can be found in Sadiku (Sadiku 2001, Page 162f). Ohm's law is only valid in the case of a macroscopic quasi-static field context of a material where charge motion (current density field $\mathbf{J}$) acts against a backdrop of zero net charge density (ρ), as discussed in Chapter 2. We can now reconstruct the derivation.

4.1.2 BACKGROUND TO THE DERIVATIONS

The process of Helmholtz decomposition and the representing EM fields as sums of potential fields has been covered in Chapter 2, where it resulted in the fundamental recognition of 'gauge' in EM, which has nothing directly to do with volume conduction. To connect the general field decomposition to volume conduction, we can use the microscopic MmE form, which will be converted to MME later. In that form, the EM fields, a sum of potentials as per Chapter 2, are

$$\mathbf{b}(\mathbf{r},t)=\nabla\times\mathbf{a}(\mathbf{r},t) \tag{4.4}$$

and

$$\mathbf{e}(\mathbf{r},t) = -\nabla\varphi(\mathbf{r},t) - \frac{\partial \mathbf{a}(\mathbf{r},t)}{\partial t}. \tag{4.5}$$

Using the MmE equations as expressed in Chapter 2, it is straightforward to reformulate MmE into two equations:

$$\nabla^2\varphi(\mathbf{r},t) + \frac{\partial}{\partial t}\left(\nabla\bullet\mathbf{a}(\mathbf{r},t)\right) = -\frac{\eta(\mathbf{r},t)}{\varepsilon_0} \tag{4.6}$$

$$\nabla^2\mathbf{a}(\mathbf{r},t) - \frac{1}{c^2}\frac{\partial^2\mathbf{a}(\mathbf{r},t)}{\partial t^2} - \nabla\left(\nabla\bullet\mathbf{a}(\mathbf{r},t) + \frac{1}{c^2}\frac{\partial\varphi}{\partial t}\right) = -\mu_0\mathbf{j}(\mathbf{r},t) \tag{4.7}$$

In the process of deriving the volume conduction equations, at this point, Plonsey and Heppner declared, "... *Now Φ and* **A** *must satisfy the Lorentz condition, namely ...etc*" (Plonsey and Heppner 1967, p661)[1]. EM gauge reflects arbitrariness of the vector potential field resulting from the lack of specification of its divergence (Jackson 1999, Section 6.3). That choice specifies the first term in the brackets of (4.7). The assertion of Lorenz gauge is actually an *optional* choice of vector potential divergence such that the bracket term in equation (13) is zero. This condition is known as the 'Lorenz condition'. Elsewhere, we are told that the Lorenz condition is equivalent to conservation of charge (Plonsey and Collin 1961, Page 323). Conservation of charge is built into the MmE, prior to any notion of gauge or vector potentials and is unavoidable. Other gauges choose different forms for DIV(**a**) and all of them conserve charge. It is not clear how the assertion of the Lorenz condition arose or why it was necessary to connect it to conservation of charge. However, these matters are ultimately moot and mentioned only to clean up these matters. The more important outcome is that when the Lorenz condition is met, equations (4.6) and (4.7) become two separated inhomogeneous wave equations in two unknowns,

$$\nabla^2\varphi(\mathbf{r},t) - \frac{1}{c^2}\frac{\partial^2\varphi(\mathbf{r},t)}{\partial t^2} = -\frac{\eta(\mathbf{r},t)}{\varepsilon_0} \tag{4.8}$$

and

$$\nabla^2\mathbf{a}(\mathbf{r},t) - \frac{1}{c^2}\frac{\partial^2\mathbf{a}(\mathbf{r},t)}{\partial t^2} = -\mu_0\mathbf{j}(\mathbf{r},t). \tag{4.9}$$

Their MME form is

$$\nabla^2\varphi(\mathbf{r},t) - \frac{1}{c^2}\frac{\partial^2\varphi(\mathbf{r},t)}{\partial t^2} = -\frac{\rho(\mathbf{r},t)}{\varepsilon} \tag{4.10}$$

and

$$\nabla^2\mathbf{A}(\mathbf{r},t) - \frac{1}{c^2}\frac{\partial^2\mathbf{A}(\mathbf{r},t)}{\partial t^2} = -\mu\mathbf{J}(\mathbf{r},t). \tag{4.11}$$

Note that the same symbol, φ, has been used for the macroscopic scalar potential. Parameters ε (F/m) and μ (H/m) are the macroscopic material permittivity and permeability, respectively. These are exactly the source equations used by (Plonsey and Collin 1961, p662) to generate equation (4.1). The similarity of the two pairs of equations tells us that if there is a macroscopic/microscopic issue, it is not due to the basic form of the field equations. The solution to this type of wave equation is well trodden ground. The MmE solution is (Jackson 1999):

$$\varphi(\mathbf{r},t) = \frac{1}{4\pi\varepsilon_0}\int_U \frac{\eta(\mathbf{r}',t)}{|\mathbf{r}-\mathbf{r}'|}d^3r' \tag{4.12}$$

$$\mathbf{a}(\mathbf{r},t) = \frac{\mu_0}{4\pi}\int_U \frac{\mathbf{j}(\mathbf{r}',t)}{|\mathbf{r}-\mathbf{r}'|}d^3r'. \tag{4.13}$$

[1] The authors also mixed up Lorenz and Lorentz. It is Lorenz to whom this idea is attributed. For a discussion see (Jackson 1999).

Note that U takes the variable of integration *r′* across the entire universe. Keeping the same symbol for the potential (a convenience only), the time domain MME form of the Plonsey versions of (4.12) and (4.13) are

$$\varphi(\mathbf{r},t)=\frac{1}{4\pi\varepsilon}\int_U\frac{\rho(\mathbf{r}',t)}{|\mathbf{r}-\mathbf{r}'|}d^3r' \tag{4.14}$$

$$\mathbf{A}(\mathbf{r},t)=\frac{\mu_0}{4\pi}\int_U\frac{\mathbf{J}(\mathbf{r}',t)}{|\mathbf{r}-\mathbf{r}'|}d^3r'\,. \tag{4.15}$$

The Lorenz gauge is interesting in that it allows both the electric and magnetic fields to be expressed by a single vector potential **A** thus:

$$\mathbf{B}(\mathbf{r},t)=\nabla\times\mathbf{A}(\mathbf{r},t) \tag{4.16}$$

$$\mathbf{E}(\mathbf{r},t)=\left[c^2\int_0^t\nabla\left(\nabla\bullet\mathbf{A}(\mathbf{r},t')\right)dt'\right]-\frac{\partial\mathbf{A}(\mathbf{r},t)}{\partial t}\,. \tag{4.17}$$

Note that these equations, insofar as they are accepted as valid, indicate the manner of expression of a vector potential **a** and a magnetic field **b** in brain material.

4.1.3 CHARGE CONSERVATION AND CONDUCTIVITY

We can now move towards equation (4.1) from MME and MmE rearranged to reveal conservation of charge:

$$\nabla\bullet\mathbf{J}(\mathbf{r},t)+\frac{\partial\rho(\mathbf{r},t)}{\partial t}=0 \tag{4.18}$$

$$\nabla\bullet\mathbf{j}(\mathbf{r},t)+\frac{\partial\eta(\mathbf{r},t)}{\partial t}=0\,. \tag{4.19}$$

Once again, we note that the similarity of the two equations tells us that if there is a macroscopic/microscopic issue, it is not due to the fundamentals of charge conservation. Now examine the ‘quasi-static’ conditions. If the right hand term of equation (4.18) or (4.19) changes slowly enough, then the DIV of the current density approaches zero. It is ‘as-if’ the current density is entirely comprised of CURL (that is, it is ‘transverse’). This is where the connection to another gauge can be made. In the Coulomb gauge, **j** is deliberately forced to be viewed as entirely transverse. Maxwell’s equations then involve a different vector potential for the same **e** and **b** fields. This does not mean that equation (4.1) is formulated in the Coulomb gauge (transverse current density is the hallmark of the gauge). It means that the potentials are, in a sense, a pseudo-Coulomb gauge, but only because the ‘quasi-static’ constraint renders the current density quasi-solenoidal when Ohm’s law applies. This will be seen shortly. In ‘quasi-static’ conditions, particular charge behaviours can temporarily support both a non-zero charge density and non-zero current density, in the same region of space, such that equations (4.18) and (4.19) merely sum to zero. This is the true underlying nature of a conductive (as opposed to convective) current, which involves the decoupling, *on average*, of charge density and current density. Quasi-static is the approximate condition, which arises when the net charge density is effectively zero because the charge density can rearrange itself so quickly in responses to changes in current density that for practical purposes:

$$\nabla\bullet\mathbf{J}(\mathbf{r},t)=0\ \text{ or }\ \nabla\bullet\mathbf{j}(\mathbf{r},t)=0\,. \tag{4.20}$$

This is the point where the microscopic/macroscopic boundary can be claimed to have been crossed; but it is a subtle point. To better unpack this situation, whilst heading towards volume conduction, we now examine a macroscopic context where current density sources exist. We can assume Ohm’s law, equation (4.3) (noting that it *only* applies to MME), by considering a region subject to modelling and for which a collection of (non-ohmic) current density sources $\mathbf{J}_s(\mathbf{r}, t)$ are added. These current sources violate equation (4.3) in a known region of space, *V*, in known ways. The rest of the space is assumed to obey equation (4.3). The total current density throughout the universe, *U*, can be written as:

$$\mathbf{J}(\mathbf{r},t) = \sigma\mathbf{E}(\mathbf{r},t) + \mathbf{J}_s(\mathbf{r},t). \quad \textbf{(4.21)}$$

Under this **J**, conservation of charge can be examined by applying MME (4.21) to (4.18). We get

$$\sigma\nabla\bullet\mathbf{E}(\mathbf{r},t) + \nabla\bullet\mathbf{J}_s(\mathbf{r},t) + \frac{\partial\rho(\mathbf{r},t)}{\partial t} = 0, \quad \textbf{(4.22)}$$

where the charge density is now *total* – of all the charge from the source and non-source origins. Next note that MME, for polarisable materials, gives us

$$\mathbf{D}(\mathbf{r},t) = \varepsilon_0\mathbf{E}(\mathbf{r},t) + \mathbf{P}(\mathbf{r},t) \quad \textbf{(4.23)}$$

and

$$\nabla\bullet\mathbf{D}(\mathbf{r},t) = \rho(\mathbf{r},t). \quad \textbf{(4.24)}$$

For simple, linear, homogeneous, stationary, polarisable materials, equation (4.23) becomes

$$\mathbf{D}(\mathbf{r},t) = \varepsilon\mathbf{E}(\mathbf{r},t). \quad \textbf{(4.25)}$$

Brain material has highly anisotropic dielectric properties, which can be recreated in MME by creating appropriate tensor forms for the conductivity and permittivity. For the purposes here, we continue with equations (4.24) and (4.25) applied to equation (4.22), giving

$$\frac{\partial\rho(\mathbf{r},t)}{\partial t} + \frac{\sigma}{\varepsilon}\rho(\mathbf{r},t) = -\nabla\bullet\mathbf{J}_s(\mathbf{r},t) \ \text{A·m}^{-3}. \quad \textbf{(4.26)}$$

Note that it is specifically the right term in (4.26) that is assigned the symbol $I_v(\mathbf{r},t)$ in (4.2). In the case where no sources are present,

$$\frac{\partial\rho(\mathbf{r},t)}{\partial t} + \frac{\sigma}{\varepsilon}\rho(\mathbf{r},t) = 0 \ (\text{A·m}^{-3}). \quad \textbf{(4.27)}$$

Note that equations (4.26) and (4.27) have the 'volume current density' units of the term $I_v(\mathbf{r},t)$ in equation (4.1). Equation (4.26) is a first order differential equation telling us how conservation of charge impacts the behaviour of charge carriers, *but only for the specific case where Ohm's law applies*. Equation (4.27) has the following response to an imposition, at time $t = 0$, of a charge density $\rho(\mathbf{r},0)$,

$$\rho(\mathbf{r},t) = \rho(\mathbf{r},0)e^{-\frac{\sigma}{\varepsilon}t} \ \text{C·m}^{-3}. \quad \textbf{(4.28)}$$

First, any disturbance in charge density through natural charge motions results in a current density divergence for a time necessary to return the disturbance to equilibrium via (4.27). Second, in a region with sources, (4.26) tells us how the source-free medium reacts to being violated by the inclusion of non-Ohmic current density sources. The charge that constitutes $\mathbf{J}_s(\mathbf{r},t)$ simply appears out of nowhere and can be considered to merely rearrange the existing charge density (no new charge is injected). For future reference, note that this is notionally consistent with the operation of transmembrane ion channel currents. The magnitude of the time constant and it implications were discussed in chapter 2. The dynamics of conductivity are not explicit in the volume conduction literature. Instead, in (Plonsey and Heppner 1967, p662), in the process of the analysis of equation (4.21), there is a simple declaration that DIV $\mathbf{J}(\mathbf{r},t) = 0$[2]. Also, in the original derivation, we find

> "Since **J** is solenoidal, $\nabla\bullet\mathbf{J} = 0 = \nabla\bullet\mathbf{J}_i + \nabla\bullet\sigma\mathbf{E}$"
> (Plonsey and Fleming 1969, p210, Plonsey and Heppner 1967, p662)

This statement is not strictly the case. Let us reformat (4.21) by making the conservation of charge in (4.19) explicit in (4.26), giving

[2] Note that the *i* (for input) suffix is used instead of the *s* (for source) used here.

$$\left.\frac{-\nabla\bullet\mathbf{J}(\mathbf{r},t)}{\sigma}\right|_A + \left.\frac{\rho(\mathbf{r},t)}{\varepsilon}\right|_B = \left.\frac{-\nabla\bullet\mathbf{J}_s(\mathbf{r},t)}{\sigma}\right|_C \ \text{A}\cdot\text{m}^{-3}. \tag{4.29}$$

This is the same first order differential equation with a solution like (4.27) where the steady state, (4.29)*A*, which is the time-rate of change of current density, approaches zero and thus (4.29)*B* and (4.29)*C* equate. Thus, the current density, albeit briefly, *is not solenoidal*. This is the true nature of the quasi-static conduction form. In reality, (4.29)*B* and (4.29)*C* track each other in time with a delay determined by the time constant ε/σ seconds as a result of (4.29)*A*. The appearance of this at long timescales is that the charge density directly reflects the divergence of the current density source. If there are no sources then the effect is that the net current density divergence approaches zero. As per the Chapter 2 discussion, with approximate conductive conditions at the appropriate spatiotemporal scale, we can validly claim that

$$\nabla\bullet\mathbf{J}(\mathbf{r},t) \approx 0 \ \text{A}\cdot\text{m}^{-3}\,. \tag{4.30}$$

However, equation (4.30) is not a statement about the solenoidality of the current density field, but a statement about an ensemble/regional temporal average under special conditions better called quasi-solenoidality. With this understanding in hand, we can, from this point, complete our derivation of (4.2). Equation (4.30) also means that equation (4.19) is telling us, through (4.29), that

$$\frac{\rho(\mathbf{r},t)}{\varepsilon} = \frac{-\nabla\bullet\mathbf{J}_s(\mathbf{r},t)}{\sigma} = \frac{I_v(\mathbf{r},t)}{\sigma}\ \text{V}\cdot\text{m}^{-2}. \tag{4.31}$$

Thus, if Ohmic conduction applies, the fields, on average, are determined by the volume current source density function I_v.

4.1.4 THE EQUATION (4.1) ASSUMPTIONS AND FORMULATION

We have almost enough to generate (4.1) from (4.14) and (4.15). First, we have to examine the 'bioelectric phenomena assumptions'. These assumptions have been in circulation since the nineteen sixties (Lindsay, Rosenberg *et al.* 2004) and have had several relatively recent reviews e.g. (Holt 1998). The assumptions first assume quasi-magnetostatic circumstances, which facilitates an assertion of Ohm's law (4.3). To this we add the 'quasi-solenoidal' nature of the current density of (4.30) (Plonsey 1964). The time rate of change of the magnetic vector potential is very small and therefore negligible. This means that magnetic induction effects are neglected and that the scalar potential alone (in (4.5)) determines the electric field. Applied to (4.3), it follows that

$$\mathbf{J}(\mathbf{r},t) = \sigma\mathbf{E}(\mathbf{r},t) = -\sigma\nabla\varphi(\mathbf{r},t)\,, \tag{4.32}$$

or

$$\frac{\mathbf{J}(\mathbf{r},t)}{\sigma} = \mathbf{E}(\mathbf{r},t) = -\nabla\varphi(\mathbf{r},t)\,. \tag{4.33}$$

In uniform media, using the fundamental MME equation for the divergence of **D** and equation (4.25), we get

$$\nabla\bullet\mathbf{E}(\mathbf{r},t) = \frac{\rho(\mathbf{r},t)}{\varepsilon} \tag{4.34}$$

The DIV of (4.33) equated to (4.34) results in

$$\frac{\nabla\bullet\mathbf{J}(\mathbf{r},t)}{\sigma} = \nabla\bullet\mathbf{E}(\mathbf{r},t) = -\nabla^2\varphi(\mathbf{r},t) = \frac{\rho(\mathbf{r},t)}{\varepsilon} = \frac{I_V(\mathbf{r},t)}{\sigma}\,. \tag{4.35}$$

If we include the current density sources, noting that the DIV of the current density behaves as per (4.29), we return to the wave equation solution (4.14) and find that

$$\varphi(\mathbf{r},t) = \frac{1}{4\pi}\int_U \frac{\rho(\mathbf{r}',t)}{\varepsilon}\frac{1}{|\mathbf{r}-\mathbf{r}'|}d^3r'\,. \tag{4.36}$$

From this, we can see from (4.33) and the constraint (4.31), that the solution to the scalar potential is

$$\varphi(\mathbf{r},t) = \frac{1}{4\pi}\int_U \frac{-\nabla'\bullet\mathbf{J}_s(\mathbf{r}',t)}{\sigma}\frac{1}{|\mathbf{r}-\mathbf{r}'|}d^3r' = \frac{1}{4\pi}\int_U \frac{I_v(\mathbf{r}',t)}{\sigma}\frac{1}{|\mathbf{r}-\mathbf{r}'|}d^3r' . \quad \textbf{(4.37)}$$

This concludes the derivation of equation (4.1). This is a very general result, and has involved no limits on I_v or considerations of geometry. In particular, it is worth noting that the result is applicable to instantaneous currents. This result has not had to take into account any of the details of brain material except for the broad conditions of quasi-magnetostatics including a uniform material version of Ohm's law. We can see that the imposition, throughout U, of non-Ohmic sources of the I_v kind has forced the potential into the form of (4.37) in an infinite, linear, stationary, homogenous, isotropic medium. This constraint forces a situation of the applicability of a Poisson equation driven by I_v. This can be seen if we insert the (4.31) right hand term into (4.35), resulting in

$$\nabla^2\varphi(\mathbf{r},t) = \frac{I_v(\mathbf{r},t)}{\sigma} . \quad \textbf{(4.38)}$$

This has the form of Poisson's equation and was asserted at the beginning of the Plonsey derivation in (Jackson 1999). This equation contrasts with the often-used Laplace equation in brain material,

$$\nabla^2\varphi(\mathbf{r},t) = 0 . \quad \textbf{(4.39)}$$

Laplace's equation is the special case when the volume source density is zero.

4.2 Some housekeeping

For the purposes of later developments of the scalar potential of a volume conduction field, we now, for consistency, develop some of the background mathematics. This sort of development has proven to be difficult to access in the literature. Indeed it has resulted from an inability to find any useful consolidation of the mathematics in the literature. Consider Figure 4-1, which depicts a scalar potential field inside and outside a notional simply connected volume V bounded by a surface S. The surface is specified by a collection of vectors $\mathbf{r}_S$ and there is a set of vectors normal to the surface for every vector $\mathbf{r}_S$. We are interested in the potential $\varphi(\mathbf{r})$ throughout U.

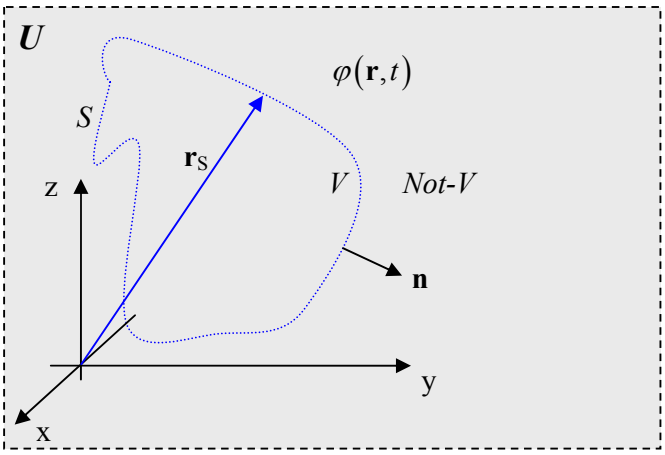

Figure 4-1 Scalar field $\varphi(\mathbf{r},t)$ through a space U inside and outside a region V with surface S.

4.2.1 Miscellaneous useful identities

Vector identities suited to the understanding of electromagnetism in biological materials tend to be spread about in the physics literature, making it difficult to become quickly apprised of techniques. To obviate the need for a set of disparate references, a few important identities are consolidated and presented. Where their proofs are non-straightforward and/or difficult to find in the literature, appendices are provided. Special care is taken in issues related to primed and unprimed variables. For example, it is known that (Manby and Knowles 2001, Equation 10)

$$\nabla\left(\frac{1}{|\mathbf{r}-\mathbf{r}'|}\right)=-\frac{\mathbf{r}-\mathbf{r}'}{|\mathbf{r}-\mathbf{r}'|^3}=-\nabla'\left(\frac{1}{|\mathbf{r}-\mathbf{r}'|}\right) \tag{4.40}$$

and

$$\nabla^2\left(\frac{1}{|\mathbf{r}-\mathbf{r}'|}\right)=-4\pi\delta(\mathbf{r}-\mathbf{r}'). \tag{4.41}$$

With a little extra manipulation, it can also be shown that

$$\nabla'\left[\frac{1}{|\mathbf{r}'-\mathbf{r}|}\right]=\nabla\left[\frac{1}{|\mathbf{r}-\mathbf{r}'|}\right] \tag{4.42}$$

and

$$\nabla^2\left(\frac{1}{|\mathbf{r}-\mathbf{r}'|}\right)=\nabla\cdot\nabla\left(\frac{1}{|\mathbf{r}-\mathbf{r}'|}\right)=3\frac{\left[\left(\mathbf{n}_{\mathbf{r}-\mathbf{r}'}\bullet\mathbf{n}_{\mathbf{r}-\mathbf{r}'}\right)-1\right]}{|\mathbf{r}-\mathbf{r}'|^3}. \tag{4.43}$$

where $\mathbf{n}_{\mathbf{r}-\mathbf{r}'}$ is a normalized vector in the direction of $\mathbf{r}-\mathbf{r}'$. Note that this equation misbehaves at $\mathbf{r}=\mathbf{r}'$ and has not been located in the literature as yet. The final accurate result of (4.41) can be reached through differentiation using a limiting process. With a bit of expansion it is also straightforward to show that

$$\nabla^2\left(\frac{1}{|\mathbf{r}-\mathbf{r}'|}\right)=\nabla'^2\left(\frac{1}{|\mathbf{r}-\mathbf{r}'|}\right). \tag{4.44}$$

More widely published is the following result for the Dirac delta function $\delta(\mathbf{r})$,

$$\int_U f(\mathbf{r}')\delta(\mathbf{r}-\mathbf{r}')d^3r'=f(\mathbf{r}). \tag{4.45}$$

Next is the relatively obscure identity (Plonsey 1964)

$$\int_U\frac{\nabla'^2 f(\mathbf{r}')}{|\mathbf{r}-\mathbf{r}'|}d^3r'=-4\pi f(\mathbf{r}), \tag{4.46}$$

where $f(\mathbf{r})$ is a suitably well-behaved function of $\mathbf{r}$ that spatially decays faster than $1/|\mathbf{r}-\mathbf{r}'|$. This is a non-trivial result. A derivation has been provided in Appendix A.

4.2.2 Green's Identity

Green's identity is a generalised property of pairs of 'well behaved' functions examined in the circumstance of Figure 4-1. It tells us that for suitable functions Φ and ψ over the volume V bounded by surface S,

$$\int_V\phi\nabla^2\psi-\psi\nabla^2\phi dV=\oint_S\phi\frac{\partial\psi}{\partial\mathbf{n}}-\psi\frac{\partial\phi}{\partial\mathbf{n}}ds, \tag{4.47}$$

where the directional derivatives in (4.47) are

$$\frac{\partial\psi}{\partial\mathbf{n}}=\nabla\psi\bullet\mathbf{n} \tag{4.48}$$

and

$$\frac{\partial\phi}{\partial\mathbf{n}}=\nabla\phi\bullet\mathbf{n}. \tag{4.49}$$

In its practical usage, (4.47) needs to be carefully expanded to reveal its use of integrand ranging. This reveals that (4.47) actually has the following form

$$\int_V \phi(\mathbf{r}')\nabla'^2\psi(\mathbf{r}') - \psi(\mathbf{r}')\nabla'^2\phi(\mathbf{r}')\,d^3r' = \oint_S \phi(\mathbf{r}')\frac{\partial\psi(\mathbf{r}')}{\partial\mathbf{n}} - \psi(\mathbf{r}')\frac{\partial\phi(\mathbf{r}')}{\partial\mathbf{n}}\,ds'. \quad \textbf{(4.50)}$$

With (4.48) and (4.49) included, (4.50) becomes

$$\int_V \phi(\mathbf{r}')\nabla'^2\psi(\mathbf{r}') - \psi(\mathbf{r}')\nabla'^2\phi(\mathbf{r}')\,d^3r' = \oint_S \phi(\mathbf{r}')\left[\nabla'\psi(\mathbf{r}')\bullet\mathbf{n}\right] - \psi(\mathbf{r}')\left[\nabla'\phi(\mathbf{r}')\bullet\mathbf{n}\right]ds'. \quad \textbf{(4.51)}$$

The important feature of (4.51) is that the directional gradients operate on *primed* variables. This requires careful attention to how ψ is defined.

4.2.3 Green's Identity with $\psi = 1/|\mathbf{r}'-\mathbf{r}|$

The procedure customizes Green's identity based on the use of $\psi = 1/|\mathbf{r}'-\mathbf{r}|$. This particular ψ is sufficiently 'well behaved' throughout V to facilitate access to useful identities for electromagnetic scalar potentials. First we prepare

$$\phi(\mathbf{r}') = \varphi(\mathbf{r}'), \quad \textbf{(4.52)}$$

where φ is our scalar potential field and

$$\psi(\mathbf{r}') = \frac{1}{|\mathbf{r}'-\mathbf{r}|}. \quad \textbf{(4.53)}$$

Note that the primed variable $\mathbf{r}'$ must be carefully interpreted when applied to Green's identity, because the role of $\mathbf{r}$ and $\mathbf{r}'$ become reversed to the sense in which the more familiar form, $1/|\mathbf{r}-\mathbf{r}'|$. is used. With (4.52) and (4.53), Greens identity becomes

$$\int_V \varphi(\mathbf{r}')\nabla'^2\left[\frac{1}{|\mathbf{r}'-\mathbf{r}|}\right] - \frac{\nabla'^2\varphi(\mathbf{r}')}{|\mathbf{r}'-\mathbf{r}|}\,d^3r' = \oint_S \varphi(\mathbf{r}')\left[\nabla'\left[\frac{1}{|\mathbf{r}'-\mathbf{r}|}\right]\bullet\mathbf{n}\right] - \frac{1}{|\mathbf{r}'-\mathbf{r}|}\left[\nabla'\varphi(\mathbf{r}')\bullet\mathbf{n}\right]ds'. \quad \textbf{(4.54)}$$

Use the various identities supplied results in

$$\int_V \varphi(\mathbf{r}')\delta(\mathbf{r}-\mathbf{r}')\,d^3r' + \frac{1}{4\pi}\int_V \frac{\nabla'^2\varphi(\mathbf{r}')}{|\mathbf{r}-\mathbf{r}'|}\,d^3r' = \frac{1}{4\pi}\oint_S \varphi(\mathbf{r}')\left[\frac{(\mathbf{r}-\mathbf{r}')}{|\mathbf{r}-\mathbf{r}'|^3}\bullet\mathbf{n}\right] + \frac{\nabla'\varphi(\mathbf{r}')\bullet\mathbf{n}}{|\mathbf{r}-\mathbf{r}'|}\,ds'. \quad \textbf{(4.55)}$$

This is a very general result that, depending on the nature of V and the origins of φ, can lead to many different useful situations. Here, however, we need only consider the special case when V goes to infinity, or, in the terms used here, $V \to U$. When this occurs, along with (4.45), (4.55) becomes

$$\varphi(\mathbf{r}) + \frac{1}{4\pi}\int_U \frac{\nabla'^2\varphi(\mathbf{r}')}{|\mathbf{r}'-\mathbf{r}|}\,d^3r' = \frac{1}{4\pi}\lim_{V\to\infty}\oint_S \varphi(\mathbf{r}')\left[\frac{(\mathbf{r}-\mathbf{r}')}{|\mathbf{r}-\mathbf{r}'|^3}\bullet\mathbf{n}\right] + \frac{\nabla'\varphi(\mathbf{r}')\bullet\mathbf{n}}{|\mathbf{r}'-\mathbf{r}|}\,ds'. \quad \textbf{(4.56)}$$

Under (4.46) this becomes

$$0 = \frac{1}{4\pi}\lim_{V\to\infty}\oint_S \varphi(\mathbf{r}')\left[\frac{(\mathbf{r}-\mathbf{r}')}{|\mathbf{r}-\mathbf{r}'|^3}\bullet\mathbf{n}\right] + \frac{\nabla'\varphi(\mathbf{r}')\bullet\mathbf{n}}{|\mathbf{r}'-\mathbf{r}|}\,ds'. \quad \textbf{(4.57)}$$

This means that regardless of the form or origins of φ, at large $\mathbf{r}$, the two 'effective sources' that are the two right hand terms, cancel each other. Where electromagnetism is responsible for φ, the particulars of the origins of φ become important. If the origins of φ are confined to a small region (say by containment of all charge and current sources to within a small region), then at distances large compared to the size of the containment region, the boundary has the property that the two pseudo-source terms must cancel.

4.2.4 Green's Identity with $\psi = 1/|\mathbf{r}'-\mathbf{r}|$ and an infinite volume conductor

Here we examine the situation of a finite volume V within an infinite volume conductor of conductivity σ. Neglecting time-dependence for the moment, from (4.35) we get

$$\nabla^2\varphi(\mathbf{r}) = \frac{-\nabla\bullet\mathbf{J}(\mathbf{r})}{\sigma} = \frac{I_V(\mathbf{r})}{\sigma}. \tag{4.58}$$

Applied to (4.55), this becomes

$$\int_V \varphi(\mathbf{r}')\delta(\mathbf{r}'-\mathbf{r})\,d^3r' + \frac{1}{4\pi\sigma}\int_V \frac{-\nabla'\bullet\mathbf{J}(\mathbf{r}')}{|\mathbf{r}'-\mathbf{r}|}d^3r' = \frac{1}{4\pi}\oint_S \varphi(\mathbf{r}')\left[\frac{(\mathbf{r}-\mathbf{r}')}{|\mathbf{r}-\mathbf{r}'|^3}\bullet\mathbf{n}\right] + \frac{\nabla'\varphi(\mathbf{r}')\bullet\mathbf{n}}{|\mathbf{r}'-\mathbf{r}|}ds'. \tag{4.59}$$

This time, in the special case when $V \to U$, we know (4.57) applies regardless of the source details of φ. Hence we get

$$\varphi(\mathbf{r}) = \frac{1}{4\pi\sigma}\int_U \frac{-\nabla'\bullet\mathbf{J}(\mathbf{r}')}{|\mathbf{r}-\mathbf{r}'|}d^3r' = \frac{1}{4\pi\sigma}\int_U \frac{I_V(\mathbf{r}')}{|\mathbf{r}-\mathbf{r}'|}d^3r'. \tag{4.60}$$

This is an alternate derivation of the classical infinite conductor volume conduction equation (4.37) with sources located anywhere in U.

4.3 Simple non-homogenous volume conduction: Discontinuity at *S*

The uniform, infinite media version of the volume conduction equations, equation (4.1), involves an integration over all space, U, to arrive at the potential at a point $\mathbf{r}$. This is the simplest form of conductivity inhomogeneity that has practical relevance to later modelling scenarios that involve a simple discontinuity as shown in Figure 4-2. The surface at which the conductivity undergoes a sudden shift has been chosen to coincide with the integration volume V used in the above analyses. On and within the surface S, the conductivity is σ. Outside S, the conductivity is zero. As a result of this confinement of conductivity, all sources are also confined to volume V.

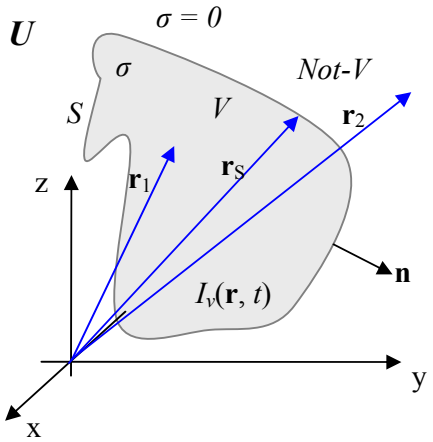

Figure 4-2 The confinement of $I_v(\mathrm{r}, t)$ to a known region V, with surface S, excised.

A further physical constraint operates on the current density as a result of charge conservation. We know that the current flow out of S must be zero. Mathematically, this is specified as

$$\mathbf{n}\bullet\mathbf{j}(\mathbf{r}_S, t) = 0. \tag{4.61}$$

The fundamental magnetostatics assumption implies that

$$\mathbf{e}(\mathbf{r},t) = -\nabla\varphi(\mathbf{r},t)\,. \tag{4.62}$$

If we consider the surface S in light of equation (4.62), the (4.61) constraint becomes

$$\mathbf{n}\bullet\nabla\varphi(\mathbf{r}_S,t) = 0 \tag{4.63}$$

or

$$\frac{\partial\varphi(\mathbf{r}_S,t)}{\partial\mathbf{n}} = 0\,. \tag{4.64}$$

As a result of the discontinuity, the volume current source density specification (4.38) applicable to (4.55) becomes

$$\nabla^2\varphi(\mathbf{r},t) = \frac{I_v(\mathbf{r},t)}{\sigma}, \mathbf{r} \le \mathbf{r}_S \tag{4.65}$$

and

$$\nabla^2\varphi(\mathbf{r},t) = 0, \mathbf{r} > \mathbf{r}_S\,, \tag{4.66}$$

where $\mathbf{r}_S$ signifies the set of all vectors representing the surface S as shown in Figure 4-2. We are interested in the field φ throughout space as a result of the 'excision'. Let $\varphi_V(\mathbf{r})$ be the potential distribution within V. Let $\varphi_{Not\text{-}V}(\mathbf{r})$ be the potential distribution outside V. Under boundary condition (4.66), and for potential $\varphi_V(\mathbf{r})$, equation (4.55) becomes

$$\int_V \varphi_V(\mathbf{r}')\,\delta(\mathbf{r}'-\mathbf{r})\,d^3r' + \frac{1}{4\pi\sigma}\int_V \frac{I_v(\mathbf{r},t)}{|\mathbf{r}'-\mathbf{r}|}d^3r' = \frac{1}{4\pi}\oint_S \varphi_V(\mathbf{r}')\left[\frac{(\mathbf{r}-\mathbf{r}')}{|\mathbf{r}-\mathbf{r}'|^3}\bullet\mathbf{n}\right] + \frac{\nabla'\varphi_V(\mathbf{r}')\bullet\mathbf{n}}{|\mathbf{r}'-\mathbf{r}|}ds'\,. \tag{4.67}$$

Noting that for points on the surface S, the gradient of φ_V is zero as per (4.64). If we now focus on points $\mathbf{r}$ *outside the integration region* V, the left-most term of (4.67) is zero and we get

$$\frac{1}{4\pi\sigma}\int_V \frac{I_v(\mathbf{r},t)}{|\mathbf{r}'-\mathbf{r}|}d^3r' = \frac{1}{4\pi}\oint_S \varphi_V(\mathbf{r}')\left[\frac{(\mathbf{r}-\mathbf{r}')}{|\mathbf{r}-\mathbf{r}'|^3}\bullet\mathbf{n}\right]ds'\,. \tag{4.68}$$

If we then customize the infinite version of the volume conduction equation (4.60) by confining all sources to V, we get

$$\varphi(\mathbf{r}) = \frac{1}{4\pi\sigma}\int_V \frac{I_V(\mathbf{r}')}{|\mathbf{r}-\mathbf{r}'|}d^3r'\,. \tag{4.69}$$

This is identical to (4.68). Let the potential φ_V in (4.68) on the surface S, for $\mathbf{r} = \mathbf{r}_S$, be $\varphi_S(\mathbf{r})$. Equation (4.68) becomes, for points $\mathbf{r}$ outside V,

$$\varphi(\mathbf{r}) = \frac{1}{4\pi}\oint_S \varphi_S(\mathbf{r}')\left[\frac{(\mathbf{r}-\mathbf{r}')}{|\mathbf{r}-\mathbf{r}'|^3}\bullet\mathbf{n}\right]ds'\,. \tag{4.70}$$

Thus, for $\mathbf{r}$ outside V, the left side of (4.70) is the same as for the infinite volume conductor with all sources contained in V. Therefore, if the medium is excised and its surface voltage measured, then the potential $\varphi_{Not\text{-}V}(\mathbf{r}, t)$ outside the excised medium can be computed using (4.70). The surface potential acts to drive the external medium as if it were an infinite medium.

4.4 Chapter summary

This chapter served to modernise and consolidate the derivation of volume conduction formalisms suited to establishing and interpreting the circumstances of later simulation. The literature reveals that much work has been done on more complex inhomogeneous media. These are evident in the trail that can be followed from early work by (Geselowitz 1967). More recent treatments include media with a complex impedance (conductive and capacitive) (Bedard and Destexhe 2009). At this stage, neither of

these treatments are relevant because the experimental method was able to achieve useful results with uniform conduction as a material model. Future forms of the EM equations, accounting for convective currents in a non-homogeneous permittivity, expressed in a realistic material layout incorporating natural charge densities, will automatically express higher frequency characteristics in a manner that can be traced to the originating field mechanisms. Meanwhile, the frequency dependence of the medium is effectively outside the scope of this work due to the use of the volume conduction formalism.

Brain material is far from being a uniform medium of the type for which (4.1) might be accurate. The rationale for the belief that (4.1) can still be useful is evident in the particulars of the spatial scale at which it is to be used. At millimetre to centimetre scales, if treated as an example of volume conduction, cortical material is effectively 'excised' in the sense that potentials are evident outside the skull, quite some distance from their deep origin in the cortical layers. The key to the use of (4.1) in this thesis is the construction of a *microscopic*, time-varying current source density function $I_I(\mathbf{r},t)$. From the microscopic perspective, with current sources expressed on the scale of nm, and fields computed on the scale of mm, the skull 'excision' is a relatively large distance away, and can be thought of as an expression of an infinite volume conductor as per equation (4.70). For this reason, further analyses are unnecessary at this stage. In adopting a microscopic perspective on the volume current density, we place ourselves at a spatial scale that renders the output of equation (4.1) relevant. As it happens, this particular configuration of the volume conduction formalism is relatively unexplored. This should not be surprising, for the 'microscopic' approach is purely numerical and computationally onerous.

4.5 Chapter bibliography

Bedard, C. and Destexhe, A. 'Macroscopic Models of Local Field Potentials and the Apparent 1/F Noise in Brain Activity', *Biophysical Journal* vol. 96, no. 7, 2009. 2589-2603.

Geselowitz, D. B. 'On Bioelectric Potentials in an Inhomogeneous Volume Conductor', *Biophysical Journal* vol. 7, no. 1, 1967. 1-&.

Gold, C., Henze, D. A., Koch, C. and Buzsaki, G. 'On the Origin of the Extracellular Action Potential Waveform: A Modeling Study', *Journal of Neurophysiology* vol. 95, no. 5, 2006. 3113-3128.

Holt, G. R. (1998) A Critical Reexamination of Some Assumptions, Implications of Cable Theory in Neurobiology. California Institute of Technology, Pasedena, California.

Holt, G. R. and Koch, C. 'Electrical Interactions Via the Extracellular Potential near Cell Bodies', *Journal of Computational Neuroscience* vol. 6, no. 2, 1999. 169-184.

Jackson, J. D., Classical Electrodynamics, 3rd ed., Wiley, New York, 1999

Lindsay, K. A., Rosenberg, J. R. and Tucker, G. 'From Maxwell's Equations to the Cable Equation and Beyond', *Progress in Biophysics & Molecular Biology* vol. 85, no. 1, 2004. 71-116.

Lorente de No, R., A Study of Nerve Physiology, Part I (Vol 131), The Rockefeller Institute for Medical Research, New York, 1947a, p. 496.

Lorente de No, R., A Study of Nerve Physiology, Part Ii (Vol 132), The Rockefeller Institute for Medical Research, New York, 1947b, p. 548.

Malmivuo, J. and Plonsey, R., Bioelectromagnetism : Principles and Applications of Bioelectric and Biomagnetic Fields, Oxford University Press, New York, 1995, pp. xxii, 482 p.

Manby, F. R. and Knowles, P. J. 'Poisson Equation in the Kohn-Sham Coulomb Problem', *Physical Review Letters* vol. 87, no. 16, 2001. art. no.-163001.

Miller, D., Out of Error, Ashgate, 2005

Milstein, J. N. and Koch, C. 'Dynamic Moment Analysis of the Extracellular Electric Field of a Biologically Realistic Spiking Neuron', *Neural Computation* vol. 20, no. 8, 2008. 2070-2084.

Plonsey, R. 'Volume Conductor Fields of Action Currents', *Biophysical Journal* vol. 4, no. 4, 1964. 317-&.

Plonsey, R. and Collin, R., Principles and Applications of Electromagnetic Fields, McGraw Hill, New York, 1961

Plonsey, R. and Fleming, D. G., Bioelectric Phenomena, McGraw-Hill, New York,, 1969, pp. xiv, 380 p.

Plonsey, R. and Heppner, D. B. 'Considerations of Quasi-Stationarity in Electrophysiological Systems', *Bulletin of Mathematical Biophysics* vol. 29, no. 4, 1967. 657-&.
Sadiku, M. N. O., Elements of Electromagnetics, 3rd ed., Oxford University Press, New York, 2001

Chapter 5

VOLUME CONDUCTION AS A BRIDGE FROM MICROSCOPIC EM TO MACROSCOPIC EM.

> "We live on an island surrounded by a sea of ignorance. As our island of knowledge grows, so does the shore of our ignorance.
>
> John Archibald Wheeler (Horgan 1992)

The previous chapters revealed how it was found that the macroscopic electromagnetism formalism (MME), can be justified as approaching the limits of its effectiveness as a describer of ultimate origins of brain EM. At this point in the research, a novel form of molecular *electro*dynamics was explored. This proved quite possible but it soon became obvious (a) that the approach, as a body of work, is far too large to achieve viable results in the available timescale, and if it did, then (b) the discontinuity in the approach makes it difficult a for mainstream neuroscientists to encounter and assimilate.

For these reasons it was decided that the science might be better served by bridging the two descriptive realms. The remainder of this thesis results from the construction and exploration of the bridge. The method squeezes the last bit of useful understanding from the uniform volume conduction equations before future molecular electrodynamics and/or inhomogeneous volume conduction takes over the responsibility. This required the application of the macroscopic uniform volume conduction form at a microscopic level. This chapter develops the mathematics of the microscopic application of the macroscopic volume conduction formalism.

5.1 Introduction

The first challenge in the construction of a volume conduction formalism, designed to reveal the EM fields produced by microscopic originating elements, is to explicitly avoid the details of atomic and molecular structure. This was achieved by choosing an elementary phenomenon, the *microscopic current filament*, as the basic building block for an EM description of the material. At this stage, nothing need be specified about the particular currents that might be implemented using the filament concept. This is a separate issue considered later. All that needs to be done here is to construct a volume source current density for use in the volume conduction equations as revealed by Chapter 4. These are

$$\varphi(\mathbf{r},t)=\frac{1}{4\pi\sigma}\int_V \frac{I_v(\mathbf{r}',t)}{|\mathbf{r}-\mathbf{r}'|}d^3r' \qquad \textbf{(5.1)}$$

and

$$I_v(\mathbf{r},t) = -\nabla \bullet \mathbf{J}_s(\mathbf{r},t), \tag{5.2}$$

where the filamentary volume current density sources are understood to be confined to volume V. Once the filament approach has been formalized, it can be applied to appropriate brain currents.

5.2 The filament cohort

To formalize the bridging mathematics for a notional abstraction of neural/astrocyte tissue, consider the abstract volume V in the volume conduction formalism to be comprised of M simply connected sub-volumes that collectively contain all the current sources in equation (5.2). This is shown diagrammatically in Figure 5-1.

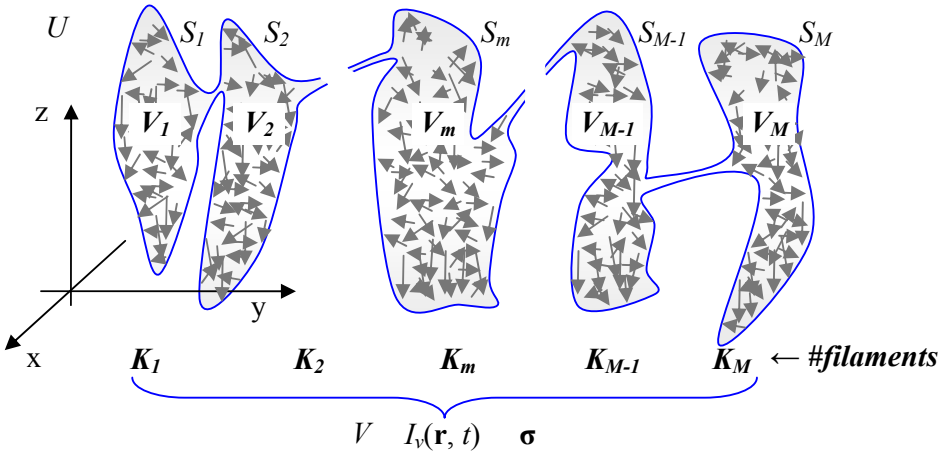

Figure 5-1 K_m filaments form cohort number m of a collection of M cohorts that define the total volume V.

Figure 5-1 depicts the universe U as an infinite, uniform, stationary, linear conductivity σ. Within U is a single volume V applicable to equation (5.1). S_m is the surface of sub-volume V_m. The 'joins' that connect the sub-volumes are notional and have zero effective area. The complete set of all sub-volumes forms a single closed surface. Filament k of a total of K_m filaments inside sub-volume m can be considered a microscopic straight line of length $L_{m,k}$ located at position $\mathbf{D}_{m,k}$ along which a notional current $i_{m,k}(t)$ flows in the direction $\mathbf{n}_{m,k}$. When presented in the form of current density, filament $i_{m,k}(t)$ becomes one component of the total volume current density $I_v(\mathbf{r},t)$, a function of position $\mathbf{r}$ and time t. This representation of brain currents can optionally include sets of diffuse/non-coherent intracellular, extracellular or transmembrane current and/or spatiotemporally coherent transmembrane current. At this stage in proceedings, the application of cohorts to particular current types is completely open. The formulation of a working volume current density will depend on what type of current is thought important or dominant in the overall expression of electromagnetic fields.

In a microscopic treatment of current, we are forced to view the current as a collection of moving charges in space. When the charges have no enforced trajectory, they are free to engage each other and the molecular environment with arbitrary motion trajectories. They become spatially incoherent even though they may collectively exhibit temporal coherence. To represent this kind of current as filament requires that time be discretized and, for each successive time slice, the spatial properties filament location $\mathbf{D}_{m,k}$ and direction $\mathbf{n}_{m,k}$ are updated. In contrast, spatially coherent filaments have a relatively fixed location $\mathbf{D}_{m,k}$ and direction $\mathbf{n}_{m,k}$. When discussing coherence in this way, the important determinant of coherence is the time-course of the filament location and direction, in comparison to the time-course of the current $i_{m,k}(t)$ travelling through it. For example, if the filaments are to represent ion channels, then the filament 'location' is fixed in the membrane and its orientation is membrane-orthogonal. If the ion channel moves laterally (in the plane of the membrane), then it is likely to be a very slow motion in comparison to the time-course of the transmembrane current. If the filaments are

to represent free charge motion, then there is no *a priori* fixed location and orientation. As long as the overall charge flow is consistent with the operational needs, any trajectory will do.

Figure 5-2 shows an individual current filament k can be handled in terms of equations (5.1) and (5.2) can be handled. 'Current' is a single notional charge of valence q_k traversing a distance L_k. This is a notional 'source-sink' situation, as shown in Figure 5-2(c). How the charge is initialized such that it can embark on this trajectory is not specified.

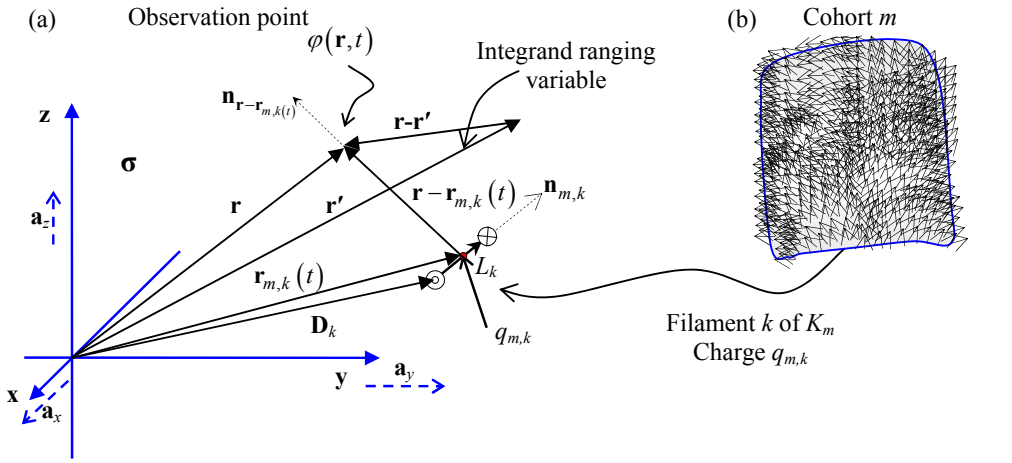

Legend

$\mathbf{r}$	equation (5.1) observation point
$\mathbf{r}'$	equation (5.1) integrand point
$\mathbf{r}_{m,k}(t)$	Charge $q_{m,k}$ location
$\mathbf{D}_k$	Filament base location (fixed)
$\mathbf{n}_k$	Unit vector in the (fixed) direction of the filament (dimensionless)
$\mathbf{n}_{r\text{-}r'}$	Unit vector in the direction $\mathbf{r}$-$\mathbf{r}$' (dimensionless)
$\mathbf{a}_x,\mathbf{a}_y,\mathbf{a}_z$	Unit vectors in the direction x,y,z resp. (dimensionless)
$L_{m,k}$	Length (fixed) of filament k in cohort m

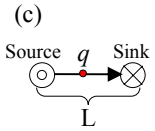

Figure 5-2 The formalism for a single filament *k* of a sub-volume of K_m, filaments.

Equation (5.2) integrand integrates $\mathbf{r}'$ notionally over the entire universe U. Because we know that the volume current density is zero outside V, $\mathbf{r}'$ ranges over V only. This is done for every observation point $\mathbf{r}$, which is the point at which a value for the scalar potential $\varphi(\mathbf{r},t)$ is computed. As a motion of charge $q_{m,k}$ along the direction of the current filament $\mathbf{n}_{m,k}$, the charge position takes on values shown as $\mathbf{r}_{m,k}(t)$. Figure 5-2 also shows other vectors whose function will become apparent in the derivation to follow. Note that at this stage, the fundamental choice is that filament position $\mathbf{D}_{m,k}$ and direction $\mathbf{n}_{m,k}$ are not functions of time. Also note that the filament length $L_{m,k}$ is also not a function of time. In the later simulations, filament length is a constant and the same for all filament types and for all filament cohorts. In principle, these constraints on filament behaviour could be relaxed in future derivations. For the purposes of the investigation of this thesis, filament length, position and direction are all fixed.

The final guiding constraint is to explicitly target ion channel behaviour for characterization by current filaments. This is specifically chosen because ion channel transmembrane currents, whether in a role in an action potential or post-synaptic transmembrane current, are unique in their spatial fixedness. It is therefore logical to expect that if there is any systematic field behaviour related to neural currents, transmembrane ion channels will express it. Note that gap-junction currents are excluded from consideration at this stage. Their role in the microscopic expression of fields is difficult to assess because their contribution to action potential current is relatively unexplored. Gap junction can be added to the analysis in future research.

5.3 Derivation of scalar potential equation for filamentary sources

A single moving charge $q_{m,k}$, operating as a current filament, creates a current density (Jackson 1999, Page 187)

$$\mathbf{j}_{m,k}\left(\mathbf{r},t\right)=q_{m,k}\mathbf{v}_{m,k}\left(t\right)\delta\left(\mathbf{r}-\mathbf{r}_{m,k}\left(t\right)\right). \tag{5.3}$$

Note that because we are dealing with microscopic sources the lower case **j** ($\mathrm{A\cdot m^{-2}}$) is used for current density. The instantaneous charge velocity as it travels along the filament is

$$\mathbf{v}_{m,k}\left(t\right)=\frac{d\mathbf{r}_{m,k}\left(t\right)}{dt}=v_{m,k}\left(t\right)\mathbf{n}_{m,k}, \tag{5.4}$$

where

$$v_{m,k}\left(t\right)=\left|\mathbf{v}_{m,k}\left(t\right)\right|=\left|v_{m,kx}\left(t\right)\mathbf{a}_{x}+v_{m,ky}\left(t\right)\mathbf{a}_{y}+v_{m,kz}\left(t\right)\mathbf{a}_{z}\right|. \tag{5.5}$$

The total volume source current density for use in equation (5.2), for all filaments of all sub-volumes, is given by

$$\mathbf{j}_{s}\left(\mathbf{r},t\right)=\sum_{m=1}^{M}\sum_{k=1}^{K_m}\mathbf{j}_{m,k}\left(\mathbf{r},t\right). \tag{5.6}$$

We can now construct the volume source density function. We first do this only for a single sub-volume m:

$$I_{m}\left(\mathbf{r},t\right)=-\nabla\bullet\mathbf{j}_{m}\left(\mathbf{r},t\right)=-\nabla\bullet\left(\sum_{k=1}^{K_m}q_{m,k}\mathbf{v}_{m,k}\left(t\right)\delta\left(\mathbf{r}-\mathbf{r}_{m,k}\left(t\right)\right)\right). \tag{5.7}$$

Ignoring the bigger picture of sub-volumes, let us first evaluate the volume source density for one particular filament k of cohort K_m. We separate out sub-volume m individual filament k from (5.7) as per

$$I_{k}\left(\mathbf{r},t\right)=-\nabla\bullet\left[q_{k}\mathbf{v}_{k}\left(t\right)\delta\left(\mathbf{r}-\mathbf{r}_{k}\left(t\right)\right)\right]. \tag{5.8}$$

We now expand the DIV operator in (5.8) on an individual vector component basis as

$$\begin{aligned}I_{k}\left(\mathbf{r},t\right)&=-q_{k}\begin{bmatrix}\frac{\partial}{\partial x}\left[v_{kx}\left(t\right)\delta\left(\mathbf{r}-\mathbf{r}_{k}\left(t\right)\right)\right]+\\ \frac{\partial}{\partial y}\left[v_{ky}\left(t\right)\delta\left(\mathbf{r}-\mathbf{r}_{k}\left(t\right)\right)\right]+\\ \frac{\partial}{\partial z}\left[v_{kz}\left(t\right)\delta\left(\mathbf{r}-\mathbf{r}_{k}\left(t\right)\right)\right]\end{bmatrix}\\ &=\left[I_{kx}\left(\mathbf{r},t\right)+I_{ky}\left(\mathbf{r},t\right)+I_{kz}\left(\mathbf{r},t\right)\right].\end{aligned} \tag{5.9}$$

Using the identity

$$\delta\left(\mathbf{r}-\mathbf{r}_{k}\left(t\right)\right)=\delta\left(x-x_{k}\left(t\right)\right)\delta\left(y-y_{k}\left(t\right)\right)\delta\left(z-z_{k}\left(t\right)\right) \tag{5.10}$$

to focus on the x component, the impact of the time dependence of the speed becomes more apparent. As a result, the x component in equation (5.9) becomes

$$I_{kx}\left(\mathbf{r},t\right)=-q_{k}v_{kx}\left(t\right)\frac{\partial}{\partial x}\left[\delta\left(\mathbf{r}-\mathbf{r}_{k}\left(t\right)\right)\right] \tag{5.11}$$

or

$$I_{kx}\left(\mathbf{r},t\right)=-q_{k}v_{kx}\left(t\right)\frac{\partial}{\partial U}\left[\delta\left(U\right)\right]\frac{\partial U}{\partial x}\delta\left(y-y_{k}\left(t\right)\right)\delta\left(z-z_{k}\left(t\right)\right), \tag{5.12}$$

where

$$U = x - x_k(t), \tag{5.13}$$

from which it follows that

$$I_{kx}(\mathbf{r},t) = -q_k v_{kx}(t)\delta^1\left(x - x_k(t)\right)\delta\left(y - y_k(t)\right)\delta\left(z - z_k(t)\right). \tag{5.14}$$

The Dirac delta superscript indicates the first spatial derivative. This makes the total volume current density for filament k:

$$I_k(\mathbf{r},t) = -q_k \begin{bmatrix} v_{kx}(t)\delta^1\left(x - x_k(t)\right)\delta\left(y - y_k(t)\right)\delta\left(z - z_k(t)\right) + \\ v_{ky}(t)\delta\left(x - x_k(t)\right)\delta^1\left(y - y_k(t)\right)\delta\left(z - z_k(t)\right) + \\ v_{kz}(t)\delta\left(x - x_k(t)\right)\delta\left(y - y_k(t)\right)\delta^1\left(z - z_k(t)\right) \end{bmatrix}. \tag{5.15}$$

We can assemble the volume current density for single filament k into the equation (5.1) integral for the potential, which can be split into three separate volume integrals. Taking care to prime the integration variable appropriately, the integral for the x component is as follows:

$$\varphi_{kx}(\mathbf{r},t) = \frac{-q_k}{4\pi\sigma}\int \frac{v_{kx}(t)\delta^1\left(x' - x_k(t)\right)\delta\left(y' - y_k(t)\right)\delta\left(z' - z_k(t)\right)}{\left|\mathbf{r} - \mathbf{r}'\right|} d^3r', \tag{5.16}$$

where $\Phi_{kx}(\mathbf{r},t)$ is the contribution of the x component of the overall potential $\Phi_k(\mathbf{r},t)$ as contributed by the k^{th} filament of the K_m in this sub-volume m. The relevant definitions of the Dirac delta are:

$$\int_{-\infty}^{\infty} f(x')\delta(x' - a)\,dx' = f(a) \tag{5.17}$$

and

$$\int f(x')\delta^1(x' - a)\,dx' = f^1(a), \tag{5.18}$$

where the superscript 1 represents the first derivative with respect to x. Again, carefully noting which variables are primed and which are not,

$$f(x,x') = \frac{1}{\left|\mathbf{r} - \mathbf{r}'\right|} = \left[\left(x - x'\right)^2 + \left(y - y'\right)^2 + \left(z - z'\right)^2\right]^{-1/2}. \tag{5.19}$$

Application of (5.17) to (5.16) yields

$$\varphi_{kx}(\mathbf{r},t) = \frac{-q_k v_{kx}(t)}{4\pi\sigma}\int \frac{\delta^1\left(x' - x_k(t)\right)}{\left[\left(x - x'\right)^2 + \left(y - y_k(t)\right)^2 + \left(z - z_k(t)\right)^2\right]^{1/2}} d^3r'. \tag{5.20}$$

Application of (5.18) to (5.20) requires the derivative of the integrand function resulting in

$$\frac{\partial}{\partial x'}\left[\frac{1}{\left[\left(x - x'\right)^2 + \left(y - y_k(t)\right)^2 + \left(z - z_k(t)\right)^2\right]^{1/2}}\right], \tag{5.21}$$

which becomes

$$\left.\frac{\left(x - x'\right)}{\left[\left(x - x'\right)^2 + \left(y - y_k(t)\right)^2 + \left(z - z_k(t)\right)^2\right]^{3/2}}\right|_{x' = x_k(t)} = \frac{\left(x - x_k(t)\right)}{\left|\left(\mathbf{r} - \mathbf{r}_k(t)\right)\right|^3}. \tag{5.22}$$

For all three components, the integral of (5.20) thus becomes the total potential, at a point in $\mathbf{r}$ in space, contributed by an individual charge k as it moves through space occupied by a conductivity σ,

$$\varphi_k(\mathbf{r},t)=\frac{-q_k}{4\pi\sigma}\left\{v_{kx}(t)\left[\frac{(x-x_k(t))}{\left|(\mathbf{r}-\mathbf{r}_k(t))\right|^3}\right]+v_{kx}(t)\left[\frac{(y-y_k(t))}{\left|(\mathbf{r}-\mathbf{r}_k(t))\right|^3}\right]+v_{kz}(t)\left[\frac{(z-z_k(t))}{\left|(\mathbf{r}-\mathbf{r}_k(t))\right|^3}\right]\right\}. \quad \textbf{(5.23)}$$

Condensing to vector form, this becomes

$$\varphi_k(\mathbf{r},t)=\frac{-q_k}{4\pi\sigma}\left[\mathbf{v}_k(t)\bullet\left(\frac{(\mathbf{r}-\mathbf{r}_k(t))}{\left|(\mathbf{r}-\mathbf{r}_k(t))\right|^3}\right)\right]. \quad \textbf{(5.24)}$$

This can be written as

$$\varphi_k(\mathbf{r},t)=\frac{-q_k v_k(t)}{4\pi\sigma}\left[\mathbf{n}_k\bullet\left(\frac{(\mathbf{r}-\mathbf{r}_k(t))}{\left|(\mathbf{r}-\mathbf{r}_k(t))\right|^3}\right)\right] \quad \textbf{(5.25)}$$

or

$$\varphi_k(\mathbf{r},t)=\frac{-q_k v_k(t)}{4\pi\sigma}\left[\frac{\mathbf{n}_k\bullet\mathbf{n}_{r-r_k(t)}}{\left|(\mathbf{r}-\mathbf{r}_k(t))\right|^2}\right]. \quad \textbf{(5.26)}$$

The final total potential at point **r** due to all K_m filaments around the periphery of a compartment m is

$$\varphi_m(\mathbf{r},t)=\frac{-1}{4\pi\sigma}\sum_{k=1}^{K_m}q_{m,k}v_{m,k}(t)\left[\frac{\mathbf{n}_{m,k}\bullet\mathbf{n}_{m,r-r_k(t)}}{\left|(\mathbf{r}-\mathbf{r}_{m,k}(t))\right|^2}\right]. \quad \textbf{(5.27)}$$

If we have M sub-volumes, all located properly with respect to the same origin as compartment k, then the final potential at a point **r** at time t can be computed from

$$\varphi(\mathbf{r},t)=\frac{-1}{4\pi\sigma}\sum_{m=1}^{M}\sum_{k=1}^{K_m}\left[\frac{q_{m,k}v_{m,k}(t)\left(\mathbf{n}_{m,k}\bullet\mathbf{n}_{m,r-r_{m,k}(t)}\right)}{\left|(\mathbf{r}-\mathbf{r}_{m,k}(t))\right|^2}\right]. \quad \textbf{(5.28)}$$

The situation has now taken the form shown in Figure 5-2, where compartment m has K_m filaments and m,k represents the k^{th} filament in compartment m. Note that this formulation can easily be expanded to allow multiple sets of different filaments currents to inhabit any single compartment m (for example, for different ion channel types). At face value, equation (5.28) requires the individual allocation, storage and management of charges and velocities for each of the filament types insofar as they represent ion channels. Equation (5.28) quantity $\mathbf{r}_{m,k}(t)$ is the position of the charge $q_{m,k}$ as it transits the filament based on a speed profile $v_{k,m}(t)$.

A useful approximation to equation (5.28) can be found as a limiting case. When the length of the filament is very small compared with the observation position **r**, the departure from **r** in the denominator of equation (5.28) is so small that the denominator can be treated as $|\mathbf{r}\text{-}\mathbf{r}_{m,k}|$, where $\mathbf{r}_{m,k}$ is the average position of the filament, over the length of the filament, which is shown in Figure 5-2. This means that equation (5.28) becomes

$$\varphi(\mathbf{r},t)=\frac{-1}{4\pi\sigma}\sum_{m=1}^{M}\sum_{k=1}^{K_m}\left[\frac{q_{m,k}v_{m,k}(t)\left(\mathbf{n}_{m,k}\bullet\mathbf{n}_{m,r-r_{m,k}(t)}\right)}{\left|\mathbf{r}-\mathbf{r}_{m,k}\right|^2}\right]. \quad \textbf{(5.29)}$$

Equations (5.28) and (5.29) effectively apply only to one charge and we do not have the speed profile for individual charges as a function of time. The empirical information we have is actually filament current at a point in space. At the cost of some generality, and for the purposes of development of equation (5.29), we can construct a rough continuum equivalent to the effect of a velocity profile. If we assume the charge reaches a constant terminal velocity v in a time is small compared with the

transit time, and that the transit happens with a roughly constant speed v, it is clear that the number of charges passing any point along the length of the filament in a given time T is

$$\frac{vT}{L}q \text{ Coulomb.} \quad \textbf{(5.30)}$$

Therefore, the average i current passing through P is

$$i = \frac{vq}{L} \text{ Amps,} \quad \textbf{(5.31)}$$

which can be written as

$$iL = vq\,. \quad \textbf{(5.32)}$$

This is a relationship that can be found in elementary treatments of conduction, e.g. (Sadiku 2001). Adapted to the local context, the charge-velocity product follows:

$$q_{m,k}v_{m,k}\left(t\right) = L_{m,k}i_{m,k}\left(t\right). \quad \textbf{(5.33)}$$

Inserting (5.33) in (5.29), we get

$$\varphi\left(\mathbf{r},t\right) = \frac{-1}{4\pi\sigma}\sum_{m=1}^{M}\sum_{k=1}^{K_m}\left[\frac{L_{m,k}i_{m,k}\left(t\right)\left(\mathbf{n}_{m,k}\bullet\mathbf{n}_{m,r-r_{m,k}(t)}\right)}{\left|\mathbf{r}-\mathbf{r}_{m,k}\right|^2}\right]. \quad \textbf{(5.34)}$$

This is the final result. Empirical measurement of a current profile located at a known, fixed position in space can be used to compute the potential. From the original volume conduction derivation, the electric field is given by

$$\mathbf{E}\left(\mathbf{r},t\right) = -\nabla\varphi\left(\mathbf{r},t\right). \quad \textbf{(5.35)}$$

Note that if we want to compute the fields produced by current for which a position and velocity profile is known, then we can revert to the more general form of (5.29). If the multiple paths in such a cohort are spatially diffuse, then there is an expectation that the resultant potential will be more noisy. For this reason, this particular formulation of macroscopic EM is expected to break down for diffuse current, when paths are not known. This use of a macroscopic scale formalism in a microscopic circumstance is, therefore, best applied to highly spatially localized, known current profiles.

5.4 The magnetic field

From the original volume conduction formalisms (magnetostatics), the magnetic field can be derived from the vector potential **A**, which is related to the current density as per Chapter 2:

$$\mathbf{A}\left(\mathbf{r},t\right) = \frac{\mu_0}{4\pi}\int_U \frac{\mathbf{J}\left(\mathbf{r}',t\right)}{\left|\mathbf{r}-\mathbf{r}'\right|}d^3r', \quad \textbf{(5.36)}$$

where the current density $\mathbf{J}(\mathbf{r},t)$ is the *total* current density throughout space, which includes all the current due to the LFP and the original set of filaments that generated it. μ_0 is the permeability of free space. Having assembled the total current density, the magnetic field can be found from

$$\mathbf{B}\left(\mathbf{r},t\right) = \nabla\times\mathbf{A}\left(\mathbf{r},t\right). \quad \textbf{(5.37)}$$

This derivation for **B** based on the current filament concept is not covered here. The key point is that the filamentary current source, in principle, leads to a computationally tractable route to both the electric and magnetic fields. This has been delegated to future work. For some guidance, see (Hamalainen, Hari *et al.* 1993, Hamalainen and Sarvas 1987).

5.5 Chapter summary

This chapter established the mathematical formula for computing the potential throughout an infinite uniform, linear, stationary volume conductor driven by a localized set of current filaments. Providing

the filament lengths are small compared with the distances over which fields are expressed, the formula produces the potential for known filament currents. A formula for the torque field produced by a filament set was also constructed. This offers the prospect of computing overall field properties without the need to compute the entire electric field system. Development of the technique will ensue in future work.

Because the filament concept has been used to target excitable cell tissue, and, in particular, ion channel behaviour, the use of the formula becomes computationally onerous due to the sheer number of filaments involved. Modern computing resources, however, make the computations quite tractable. Supplied with appropriate currents and computing resources, the derived formula can directly compute the field systems of a set of filaments. It is to the practical matters of their application to brain material that we now turn.

5.6 Chapter bibliography

Hamalainen, M., Hari, R., Ilmoniemi, R. J., Knuutila, J. and Lounasmaa, O. V. 'Magnetoencephalography - Theory, Instrumentation, and Applications to Noninvasive Studies of the Working Human Brain', *Reviews of Modern Physics* vol. 65, no. 2, 1993. 413-497.

Hamalainen, M. S. and Sarvas, J. 'Feasibility of the Homogeneous Head Model in the Interpretation of Neuromagnetic Fields', *Physics in Medicine and Biology* vol. 32, no. 1, 1987. 91-97.

Horgan, J. 'The New Challenges', *Scientific American* vol. 267, no. 6, 1992. 16-&.

Jackson, J. D., Classical Electrodynamics, 3rd ed., Wiley, New York, 1999

Sadiku, M. N. O., Elements of Electromagnetics, 3rd ed., Oxford University Press, New York, 2001

Chapter 6

THE PRACTICAL USE OF VOLUME CONDUCTION WITH FILAMENTARY CURRENT SOURCES IN A NEURON MODELLING CONTEXT

The whole of science is nothing more than a refinement of everyday thinking. It is for this reason that the critical thinking of the physicist cannot possibly be restricted to the examination of concepts of his own specific field. He cannot proceed without considering critically a much more difficult problem, the problem of analyzing everyday thinking.

On the stage of our subconscious mind appear in colorful succession sense experiences, memory pictures of them, representations and feelings. In contrast to psychology, physics treats directly only of sense experiences and of the "understanding" of their connection. But even the concept of the "real external world" of everyday thinking rests exclusively on sense impressions.

Albert Einstein (Einstein 1950)

6.1 Introduction

The previous chapter derived the potential field in a uniform volume conductor that results from a set of current filaments as

$$\varphi(\mathbf{r},t)=\frac{-1}{4\pi\sigma}\sum_{m=1}^{M}\sum_{k=1}^{K_m}\left[\frac{L_{m,k}i_{m,k}(t)\left(\mathbf{n}_{m,k}\bullet\mathbf{n}_{m,r-r_{m,k}}\right)}{\left|\mathbf{r}-\mathbf{r}_{m,k}\right|^2}\right]. \qquad \textbf{(6.1)}$$

The filaments are divided into a set of M cohorts where cohort m has a total of K_m filaments. Provided a current profile $i_{m,k}(t)$ can be supplied for every filament, equation (6.1) can be used to compute the potential at a point $\mathbf{r}$ at a time t. Here we examine the adaptation of the filament cohort concept to known sources of current via known systems of modelling. We must examine how filaments can realistically represent real neural tissue currents and how the currents used in (6.1) are constructed. The most widespread neural modelling system that involves 3-dimensional (3D) structure is the compartmental model based on cable equation theory. This chapter delivers a collection of practical issues, tools and utilities needed when compartmental model data is used to produce 'extracellular fields' via equation (6.1).

6.2 Compartmental cable equation models as a source of current data

Compartmental neuron modelling uses a distributed circuit element model based on non-linear elements originating in the work of Hodgkin and Huxley (Hodgkin and Huxley 1952a, Hodgkin and Huxley 1952b, Hodgkin and Huxley 1952c, Hodgkin and Huxley 1952d, Hodgkin, Huxley *et al.* 1952). This original work forms the cornerstone of a highly developed discipline of 1D compartmental neural modelling(Aidley 1998, Dayan and Abbott 2001, Hille 2001, Johnston and Wu 1995). The classic equivalent circuit for a notional section of membrane is shown in Figure 6-1, which shows how (a) the 3D original cell structure becomes (b), a (bifurcating) 1-dimensional (1D) cable model. This, in turn, becomes (c), an equivalent series/parallel circuit element model, which then becomes a set of equations describing currents and voltages along a 1D spatial axis (notionally x). The cable-equation 1D model preserves the operational voltage and current relationships between compartments. The process disposes of the 3D spatial relationships that form the basis of the expression of the extracellular field system. This is achieved by encoding the spatial attributes in the circuit element model through the use of 'per unit length' and 'per unit area' parameters.

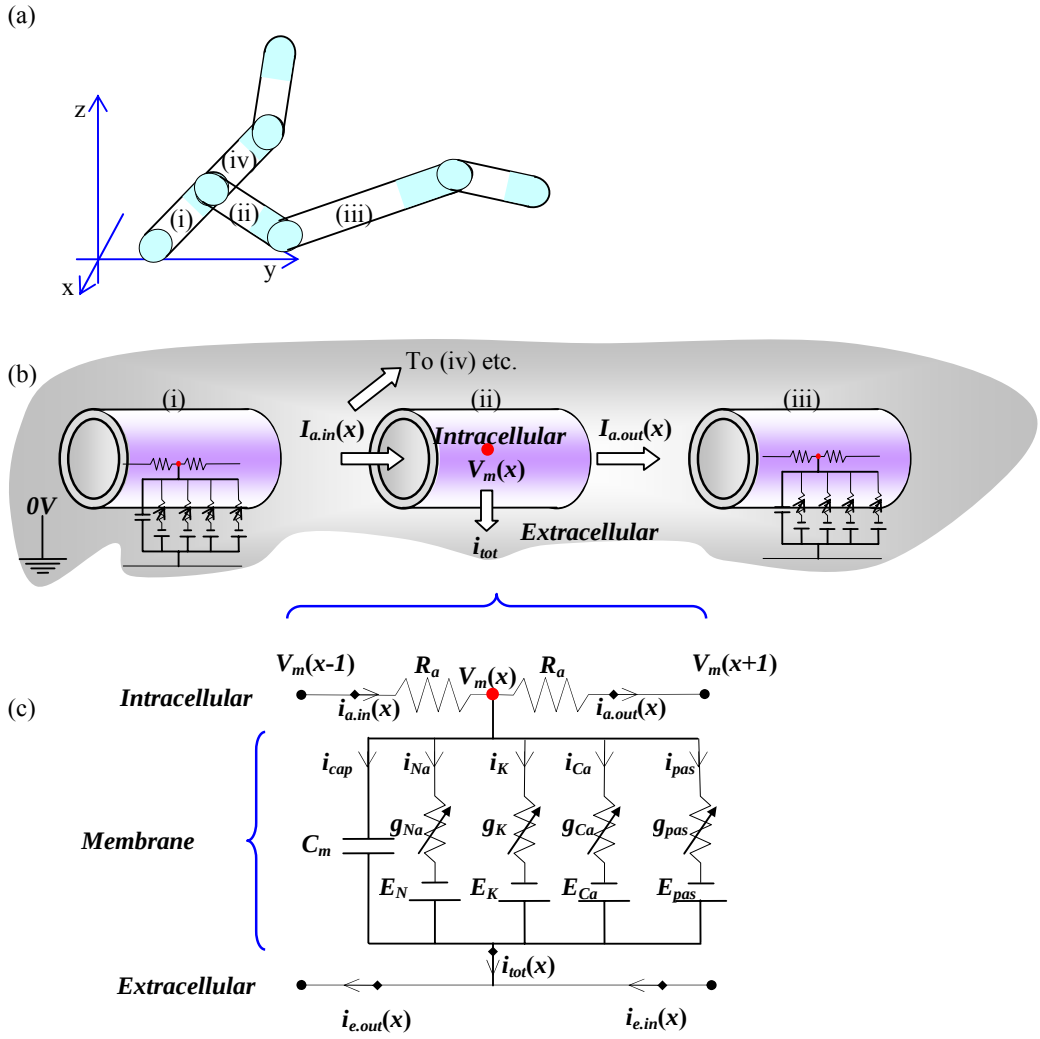

Figure 6-1 The classic compartmental cable-theoretic model.

Figure 6-1(c) shows the equivalent circuit equivalent of a single compartment at a notional location x within a 1D frame of reference with five transmembrane current types implemented with four (only) ion channel types. In practice, individual ion currents can have multiple different ion channels. For

example there could be several different kinds of Na channels, each with their own dynamics. In the Figure 6-1(c), inter-compartment temporal coherence can be understood on a total current or per-ion-channel-type basis. The compartmentalization process in Figure 6-1 demonstrates the loss of realism in spatial coherence, although the temporal relations between currents is conserved. Note that ECS and ICS currents $i_{a\_in}(t)$, $i_{a\_out}(t)$, $i_{e\_in}(t)$, and $i_{e\_out}(t)$ of Figure 6-1(c) are managed by the circuit model as totals. In reality, the charges that actually implement the currents have no preferred path and will be spatially incoherent as discussed in Chapter 2. The compartment model expresses consistent temporal relationships between currents and rough spatial locations in the sense of their relative temporal activity within the overall neuron structure. The compartment model is therefore useful as an accurate generator of overall currents that preserve their relative timing in relation to the basic branching of the neuron, but not the original 3D detail of the actual transmembrane activity.

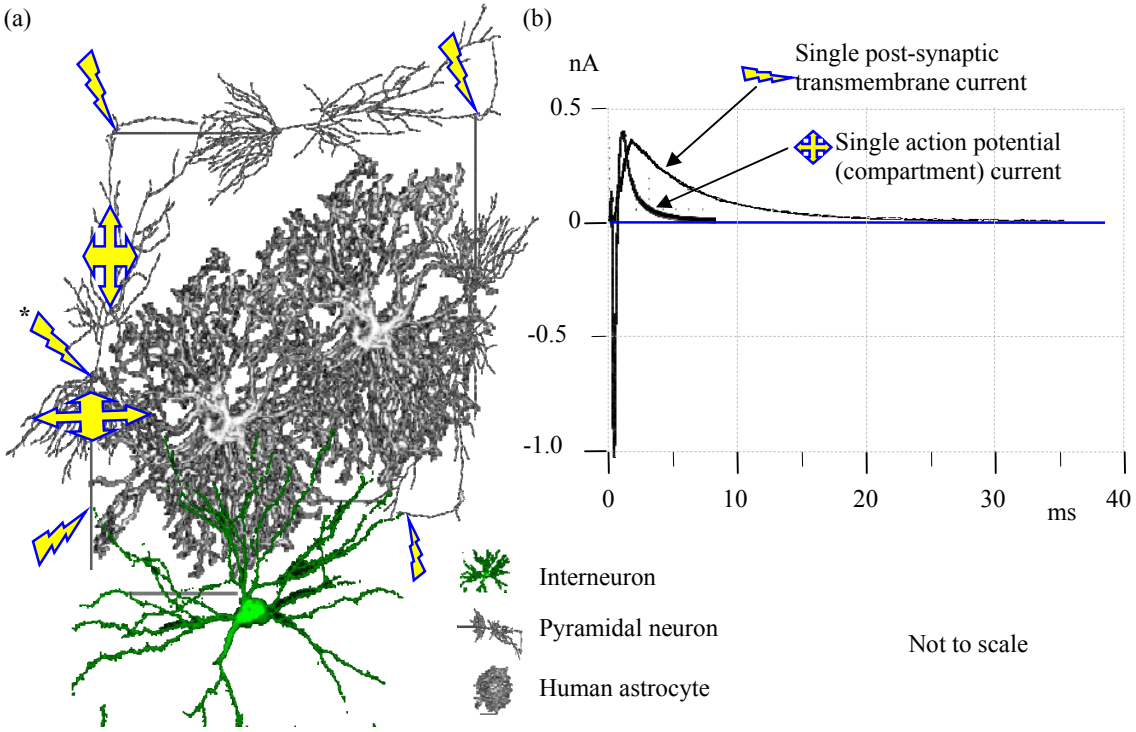

Figure 6-2 (a) shows the recurrent looping that determines the timing of synapses. The * indicates a soma synapse. The crossed arrows indicate the progression of an action potential. (b) shows the relative time-course of the post synaptic current of a single excitatory synapse (Based on (Dayan and Abbott 2001, p 181)) as compared with the action potential compartment current as per Figure 6-11.

Given that a compartmental model is a viable source of equation (6.1) currents, we have access to some representation of equivalent filament magnitude and relative timing. The problem then becomes one of reintroducing the spatial reality of the currents by defining filament location and direction. This is where the first challenge arises in the source volume current recognition of (a) single vs. multiple unit contributions and (b) synaptic vs. action potential contributions. Both synaptic currents and action potential currents involve cohorts of coherently acting transmembrane ion channels. At this early stage of development, the great bulk of simulations are of single neurons that are artificially stimulated through manually applied synaptic input, or through 'numerical stimulation probes' that directly modify compartment properties in artificial ways. Action potential current dynamics (and therefore their level of coherence) is specified by the neuron itself (a single-unit phenomenon). However, synaptic current dynamics (the relative temporal expression) is determined by network activity and relations *between* neurons (a multi-unit phenomenon). It follows that, at this early stage of development, we must confine exploration to the action potential current contributions only. This outcome may impoverish the revealed equation (6.1) field expression in terms of its completeness, but at least it will reveal maximal accuracy in the expression of the action potential contribution to the

fields. In future, much larger realistic multi-unit simulations, synapse contributions become a viable contributor. This appears to be the natural developmental path towards an understanding of the full LFP expression in real tissue. Understanding the difference between the time course of action potential current and synaptic current is quite helpful and is shown in Figure 6-2.

Figure 6-2(a) depicts, in rough terms, the physical origins of recurrent loop activity that determines the relative times of synaptic activity. In reality, the density of neurons and astrocytes is far higher than that shown in Figure 6-2(a). Thousands of synapses stimulate any individual neuron, so the relative contribution of synaptic currents, of the kind shown in Figure 6-2(b), can be expected to be large. Figure 6-2(b) shows the relative time-course of the two main types of current. Post-synaptic plaques comprised of Na and K channels produce the Figure 6-2(b) waveform. The magnitudes of the two currents in Figure 6-2(b) are not strictly comparable. However, the diagram serves to illustrate the competing influences driving the equation (6.1) current term. When the field expression is dominated by synapse activity, at any particular point in space, it will have the form of the synapse current in Figure 6-2(b). When dominated by action potential currents, the potential at any particular point in space will take on the time-course of the action potential current in Figure 6-2(b). When contributing in simular amounts the field will be a superposition of the two waveforms. It is important to note that the Figure 6-2(b) waveforms are artificially synchronized. The actual relative time-course of synapse currents and the action potential currents will depend on many factors including recurrent loop dynamics, where in space you are observing, and where the compartment is in the overall neuron structure.

6.3 Ion channels as filaments

Having isolated transmembrane current as the most spatiotemporally coherent, we immediately know the direction of all possible filaments: *orthogonal to the membrane*. If included in a 3D compartmental model, these ion channels would be shown orthogonal to the compartment external boundary, regardless of their location. No example has been found in the literature of any transmembrane protein complex involved in cell excitability that has its pore oriented in any other way. The transmembrane protein C-terminal and N-terminal end-structures (extending into the ECS and ICS) can have oblique angles, but the main functional transmembrane region is oriented at right angles to the membrane. The ICS and ECS portions of the charge trajectory have already been argued as insignificant in the closing stage of the development of equation (6.1).

It has been known for a long time that real ion channels operate stochastically with a net (ensemble) effect that results in the stereotypical transmembrane current(s) (Dayan and Abbott 2001, Hille 2001). This behaviour is modelled with a ‘virtual conductance’ that has nonlinearities commensurate to the complexities of the stochastic state of the channel molecules. The simplest relationship that one can establish between current filaments and real ion channel currents is one that accounts for mean current of an aggregate of channels. Such an average is implicit in the form of the transmembrane currents of a compartmental model. Accepting that compartment current adequately represents ion channel current aggregates, the question then becomes one of how the physical channels are to be represented by filaments. A single ‘filament’ carrying the entire transmembrane current is numerically equal to 100 filaments each carrying 1% of the transmembrane current. If all 100 filaments were collocated in space, they would result in an identical field expression. However, if the 100 filaments were allocated separately, a completely different field pattern would be expressed by the same transmembrane current. In dividing the total current between all the filaments, all the filaments remain perfectly temporally coherent. What varies, when filaments are fixed in space, is their spatial coherence.

The next issue in the filament/channel relationship is one of current *type*. In Figure 6-1, there are five current types: capacitive, passive, Na^+, K^+ and Ca^{2+}. For each of these currents, there may be different types of ion channel used in the underlying NEURON model. Each of these may involve a very different time-course. It is, therefore, sensible to wonder if the current filament population might be segregated according to type and allocated their own spatial coordinates. This raises the issue of the co-location or otherwise of the various channel types. This issue is particularly awkward in the case of the capacitive current, where the mechanism (disturbances in polarisation of the membrane lipid

bilayer as a dielectric) involves no actual channel currents at all, so the whole idea of current localisation is invalid. One might invent a 'virtual channel' and distribute it uniformly over the compartment surface or associate it with particular groupings of ion channels. The non-specific ion traffic involved in the 'passive' current raises a similar issue.

Resolving the filament/ion channel relationship therefore requires detailed knowledge of the locations of ion channel species around the neural membrane. There can be variability across neuron types, variability within a neuron (e.g. apical vs. basal) and patterns of co-location of channels within the same region (e.g. on the soma). A significant body of empirical neuroscience has been carried out that has described, for particular neuron types, gross variations in ion channel densities across neuron regions. For example, the densities of certain channels may vary with the distance from the soma. Some channels are only found in synapses, which are one of the specializations involving high density localized channel populations. Another well described high density region is the axon hillock, where Na^+ and K^+ channels are mixed. Histology images that tag ion channel species sometimes indicate higher densities at process junctions. Sometimes there are no discernable density peaks. As far as can be ascertained, there is little empirical data that specifies the passive currents in regional detail or correlates it with other ion channel species' locations. Likewise, there is little or no attempt to co-localize capacitative currents with the local channel type that actually causes the capacitative current. Capacitive currents result from ion channel field dynamics that locally polarize and depolarize the membrane.

A complete specification of the relationship between ion channels and their filament equivalents therefore requires significantly more information than tends to be routinely available. At this stage, there is no good reason for doing anything other than distributed abstract filaments that collectively carry the whole compartment current. In this way, we can examine general claims about transmembrane current field behaviours, without having to qualify them to any particular ion species or channel type. Later, with more complete empirical data, we can begin to use filament cohorts that more directly relate to known individual ion channel and current types and location tendencies and, in the case of the capacitive current, local dielectric behaviour. This can be added in the future and explored for the kinds of variability it introduces.

6.4 Creating filament cohorts orthogonal to a conical frustum

For modelling the original cell structure, the NEURON (Hines and Carnevale 1997, Hines and Carnevale 2003) package uses a conical frustum as the basic 3D compartment element. This section develops the method that creates filaments that are orthogonal to the surface of a conical frustum (unit vectors) with one end embedded in its surface. What follows here is the basic exploration of the mathematics of computationally positioning small vectors orthogonal to a surface defined by a conical frustum. Here, the presupposition is that a full set of data is available that specifies, with respect to an overall absolute reference frame origin, the location of the centre of the ends of a conical frustum and the diameter of each end. To populate such a surface with orthogonal vectors, there is a design choice to be made between (a) population of the orthogonal vectors onto a standard frustum followed by a mapping to the actual frustum position and (b) the population of each frustum in situ. I chose (a) although I suspect that (b) would work equally well. The choice merely changes the order of the mappings.

6.4.1 Conical frustum 'compartment' as a container of a current filament cohort

Here we relate the simulation compartment to the V_m volumes in the volume conduction equation. The NEURON compartment shown in Figure 6-3(a) forms the notional inner surface of the integration sub-volume V_m as shown in Figure 6-3(b). Current filaments are, therefore, embedded in and oriented orthogonally to the outer surface of the conical frustum. Volume V_m in Figure 6-3 is a thickened boundary of the original frustum surface. In practice, there is no need for any fixed shape for volume

V_m. It could be further refined to be a small filament-shaped cylinder around each filament in the cohort, with all filaments linked in some way. The important concept is that as a result of the Figure 6-3(b) construct, the potential can be computed for points *inside* the compartment. This is shown by the red vector **r** in Figure 6-3. The computation of potentials inside the region defined by the chosen V is accurate provided the filament size is very small compared to the diameter of the frustum. In the practical simulation situation, this ratio of compartment diameter to filament size is roughly 100:1 and the computations inside the frusta remained useful.

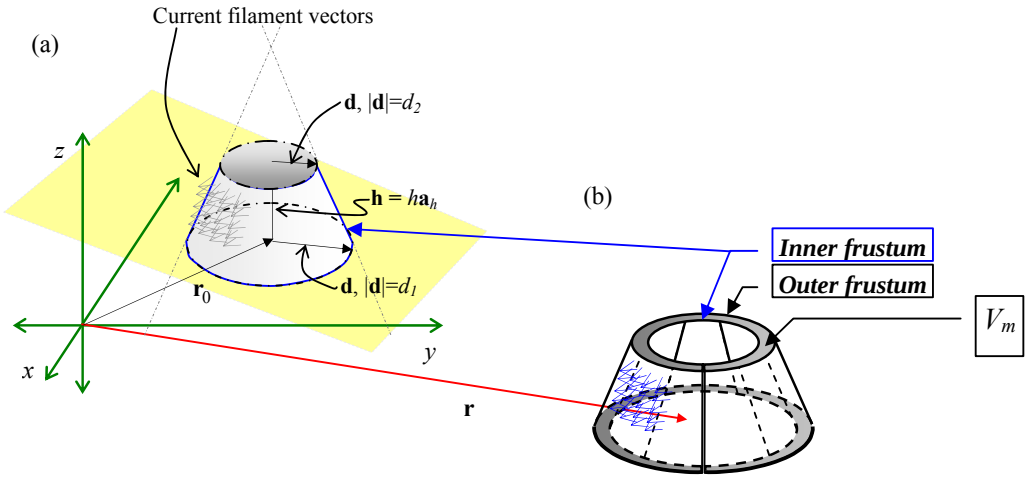

Figure 6-3 The NEURON 'compartment' as a conical frustum. The NEURON (Hines and Carnevale 1997) simulation environment constructs a neuron as a set of collocated conical frusta typified here. A frustum is located at position determined by r_0. It has a base radius d_1 and its axis is oriented along vector a_h. The frustum has a height h and a top radius d_2. When base radius d_1 is the same as top radius d_2, the compartment becomes a cylinder.

6.4.2 Euler angles and 3D rotation

The positioning of the filament vectors in their final location requires their rotation and their translation. The first of these transformations, rotation, is well described in the literature as requiring three parameters. 'Euler angles' are one particular set. Euler angles represent three successive rotations that move a given source reference frame to a given target reference frame (Goldstein, Poole *et al.* 2002, Landau, Lifshits *et al.* 1984)[1]. Each rotation can be decomposed as a rotation matrix as shown in Figure 6-4. If one has a designed/known (post-rotation/translation) final resting place for the vectors, this method can be somewhat laborious and experimental because it becomes necessary to undo the combined action of the three rotations in order that the initial position of the vectors be determined.

6.4.3 The vector form of a circle and sphere in 3D

A circle of known radius d with a centre at a known position $\mathbf{r}_0$ in a plane orthogonal to a known unit vector $\mathbf{a}_h$ is established geometrically and shown in Figure 6-5. The circle is established in Figure 6-5(a) by limiting all positions **r** to only those that satisfy the constraint that the component of $(\mathbf{r}\text{-}\mathbf{r}_0\text{-}\mathbf{a}_h)$ in the direction of $(\mathbf{r}\text{-}\mathbf{r}_0)$ has the dimension d. This constructs a circle in the plane. Mathematically, this is

$$\left(\mathbf{r}-\mathbf{r}_0\right)\bullet\left(\mathbf{r}-\mathbf{r}_0-\mathbf{a}_h\right)=d^2\,. \qquad \textbf{(6.2)}$$

Alternately, this formula is equivalent to the set of points of the intersection of (bisection of) a sphere of radius d located at centre $\mathbf{r}_0$ and a plane orthogonal to $\mathbf{a}_h$ as shown in Figure 6-5(b). The formula for a plane containing a point $\mathbf{r}_0$ that has a unit vector normal $\mathbf{a}_h$ at that same point is

$$\mathbf{a}_h\bullet\left(\mathbf{r}-\mathbf{r}_0\right)=0\,. \qquad \textbf{(6.3)}$$

[1] See http://mathworld.wolfram.com/EulerAngles.html

The formula for a sphere of radius d with its centre located at $\mathbf{r}_0$ is

$$\left|\mathbf{r}-\mathbf{r}_0\right|^2=\left(\mathbf{r}-\mathbf{r}_0\right)\bullet\left(\mathbf{r}-\mathbf{r}_0\right)=d^2\,. \tag{6.4}$$

Equate (6.3) and (6.4) and rearrange to get equation (6.2).

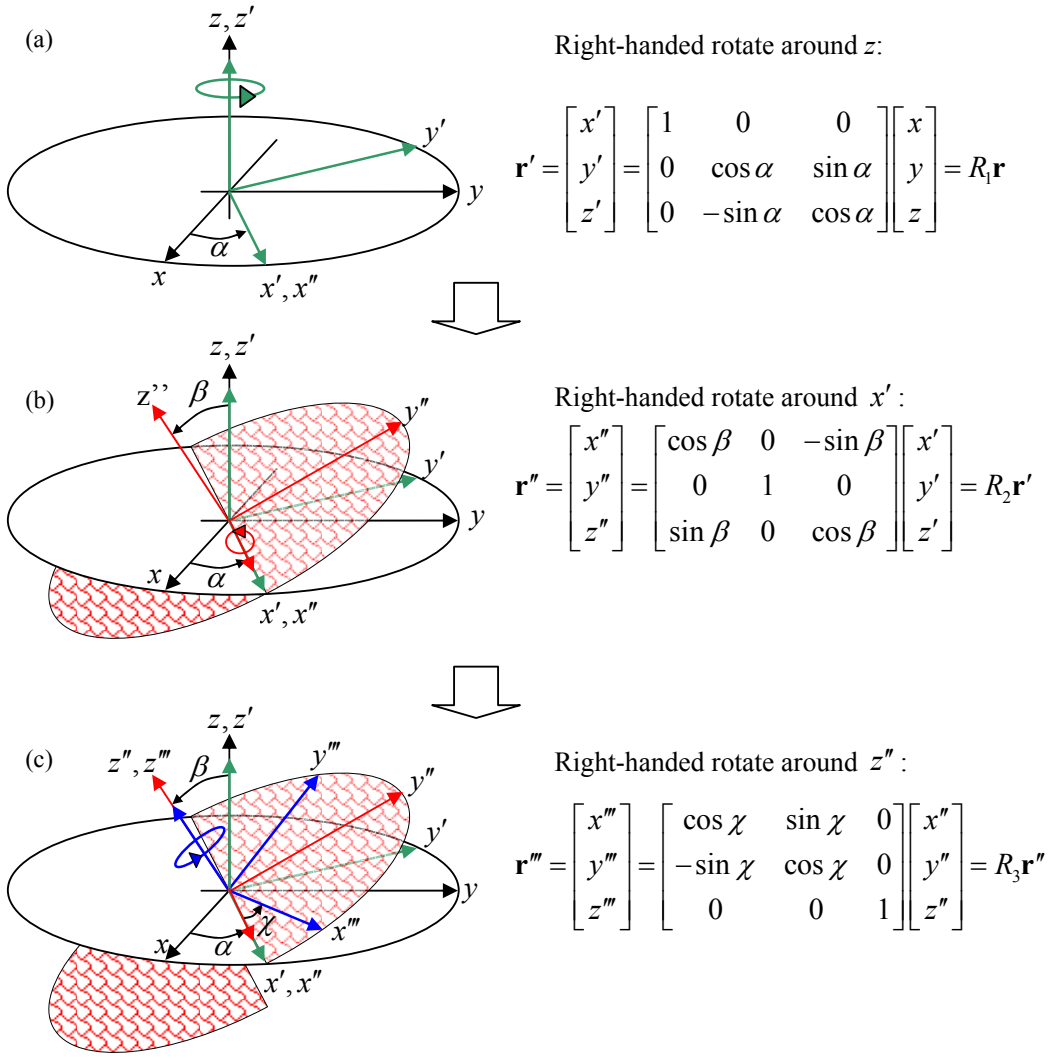

Figure 6-4 Euler angle rotation matrices.

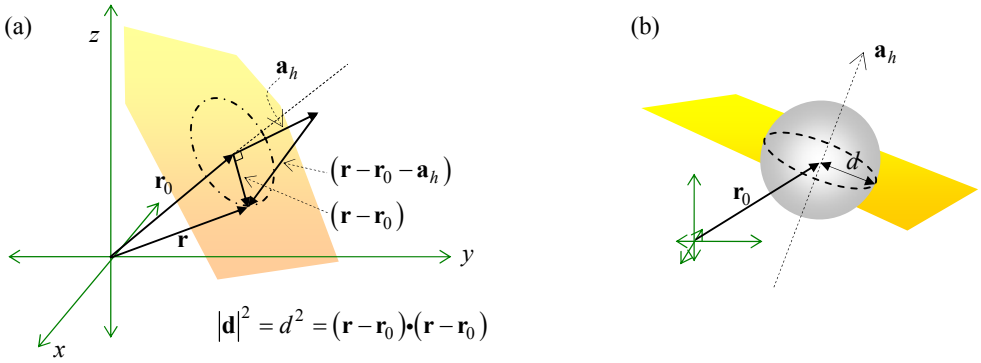

Figure 6-5 Establishing the generalised equation for the base of a conical frustum.

6.4.4 Coordinate system transformation/reference frame selection

Before we proceed, we have to organise a set of reference frames that will be used later. We have to establish a transform that is, in effect, a change of co-ordinate systems specialised to suit the circumstances of frustum generation. The original frame of reference F contains point $P = (x,y,z)$, which we manipulate as a vector $\mathbf{r}$. The transformation locates the same point in a frame of reference F' with points located at (x',y',z'). This transformation is merely a coordinate system conversion. The representation of the same point in the two reference frames shown in Figure 6-6. This transformation performs a rotation and a translation as per

$$\mathbf{r}' = A\mathbf{r} + \mathbf{b}\,, \tag{6.5}$$

where A is a suitable 3x3 matrix to be constructed later.

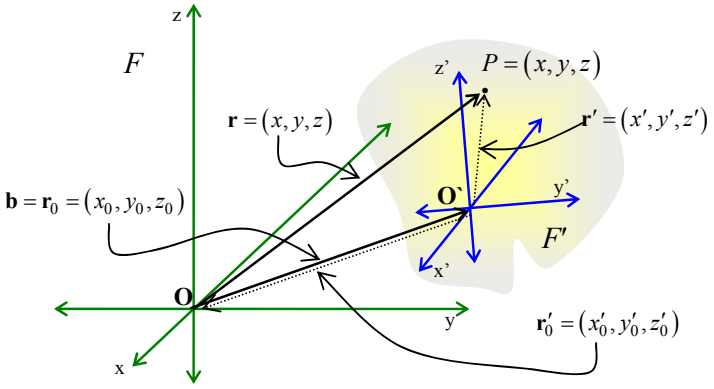

Figure 6-6 The same point P in two linearly related, length conserving reference frames related as per equation (6.9).

The position vector $\mathbf{b}$ is the location of the origin of F in frame F'. In general, A could also involve scaling, which would not preserve distances. Later, we outline the properties of A that are invoked if distances are to be preserved. In the F' frame, the position of the origin of the F frame ($\mathbf{r} = \mathbf{0}$) is

$$\mathbf{r}' = \mathbf{b} = \mathbf{r}_0'\,. \tag{6.6}$$

Equation (6.5) has an inverse

$$\mathbf{r} = A^{-1}(\mathbf{r}' - \mathbf{b}) = A^{-1}(\mathbf{r}' - \mathbf{r}_0')\,. \tag{6.7}$$

The origin in the F' frame, $\mathbf{r}' = 0$ is given by $\mathbf{r} = \mathbf{r}_0$ in the F frame. Equation (6.7) tells us that

$$-A^{-1}\mathbf{r}_0' = \mathbf{r}_0 \text{ or } \mathbf{b} = -A\mathbf{r}_0\,. \tag{6.8}$$

Therefore, equation (6.5) can be written as

$$\mathbf{r}' = A\mathbf{r} - A\mathbf{r}_0 = A(\mathbf{r} - \mathbf{r}_0)\,. \tag{6.9}$$

Equations (6.7) and (6.9) are the mappings to/from F and F′ based on known origin locations. All that is required of A is that it have an inverse. The 'length-preserving' constraint on A requires additional work and needs a couple of general identities. I manually constructed two identities for arbitrary n-vectors $\mathbf{a}$ and $\mathbf{b}$, and arbitrary (n x n) matrices Q and R. They are

$$\mathbf{a}\bullet Q\mathbf{b} = Q^T\mathbf{a}\bullet\mathbf{b} \tag{6.10}$$

and

$$R\mathbf{a}\bullet Q\mathbf{b} = Q^T R\mathbf{a}\bullet\mathbf{b}\,. \tag{6.11}$$

We now use these identities to implement the length-conserving constraint on A that would conserve a distance L which is the length of a vector $\mathbf{L}$ in the F frame and is the difference between vectors $\mathbf{L}_1$ and $\mathbf{L}_2$, giving

$$L^2 = |\mathbf{L}| = |\mathbf{L}_1 - \mathbf{L}_2| = (\mathbf{L}_1 - \mathbf{L}_2)\bullet(\mathbf{L}_1 - \mathbf{L}_2) = (\mathbf{L}_1\bullet\mathbf{L}_1 - 2\mathbf{L}_1\bullet\mathbf{L}_2 + \mathbf{L}_2\bullet\mathbf{L}_2)\,. \tag{6.12}$$

Similarly, in the F′ frame we have

$$L^2 = \left|\mathbf{L}'\right| = \left|\mathbf{L}'_1 - \mathbf{L}'_2\right| = \left(\mathbf{L}'_1 - \mathbf{L}'_2\right)\bullet\left(\mathbf{L}'_1 - \mathbf{L}'_2\right) = \left(\mathbf{L}'_1\bullet\mathbf{L}'_1 - 2\mathbf{L}'_1\bullet\mathbf{L}'_2 + \mathbf{L}'_2\bullet\mathbf{L}'_2\right). \tag{6.13}$$

If we operate on (6.13) to map it to the F frame using

$$\mathbf{L}'_1 = A\left(\mathbf{L}_1 - \mathbf{r}_0\right) \text{ and } \mathbf{L}'_2 = A\left(\mathbf{L}_2 - \mathbf{r}_0\right), \tag{6.14}$$

we get

$$L^2 = \left|\mathbf{L}\right| = \left(A^T A\mathbf{L}_1\bullet\mathbf{L}_1 - 2A^T A\mathbf{L}_1\bullet\mathbf{L}_2 + A^T A\mathbf{L}_2\bullet\mathbf{L}_2\right). \tag{6.15}$$

Equating (6.13) and (6.15), we reveal the adjoint condition of A necessary for conservation of distances,

$$A^T A = I_n. \tag{6.16}$$

This can be put in the form

$$A^T = A^{-1}. \tag{6.17}$$

Now we can establish a suitable A matrix. We can do this using the Euler angle transformation introduced above, which is shown in Figure 6-4. The idea is to find the three angles suited to parameterisation of our frustum. The frame F′ is the result of three separate rotations by three matrices R_1, R_2, R_3 as shown in Figure 6-4. Thus

$$\mathbf{x}' = A\mathbf{x} = R_3R_2R_1\mathbf{x} \tag{6.18}$$

and

$$\mathbf{x} = A^{-1}\mathbf{x}' = R_1R_2R_3\mathbf{x}'. \tag{6.19}$$

Multiplying out the Figure 6-4 rotation matrices as per equation (6.18) gives

$$A = \begin{bmatrix} \cos\chi\cos\phi - \sin\chi\cos\theta\sin\phi & \cos\chi\sin\phi + \sin\chi\cos\theta\cos\phi & \sin\chi\sin\theta \\ -\sin\chi\cos\phi - \cos\chi\cos\theta\sin\phi & -\sin\chi\sin\phi + \cos\chi\cos\theta\cos\phi & \cos\chi\sin\theta \\ \sin\theta\sin\phi & -\sin\theta\cos\phi & \cos\theta \end{bmatrix}. \tag{6.20}$$

Note that the Euler angles all have a right-handed orientation when rotating in the ‘positive’ (increasing) direction.

6.4.5 The parametric formula of a conical frustum

A parametric elaboration of the above circle can construct the needed surface of a frustum. We start by elaborating the above formula for a generalised circle in such a way as to generate a truncated cone, which is the conical frustum shown in Figure 6-7(a). Note that a few example orthogonal vectors are shown, indicating the ultimate target of this procedure. Figure 6-7(b) depicts a standardised frustum located in the destination frame F` (ultimately in an arbitrary location/orientation in space) centred on the origin and oriented in the z' direction. The base circle equation (6.2) can generate a frustum by letting $\mathbf{r}_0$ range over the height of the frustum in the z' direction as per

$$\mathbf{r}'_0 = \left(0, 0, z'\right) \tag{6.21}$$

and

$$\mathbf{a}'_h = \left(0, 0, 1\right). \tag{6.22}$$

We also note that the circle radius d must vary linearly from d_1 to d_2 over the height h of the frustum. Therefore,

$$d = \frac{\left(h - z'\right)}{h}\left(d_1 - d_2\right) + d_2. \tag{6.23}$$

If we insert (6.21)…(6.23) into (6.2) and rearrange on an individual vector component basis, we get

$$x'^2 + y'^2 = \left(\frac{\left(h - z'\right)}{h}\left(d_1 - d_2\right) + d_2\right)^2. \tag{6.24}$$

This can be put in the more formal surface definition form

$$C(\mathbf{r}') = C(x', y', z') = x'^2 + y'^2 - \left(\frac{(h - z')}{h}(d_1 - d_2) + d_2 \right)^2 = 0 . \quad \textbf{(6.25)}$$

This surface defines all points on the frustum as z' varies from 0 to h. To parameterise this, we use u to vary the z' dimension and φ to cover x' and y'. Therefore,

$$x' = \left(\frac{(h-u)}{h}(d_1 - d_2) + d_2 \right) \cos\varphi \, , \; y' = \left(\frac{(h-u)}{h}(d_1 - d_2) + d_2 \right) \sin\varphi \, , \; z' = u . \quad \textbf{(6.26)}$$

The parameters operate over the range

$$u \in [0, h], \varphi \in [0, 2\pi) . \quad \textbf{(6.27)}$$

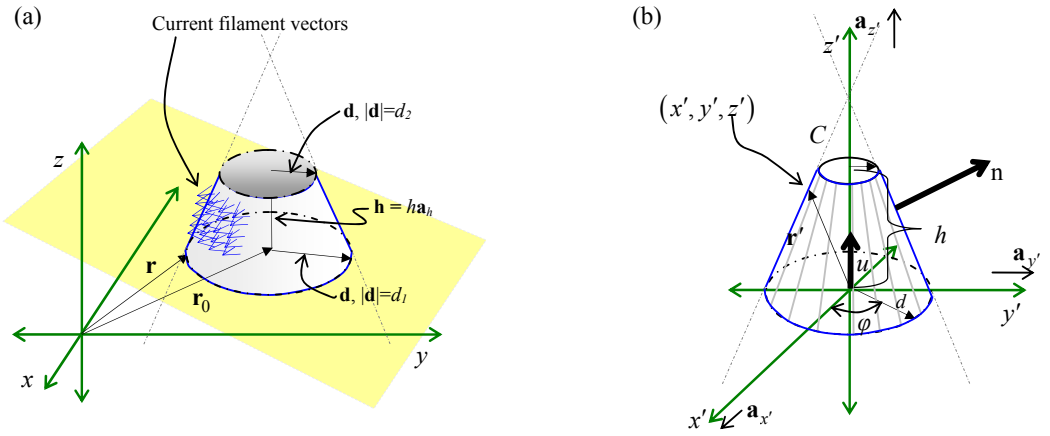

Figure 6-7 (a) The basic form of a single frustum with a base circle of the equation (1) form. In (b) we see the parametric generator for a frustum of height h centred on the origin with its apex oriented in the z' direction. Two parameters are required: u and φ.

6.4.6 Generating orthogonal vectors in the surface

If a surface S is given implicitly as the set of points (x, y, z) in a reference frame F satisfying $C(x,y,z)=0$, then, a normal at a point (x, y, z) on the surface is given by the vector

$$\nabla C(x, y, z) = \frac{\partial C}{\partial x}\mathbf{a}_x + \frac{\partial C}{\partial y}\mathbf{a}_y + \frac{\partial C}{\partial z}\mathbf{a}_z , \quad \textbf{(6.28)}$$

where the **a** vectors are the unit vectors of the reference frame F. The magnitude of the vector reflects the 'greatest rate of change' at that point. In our case, we have the surface defined by equation (6.24). If we take the gradient in the F` frame of Figure 6-8(b) as per (6.28), we get the vector function

$$\nabla' C(x', y', z') = 2x'\mathbf{a}_{x'} + +2y'\mathbf{a}_{y'} + 2\frac{(d_1 - d_2)}{h}\left[\left(\frac{(h - z')}{h} \right)(d_1 - d_2) + d_2 \right]\mathbf{a}_{z'} . \quad \textbf{(6.29)}$$

If we now insert the parameterised versions of the components as per (6.26), equation (6.29) becomes

$$\nabla' C(x', y', z') = 2\left[\left(\frac{(h-u)}{h} \right)(d_1 - d_2) + d_2 \right]\left[\cos\varphi \mathbf{a}_{x'} + \sin\varphi \mathbf{a}_{y'} + \frac{(d_1 - d_2)}{h}\mathbf{a}_{z'} \right] . \quad \textbf{(6.30)}$$

Note that the magnitude of this vector changes as u increases, even though the direction remains constant. This is because the 'maximum rate of change of the gradient' changes as U changes and the curvature of the cone changes. To use equation (6.30) to generate uniform-magnitude orthogonal vectors means normalising the vector to produce a set of surface-normal **n** (see Figure 6-7(b)). Therefore,

$$\mathbf{n} = \frac{\nabla' C(x', y', z')}{\left|\nabla' C(x', y', z')\right|}. \tag{6.31}$$

To populate the surface with a given set of ion channels requires dividing the current up into a known number of ion channels and then generating a set of unique u and φ.

6.4.7 Generating a set of Euler angles for the frustum

Figure 6-8 shows the mapping of a frustum from the origin to its final position.

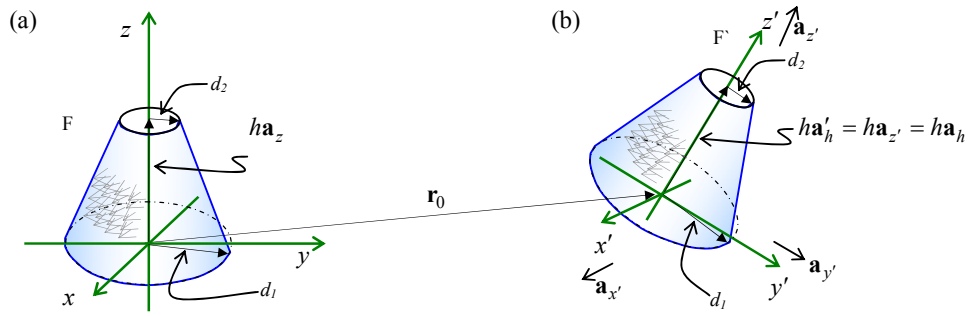

Figure 6-8 (a) The single frustum used to populate with filaments and (b) the final location of the frustum in space.

The important specialisations in Figure 6-8(b) are that the F` frame has its origin at the position of the translated frustum and the frustum base is centred on the origin. The frustum axis is aligned ($\mathbf{a}_h$) with the z' axis. This results in a specialised set of Euler angles that can now derived from known information. We know $\mathbf{r}_0$ and $\mathbf{a}_h$. Figure 6-8(a) and (b) also show that the F→F` transform maps $\mathbf{a}_h$ onto the z' axis so that equation (6.5) becomes

$$\mathbf{a}_{z'} = A\mathbf{a}_h \text{ or } \begin{bmatrix} 0 \\ 0 \\ 1 \end{bmatrix} = A \begin{bmatrix} x_h \\ y_h \\ z_h \end{bmatrix}, \tag{6.32}$$

where A is as per equation (6.20). Rearranging using (6.17) results in

$$\mathbf{a}_h = \begin{bmatrix} x_h \\ y_h \\ z_h \end{bmatrix} = A^T \mathbf{a}_{z'} = \begin{bmatrix} \sin\theta\sin\phi \\ -\sin\theta\cos\phi \\ \cos\theta \end{bmatrix}, \tag{6.33}$$

from which it immediately follows (remembering $\mathbf{a}_h$ is already normalised) that

$$\theta = \cos^{-1} z_h \tag{6.34}$$

and

$$\phi = \sin^{-1}\left[\frac{x_h}{\sqrt{1 - z_h^2}}\right]. \tag{6.35}$$

The remaining Euler angle is arbitrary, so we set it to zero,

$$\chi = 0. \tag{6.36}$$

This makes the final transform matrix:

$$A = \begin{bmatrix} \cos\phi & \sin\phi & 0 \\ -\cos\theta\sin\phi & \cos\theta\cos\phi & \sin\theta \\ \sin\theta\sin\phi & -\sin\theta\cos\phi & \cos\theta \end{bmatrix}. \tag{6.37}$$

From (6.33) …(6.35), we find y_h is

$$y_h = -\sin\theta\cos\phi = -\sqrt{1-z_h^2-x_h^2}\,. \tag{6.38}$$

This is what you would expect for a unit vector. Finally, we can set up the A matrix using (6.34), (6.36) and (6.38). Then put it in the final form of equation (6.9) thus:

$$\mathbf{x}' = \begin{bmatrix} \dfrac{y_h}{\sqrt{1-z_h^2}} & \dfrac{x_h}{\sqrt{1-z_h^2}} & 0 \\ \dfrac{-z_h x_h}{\sqrt{1-z_h^2}} & \dfrac{z_h y_h}{\sqrt{1-z_h^2}} & \sqrt{1-z_h^2} \\ x_h & -y_h & z_h \end{bmatrix} \left(\mathbf{r}-\mathbf{r}_0\right). \tag{6.39}$$

It is simple to verify equation (6.16) holds for this matrix.

6.5 Choosing and adapting a particular compartmental model

The currents used in the simulations done for this thesis originated in the NEURON (Hines and Carnevale 1997) compartmental simulation environment[2]. The NEURON package includes compartment mechanisms for general ion channel activity, synapses, gap junctions, ion storage and measurement points. NEURON was chosen because (i) it is the most widespread in use, (ii) it has a very mature online support base, and (iii) a suitable pre-packaged wild-type neuron was located in the publicly available model database.

6.5.1 The EAPS package and the D151 neuron

We use a compartmental model of a rat hippocampus CA1 pyramidal neuron identified as D151 that is supplied within a model available via the NEURON ModelDB website[3] under database number 84589. Neuron D151 is highly documented and has been microscopically engineered with the best available physiological information. The D151 model includes 12 different current types. The underlying ion channel densities account for the best known physiologically realistic variations throughout the D151 structure (Gold, Henze *et al.* 2007, Gold, Henze *et al.* 2006). Figure 6-9 shows four views of neuron D151 along with its geometric (spatial) mean computed without the axon. The axon is an artificial construct with standardised dimensions and properties (Gold, Henze *et al.* 2007, Gold, Henze *et al.* 2006).

EAPS stands for 'Extracellular Action Potential Simulation'. This package was originally created using a formula for the local field potential that is very different to equation (6.1). It uses the 'Line Source Approximation' (LSA) method. The LSA method locates all the transmembrane current as emanating uniformly and radially from a single line coincident with the compartment centreline(Gold, Henze *et al.* 2007, Gold, Henze *et al.* 2006, Holt 1998, Holt and Koch 1999). As such it is incapable of revealing field expression resulting from the non-uniform spatial disposition of the real currents. The filament acts at the compartment centreline and emits current uniformly in all directions. This causes the field expression to become unrealistically homogeneous in the azimuthal direction. The LSA/EAPS functionality of ModelDB 84589 was not used. The EAPS package was only used to source the underlying model and structure of the D151 neuron, which has proven to be of value as a benchmark in the study of the origins of the local field potential and the effects of the extracellular fields on cell excitability. D151 has enabled a small but useful lineage of publications, the most recent being (Anastassiou, Montgomery *et al.* 2010).

[2] See www.neuron.yale.edu.

[3] http://senselab.med.yale.edu/modeldb/

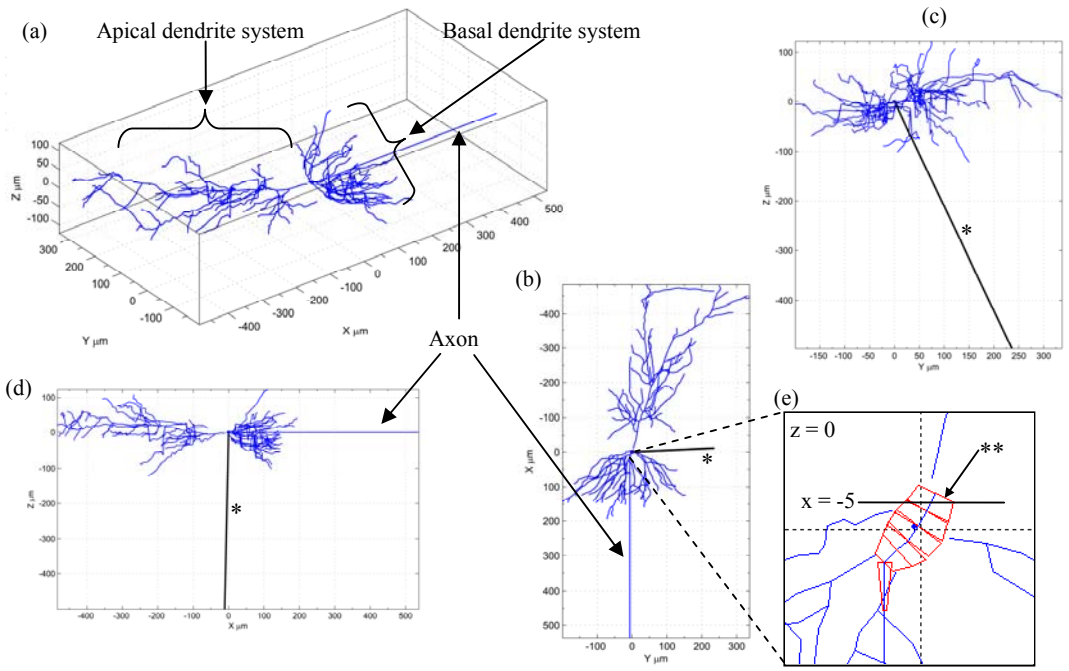

Figure 6-9 Rat hippocampus CA1 neuron D151 shown in (a) isometric view, (b) XY plane viewed from +Z, (c) ZY plane viewed from +X and (d) ZX plane viewed from –Y. The * indicates the single vector representing the net geometry of the apical and dendrite compartments when the compartment's frustum centreline is treated as a vector. (e) The soma shown as fully expressed compartments in an exploded view of the origin and environs. The ** marks frustum 1, a soma compartment which is important in later experimental work. The soma compartment diameters average roughly 8μm and their height is roughly 4μm.

6.5.2 Involvement of the NEURON simulation

Having chosen the D151 neuron in the EAPS package, the only functionality actually used was the NEURON simulation of a single action potential. The EAPS package was downloaded and installed. It was then modified to access compartmental currents in a manner suited to the new local field potential computation. Otherwise, the default settings for the entire neuron were 'out of the box', including the facility for triggering the single action potential. In this way, we hope to maximally facilitate the possibility that others can replicate the upcoming results. All future users of the EAPS package should be able to replicate the test conditions used in this thesis.

6.5.3 Modification of the EAPS neuron simulation

Specific EAPS NEURON `.hoc` files were modified to (a) report a more detailed current breakdown and (b) to project the final currents back into the original 3D structure. The targeted currents are shown here in Table 6-1.

Original	Description	As documented
`I_tot`	Total membrane current	$I_{Tot}(t)$
`V`	Membrane potential	--
`I_cap`	Capacitive component of the membrane current	$I_{cap}(t)$
`I_k`	Potassium component of the membrane current	$I_{K}(t)$
`I_na`	Sodium component of the membrane current	$I_{Na}(t)$
`I_ca`	Calcium component of the membrane current	$I_{Ca}(t)$
`I_pas`	Passive mechanism component of the membrane current (leak current)	$I_{pas}(t)$

I_in	Axial current from the "0" end of the compartment	--
I_out	Axial current going to the "1" end the compartment	--

Table 6-1 Modified NEURON compartmental current breakdown.

NEURON facilitates the 3D specification of a full neuron structure. That done, the 3D structure is used to create the 1D model parameters. The practical issue here is that the original 3D frusta and the simulation 'compartments' (NEURON 'segments' and 'sections') are not related 1:1. Multiple 3D frusta, all of varying lengths, diameters and orientations, can be treated as a single NEURON 'section'. That 'section' is then divided into *nseg* NEURON 'segments'. The currents are computed for each NEURON segment. To get the current in the original 3D frusta, in the original EAPS/LSA system, a procedure was written to project the NEURON 'segment' currents back onto the original 3D geometry. This procedure is detailed shortly, and was also modified to project the expanded current decomposition back onto the original 3D structure. For reference, the Table 6-1 currents are computed in `current_util.hoc` procedures `read_compartment_currents( )` and `calc_axial_currents( )`. With the exception of the passive and capacitive currents, the current computations are based on underlying NEURON MODL code in the `eaps\mod` directory. For every current established with a `USEION` statement, NEURON automatically totals the current for the ion. In the case of `i_cap` and `i_pas`, the totals are built into every compartment. The details are in the main NEURON package (details in the 'mechanisms' help).

6.5.4 Channel density considerations

The procedure that projects the D151 NEURON currents back into the original 3D geometry does not retain the ion channel density information except insofar as the underlying NEURON simulation parameters, and hence the transmembrane currents, are affected. To this extent, the filament sources used in the subsequent field computations will reflect regional variability in ion channel density. All other specification of filament density and filament layout are manually determined experimental setpoints.

6.5.5 Projecting NEURON compartment currents onto their original 3D structure

As discussed above, for use in equation (6.1), the simulation currents have to be projected back into the original 3D frusta. The accurate reverse-mapping of currents thus became one of the developmental tasks of the project. The projection method was reverse engineered and is provided in Figure 6-10 so that the technical issues are properly documented. A 'line segment' is the NEURON terminology that refers to the centreline of the conical frustum in the 3D specification of the neuron morphology. In NEURON, a 'Section' refers to a collection of contiguous 3D 'line segments'. Once defined, a 'section' is divided into `nseg` NEURON compartments. Each compartment's components (of the kind represented in Figure 6-1 equivalent circuit componentry) have parameters customised based on the lengths and areas of the 3D frusta. These are then projected into the `nseg` NEURON compartments. This projection is the reason why the reverse projection of the resultant currents is a non-trivial exercise.

The sequence of joined (and branching) frusta in space are set out such as to inscribe, in space, a monotonically increasing arc length (back to the overall origin). The arc length is computed and maintained within NEURON. The mapping of NEURON segment currents to 3D line segments proceeds linearly based on allocation proportional to the spatial occupancy as revealed by the NEURON `arc3d( )` function. All lengths are normalised to 1. Segment current is computed by NEURON at the compartment centre (shown as ●). There are always [`n3d( )-1`] 3D points covering the idealised 1D NEURON 'section' of length L (which is normalised to length 1 as shown), which is divided into `nseg` 'segments'. There is no fixed relationship between the 'line segment' and the NEURON 'segment' except for the requirement that the `arc3d` reveal monotonically increasing arc lengths.

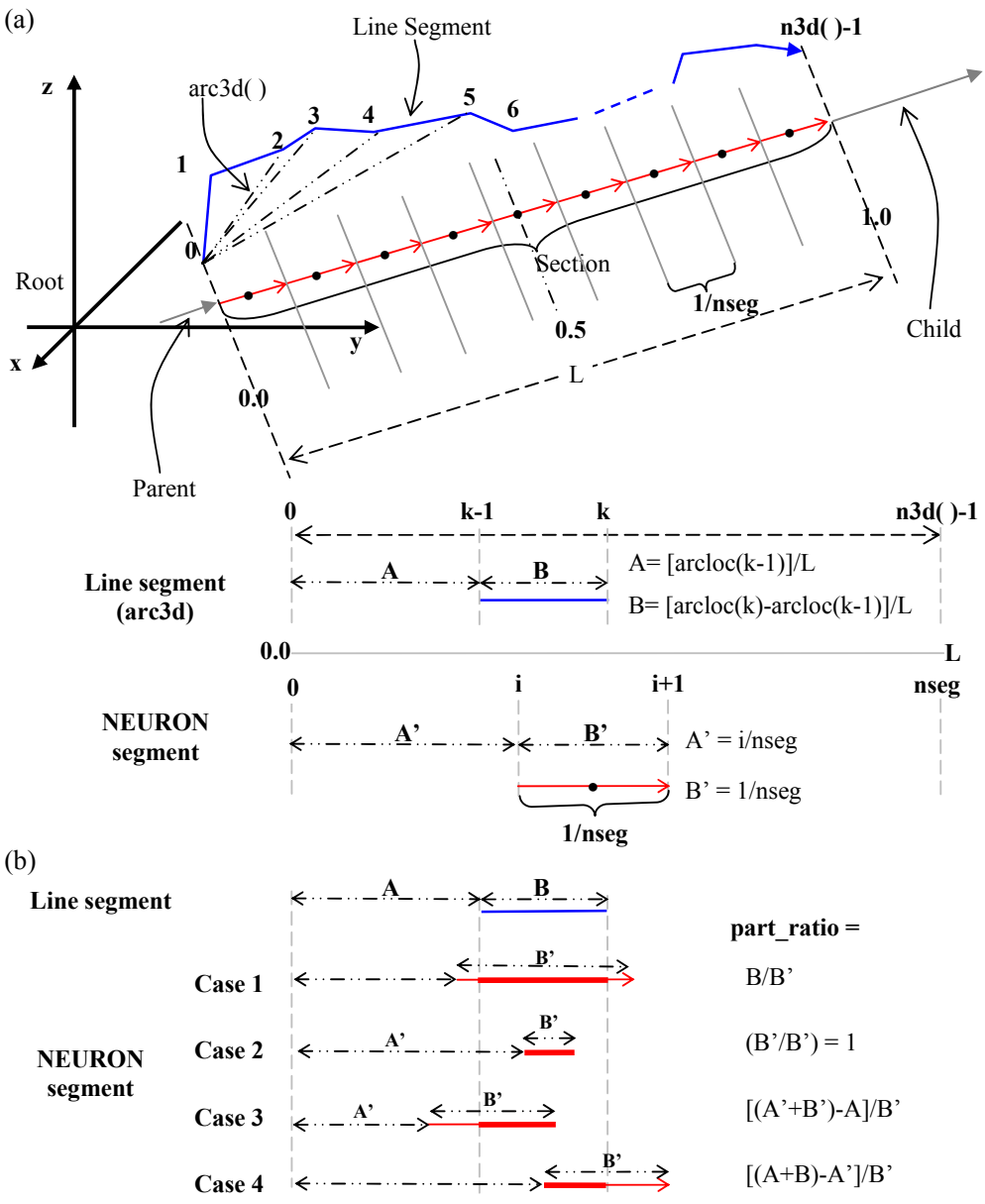

Figure 6-10 (a) NEURON segment ⇔ line segment (frustum) geometrical relationship. (b) Mapping the allocation of NEURON segment current to line segment current.

Figure 6-10(b) shows the relationship between the currents as computed for the 3D 'line segment' **B** based on apportioning the underlying NEURON segments' contribution to it. The current is divided based on the occupied arc length as produced by `arc3d` as shown. For example, if the NEURON segment is entirely within the 3D 'line segment', then 100% of the current is allocated to the line segment. If the NEURON segment is different (partially overlapping) to the 3D 'line segment', then the NEURON segment's current is apportioned to adjacent 'line segments' as shown.

6.5.6 The 'action potential'

With the NEURON 'EAPS' package modified and tested, a single action potential was triggered. It provided data as per Table 6-1 for each of the 1128 compartments of the D151 model over a period of 25ms (with variable time intervals of roughly 50-100µs). This resulted in a 159-sample time-series for all recorded values for every compartment in the model. The action potential occurred around 12ms and continued until roughly 15ms, during which all compartment currents go through the stereotypical

variations associated with the various ion current types. The balance of the 25ms period allowed the system to settle. A sample of the output of the modified NEURON simulation is provided in Figure 6-11.

(a)

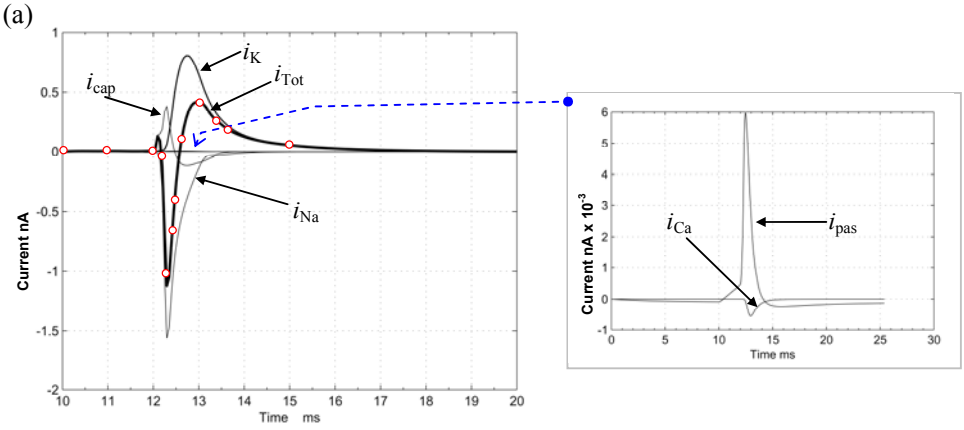

(b)

Time t legend (ms)
10.000
10.994
11.997
12.195
12.396
12.501
12.557
12.613
12.997
13.368
13.602
15.044

Figure 6-11 (a) Actual 3D compartment (soma) currents. The dark line is the total transmembrane current i_{Tot}. Currents i_{Na}, i_K, i_{cap}, are the dominant sodium, potassium and capacitative components, respectively. Currents i_{Ca} and i_{pas} are the smaller calcium and passive currents and are shown in an exploded view with a different vertical scale. The plot starts at simulation time 10ms, which is shortly before the action potential is triggered in compartment 7. Positive current corresponds to outward flow of positive ions. (b) Samples of key time-stamps that resulted from the NEURON simulation. The red circle indicate the representative times used in later figures (future chapters).

Notice that the original NEURON compartment voltage and the axial currents are not shown. These are irrelevant to equation (6.1) and were ignored. Notice that the NEURON package has not computed the extracellular currents (shown in Figure 6-1). In this way, the ECS and ICS currents, previously identified as relatively incoherent, are sidelined. Transmembrane currents remain the only currents relevant to equation (6.1).

6.5.7 Other simulation issues

Mathematically, the NEURON model 3D frusta are discontinuous notional constructs in a continuous conductive medium in space with a conductivity chosen as 1/3 Sm^{-1} (da Silva and Van Rotterdam 2005). This conductivity is order-of-magnitude accurate and is a determinant of field magnitude rather than the more interesting structure and dynamics. Despite this high level of material abstraction, useful realism will be shown to result. The realism can be attributed to the physiological accuracy of the underlying current dynamics and cell morphology.

In its implementation, the total transmembrane current i_{Tot} was divided equally throughout each cohort of current filaments. The filaments were allocated a length equal to the cross-sectional width of a typical lipid bilayer penetrated by a large channel protein (L_k = 7.5nm filament length was used). Regardless of the (variable) spatial allocation policy chosen to position filaments on a particular compartment surface, what remains the same throughout this variability is the total transmembrane current.

6.5.8 Software and supercomputing issues

Once a set of compartment currents has been recorded, the LFP can be computed and explored using equation (6.1). The statistics of compartment number, spatial resolution, time resolution and filament number combine to make the full computation of equation (6.1) potentials throughout regions of space, and over time, an onerous computational load. The good news is that the field computation is strongly scalable, making it amenable to being spread across multiple processors with no need for inter-processor communication. Each processor can execute the same code for a different slice of

space and time. At the end, all the results can then be stitched back together to reveal the field throughout the computed region of space.

Following the modifications to the NEURON 'EAPS' package, MATLAB was used to automate the process of locating large cohorts of filaments, in an easily adaptable way, throughout the 1128 compartments of the D151 neuron. For the one set of single action potential current data from the D151 neuron, the field computations of equation (6.1) were computed in a desktop environment. Once this basic framework was tested and functional, the software was adapted to a non-graphical environment suited to large-scale field computations throughout user-defined slices of large regions of space at adjustable spatial resolution and as per a menu/library of other adjustable settings. The software divided the application into spatial and time slices and then generated all the data, program files and batch launch scripts. Further software automated the loading and launching of batch jobs for use by the high-performance computing (HPC) platform. Once HPC computing was complete, further processing combined all the space/time slices into a single collection of field potential data. With the experimental field potential data thus assembled, a whole suite of analytical and display tools was written to analyse and present the final results. Over the course of the experiments, in excess of 175,000 hours of CPU time was consumed under the VLSCI grant number VR0003[4].

6.6 Chapter summary

This chapter set about the practical business of assembling a considerable number of disparate elements into a single experimental regime as follows:

- Sourcing a set of biologically realistic currents (via compartmental modelling).
- Examining the relationship between ion channels and filaments so that simulation results can be appropriately interpreted. In particular, it was ascertained that whole-compartment currents be divided equally between any set of allocated filaments. This policy is necessary, at this early stage of knowledge, so that results can be assessed and compared.
- It was recognized that the experimentation must proceed without realistic synapse currents (using action potential currents only).
- The mathematics of populating 3D model compartments with filament cohorts was developed.
- A working model (NEURON ModelDB 84589, Rat Hippocampus CA1 pyramidal neuron) was sourced. This model is particularly appropriate because it already has a track record of being used in earlier explorations of excitable cell electromagnetism.
- Adapting the model to deliver a suitable collection on of compartmental action potential currents, including their projection into the 3D structure of the D151 neuron.
- The process of creation of an experimental environment using supercomputing resources to implement the field potential computations.

This chapter captures the essence of the background work required to enable experimentation to proceed in an organized fashion, with some confidence that the experimental results are accurate and able to be usefully interpreted, later, in the wider context of real tissue fields. Using these basic elements, any motivated experimentalist should be able to create a system capable of revealing the same experimental results.

6.7 Chapter bibliography

Aidley, D. J., The Physiology of Excitable Cells, 4th ed., Cambridge University Press, New York, 1998, pp. xii, 477.

Anastassiou, C. A., Montgomery, S. M., Barahona, M., Buzsaki, G. and Koch, C. 'The Effect of Spatially Inhomogeneous Extracellular Electric Fields on Neurons', *Journal of Neuroscience* vol. 30, no. 5, 2010. 1925-1936.

da Silva, F. H. L. and Van Rotterdam, A. (2005) Biophysical Aspects of Eeg and Magnetoencephelogram Generation. In E. Niedermeyer, and F. H. L. da Silva (eds.).

[4] http://www.vlsci.unimelb.edu.au/

Electroencephalography : Basic Principles, Clinical Applications, and Related Fields, Lippincott Williams & Wilkins, Philadelphia.

Dayan, P. and Abbott, L. F., Theoretical Neuroscience : Computational and Mathematical Modeling of Neural Systems, MIT Press, Cambridge, Mass. ; London, 2001, pp. xv, 460.

Einstein, A., Out of My Later Years, Philosophical Library, New York, 1950, p. 282.

Gold, C., Henze, D. A. and Koch, C. 'Using Extracellular Action Potential Recordings to Constrain Compartmental Models', *Journal of Computational Neuroscience* vol. 23, no. 1, 2007. 39-58.

Gold, C., Henze, D. A., Koch, C. and Buzsaki, G. 'On the Origin of the Extracellular Action Potential Waveform: A Modeling Study', *Journal of Neurophysiology* vol. 95, no. 5, 2006. 3113-3128.

Goldstein, H., Poole, C. P. and Safko, J. L., Classical Mechanics, 3rd ed., Addison Wesley, San Francisco, 2002, pp. xviii, 638 p.

Hille, B., Ion Channels of Excitable Membranes, Third ed., Sinauer Associates, Inc., Sunderland, MA., 2001

Hines, M. L. and Carnevale, N. T. 'The Neuron Simulation Environment', *Neural Computation* vol. 9, no. 6, 1997. 1179-1209.

Hines, M. L. and Carnevale, N. T. (2003) The Neuron Simulation Environment. In M. A. Arbib (ed.). *The Handbook of Brain Theory and Neural Networks*, MIT Press, Cambridge, Mass.

Hodgkin, A. L. and Huxley, A. F. 'The Components of Membrane Conductance in the Giant Axon of Loligo', *Journal of Physiology-London* vol. 116, no. 4, 1952a. 473-496.

Hodgkin, A. L. and Huxley, A. F. 'Currents Carried by Sodium and Potassium Ions through the Membrane of the Giant Axon of Loligo', *Journal of Physiology-London* vol. 116, no. 4, 1952b. 449-472.

Hodgkin, A. L. and Huxley, A. F. 'The Dual Effect of Membrane Potential on Sodium Conductance in the Giant Axon of Loligo', *Journal of Physiology-London* vol. 116, no. 4, 1952c. 497-506.

Hodgkin, A. L. and Huxley, A. F. 'A Quantitative Description of Membrane Current and Its Application to Conduction and Excitation in Nerve', *Journal of Physiology-London* vol. 117, no. 4, 1952d. 500-544.

Hodgkin, A. L., Huxley, A. F. and Katz, B. 'Measurement of Current-Voltage Relations in the Membrane of the Giant Axon of Loligo', *Journal of Physiology-London* vol. 116, no. 4, 1952. 424-448.

Holt, G. R. (1998) A Critical Reexamination of Some Assumptions, Implications of Cable Theory in Neurobiology. California Institute of Technology, Pasedena, California.

Holt, G. R. and Koch, C. 'Electrical Interactions Via the Extracellular Potential near Cell Bodies', *Journal of Computational Neuroscience* vol. 6, no. 2, 1999. 169-184.

Johnston, D. and Wu, S. M.-s., Foundations of Cellular Neurophysiology, MIT Press, Cambridge, Mass., 1995, pp. xxxi, 676 p.

Landau, L. D., Lifshits, E. M. and Pitaevskii, L. P., Electrodynamics of Continuous Media, 2nd ed., Pergamon, Oxford [Oxfordshire] ; New York, 1984, pp. xiii, 460 p.

Chapter 7

EXPERIMENTAL OUTCOMES

> "*The sensation of seeing is, for us, very different from the sensation of hearing, but this cannot be due to the physical difference between light and sound. Both light and sound are, after all, translated by the respective sense organs into the same kind of nerve impulses. It is impossible to tell, from the physical attributes of a nerve impulse, whether it is conveying information about light, about sound or about smell.*"
>
> Richard Dawkins (Dawkins 2006)

7.1 Introduction

This chapter revealed the results of a computational exploration of the delivery of an endogenous electromagnetic (EM) field system into the bulk environment of excitable cell tissue by the 'coherent-current filament' model established in the previous chapters. The experiments are directly aimed at the Chapter 3 hypotheses. The tests examined the electric field system. The first hypothesis requires an examination of the capability of the cells to systematically create a unified field. The second hypothesis requires an examination of the configuration freedom of the electric field. In particular, that the same action potential be consistent with multiple (degenerate) field systems. In principle, this will permit a neuron to adapt based on cues from the electric field environment, forming a secondary line-of-sight feedback mechanism.

7.2 Test regime

In this experimental regime, the LFP and/or electric field produced by current filaments involved in a single action potential is computed for the D151 neuron model and some artificial constructs based on it. To explore how different filament systems express EM fields under equation (6.1), a group of tests is assembled as follows:

Test 1 Reveal how the transmembrane currents unfold in space and time throughout the entirety of neuron D151

Test 2 Examine the microscopic LFP expressed by individual filaments in a compartment context

Test 3 Compute the collective LFP expressed by the entire neuron with a randomly positioned set of filaments

Test 4 Test 3 field is decomposed into 3 subsets: apical, basal and soma components.

Test 5 Explore how filament position affects the overall LFP expression by

	generating multiple sets of the same filaments as Test 3, but positioned differently on D151 compartments
Test 6	Test the effect of cell morphology on LFP expression by generating a simplified structure using only one of D151 basal processes and its soma, hillock and initial segment. It is populated with a regular array of filaments and is driven with the original compartmental currents. Then soma is then rotated to three positions and the field system is computed for each position
Test 7	A secondary examination of the effects on the LFP due to cell morphology. The Test 6 basal dendrite structure is proliferated and the affect on the LFP is measured.
Test 8	Visualisation of the electric field corresponding to the LFP expression in Test 3.

Table 7-1 List of experimental arrangements.

All of these tests, unless otherwise specified, use the natural compartment current expressions during the same action potential produced by the NEURON package outlined in Chapter 5. The bulk of the results are video presentations included as online supplementary material. The supplementary files are prepended with the tag Sn, where n is an integer. This tag is used as a reference in the chapter text.

7.2.1 Filament currents

The available currents are, for each compartment, i_{Tot}, i_{Na}, i_K, i_{Ca}, i_{cap} and i_{pas} are the total, sodium, potassium, calcium, capacitative and passive components. The discussion in chapter 6 recognized that, in the D151 model neuron, the exact location of ion channels is not known. The mix, densities and collocation properties of the twelve different channel types in any given location is also unknown. Having gone to the trouble of separating out the six current types, it was decided to use on the total compartment current in the upcoming exploration. In view of the fundamental principles that are being sought as support for hypotheses (1) and (2), using the total compartment provides a basic mechanism without involving arguments about choices of filament mix, densities and collocation. The specifics can be introduced later based on accurate physiological knowledge. For every test performed here, when a compartmental current, i_{Tot}, is applied to a compartment with Km filaments, each filament has a current i_{Tot}/Km.

7.3 Test 1: Compartmental transmembrane currents

The single action potential provided transmembrane currents for all 1128 compartments of the model over a period of 25ms (with variable time intervals of roughly 50-100μs). This resulted in a 159-sample time-series for all six currents for every compartment in the model. Following a trigger at 10 ms, the action potential occurs around 12ms and continues until roughly 15ms, during which all compartment currents go through the stereotypical variations associated with the various ion current types as discussed in the previous chapter. The balance of the 25ms period allowed the system to settle. The total compartmental (transmembrane) current is graphically examined throughout the entire structure in a way that enables a compartment polarity comparison. For reference, Figure 7-1 shows the transmembrane current for compartment 1 (also seen in chapter 5).

7.3.1 RESULT: Wavefronts of evanescent virtual dipoles are created by an action potential

Figure 7-2 and supplementary videos S1 and S2 show the overall progression of compartmental transmembrane currents in space. ECS and ICS currents are not involved. This reveals the spatial relationships between compartment currents in a manner that highlights regions of differing total transmembrane current polarity. RED indicates positive (outward) current flow, and BLUE represents negative (inward) current flow. Line thickness is a rough indicator of current magnitude. The action potential begins in the axon initial segment and immediately spreads dromically, quickly down the

axon and more slowly, antidromically, via the soma. This cannot be seen in Figure 7-2 because it is obscured. To witness the initial segment, a zoomed video S2, of the soma area, is provided in the supplementary material. The sequence reveals two moving virtual dipole fronts spreading apart in the basal and apical dendrites.

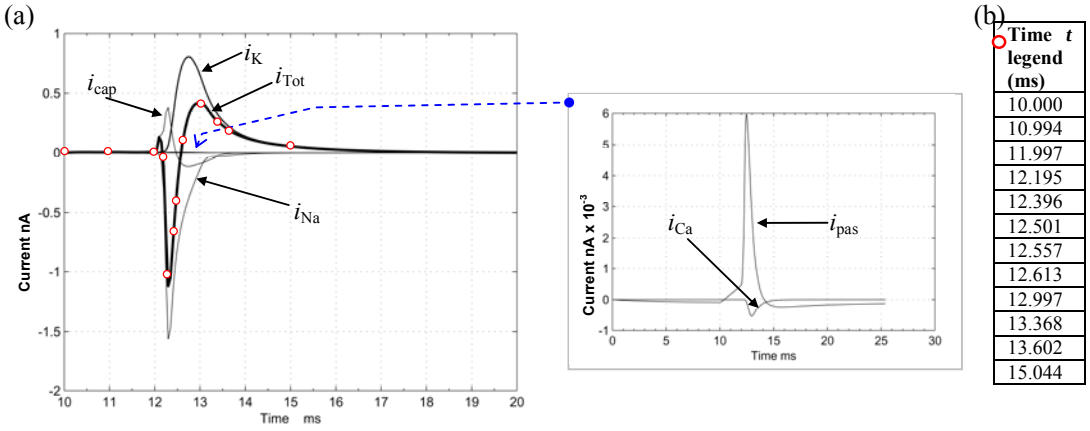

Figure 7-1 D151 compartment 1 transmembrane current. The convention is that positive current flows out of the cell.

The early RED appearance in Figure 7-2(a)…(c) reflects the build up of soma potential by synapse manipulation and the initial positive current excursion shown in Figure 5-11. The change to BLUE in Figure 7-2(d)…(f) then reflects the deep negative swing due to sodium current. The later RED in Figure 7-2(g)…(l) reflects the return overshoot (potassium) region of the current. There is a progression of a RED/BLUE wave-front of spreading virtual dipoles that characterises all the fields in the subsequent tests. Two separate RED/BLUE interfaces emerge: a pair of wave fronts that move apart as they progress throughout the apical and basal dendrites. The first is during the rapid negative swing (e.g. Figure 7-2(e)). The second virtual dipole front occurs when the return to positive current overshoots (e.g. Figure 7-2(i)). This activity is largest in and around the soma. When one compartment dips negative, nearby compartments can be positive. An evanescent virtual dipole is created, existing only for the duration of a current polarity disparity. The process of spreading evanescent dipoles can be seen in Figure 7-2 in the spreading interface of RED and BLUE, characterising the net field structure revealed in subsequent tests.

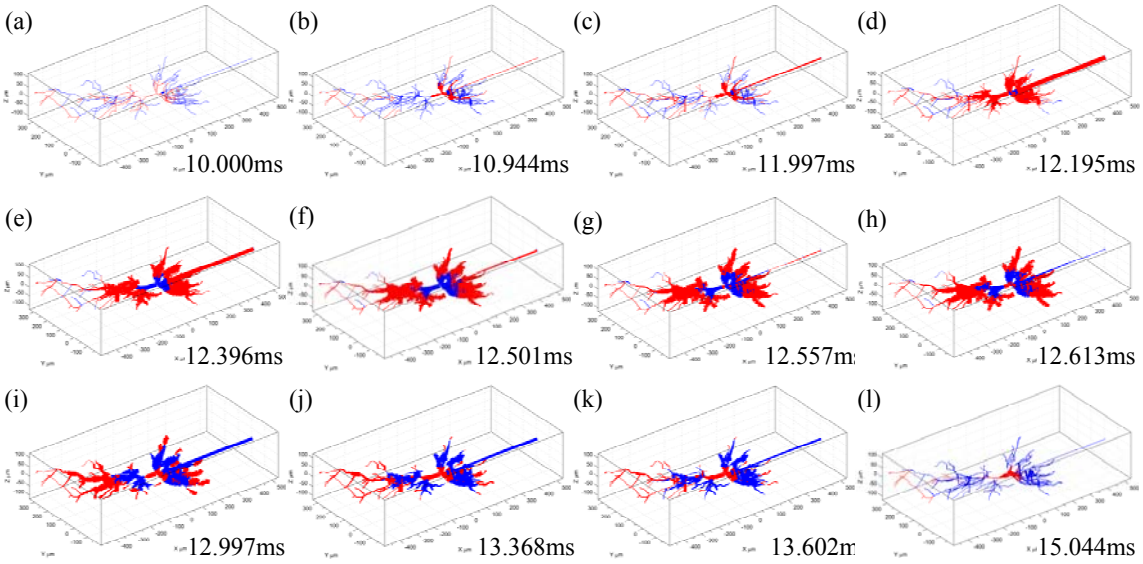

Figure 7-2 Test 1. The current progression throughout D151 as a result of action potential dynamics. It reveals wave fronts of virtual dipoles.

7.4 Test 2: Explore basic channel physics

Here the LFP produced by an individual current filament is examined. This can be done in the NEURON (Hines and Carnevale 1997) D151 context by using single compartment/frustum number 1 of 1128 (the first of 5 soma frusta, marked ** in Figure 6-9). Figure 7-3 shows that the frustum is populated with 8 rows of 3 filaments equally distributed radially around the surface. This was achieved by appropriately forcing the two parameters u and φ in equations (6.26) and (6.27) for the conical frustum surface equation. The dotted line is the centreline of the frustum. The dashed lines form a rough outline of the frustum. The total compartment current of Figure 7-1 is evenly distributed throughout the 24 filaments. The LFP for the lone frustum is computed, using equation (6.1) over the interval 11.839ms to 15.044ms to a spatial resolution of 0.1μm.

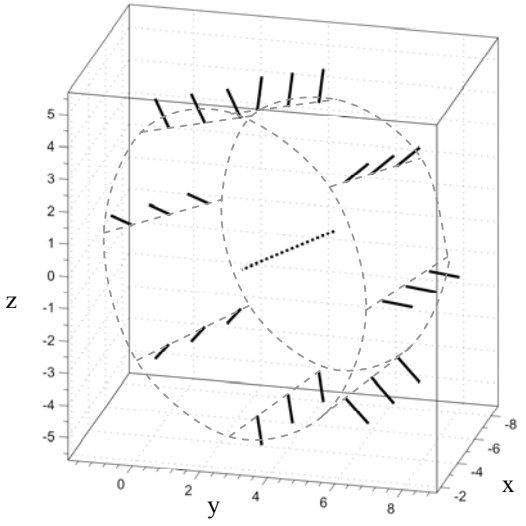

Figure 7-3 Regular filament structure for Test 2. Filaments (.0075μm long) are shown exaggerated, not to scale. The dotted line is the frustum centreline. The dashed line is a rough (not to scale) outline of soma frustum 1. The scale is in μm.

7.4.1 RESULT: Compartment shaped current filament disposition produces a compartment-shaped uniform LFP region

Figure 7-3 and supplementary videos S3, S4 and S5 show the microscopic scale filamentary LFP produced by the single soma compartment. The colours in Figure 7-3 reflect the magnitude and sign of the total current waveform in Figure 7-1. The electric field lines are orthogonal to the isopotential contours (of equal colour). Selected snapshot frames (from the times indicated in Figure 7-1(b)) show that the computations covered a volume 25 x 15 x 20μm centred on [x = 0, y = 2.5, z = 0] μm. Slices through this LFP volume were taken as follows: XZ plane at y = 0μm, YZ plane at x = -5μm, XY plane at z = 0μm.

Figure 7-4shows that each filament delivers an extended electric field system projecting distally along the filament centreline. A metaphorical way to view the images and videos is that of a pressure vessel first relieving and then re-establishing the pressure. Spatially collocated filaments tend to create a spatial outline of an extreme potential gradient located near, and similar in shape, to the underlying frustum. This naturally creates a field structure consistent with the physical presence of a lipid bilayer dielectric in the real cell. This suggests that the primitive (uniform conductivity) model used here has managed to capture the basic physically realistic spatial properties of the field expression. The polarity of the field is consistent with typical transmembrane differential potentials, but not with the usual convention of the ‘extracellular’ medium being a reference potential of zero volts, which only applies in the original NEURON model.

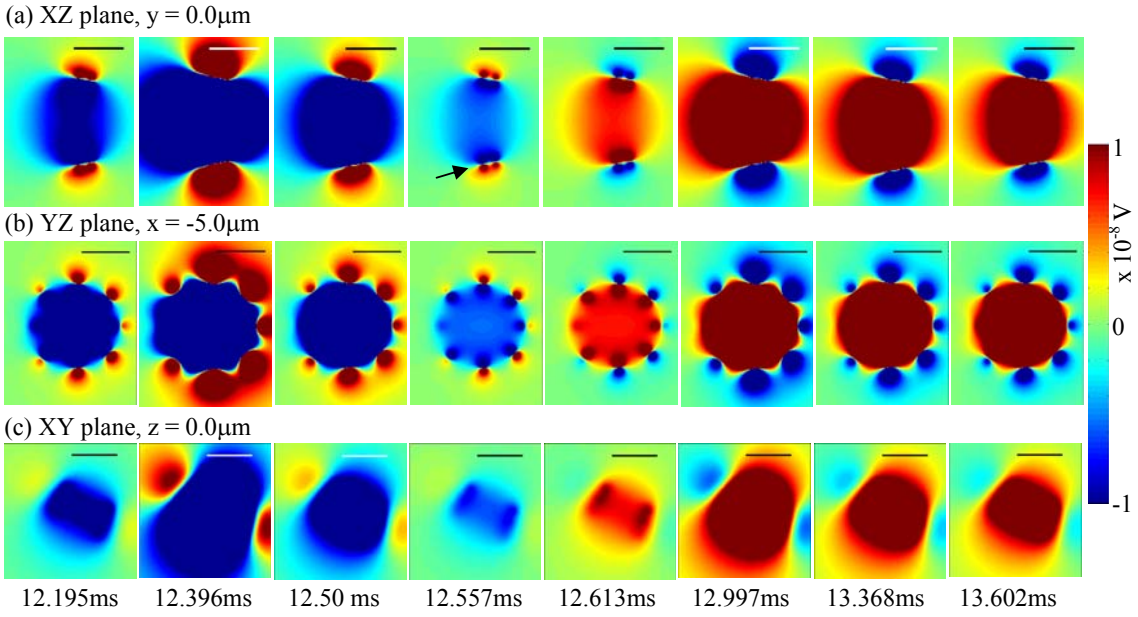

Figure 7-4 Test 2 results. LFP plots of slices (a) y = 0, (b) x = -5 and (c) z = 0 for the single frustum shown in Figure 7-3. The arrow points to the filament-width planar region that would be the location of the lipid bilayer in the real material. Calibration bar = 5μm.

7.5 Test 3: Compute D151 LFP for a randomly located filament set

Each D151 compartment is allocated filaments based on a notional 'filament density' of 1 per μm^2 over the compartment outer (known) surface area, but with an enforced minimum of 10 and a maximum of 25 filaments on any individual compartment. This ensures some level of spatial distribution of the current for small (low external surface area) compartments and minimises computation time, respectively. These constraints resulted in 19,066 filaments. Each filament is embedded orthogonally to the surface and is located by using the MATLAB random number generator to randomly determine the two parameters u and φ in equations (6.26) and (6.27) for the conical frustum surface equation. Figure 7-5 shows the actual filament population in the soma locality. The action-potential transmembrane compartment currents, revealed in test 1 for every compartment, were then divided up equally amongst each compartment's filaments. The LFP was then computed, at a resolution of 1μm, over a portion of the total time-course of the action potential.

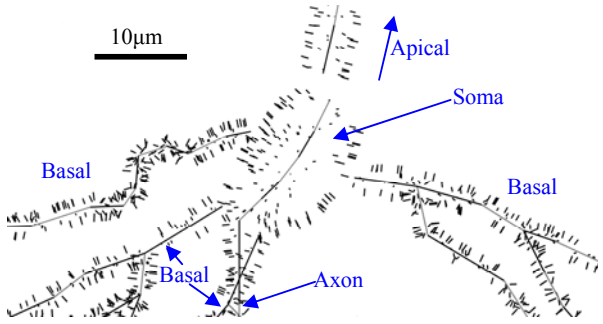

Figure 7-5 An isometric view of a subset of the random filament positions of Test 3. Filaments (.0075μm long) are shown exaggerated, not to scale. The line is the frustum centreline.

7.5.1 RESULT: Action potential LFPs can have a spatially large, unified sweeping pattern in space

The video presentation is the best way to properly appreciate the result. Figure 7-6 shows a series of snapshots from the XY plane supplementary videos (S6). The video for the XZ plane is also provided (S7). Each video frame took close to 500 hours to compute. The two orthogonal LFP planes were computed for D151 centred on the origin over the following ranges: XY plane, [(-550 ≤ x ≤ +550), (-550 ≤ y ≤ +550), (z = 0)] µm, times: 11.112ms ≤ t ≤ 15.044ms; XZ plane, [(-550 ≤ x ≤ +550), (y = 0), (-550 ≤ z ≤ +550)] µm, times: 11.782ms ≤ t ≤ 14.451ms. Figure 7-6 shows the XY plane results at times indicated in Figure 7-1(b). The XY slice at z = 0µm passes obliquely through the soma, which is located near the origin. Straight arrows are used to indicate non-rotating fields that are shrinking/growing at a rate roughly proportional to arrow length. Curved arrows indicate rotating fields that may have an excursion in the Z direction. It consists of a dipole-like field centred on and rotating around the soma/hillock/initial segment locale. The net interaction of all the filaments produces a lobed field structure that establishes itself laterally, rotates, shrinks when it aligns with the axon and grows again when laterally aligned. It then contracts back to the resting state. Note that the behaviour is only a slice through a more detailed 3D lobe-trajectory.

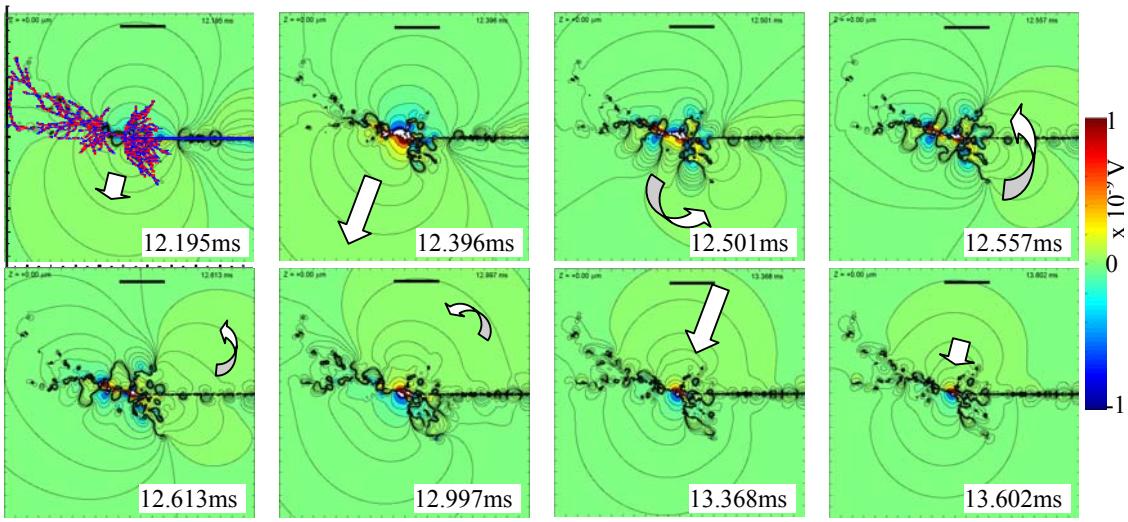

Figure 7-6 The LFP computed for the 19,066 filaments randomly positioned on neuron D151. It shows an XY slice through the LFP at z = 0.0µm during the single action potential. XY and XZ videos are in supplementary S6 and S7 resp. The top left panel has the D151 structure superimposed. The straight arrows depict growth/shrinkage rates of a relatively stationary field pattern. The curved arrows indicate a rotating field pattern that have an excursion in the Z direction (into/out of the page). The scale bar is 200µm.

The results of this test are reminiscent of antenna behaviour. The field is unified, large, highly directional, with the lobes of the field system exhibiting focus, sweep and dwell that creates different behaviours laterally (e.g. laminar) and longitudinally (e.g. columnar), both in magnitude and dwell time. Overall, this is suggestive of the possibility that ion channel locations could provide some level of electromagnetic avoidance/preference for the columnar and/or lateral axes. This result supports the possibility that biologically realistic, coherently driven transmembrane filamentary action-potential currents can cause a unified electric field behaviour with a specific extended spatial structure and with temporal dynamics related to the distributed transmembrane current dynamics. This field system swathe will be delivered, in a consistent fashion, to its neuron and astrocyte neighbours and any processes in its locale, including itself. Figure 7-6 shows that, at its peak, the field system spatial extent establishes a distinctive structure over a spatial region larger than the basal dendrite structure, although its influence in real tissue will ultimately depend on the field contributions from other neurons in the same locale. Theoretically the field system extends to infinity, which in practice has been identified (see chapters 1/2/3) as the macroscopic realm of the extra-cortical region.

7.6 Test 4: Decompose Test 3 LFP into regions

The Test 3 result for $z = 0$ is recomputed for three subsets of the D151 geometry. The soma/axon subset (compartments 1-17) includes the hillock and axon initial segment. Compartments 18 to 507 includes all basal dendrites. Subset 508 to 1128 includes all apical dendrites. It is to be verified that the sum of the decomposed potentials results in an LFP identical to Test 3. The computed LFP for each time-step exists in a 2D array indexed by spatial location. The MATLAB arrays for test 3 and test 4 have the identical structure and are indexed identically. If the test 3 LFP is $LFP_{1\text{-}1128}(x,y,t)$, then each decomposed subset can be considered to be $LFP_{1\text{-}17}(x,y,t)$, $LFP_{18\text{-}507}(x,y,t)$, $LFP_{508\text{-}1128}(x,y,t)$. Checking that the LFP for test 3 is the same as the total LFP for test 4 involves checking to see if

$$LFP_{1\text{–}1128}(x,y,t) = LFP_{1\text{–}17}(x,y,t) + LFP_{18\text{–}507}(x,y,t) + LFP_{508\text{–}1128}(x,y,t). \quad \textbf{(7.1)}$$

7.6.1 RESULT: Regional subsets of the field pattern express similar versions of the Test 3 field pattern that sum to the whole

Figure 7-7 shows that the decomposition of the Test 3 filament set's field pattern reveals three rotating dipoles (videos are provided in supplementary S8, S9, S10). Two rotate roughly in the XY plane and are due to the basal and apical dendrites. The third rotates orthogonally (roughly in the YZ plane) and is associated with the soma/axon complex. The three fields were verified to sum to the Test 3 result. This was conducted by verification that (7.1) applied for a variety of randomly selected spatial locations and times.

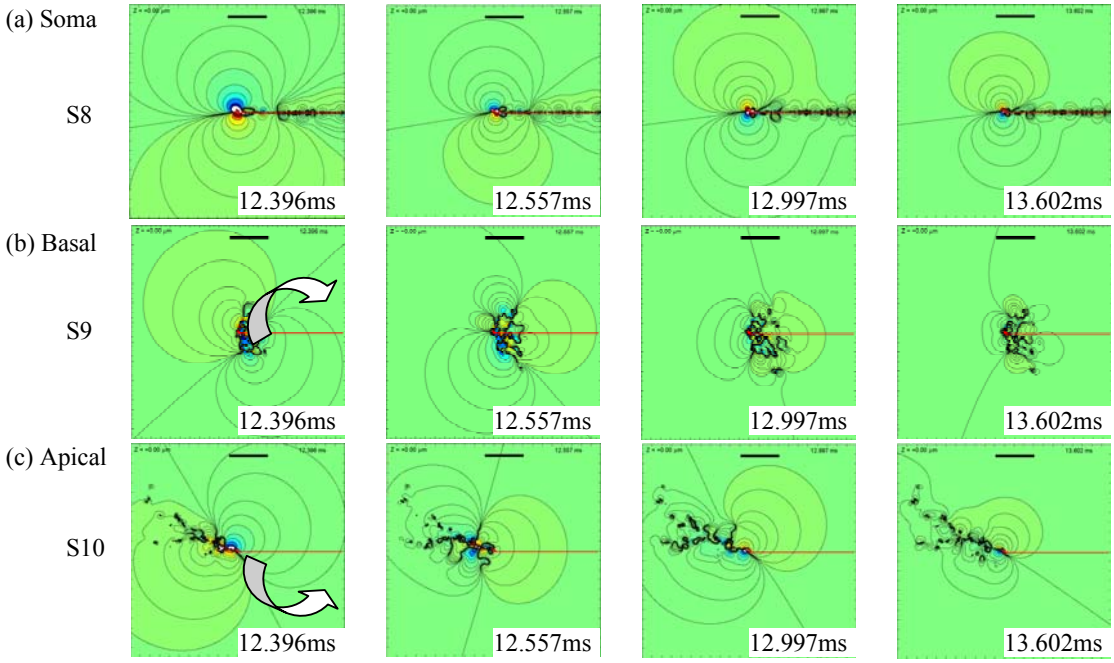

Figure 7-7 Test 4 results. The Test 3 field system for $z = 0$ is decomposed into three compartment regions (a) soma/axon, (b) basal dendrites and (c) apical dendrites. The scale bar is 200µm. Colour scale as per Figure 7-6.

Figure 7-7(a) shows the field of the soma and axon compartments. Figure 7-7(b) shows the field of the basal dendrite system. Figure 7-7(c) shows the field of the apical dendrite system. The soma/axon compartment structure (compartments 1-17) is superimposed in red (it lies in the XY plane). The soma/axon field system rotates in the YZ plane (in/out of the page). The basal and apical field systems contra-rotate (directions given by the arrows) largely in the XY plane, but with trajectory including Z excursions into and out of the page. The contour densities reflect penetrations of this XY plane at z = 0 by the respective processes.

The decomposition in Test 4 indicates that temporally coherent dipole activity sums into temporally coherent dipole activity, providing a form of scale invariance. If one continues to divide the neuron into smaller subsets, the result is more dipoles until finally the individual filaments are reached. This is an expected property of the original vector equation (6.1), where the overall field system inherits the fundamental dipole-like character of the original active element: a current filament that originates a small LFP dipole. The test 4 result demonstrates that when the LFP is 3D-decomposed it will (a) continue to reveal dipole-like behaviours, and (b) have a time-course, at any particular point in space, that resembles the transmembrane current of the dominant nearby contributing channels, as per Test 3. For example, when near soma, the somatic LFP should resemble the transmembrane current time course. When dominated by synapses, the LFP should resemble the post-synaptic current time course. This generally aligns with previous computational results, e.g. (Holt and Koch 1999), and with empirical observation, e.g. (Gold, Girardin *et al.* 2009).

7.7 Test 5: Examine LFP sensitivity to channel position

To investigate sensitivity to ion channel position alone, the field system produced by the same number of current filaments (per compartment) as Test 3 is examined. The difference is that the new set of filaments is located differently on the compartment surface. Ten new sets of 19,066 randomly positioned filaments are generated using the random process used in test 3. Everything else is the same as Test 3. The same total transmembrane current acts identically throughout the cell, again divided equally between current filaments. For each set of filaments, the LFP in the XY plane at z = 0 μm is computed for t = 12.195ms and t = 12.501ms.

7.7.1 Test 5: The details of the final field pattern depend on the details of individual filament location

The results for the ten filament sets are shown in Figure 7-8, Figure 7-9, Figure 7-10 and Figure 7-11. The LFP is computed at times (a) 12.195ms and (b) 12.501ms for 10 different sets of randomly positioned filaments. It shows an XY slice through the LFP in the same circumstances as Test 3.

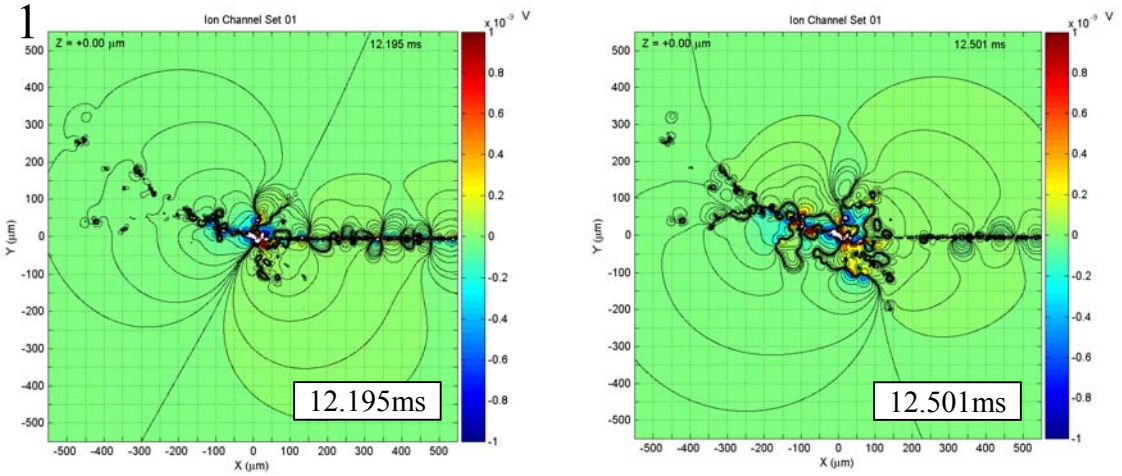

Figure 7-8 Test 5. Filament set 1. LFP variability with filament position. Colour scale as per Figure 7-6.

2

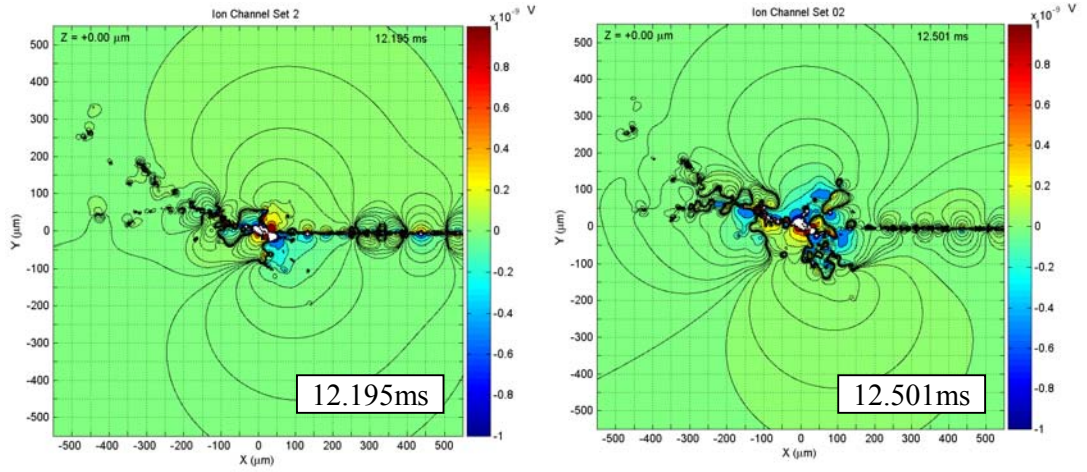

3

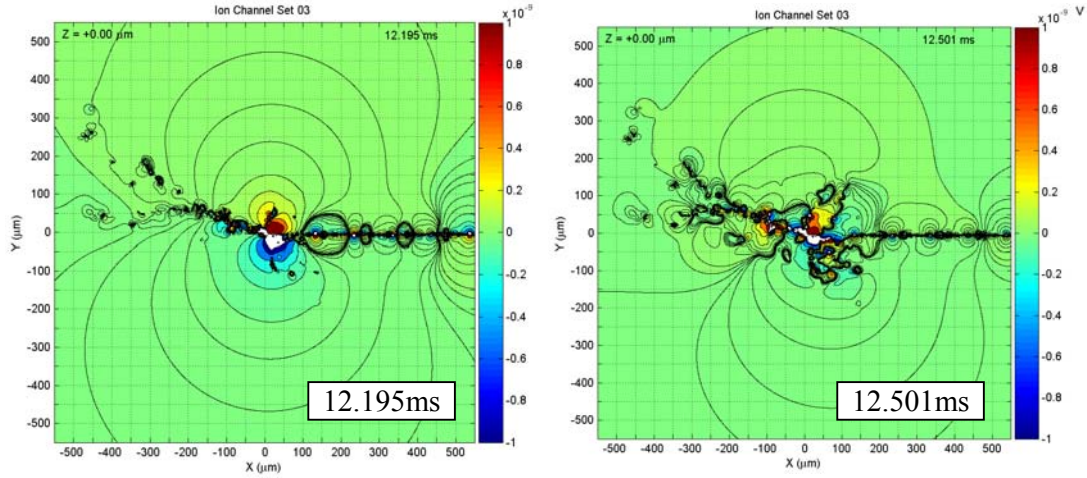

4

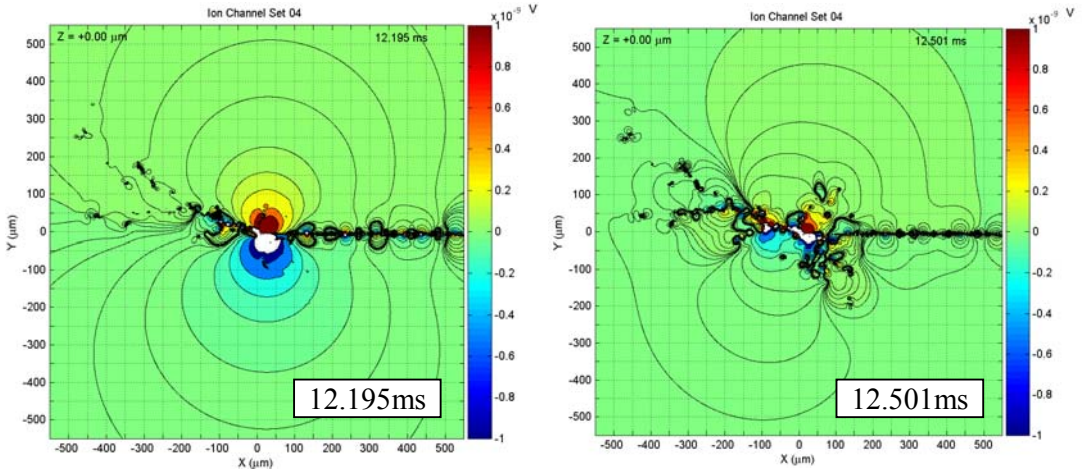

Figure 7-9 Test 5 results (cont.). Filament sets 2,3,4. LFP variability with filament position. Colour scale as per Figure 7-6.

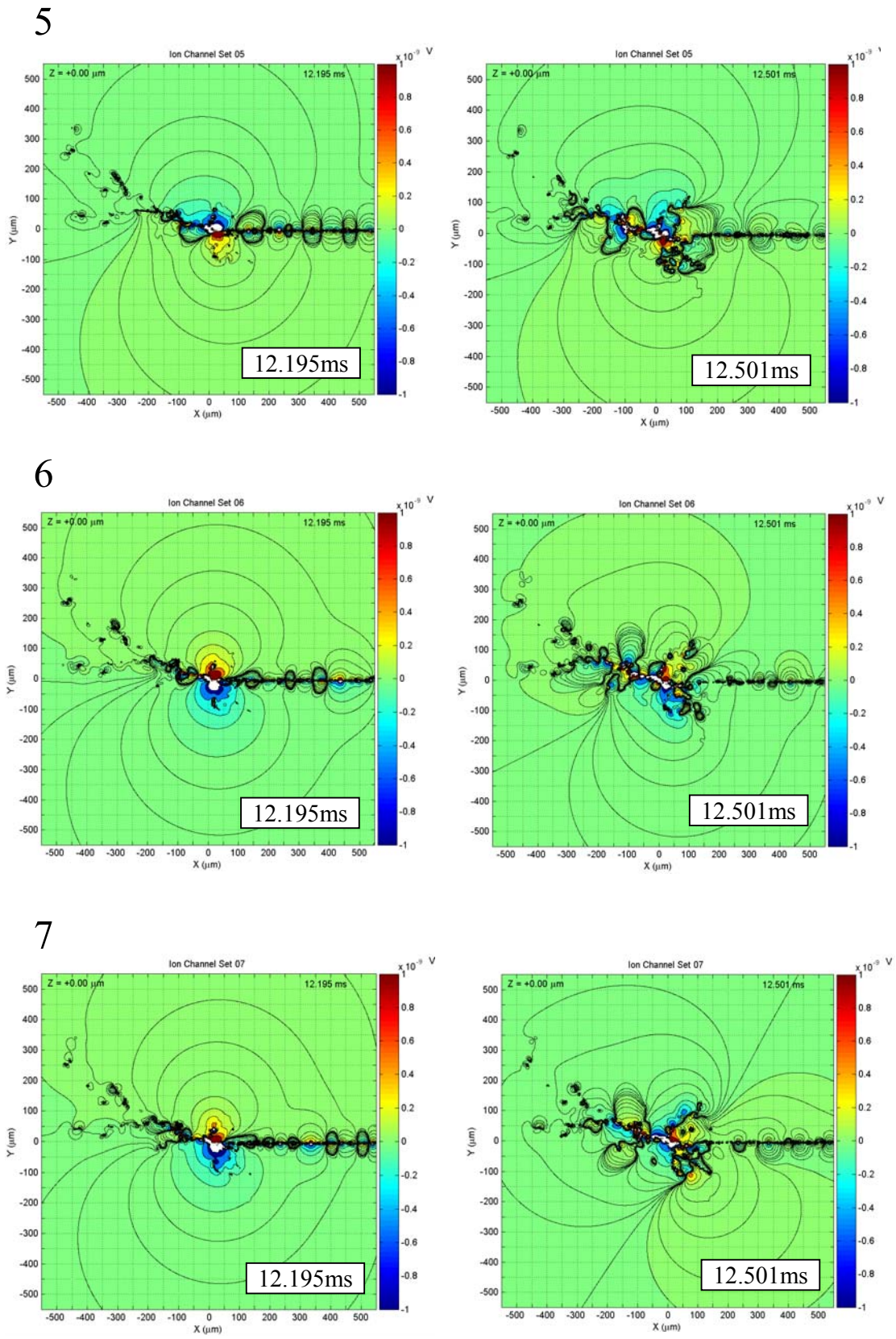

Figure 7-10 Test 5 results (cont.). Filament sets 5,6,7. LFP variability with filament position. Colour scale as per Figure 7-6.

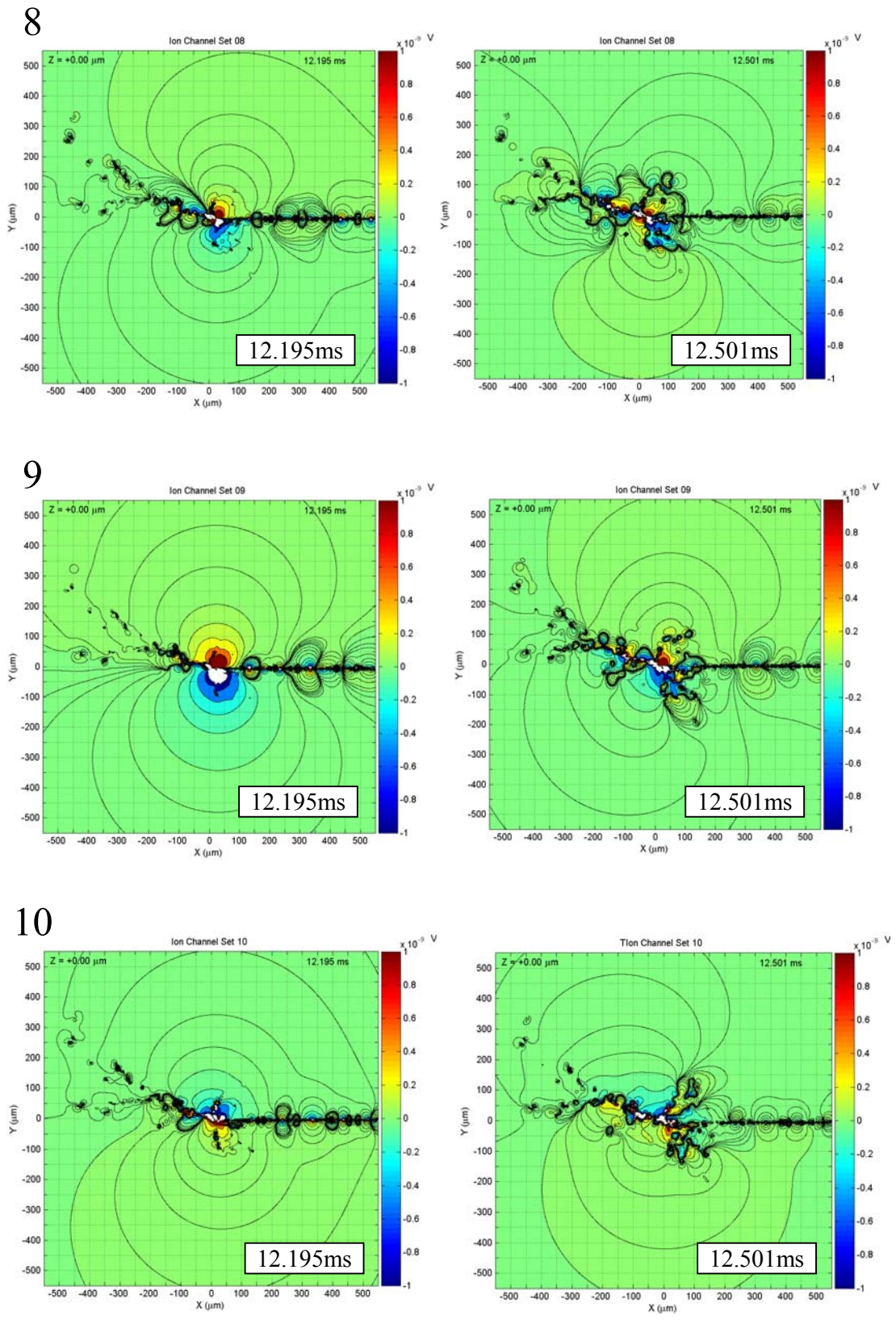

Figure 7-11 Test 5 results. Filament sets 8,9,10. LFP variability with filament position. Colour scale as per Figure 7-6.

7.7.2 The variability due to ion channel position.

To quantify the nature of the variability in the field expression that results from filament position, the coefficient of variation (*COV*) was computed for the magnitude of the electric field across 50 sets of filaments at 11 positions and at two times. The results are shown in Figure 7-12:

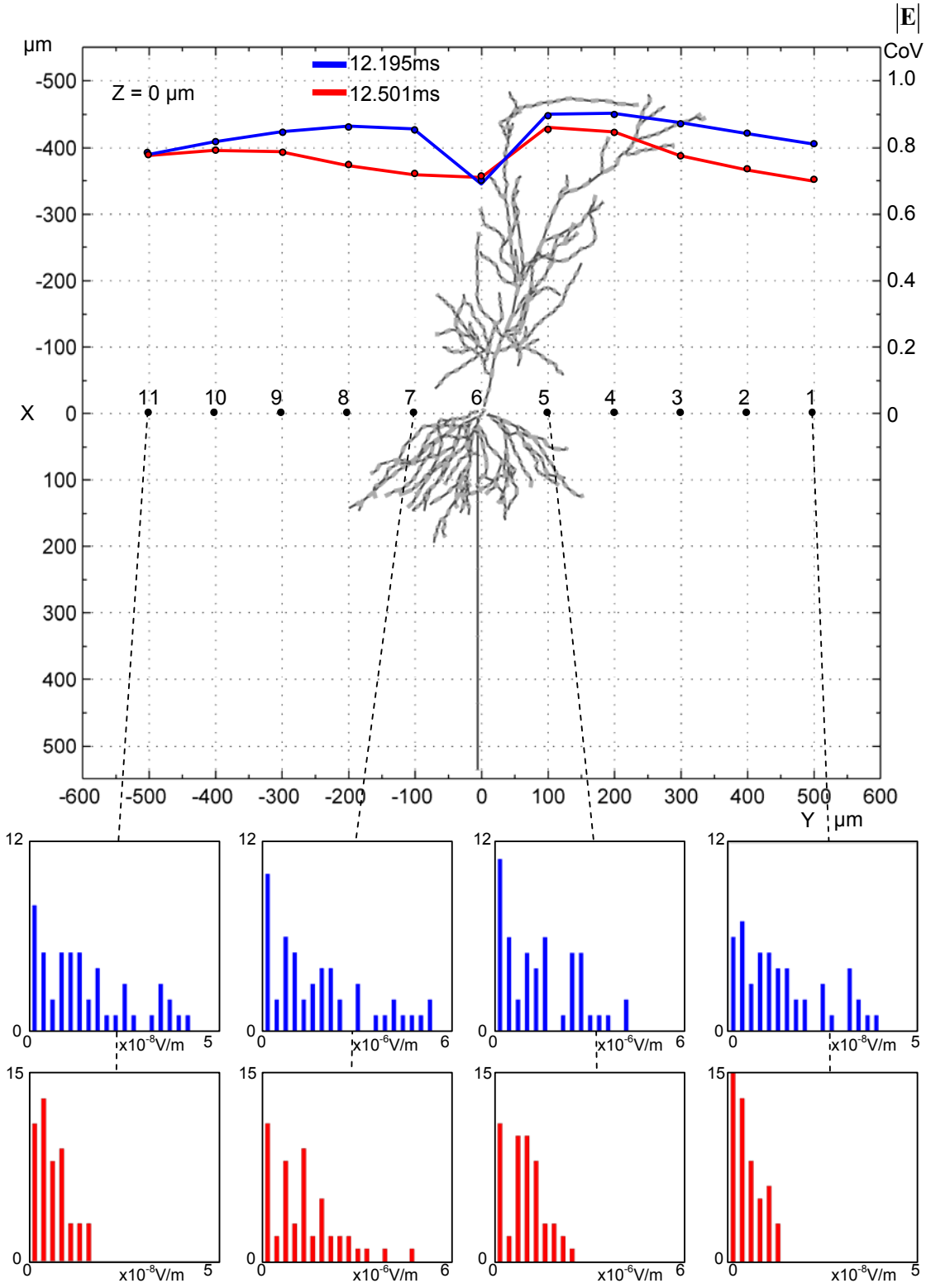

Figure 7-12 |E| variability due to filament (ion channel) position, quantified.

The *COV* (top) shows the variation across spatial position for the two times in the previous section 7.7.1 (Blue for time 12.195ms, red for time 12.501ms). The *COV* is computed using the ratio of the simple mean (μ) and standard deviation (σ) as per:

$$COV = \frac{\sigma}{\mu}, \tag{7.2}$$

where the mean and standard deviation are computed for |**E**|. The *COV* was computed for the *magnitude* of the electric field because the physical quantity is non-negative (a 'ratio measurement'). The resultant *COV* is therefore a valid statistic that understates the variability to the extent that it loses the directionality of the electric field vector. If there is significant variability in |**E**|, then there is some confidence that the **E** field variability is significantly greater than that revealed by the *COV*. The electric field was used because at any specific point in space, it is the ultimate determinant of the influences exerted at that point in space. To ensure the origin of the variability is confined to filament position, a collection of specific points in space were considered at specific times, as shown in Figure 7-12. Eleven positions were set along the y axis at z = x = 0, spanning 1mm in 100μm increments. A further 40 sets of 19066 filaments were created, making a total of N = 50 sets. The electric field was computed at the points of interest for the times shown above for all 50 sets. The variability at a specific point, at a specific time, can only be attributed to the change in position of the filaments on the surface of its host frustum. Any individual filament has only been moved within the surface of its host frustum. These are therefore highly localised, but globally applied filament movements creating variability at the spatial scale of the field expression of the whole neuron.

Figure 7-12 also shows representative 20-bin histograms of |**E**| for four of the eleven positions at the times depicted in the previous figures. The lack of obvious settled structure in the shape of the histograms is indicative of the kind of non-linear randomness at invoked by the filament positions. If N was greatly increased the distribution for the field **E** is predicted to approach Gaussian (with a mean of zero) due to the central limit theorem. Note that there is two orders of magnitude drop in the field intensity between points near the origin (soma region, 5 and 7) and points distal (y = ±500μm, 1 and 11). The *COV*, shown over the entire position range for the two times, is high and does not vary significantly with position. If position-related order was observed, then one might claim that host neuron structure dominates filament position. This is clearly not the case. The variation over the 50 sets of filaments is almost as big as the mean itself. Given that the field variation also has a directional aspect not included, the variability apparent in the LFP plots (for samples 1...10) is therefore quantitatively confirmed.

Figure 7-8, Figure 7-9, Figure 7-10 and Figure 7-11 demonstrate that the macroscopic collective electric field structure and time-course is hypersensitive to the specifics of current filament spatial distribution patterns. The images typify the kind of radical effect the channel locations have on the ultimate field pattern and its temporal progression. The result indicates that if a different filament set was used in Test 3, a different set of videos would have been generated. It is notable that all ten examples show a common spatial theme of a concentration of field around the soma, and a dynamic spatial dipole structure with variable levels of diffuseness and directionality. The most variable attribute of the field pattern is that the overall polarity and time-course of the field is radically altered by filament positioning.

Clearly, many different field patterns are consistent with one set of coordinated transmembrane compartmental currents. Therefore, the field patterns computed in Test 3 cannot be claimed to be the final/fixed field behaviour for the given cell morphology. It can be claimed that a particular field pattern will result from a particular filament set, but only knowledge of filament details at a specific time can determine the final field pattern at that time. This supports an expectation that, in real cells, ion channel locations and densities can be expected to result in a specific field pattern. However, without detailed ion channel data, the specific pattern cannot be predicted. This flexibility in the field expression can be interpreted as a novel degree of configuration freedom in neurons. The literature presents evidence of regularity in the ion channel type and density distributions. This general information from multiple neuron types was actually used to construct the D151 model. Neurons clearly have the capability to self-configure ion channel type composition and densities in a way that is

to some extent predictable. Test 5 therefore tells us that having adopted a particular configuration, the field system will become generally predictable using the method presented here or a more accurate future development of it. The obvious question is one that asks how the field influences (from self and other neurons) involve themselves in bringing about the final stable ion channel configuration, and how dynamic that configuration might be during normal and pathological brain activity. The obvious suggestion for the physical mechanism, the Lorentz force, has already been raised in chapter 1. Exactly where and when this force may involve itself in ion channel establishment and dynamics remains to be seen and is beyond the scope of this work. The obvious possibility is lateral motion of ion channels in the plane of the membrane.

7.8 Test 6: Examine LFP sensitivity to cell morphology

To isolate the LFP dependency on cell morphology, a small subset of the wild-type soma/basal compartments is extracted and remodelled into a simplified artificial neuron. An arbitrarily chosen single entire branch of a basal dendrite is extracted and pulled straight while keeping the compartment diameters and lengths the same. The dendrite temporal dynamics is a function of the compartment lengths and diameter. Therefore, if the lengths and diameters are maintained, when filaments are installed in the straightened dendrite, the field production will be maximally realistic. To better see how the straightening process works, consider the following generic representation of the D151 neuron geometry data:

x_1	y_1	z_1	d_1	arc_1	x_2	y_2	z_2	d_2	arc_2
etc	→								
x_{n1}	y_{n1}	z_{n1}	d_{n1}	arc_n	x_{n2}	y_{n2}	z_{n2}	d_{n2}	arc_{n+1}
x_{n2}	y_{n2}	z_{n2}	d_{n2}	arc_{n+1}	$x_{(n+1)2}$	$y_{(n+1)2}$	$z_{(n+1)n2}$	$d_{(n+1)2}$	arc_{n+2}
etc	→								

Table 7-2 EAPS package 3D data storage format.

Table 7-2 relates to Figure 7-13(a). The table defines two contiguous frusta, *n* and *n+1*. Each row entry in the table specifies a complete frustum. For example, in the case of the D151 neuron there are 1128 rows in the table. Because of the table structure, there is some redundant data. The vector (x_{n1}, y_{n1}, z_{n1}) and (x_{n1}, y_{n1}, z_{n1}) entries specify the absolute position of the frustum end centre points. The values d_1 and d_2 are the frustum end radii, resp. The values arc_1 and arc_2 are the arc lengths (produced by the NEURON function `arc3d( )`) for the Figure 7-13(a) vectors for the two ends of the frustum. The end points, radius and arc length for frustum *n* become the starting values for frustum (*n+1*). The height h_n of frustum *n* is computed from the end point vectors $\boldsymbol{d}_{n1}$ and $\boldsymbol{d}_{n2}$ as shown in Figure 7-13(a). To straighten out the sequence of frusta, the height of every frustum is calculated and, based on an initial position for the first frustum in the sequence, the end of each frustum is recalculated based on simply computing the end of the frustum in the same direction as the first (reference) frustum. The absolute entries are then simply installed into the table and copied appropriately. See Figure 6-10 for further information about the arc length concept.

Manual inspection isolated an appropriate dendrite, which was non-consecutively stored in the D151 3D data table. Compartments 1…7 comprise the soma(5), hillock(1) and initial segment(1). These are the compartments rotated, as a group, in each version of the test. The original dendrite is comprised of 46 D151 compartments straightened according to the above procedure. The dendrite was straightened in such a way as to keep the first frustum (72) end at its original location, then direct each frustum in the $z = 0$ plane at an angle of 45 degrees to the x-axis. The dendrite structure is then mirrored in the YZ plane, producing a second dendrite in the XY plane. The entire structure therefore has [7+46+46=99] frusta. The result is shown in Figure 7-13.

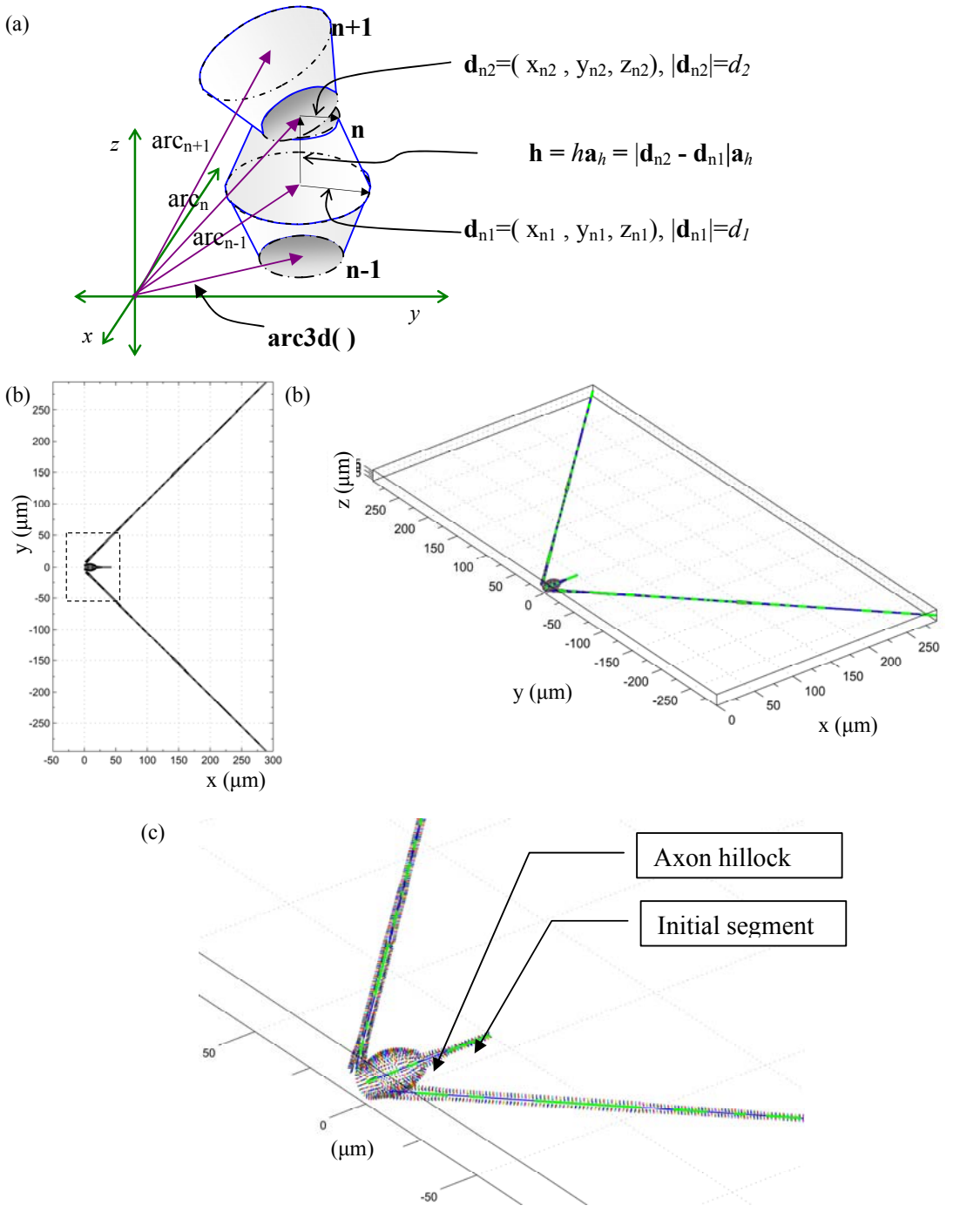

Figure 7-13 (a) EAPS package 3D frustum data storage concept. (b) The artificial neuron morphology and filament mesh for the first of the three test variations. In (b) and (c) the frustum centrelines are coloured so that the individual frusta are visible. The dotted box in (a) shows the location of zoomed views in Figure 7-14.

The compartments were then populated with a variable number of ion channels in a regular array of longitudinal 'stripes' of filaments spaced with a pitch of 1µm spacing. This creates rings of ion channels. The variability in channels is accounted for by the length to (average) diameter ratio. The smaller the length/diameter ratio, the larger the number of filament stripes along the length of the compartment, with a minimum of four. This assured field expression is symmetrical around the frustum circumference and resulted in a total of 4068 ion channels. Their allocation, on a per-compartment basis, is included in Appendix C along with the details of the striped layout scheme.

Following population with this uniform filament mesh, the structure is driven by the appropriate original D151 compartments currents. Holding the filament population size and spatial distribution constant, the resultant field system is computed for three different soma orientations covering a rotation of 180 degrees. This was achieved by regenerating the frustum geometry data for frusta 1…7 using a slightly modified version of the dendrite straightening technique. Notice that in (b) and (c) the soma rotation has resulted in the collocation of soma and dendrite processes. This is of no practical concern because the filament sets operate in a uniform conductivity and their fields superpose in a manner identical to all other field systems presented here. This colocalisation was always possible; it simply has not been encountered until now. While being physically unrealistic, it is simpler this way. The dendrite positions were kept identical to ensure (b) and (c) uniqueness is entirely confined to soma rotation.

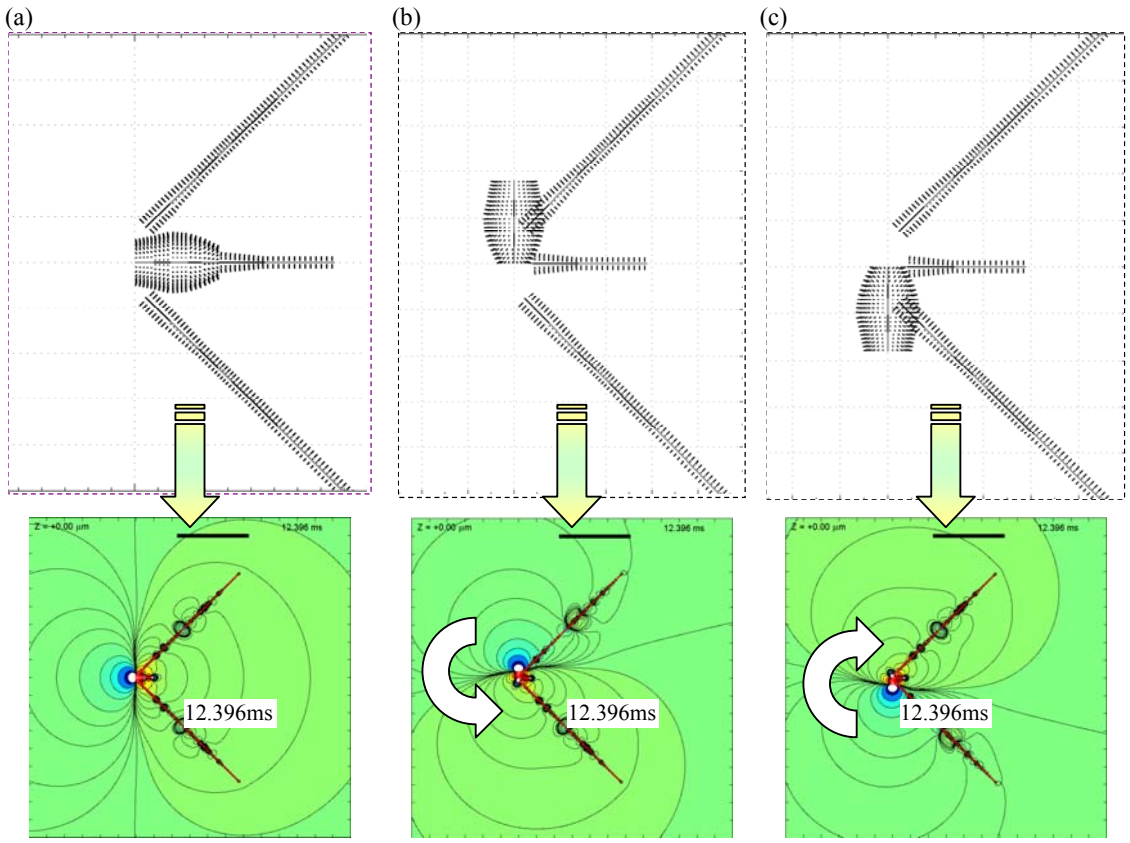

Figure 7-14 LFP variability with cell morphology. (a) Video S11. (b) Video S12. (c) Video S13. Scale bar is 200µm. Colour scale as per Figure 7-6.

7.8.1 RESULT: Identical filament sets moved by cell morphological shift create changes in the field expression

Figure 7-14(a), (b), (c) are snapshots of the field system at spatial slice $z = 0$ produced by the two-dendrite artificial neuron at $t = 12.396$ms. The circumstances of Figure 7-14(b) and (c) are identical in all respects to (a) except that in (b) the soma is rotated 90 degrees counterclockwise around the left end base centreline and in (c) the soma is rotated 90 degrees clockwise around the left end base centreline. A video for each soma position is provided in supplementary S11, S12 and S13. Soma rotation results in the reorientation of the plane of rotation of the field pattern from the ZX plane to the XY plane and can result in a reversal of rotation direction in the XY plane. The arrows indicate that (b) and (c) field patterns rotate in the XY plane. No arrow is included in (a) because it rotates in the YZ plane. Because of the circumstances, the differences in behaviour can only result from the alteration of the spatial relationship between the soma and its dendrites.

In this test it is revealed that fixed filament locations on a compartment can still express radically different field systems dependent on the dimensions and relative locations of whole compartments.

The temporal relationships between the progression of the currents result in electric field superposition that can have very different results. This tells us that even if ion channel types and densities were rigidly elaborated on the membrane, the field structure is still radically dependent on the shape of the membrane. Cell morphology is therefore as much a determinant of the field detail as ion channel deployment.

7.9 Test 7: Examine how LFP behaviour relates to basal dendrite proliferation

Using the same technique as Test 6, the artificial neuron (Figure 7-15(a), blue) dendrite was copied another 10 times. Each new dendrite was located and oriented to form a symmetrical skirt as shown in Figure 7-15(b) (black). When viewed at close range from the direction of the axon initial segment, the full filament structure becomes evident as shown inFigure 7-15(c). The experimental control is the 2-dendrite system explored in Test 6. In this test the LFP of the 2-dendrite system is compared with that of the the 12-dendrite system. The LFP comparison is between two points on the X axis in the XY plane, ■(-300,0,0) and □(300,0,0), equidistant from the origin, are contrasted. Measurements of the time-course at these points can reveal how the intensity is affected and how the effect extends in time. The dendrites are identically driven by the same compartmental currents throughout the structure. With the presence of a much larger filament set in space, the overall LFP magnitude is expected to be greater at all points in space. In addition, the proliferation of dendrites in the positive half of the X axis should produce a field more biased in that direction.

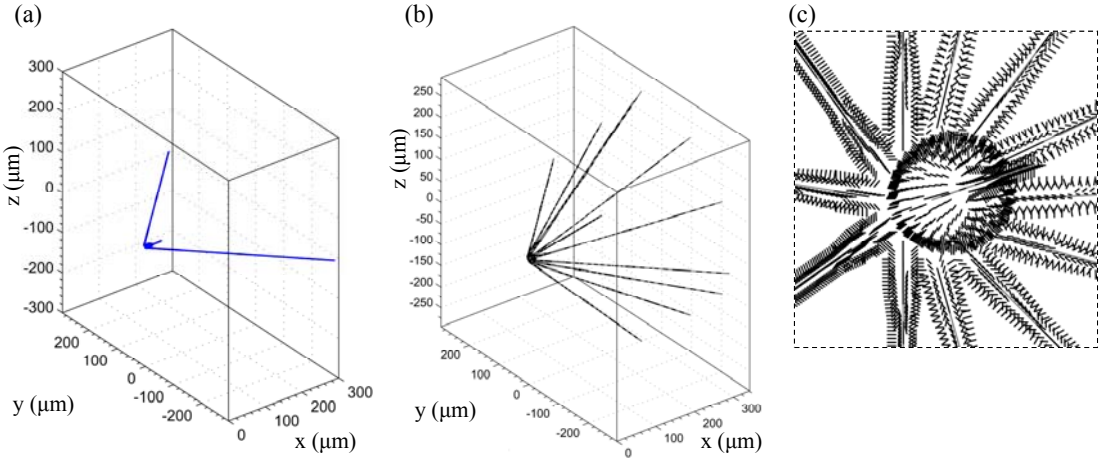

Figure 7-15 Proliferation of artificial dendrites from 2 to 12.

7.9.1 RESULT: Dendrite density operates to modulate field intensity and dynamics.

Figure 7-16 shows that the observed LFP at the two chosen points, ■(-300,0,0) and □(300,0,0), (**12-dendrite, 2-dendrite**) are rough inverses of each other. As predicted in chapter 2, the time progression of the LFP, at any point throughout space, inherits the basic properties of the original source volume current density. Therefore the actual time-course of the LFP voltage at any particular point resembles the transmembrane current, reflecting its various epochs. LFP waveforms like this are measured in practice. In Figure 7-16(F) and (G) clearly show that, at both positions ■ and □, the 12-dendrite system (black) produces a significantly higher magnitude LFP than the 2-dendrite system (blue) in both the initial reversal peak and the return overshoot peak. Figure 7-16 time (A) = 12.297ms is the initial peak, (B) = 12.613ms is the moment of polarity reversal, and the return overshoot peak is at time (C) = 12.941ms. The (B) reversal occurs at exactly the same time at both positions and in both dendrite structures. This makes it easy to see the increased dwell time at □(300,0,0), (E) for the 12-dendrite

structure compared to (D) for the 2-dendrite system. The LFP reaches the chosen threshold earlier and stays above that level longer.

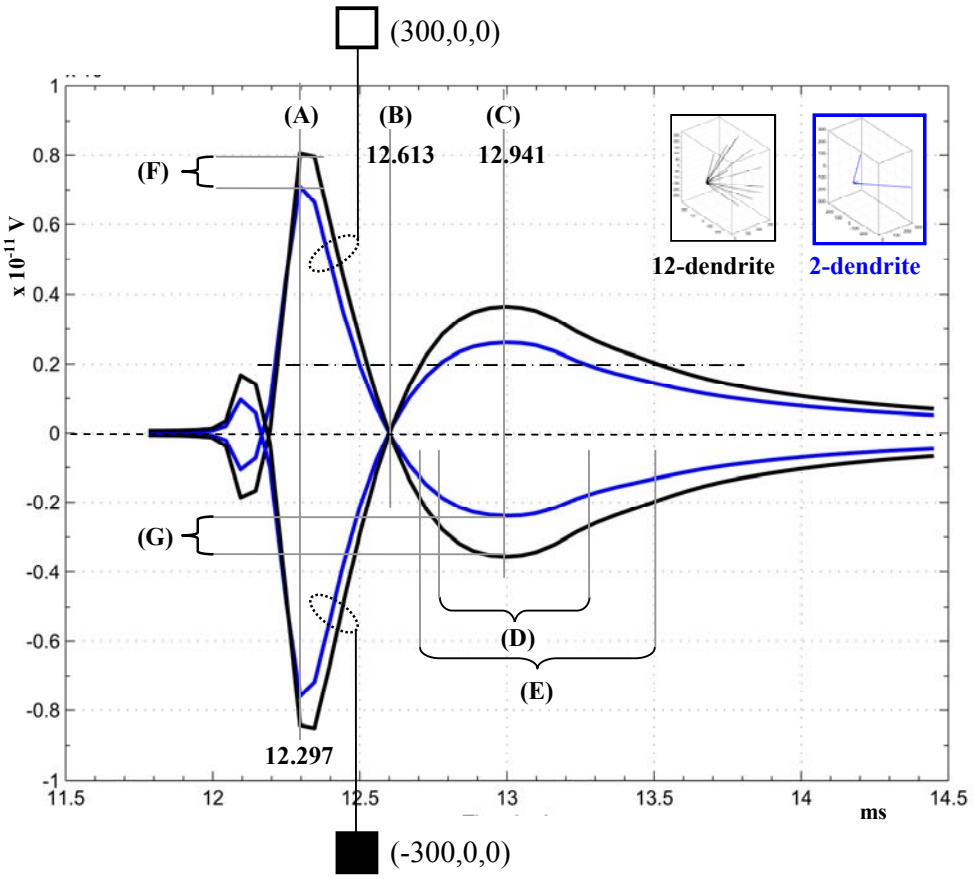

Figure 7-16 The LFP waveforms at points ■(-300,0,0) and □(300,0,0) are plotted over time. All else equal, extra dendrites increase LFP magnitude and dwell. [1]

Having noted the difference in LFP, it is interesting to see the actual spatial LFP structure, which is dipole-like as usual. This is shown in Figure 7-17 at the three times (A), (B) and (C) of Figure 7-16. It is possible to see the gross dipole reversals involved but, in comparing Figure 7-17(a) with Figure 7-17(b), it is slightly more difficult to see the difference in the LFP spatial patterns. The variability in LFP can be seen in the supplementary videos S14 (2-dendrite) and S15 (12-dendrite), where the iso-potential contours have been made explicit.

By inspection of the iso-potential contours in Figure 7-17, that the spatial distribution pattern of LFP, for the 12-dendrite and 2-dendrite, can vary quite markedly at the three specific times (A), (B) and (C). That variability is not obvious by inspection of Figure 7-16. This is important in understanding the extent of spatial and temporal variation in the electric field, which is not apparent in LFP plots. The electric field is proportional to the spatial gradient of the LFP. As it stands, test 7 supports a claim that dendrite number and morphology can reveal the in-principle potential for field structure modulation of proximal neurons and astrocytes. Test 7 also reveals that the modulation can be enhanced/degraded by the targeted involvement of greater/fewer dendrite processes, respectively. Without detailed examination of the electric field, the physical extent of the modulation cannot be addressed directly by test 7.

[1] NICTA Lab book 193 Test 0091, Test 0095; Lab book 196 Test 0100

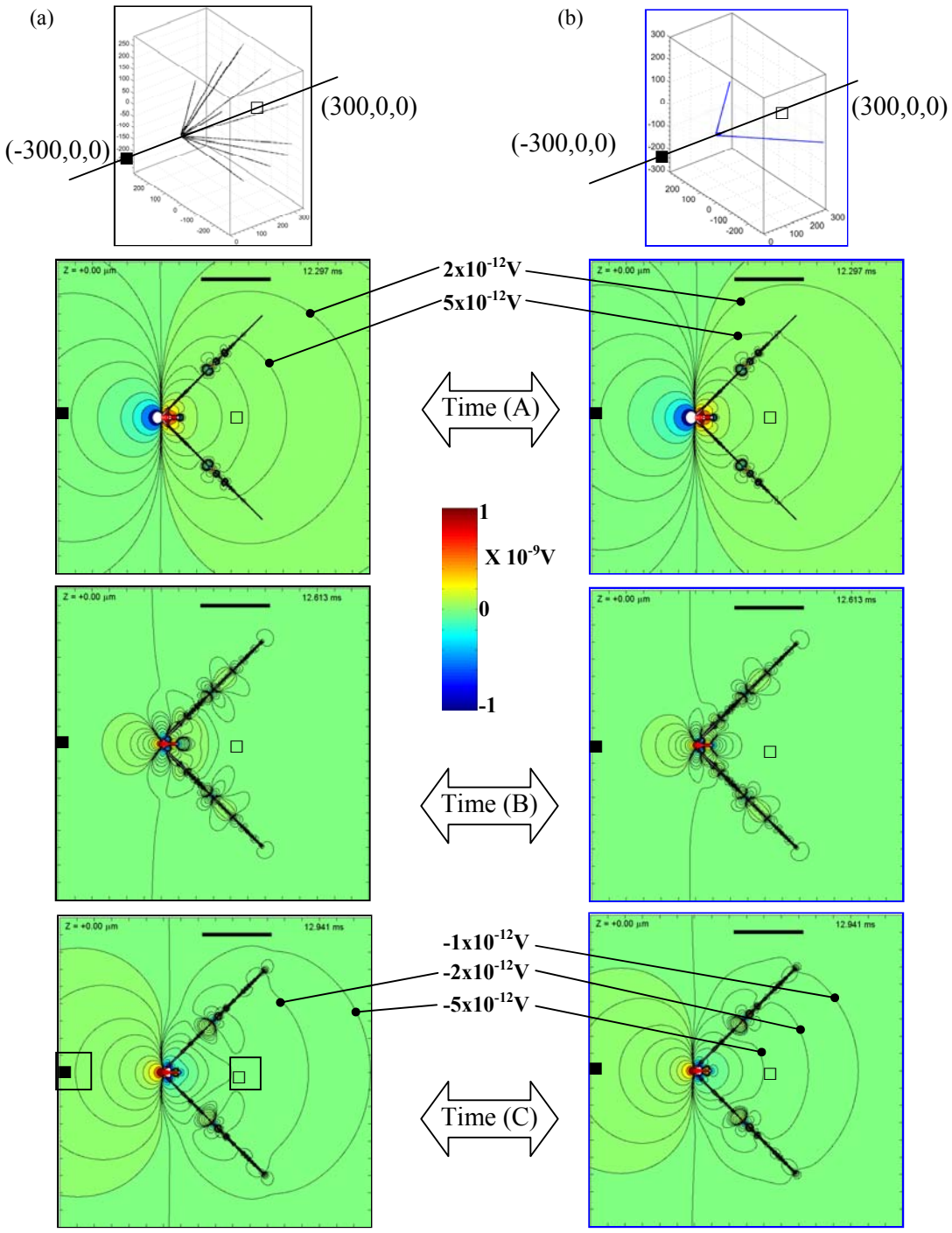

Figure 7-17 (a) 12-Dendrite (Video S15) spatiotemporal LFP progression compared to the (b) 2-Dendrite (Video S14) spatiotemporal progression. The time points (A), (B) and (C) are shown in Figure 7-16. Scale bar is 200µm.

7.10 Test 8: Electric field visualisation

The visualisation of the LFP has been relatively simple because it is a scalar quantity. The visualisation of the electric field is made more complex because it is a vector field. In addition, the computational processes that produced the LFP only produced the LFP in a plane. The appropriate equation for the electric field, equation (2.12), is

$$\mathbf{e}(\mathbf{r},t) = -\nabla\phi(\mathbf{r},t) - \frac{\partial \mathbf{a}(\mathbf{r},t)}{\partial t}. \tag{7.3}$$

In line with the volume conduction formalism, the magnetic vector potential term is regarded as vanishingly small. Therefore equation (7.3) becomes

$$\mathbf{e}(\mathbf{r},t) = -\nabla\phi(\mathbf{r},t) = -\left[\frac{\partial\phi(\mathbf{r},t)}{\partial x}\mathbf{a}_x + \frac{\partial\phi(\mathbf{r},t)}{\partial y}\mathbf{a}_y + \frac{\partial\phi(\mathbf{r},t)}{\partial z}\mathbf{a}_z\right], \tag{7.4}$$

Where $\mathbf{a}_x$, $\mathbf{a}_y$, $\mathbf{a}_z$ are unit vectors in the x,y and z directions respectively. Test 3 Figure 7-6 shows the XY plane representation of the LFP. As a result, the $\mathbf{a}_z$ contribution is not available because only the slice at Z = 0 was computed. The field magnitude and direction will be unrealistic to that extent. Nevertheless, it is revealing to use the Z=0 plane to get a rough representation of the field magnitude and direction. To be specific, the field system to be displayed in the following images and videos is

$$\mathbf{e}(\mathbf{r},t) = -\left[\frac{\partial\phi(\mathbf{r},t)}{\partial x}\mathbf{a}_x + \frac{\partial\phi(\mathbf{r},t)}{\partial y}\mathbf{a}_y + 0.0\mathbf{a}_z\right]. \tag{7.5}$$

7.10.1 RESULT: A dipolar electric field system of functionally relevant magnitude can be expected in tissue of appropriate neural and synapse density

The images have two components, the electric field magnitude (contour plot) and the electric field direction (quiver plot). Both are colour coded as shown in the figure legends. The electric field system has been plotted for the identical filament set and as per times shown in Figure 7-6. The two sets of images can therefore be directly correlated. In addition, a set of images has been supplied showing the electric field magnitude only and for the region within 75µm of the soma.

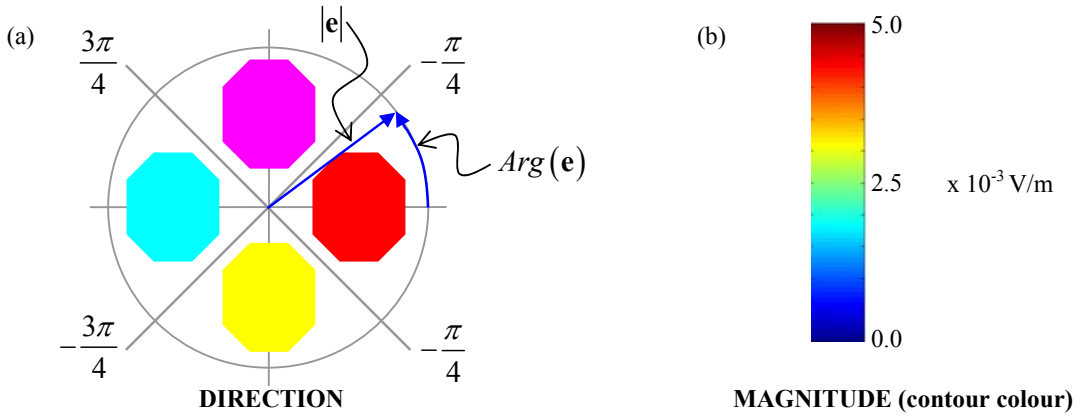

Figure 7-18 LEGEND. (a) Electric field direction vector angle. (b) Iso-electric field magnitude contour colour map.

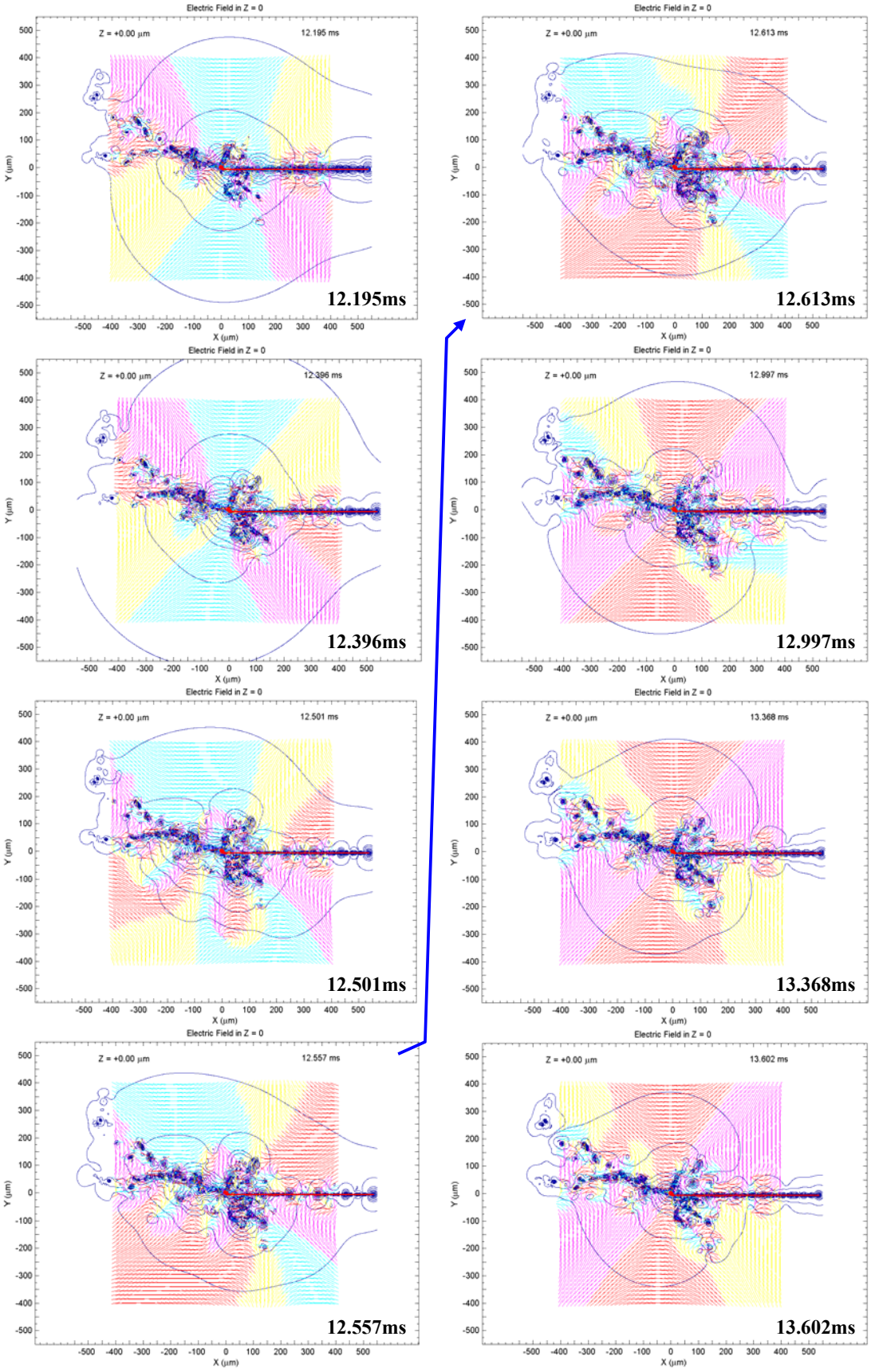

Figure 7-19 Test 8: Electric field components x and y for D151 under test 3 conditions (refer Figure 7-6 for LFP corresponding to this field).

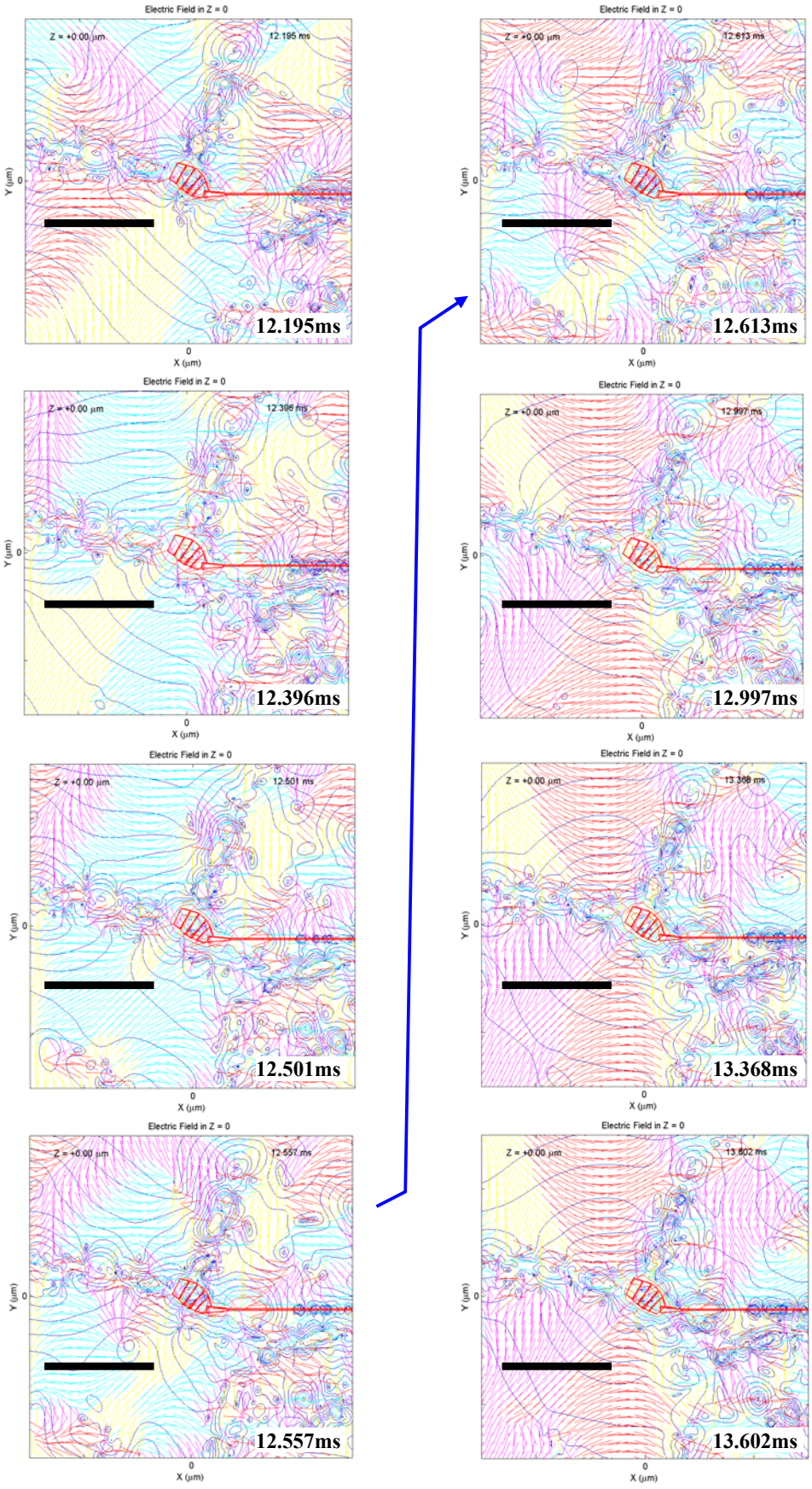

Figure 7-20 Test 8: ZOOM VIEW, electric field direction and magnitude Scale bar 50µm.

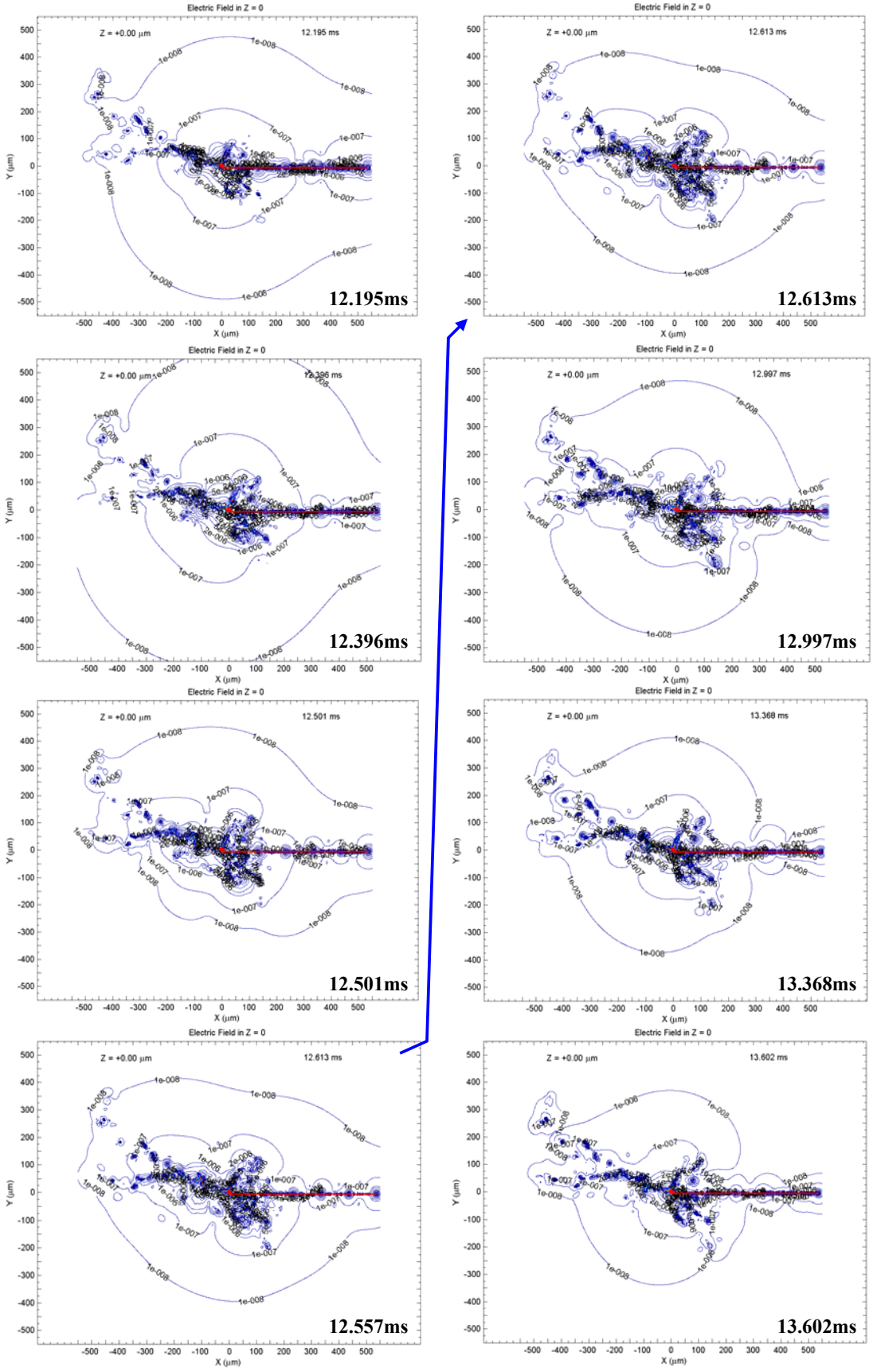

Figure 7-21 Test 8: WIDE VIEW, electric field magnitude contour only.

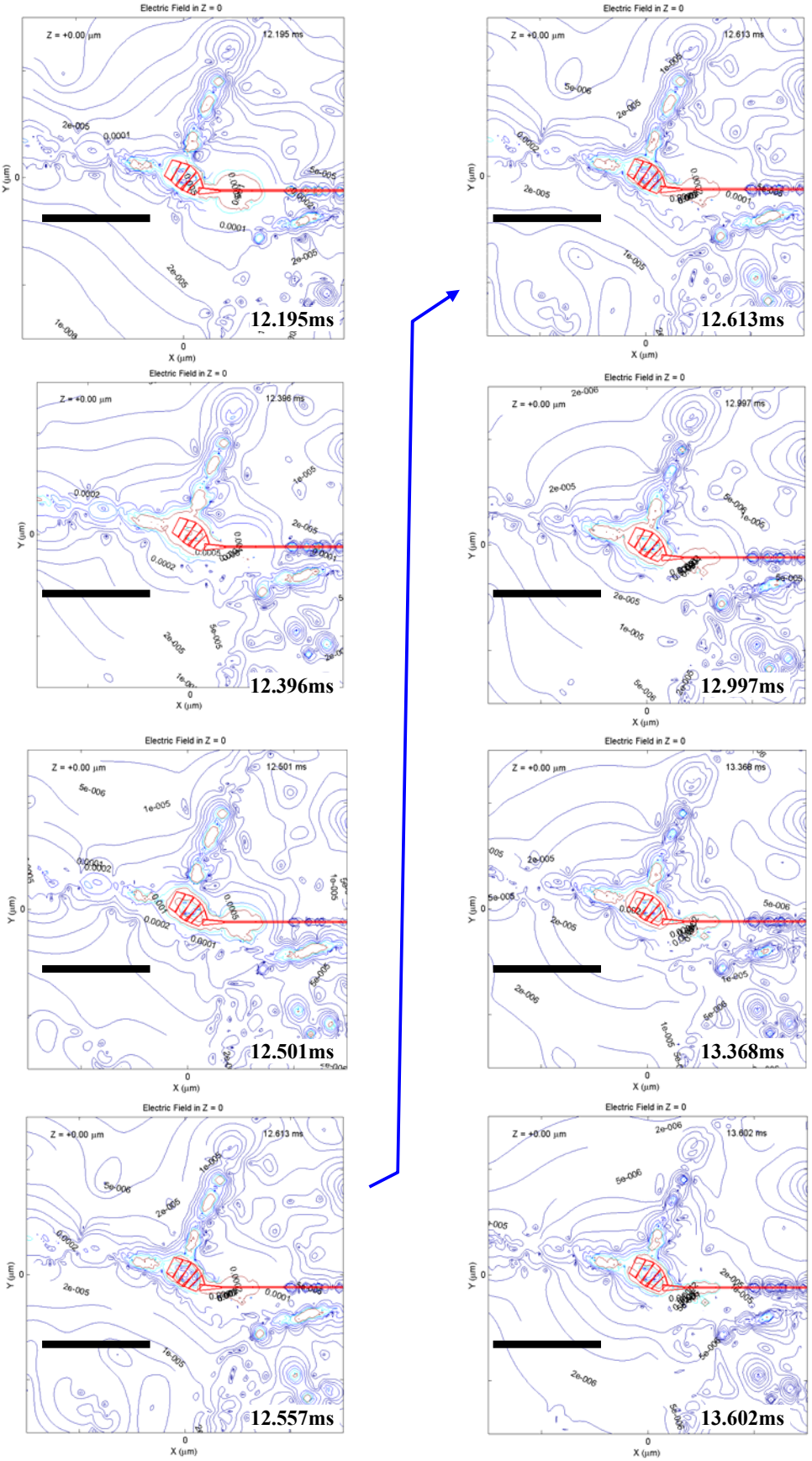

Figure 7-22 Test 7: ZOOM VIEW, Electric field magnitude only. Scale bar 50µm.

7.11 Supplementary Files

TEST	VIDEO (.AVI)	Nicta Lab Book/Experiment
TEST 1	S1,S2	196/0101
TEST 2	S3, S4,S5	181/0067
TEST 3	S6 S7	180/0044 193/0097
TEST 4	S8,S9,S10	180/0051,0048,0047
TEST 5	n/a (stills)	193/0087, 196/0103
TEST 6	S11,S12,S13	193/0091,0092,0093
TEST 7	S14,S15	193/0091/0095
TEST 8	n/a (stills)	196/0102

Table 7-3 List of supplementary information and experiment details.

7.12 Discussion

The above results deliver evidence in support of the chapter 1 hypotheses, although discussion of the extent to which the hypotheses are supported is deferred until the next chapter. Here the basic outcomes, context and their limitations are interpreted.

7.12.1 Results: Tests

Test 1 shows that the stereotypical progression of action potential current throughout the structure of a neuron will, depending on the particular structure of the neuron, result in a structured progression of virtual dipoles through space. This must happen to some extent because it derives from the dromic/antidromic travelling action potential waves of transmembrane potential reversals. Clearly, symmetry and asymmetry in the cell morphology will result in field system structure symmetry/asymmetry in the virtual dipole system. The 'breaking' of symmetry by cell morphology leads to more directionality and anisotropy in the field structure in the virtual dipole system. In addition, the physical form of the resultant fields will depend on the details of how the virtual dipole's currents are impressed on space as the overall current behaviour plays out. The essential ingredient in the progression is the coordination of currents. This coherence (causal interlocking) of currents in space can be seen as the important originating phenomenon.

To reveal the details of the establishment of a field system by the reality of current filament impression in space, in lieu of ion channel operation, test 2 showed how each filamentary current creates a small, symmetrical field system of its own with an intensity proportional the current magnitude. It is therefore expected that average ion channel behaviour will express this general kind of field system. At greater spatial scales, in aggregate, in their location along a compartmental boundary, the figure shows that the filaments construct a compartment shaped field system that will be temporally modulated according to the relative time-course of individual filament currents. As a result of the filament spatial disposition, the field system will be further modulated. A fixed spatial disposition of ion channels can be regarded as spatial field coherence that also modulate the collective field system, with its own unique character. In test 3 is a typical example of the LFP for the whole D151 cell produced by filamentary currents of an action potential progression. It revealed a large rotating dipole. Test 4 showed how the test 3 field system decomposes into morphologically similar subsets that aggregate to form the final dynamic dipole field system.

Test 5 shows that the specific spatiotemporal activity of the field is highly sensitive to the details of current filament location. However, the variability occurs within an overarching theme of a dynamic dipolar field expression. More or less structure in the final field system will result, depending on ion channel location and densities. Given that real neurons have stereotypical regional ion channel distributions that were actually used to specify the underlying compartmental transmembrane conductivities, it is reasonable to conclude that neurons naturally contrive to use whatever natural cueing systems (including EM field forces) to assemble, maintain and modulate the ion channel

locations, compositions and densities. The same kind of variability was also found in test 6, which showed how the same set of ion channels in exactly the same compartment locations, resulted in very different field dynamics based on compartment location/orientation. The movement of a compartment is, therefore, merely a more structured way of modulating whole sets of current filament locations. The difference is that the final result radically changes the overall dynamics, rather than merely modifying the details of a particular dynamical form.

Test 7 showed that a neuron can control the spatiotemporal expression of the field system by simply proliferating processes. Overall it is possible to conclude that, regardless of the mechanism by which the filament currents acquire their operational location, the particulars of an individual filament spatial disposition will result in a particular field pattern. The spatial disposition of filaments will depend on filament densities and spatial locations, which in turn depend on cell morphology. Only when the final disposition is known will the action-potential field pattern be fully specified.

Test 8 examined the electric field system as revealed by the gradient of the LFP, revealing the X/Y portion electric field system for the test 3 LFP. If the z component were added, the field magnitude would be greater – the field strength is therefore under-stated. The LFP and the corresponding electric field system depict a lobed rotating dipole, which projects a set of structured electric field 'arms' in space, creating a dynamic hill/valley system of forces that will impact the medium in a consistent directional manner. Local conditions can be expected to reflect the repeated action of such a field system. Test 8 used the *gradient* function in MATLAB, while recognizing that the result will be somewhat distorted. Once particularly curious problem is that the MATLAB *gradient* function introduces a negative sign, thereby completely inverting the field system. Nevertheless, the results have been documented as shown. Since assembly of this thesis, further work has constructed a closed form equation for the electric field. When a comparison is made between the gradient solution and the closed form solution for a single filament, significant differences appeared. There are more problems with the field determination than merely the missing Z component. It appears that the MATLAB algorithm has poor performance in regions of rapid change, making it more suited to simpler field system with low-order dynamics. This means that there are aspects of the graphical results that are, to some extent, misleading. In particular the electric field orthogonal to the filaments appears to be affected. Nevertheless, the results have been left as they appeared. As a general indicator of expectations of the overall field system structure, they are adequate. A more detailed exploration of the electric field is already under way, to be published as future work.

7.12.2 Results: overall interpretation

The results clearly demonstrate that a system of spatiotemporally coherent filamentary currents can produce a large, structured, unified field system that inherits a structural dipolar nature from the filaments and dynamics from the spatiotemporal coordination of currents. The filamentary currents, as proxies for ion channels, inform us of the likely nature of the field system. The overall outcome is that filamentary current-based field systems inherit structure based on both temporal coherence in filament current and spatial coherence based on filament location. If you degrade either of these attributes, then the field system will randomize to the extent of the degradation. For example, if the currents had no structured average, but varied randomly, then the field system would turn to temporal noise. If the spatial location of the current were randomised (such as in simple convection in an electrolyte) then the field system would turn to spatial noise. In this way it is reasonable to expect, that if there is structure in the endogenous EM field system, then it arises from the combined spatial and temporal coherence of ion channel currents. This means that the comparative randomisation of the ECS and ICS charge trajectories is likely to contribute field noise that will superimpose on the basic coherent field structure produced by ion channels.

7.12.3 Lack of synapse currents

The system of filamentary currents lacked those due to synapses. Given that the post-synaptic currents are directly causally antecedent to the action potential in a temporally coordinated way, it is expected that synapse currents will modify the structure of the field in systematic ways that will result, again, in

a single, unified dynamic dipolar electric field. The synapses will add to the overall magnitude of the electric field in ways yet to be determined.

7.12.4 The limitations of 'volume conduction'

As discussed in earlier chapters, the volume conduction formalism itself is an extreme abstraction that fails to capture many of the significant properties of the tissue. A properly constructed model would account for the material's syncytium form, its tortuous ECS, its native convective operation, and its charge density mosaic. If the volume conduction model was correct, then all the above LFP results would have been superimposed on the large, static, background potential profile/mosaic of the kind depicted in Figure 2-6. It is for this reason that the above LFP results can only claim to capture the 'dynamic component' of the total LFP. Claims can be made based on the above results, provided all interpretations are qualified to that extent.

7.12.5 Compartment artefacts

Real neurons are not compartmentalized. For example, the soma of the original D151 neuron was not divided neatly into slices with their own set of currents. In reality, as already discussed, the various current components potentially enact their role in different places through relatively sparsely located populations of ion channels. As a result of this, the presentation of the fields produced by a compartment and the presentation of the field of the original cell are likely to be different even though the overall current dynamics are the same. In the same way that compartment geometry introduced variability in the final fields through the relocation of ion channels, the very existence of compartments will affect the field pattern. A good example of a site of 'compartment artefact' can be seen in the Test 4 decomposition, which revealed a rotating dipole at the soma location due to soma and axon activity only. If the soma was symmetrical and had uniform channel densities, one would expect, on its own, a field pattern much more closely resembling a pulsing monopole. Because the soma is elongated with non-uniform ion channel positions and is associated with process compartments with their own geometry and currents, a rotating dipole was the result.

In the overall scheme of the simulation, compartment artefacts are no less or more distracting than the other kinds of variability explored here. Instead, compartment artefact presents a more fundamental problem for the exploration of accurate fields using only 1D cable-equation models. The implication of the eradication of compartmental artefacts is that the 1D cable equation system must be upgraded in a way that intrinsically retains the 3D structure and all the ion channel details discussed above. The final conclusions of this work must be tempered by this reality.

7.13 Chapter summary

This chapter revealed the results of a large computational study of the electric field system of a single firing neuron, but only for the contributions due to the action potential. It used a compartmental/cable-equation model currents to drive system of filamentary current sources as proxies for ion channel behaviour. Despite the primitive nature of the volume conduction formalism, it has been able to supply evidence in support of an expectation that ion-channels can express a spatially large, unified, regular and dynamic electric field system in space. It is reasonable to expect that the ECS and ICS currents, as causal descendents of the ion channel currents, will contribute only noise into the field system.

The revealed field system puts the neuron in contact with proximal cells (at roughly mm scales) in real tissue in (a) a *configurable* and (b) in a line-of-sight fashion. The existence of various artefacts and more fundamental limits on the volume conduction formalism, and the lack of synaptic currents suggest that the actual field system will be more intense than revealed so far. Nevertheless, the field system as revealed, in the context of thousands of synchronous proximal neurons, is within the practical bounds of expression of a significant field system that is, through the operation of the Lorentz force, functionally active.

7.14 Chapter bibliography

Dawkins, R., The Blind Watchmaker, Penguin, London, 2006, p. 340.

Gold, C., Girardin, C. C., Martin, K. A. C. and Koch, C. 'High-Amplitude Positive Spikes Recorded Extracellularly in Cat Visual Cortex', *Journal of Neurophysiology* vol. 102, no. 6, 2009. 3340-3351.

Hines, M. L. and Carnevale, N. T. 'The Neuron Simulation Environment', *Neural Computation* vol. 9, no. 6, 1997. 1179-1209.

Holt, G. R. and Koch, C. 'Electrical Interactions Via the Extracellular Potential near Cell Bodies', *Journal of Computational Neuroscience* vol. 6, no. 2, 1999. 169-184.

Chapter 8

DISCUSSION, CONCLUSIONS, IMPLICATIONS & FUTURE DIRECTIONS

> "*… the physicist Erwin Schrodinger pointed out the curious fact that the great theories of physics did not contain or address sensation or perception but simply assumed them.*"
>
> Gerald Edelman (Edelman 2006, p72) per (Schrödinger 1992)

8.1 Introduction

To complete the program of work, this chapter delivers an analysis of the extent to which Chapter 3 hypotheses H1 and H2 have been supported. There are a number of immediate practical implications and a collection of wider implications that are logically entailed by the underlying circumstances and a convergence of issues surrounding brain endogenous EM.

8.2 The Hypotheses

8.2.1 Hypothesis H1

Ion channel current coherence in a single neuron can project and direct a configurable, faint electric field system large enough to bathe itself and its local neural/astrocyte neighbours. **(8.1)**

Chapter 7 delivered multiple instances of the H1 phenomenon. It has been demonstrated that coherent current filaments created an extended electric field structure, projecting a field system over distances several orders of magnitude larger than the filament size. The essential ingredient: *coherence*, was built into the fabric of the volume conduction model that expressed the results. Coherent currents have been exclusively used. Figure 8-1 shows a typical example. With such a clear result, its future relevance will depend on the accuracy of the model and the field's causal efficacy in real tissue. In the matter of accuracy, the primary doubts arise in

(a) The extreme abstraction of uniform conduction and whether it over or understates the field magnitude.
(b) The absence of contributions from synapses (chemical and electrical).

(c) The assumption of only a noise contribution by ECS and ICS currents.
(d) Inaccuracy resulting from the use of undifferentiated current species applied in spatially unrealistic ways.
(e) The use of conduction in a convective medium.
(f) The use of Maxwell's macroscopic equations.

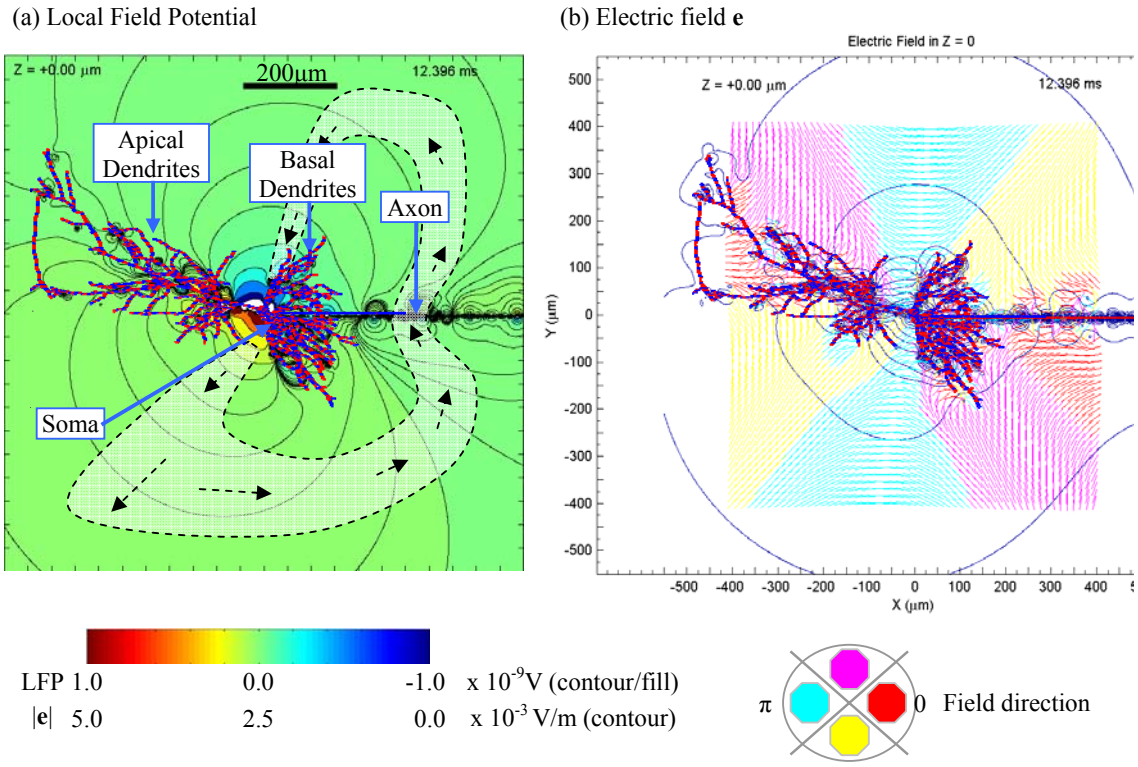

Figure 8-1 From Chapter 7, (a) test 3 and (b) test 7 show the LFP and electric field, respectively, at t = 12.396ms, z = 0mm. The faint but extensive, rotating dipole LFP is expressed by action potential-related transmembrane filamentary currents. The gradient of the LFP makes the LFP significant proximal to the neuron. In (a) the dashed arrows indicate XY portion of the field lobe-structure's path.

Assumption (a) has been used in multiple depictions of brain material for decades. To contest the result on this basis is to suddenly deny the usefulness of evidence it provides, when the same evidence has been found quite acceptable previously. The most recent version of claimed access to an LFP computation used the identical volume conduction equation (with a different source model, and ignoring the accuracy issue raised in Chapter 1) on the same model neuron (Milstein and Koch 2008). If the H1 outcome is to be held as invalid, then there is a large lineage of science outcomes that must also be found invalid. Volume conduction results in a severely simplified material model and this has been discussed at length and accepted, for now, in the research strategy. The historical usage of a model does not, in itself, make the model right. The model has simply been revealing enough, and this is all that is claimed here. The same argument applies to reasons (e) and (f).

The (c) neglect of ECS and ICS current contributions to the field system has been posited based on good physical reasons. The ECS and ICS currents, causally originating in the transmembrane ion channel current, are not the simple passage of a charge through a conductive medium. The charges originate and terminate in a vast collection of paramembrane charge. A reasonable mental picture of this activity is the ingress/egress of a ball from/to a drain in a huge shallow pool of identical balls. The subtle disturbance/rearrangements of all the balls in the pool is the final result, not a single ball trajectory. If ECS and ICS currents were included, the likely outcome is that the field system in Figure 8-1 would be 'fuzzy' with superimposed noise. Note that because the ion channel currents causally

originate both the ECS and ICS currents, there may be a temporal coherence aspect to the ECS and ICS currents (in the near vicinity of the pore ends) that actually *adds* to the field system structure. It is not a clear cut issue. An investigation of the extent and kind of interference in the overall pattern merits future attention. However, at this stage there is no compelling reason to use (c) to deny the H1 claim.

The 'bridging' form of the volume conduction equation has been used in full knowledge that it needs major rework if future field investigation are to approach numerical accuracy in real tissue models. The electric field system intensity, as revealed by this very limited model, has been shown to be within the bounds needed for a causal role in real tissue (1V/m, (Anastassiou, Perin *et al.* 2011)). Objection (d), that current composition and spatial location is unrealistic, cannot be claimed to invalidate H1. Because actual channel densities are highly inhomogeneous (Hille 2001), the deployment and co-location of decomposed current filaments into realistic collocated densities throughout a neural structure is likely to cause a more focused and differentiated beam system of even higher local magnitude. The randomization of the field contributions used in the generation of the main results will simply not apply. Objection (d) delivers no *a-priori* reason to defeat the H1 claim. It is the overall *spatiotemporal coherence* that is claimed to be the significant determinant of the field system. The particulars of the current types and their collocation do not impact the coherence aspect of the claim. This argument also applies to the other artefact(s) discussed in Chapter 7.

8.2.2 Hypothesis H2

The collective dynamics of excitable cell tissue based on neurons is more completely described as a two-axis mutual Action-potential-electromagnetic (AP/EM) resonance than the traditional single axis action potential (AP) description alone. **(8.2)**

Hypothesis H2 required an investigation of the potential for neurons, under the volume conduction assumptions, to express EM field behaviour with a degree of configuration freedom from the action potential (and synaptic activity) that generated it. Chapter 7 provided multiple mechanisms for this degree of freedom. First, the EM field of Figure 8-1 is shown to be hypersensitive to ion channel locations. In being thus sensitised, the dependency on channel type, numbers and densities is a further source of variability. At the most basic level we now know that if filamentary currents are located in different positions along the membrane, a different field system results for the identical set of overall transmembrane currents. Maintaining an identical set of ion channels (per compartment) and altering cell morphology (e.g. reorient a segment of the cell), again, a radically different field pattern can result. Chapter 7 also showed that proliferation or denuding of cell processes adds/subtracts structure (intensity and focus) to the field system. These behaviours resulted from the same set of transmembrane currents. In this way, every neuron has the extra degree of freedom required for hypothesis H2 to hold. The EM field has its own adaptability, a life that is, to some extent, independent of its axo-dendritic action-potential behaviour. As a result, many different line-of-sight EM causal affects are consistent with the same basic action potential (axo-dendritic) originating event. The obvious question is why the EM field spatiotemporal structure should take on any *particular* form and exactly what physical phenomena stabilizes it in that state.

The extra degree of independence between the action potential expression and the electric field expression suggests the 'axis' idea of H2, where are the two axes for which some degree of relative independence is claimed. While hypothesis H2 supports the *kind* of expected dynamics, what is not specified is the *degree* of the independence. The degree of independence is likely to be a function of the details of tissue type and composition that can be examined in future work. The historical view is that these two axes were in permanent lock-step, the specifics of which were regarded as relatively unimportant because the EM field was assumed to be causally inert. Under hypothesis H2 the two axes are less tightly coupled than previously thought. For example, the EM-axis could express structured fields in the medium merely through sub-threshold oscillations. No action potential need be involved.

In consideration of a causal role for the field system, in principle it is easy to see that localized line-of-sight membrane hyperpolarizations (inhibition) and depolarizations (excitation) may result from the

remote field system of nearby firing neurons. Simple application of the Lorentz force equation tells us that multiple superposed field system cancellation or reinforcement zones will experience different electromagnetic adaptation cues. If the combined EM field is chaotic then the local conditions will experience multiplicative noise. If the combined EM field is coherent then the local conditions will experience the impact of that superposition of influences. It is the nature of the transitioning between these two activity states that will determine the extent to which local adaptations are habituated.

For example, in the extracellular space, ions could be shifted systematically by persistent field conditions (perhaps generated by burst mode spike activity), thus modifying local ion stocks. This process suggests a possible involvement in synaptic plasticity, for example. It is well known that gap junction hemi-channels find their 'mate' on the apposed membrane by lateral diffusion in the plane of the membrane (Bennett and Zukin 2004). EM field-mediated translocation, in the plane of the membrane, of membrane-embedded molecules can be expected. It seems natural to expect that the EM field may be involved in transport guidance cuing for gap junctions and for ion channel disposition. In development, 'growth-cone' susceptibility to EM field cuing also seems a reasonable expectation. Such effects have been observed/used for many years in the experimental techniques of membrane electroporation, membrane composition modulation, cell division, cell migration and field-guided neurite growth (Bedlack, Wei *et al.* 1992, Hong and Nishiyama 2010, Maggio, Borioli *et al.* 2008, McCaig, Song *et al.* 2009). Cell density variations between hippocampus region involving ECS volume changes can result in extracellular conductivity changes of threefold to fivefold (Faber and Korn 1989). These and other field-mediated phenomena can be re-examined in light of the nature of the endogenous field system revealed by H1 and H2.

The upholding of H2 therefore adds an extra dimension of investigation of the details of the specific functional/causal roles enabled by the increased degree of freedom afforded by the EM-axis. The two axes, AP and EM, can be claimed to mutually resonate and thus modify each other. The former acts in a slow, tortuous trajectory along the membrane (membrane-longitudinal activity). The latter acts at the speed of light along a line-of-sight trajectory (membrane-transverse activity). In terms of general systems theory, the independent role of the EM field 'axis' is usefully viewed as that of a competing dynamic state attractor resulting from a cell's use of degeneracy in the EM field expression by ion channels.

8.2.3 Overview

The justified view of results H1 and H2 is that a plausible specific mechanism has been found where there previously was no specificity. What has not been supplied is proof that this specific mechanism is capable of requisite V/m field strengths needed to support a functional role in real tissue. However, given the inaccuracy of the volume conduction model, the lack of synapse contributions, the neglect of the $>10^6$MV/m transmembrane field throughout the material, the fact that with >50,000 synchronous neurons in a mm^3, and the fact that the mechanism also delivers the magnetic field, it is within the realms of possibility that the ion channel fields of the kind revealed by H1 and H2 could indeed be the originating mechanism for the endogenous fields. The final result is probably best couched a compelling justification for the continuation of the development of the model to future versions capable of more accurate and fully quantified field expression.

8.3 Practical consequential outcomes

The above outcome has a number important practical implications that will shape our attitudes to future research. These outcomes are already encoded implicitly in H1 and H2. They are made explicit so that the users of the results have some guidance.

8.3.1 The combination of spatial and temporal coherence causes the functionally relevant endogenous EM field.

The endogenous EM field system can be claimed to originate in the magnetostatics of brain tissue and, in particular, in the combined effects of spatial and temporal coherence of current density activity. As

discussed in Chapter 2, the term ‘coherence’, as applied to EM fields, is a relatively strong use of the word. In the context of EM fields, coherence is more than temporal synchrony. Coherence, in the deep sense of physics, corresponds to a new state (phase) of matter. Coherence of quantized electromagnetic field contributors literally results in an atom, for example. The idea of coherence as thermodynamic matter phase has been recognized in a neuroscience context for a very long time (Wright 2009). It is in this deeper and stronger sense of causality that this study suggests is more appropriate to a description of EM field-related coherence in brain function than the other terms (synchrony, resonance, oscillation, reciprocation and correlation). There may be multiple instances of synchrony between brain regions that have no actual causal basis, and hence cannot be called coherent in the stronger sense of EM field coherence.

8.3.2 The direct computation of the tissue-level ‘Local Field Potential’ is within reach.

Chapters 1-7 showed a plausible mechanism for the production of the ion-channel LFP component due to a single cell action potential. To extend this to the whole-tissue LFP is, in principle, straightforward although computationally onerous. The model must be upgraded to include the ion channel activity of synapses (chemical synapses alone, initially). With synapses appropriately driven, the combined set of ion channels will reveal the LFP produced by a single neuron. Taking the process further, the superimposed fields of multiple neurons in a suitably interconnected cohort can be computed. The cohort must be large enough to include (i) the ‘line of sight’ range of influence of a central neuron of interest, say neuron A, and (ii) the neurons surrounding neuron A must be interconnected and behaving normally. When these conditions are met, then the combined LFP around neuron A can be directly computed. If the model has been upgraded to include the adaptive effects then more realism can result. With a suitable spatial averaging ‘numerical probe’, the actual tissue LFP, as measured by a realistic probe in real tissue, can be computed.

8.3.3 The solution to the origins of the EEG and MEG signals is within reach.

Despite its various inaccuracies, the transmembrane filament volume conduction model supplies a clear, simple route to both the electric *and* magnetic fields. The electric field and the magnetic field originate in the same currents. As a result of the knowledge behind 8.3.1, in its future development and application to even larger spatial scales (than 8.3.2) involving networked populations of neurons (such as a cortical column), the origins of both the EEG and MEG signals, in principle, are directly computable. This becomes, in effect, the long sought solution to the ‘forward problem’ (Niedermeyer and da Silva 2005, Nunez and Srinivasan 2006).

8.3.4 The EM fields can no longer be claimed to be a parasitic epiphenomenon of axo-dendritic activity.

In the existing view, the EM field ‘axis’ has been parasitically coupled to the axo-dendritic axis (Frohlich and McCormick 2010). This renders the EM field functionally inert in the sense that to examine axo-dendritic function (synaptic connection dynamics) alone is to implicitly, indirectly examine brain electromagnetism. Put in specialist terms, this is the view that the EM field is merely an epiphenomenon of axo-dendritic coupling behaviour with no causal role. The explanation of EEG waveforms, for example, usually involves description of synaptic activity alone (Niedermeyer and da Silva 2005, Nunez and Srinivasan 2006). In the proposed new model, with mutually resonating EM and axo-dendritic axes, decoupled to some extent, the description of each axis becomes a separate exercise. Their coupling may be suited to purpose and tight or loose, depending tissue requirements and even vary based on moment to moment dynamics. Additionally, when EM fields get a life of their own, through the action of the Lorentz force, they can have line-of-sight causal consequences not described by axo-dendritic connectivity. This is fertile ground for a complex non-stationary system to evolve using excitable cells as a basic building block.

8.3.5 Describing the endogenous EM fields requires a 2-axis approach

A direct consequence of 8.3.4 is that in describing brain dynamics, it is no longer sufficient to use only neuron interconnection as a guiding principle. Both the tortuous network interconnections and the line-of-sight EM fields have a joint role in brain dynamics.

8.4 Future work

The thesis outcome suggests a number of productive avenues of investigation.

8.4.1 Synapses & single/multi-unit simulations

Computing the field system for a single synapse is an early and straightforward exercise. Only the post-synaptic current profile is needed. The D151 NEURON model does not include realistic synapse activity. However, artificial assemblies with user-generated levels of coherence may provide a useful starting point. The proper examination of the synaptic contribution cannot be assessed until small recurrent loops can be assembled with more than one neuron, and interacting naturally. Only then will relative synaptic timing become realistic. To get close to predicting the LFP, realistic multi-unit simulations need to be carried outEstablishing a fully quantitative LFP prediction requires the accurate 3D model of a neuron including all its synapses (ion channel densities and their spatial locations and orientations. Establishing a fully quantitative LFP prediction also requires that all ion channel densities involved in action potentials be accurately located in space. Establishing a fully quantitative LFP prediction also requires neuron interconnections and natural dynamics to be realistically expressed so that all the coherence effects involved in all contributing neurons can be realistically expressed. Exactly where will a boundary be drawn? This process will not be possible until our structural/anatomical techniques can reveal sufficient detail. Primitive artificial structures may be the only possible early targets of study, more involved in development of the computational technique than in claims of quantitative accuracy in LFP prediction. Once some confidence in the LFP has been acquired it is probable that we will have some clarity in how to use the results to begin predicting EEG and MEG signals.

8.4.2 Further examinations of field dependencies on ion channel details and cell morphological variability.

More work is required to elaborate the dependency of field expression on ion channel type, position, type spatial composition and individualised dynamics. In the chosen method, the currents have been artificially merged into a single transmembrane current. The filament metaphor needs to be reworked to separately express each current type. Ion channel densities throughout the neuron structure need to be provided. Once this aspect of realism is addressed, further exploration of artificial constructs should be amenable to the creation of more statistics than were offered in Chapter 7. At this early stage of development, such activities do not add anything to the major aims of the thesis and are deferred to ‘future work’. Cell morphology-related field variability will come along with future more detailed anatomical data (see 8.4.1). Certain cell primitives may be abstracted, such as an interneuron.

8.4.3 Inhomogeneous volume conduction

There is some merit in continuing to extract more realism from the volume conduction equations by constructing an inhomogeneous version. In that case, the conductivity can be partitioned into a syncytium-shaped media corresponding to neurons, astrocytes along with their ECS and ICS fluids.

8.4.4 Magnetic field

It is technically straightforward to construct an equation for the magnetic field. The same exploratory process can then be carried out for the magnetic field.

8.4.5 New microscopic convective field equations

Because of the complexity of the material and the limitations of macroscopic electromagnetism discussed in Chapter 2, it may prove more productive to construct a specialised set of microscopic electromagnetism equations tailored to the specialized needs of neuroscience. The material is so complex that, in the end, the traditional generic constitutive forms of Maxwell's equations are unlikely to be expressive enough to reveal the full detail of the tissue. In particular, there is a need to account for realistic electrodiffusion behaviour of dynamic, specialized ion populations located in ECS and ICS and in intracellular organelles. Such a set of equations will be able to get arbitrarily close to the real tissue without resorting entirely to molecular dynamics.

8.4.6 TORQUE/Source reconstruction

Computing the fields throughout a region due to thousands of filamentary currents is a computationally intensive task. For this reason some time was expended developing a metric that might extract, from the basic filament current and ion channel positions, a summary characteristic of the field as a whole. This has been done already, although it is unpublished and is not included here because it doesn't directly act to support the thesis hypotheses. The method computes the net torque vector. When appropriately selected, this vector tracks the direction and intensity of the lobe structure of the net field. It also decomposes in the way the field system decomposes into regional contributions. This metric will be evaluated further and published in due course. Once the synaptic contributions have been added to the field current sources, the torque metric offers a convenient tool for EEG (and, in future, MEG) source reconstruction research. Using the torque metric, a more spatiotemporally accurate collection of possible sources can be assembled. The torque metric may have to be assembled into, say, cortical-column-sized populations. This will provide accuracy with far less computational load and provide more physiologically justified sources.

8.4.7 Dual-axis tissue classification

The dual-axis-syncytium characterization will, over time, become more amenable as a means of classification of excitable cell tissue types by virtue of the extent of the involvement of one or both axes. Some basic groundwork directed at this goal is suggested. Operational contribution and relative dominance of the EM/Transverse vs. the AP/Longitudinal feedback mechanisms. For example, consider that in a sparse syncytium with fewer, highly interconnected (AP axis) neurons, the transverse EM-axis feedback will exert a lesser influence. Contrasts this with a collection of excitable cells that have no AP-axis longitudinal connections at all, when the EM-axis will dominate, but only if the cells are packed densely enough. An example of such a tissue is smooth muscle. If the syncytium has neurons that are morphologically asymmetric or otherwise electromagnetically polarized, the transverse axis will inherit some level of operational asymmetry. Such asymmetry has already been demonstrated in Chapter 7 and is exemplified in Figure 8-1. In specialised tissue such as the plexes of the gut wall (myenteric and submucosal), we find a hybrid layered structure. In these plexes, the active nervous syncytium is only a few cells thick and closely apposed to the longitudinal and transverse smooth muscle 'syncytia' (Furness 2005). In this way we can see that the recognition of a second feedback axis facilitates some kind of deeper, yet to be properly formalized, classification of excitable cell tissue types. It would be based on cell type, cell morphology, cell density, tissue asymmetry and cell asymmetry.

8.4.8 EM axis pathology

It is possible that some pathological nervous system conditions may been to be reclassified as dysfunctions of the EM-axis. One possibility is epilepsy. Electromagnetic coupling already has a significant but equivocal history in the epilepsy literature (Dudek, Yasumura *et al.* 1998). The results of this thesis may be able to be used to introduce more clarity in the area .

8.5 Discussion: Rethinking the endogenous EM field

H1 and H2 are now examined for their role in altering the process of scientifically describing the brain.

8.5.1 The neuron and its filamentary processes: an antenna system

Consider the situation of an implementation of an inorganic version of a filament-driven volume conductor using a lump of uniform but poor crystalline conductor embedded with nano-wires through which current can be pumped. To describe the material fields, the same volume conduction equation and the same results would be expected throughout the crystal. If an electrical engineer were informed about the similarity that the crystalline version has with the neural/astrocyte equivalent, they would be not be surprised that brain material is capable of the hypothesis H1 outcome. There is nothing special about biologically-organized electromagnetism because it is all ultimately generated by the same collection of atoms from the same periodic table of the elements. The only difference is that instead of ions, the crystalline version would use electrons/holes as charge carriers.

To an electrical engineer, the spatial 'lining up' (coherence) of ion channels along cell soma and processes, and their temporal 'lining up' (coherence), is consistent with *active phased array* antenna operation with multiple coordinated drive points (sets of compartment transmembrane currents). Such antennas can steer their lobe system in the same way we have seen D151 operate with the preferred directionality of its lobes. A remarkable feature of the D151 wild-type structure exhibits a basal/apical geometric balance to within about 5% of the soma (see Figure 6-9). That is, the vectorially added spatial extents (centrelines) of all apical and basal dendrites is almost balanced, centred on the cell soma. For an interpretation of the neuron structure as a combined send (basal) and receive (apical) antenna system, geometric balance is important from an energetics and coherence ('impedance matching') viewpoint. The aforementioned dipole wave front can easily be held responsible for phased array antenna behaviour. The specifics of any 'directed beam' produced by a neuron will depend on soma symmetry, dendrite proliferation and morphology, ion channel population composition and deployment and synapse orientation. Only more complete models will reveal the full beam system of a cell 'antenna' and its communication protocol with nearby receivers.

Note that the field system is not expected to radiate like a metallic conduction antenna. The field system is a result of magnetostatics and is not able to radiate in the sense usually attributed to broadcast antennae. In real neural tissue with endogenous fields of the kind revealed in the above results, there may be a very small, very short distance radiation at the most rapidly spatiotemporally varying regions of the field system. This phenomenon cannot be revealed by volume conduction formalisms, because the electromagnetism term needed to cause the radiative effects is simply not used. As a means to customize 'antenna' behaviour, neuron morphology seems well suited. The D151 neuron is asymmetrical in the manner of all pyramidal cells. More symmetrical neurons with diffuse dendrites (or even none) and/or ion channel population composition and deployment will have a more omni-directional and stable field system, probably of lesser magnitude (gain). Such neurons can be expected to have a lesser role in whatever impact the endogenous EM fields ultimately enact, than, say, pyramidal cells in the same locale. In this way, we can see that the antenna concept helps us understand how line-of-sight electromagnetic influences may act in addition to, and to some extent independent of, non-line-of-sight connectivity. Together they offer the prospect of forming a more complete picture of the way the tissue operates; one in which physical structure matters as much as connectivity.

8.5.2 The EM field system as an active 'backpropagation' mechanism

As previously noted, historically, the EM field has been portrayed as is purely epiphenomenal, that is, the field system is a parasitic by-product of excitable cell activity with no functional relevance. This thesis lends support to a more active role for excitable cell tissue endogenous EM phenomena. At the level of individual cells and sub-cellular regions, under appropriate levels of coherence, the EM field

can operate as an active feedback mechanism. That is, cell excitability can be modified in functionally important ways by a line-of-sight mechanism that is currently not in any excitable cell model. Furthermore, the same action potentials can cause radically different field behaviours by virtue of different ion channel deployments. This significant source of degrees of freedom means that the actual state of an active neuron can be far more degenerate (represent far more, in a cognitive sense, in terms of information content) than the action potential alone might indicate. This is not a new observation, but this thesis adds a level of novel support (Bullock 1997). Adding to this complexity is support for the claim that the EM field is actively involved in adaptation (learning) in ways that are currently not in excitable cell tissue models. From a revisit of Figure 1-1, consider Figure 8-2(a), which shows how the traditional 'epiphenomenal view' operates in the tissue. Contrast this with the recent revision Figure 8-2(b) by (Frohlich and McCormick 2010). As a result of H1 and H2, Figure 8-2(b) becomes the more technically precise Figure 8-2(c).

(a) Epiphenomenal view.

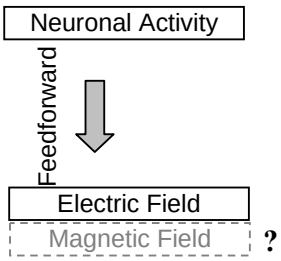

(b) The Frohlic & McCormick revision

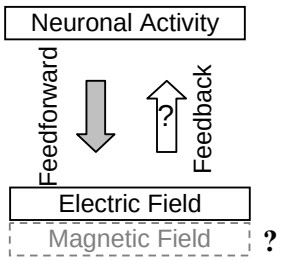

Based on (Frohlich and McCormick 2010), figure 1E.

(c) The suggested development.

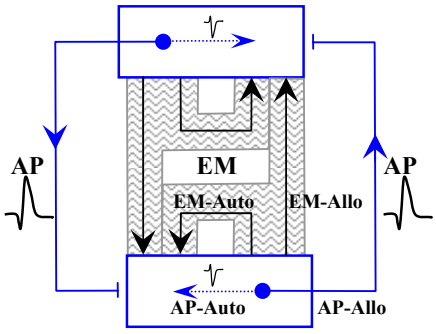

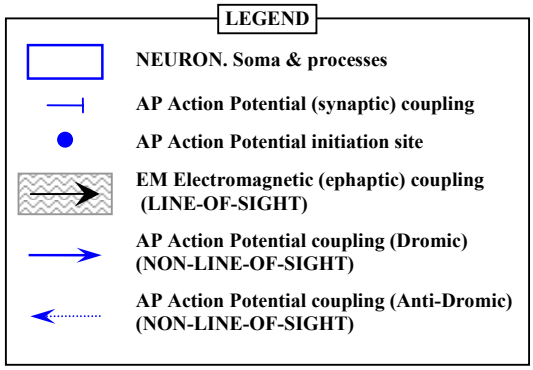

Figure 8-2 (a) Shows the traditional view where the electric field is an epiphenomenon and the magnetic field is essentially absent. In (b) we see the recent suggested upgrade in which the electric field has a causal role and the magnetic field continues to be ignored. (c) is a suggested more accurate upgrade The two-axis (AP and EM) back-propagation mechanism includes both electric and magnetic fields. A neuron is coupled to itself (AUTO) and a neighbour (ALLO) in two ways: A line-of-sight electromagnetic coupling and a non-line-of-sight (Action potential/synaptic) coupling. Their causal effect is mutual and symmetric.

Figure 8-2(c) recognizes the origins of the field system as being individual neurons that express the two axes (AP and EM) of H2 on themselves (auto-) and other neurons (allo-). Any given neuron need not have both EM and synaptic coupling. It can be either. The essential idea is one of coherent activity that reacts to and then modifies the superposed effects of all the neurons in a region (say a cortical column). Figure 8-3 shows a rough physical equivalent to Figure 8-2 along with the basic sequence of mutually resonating events as understood by considering the causal relations between activities. Based on the results of Chapter 7 and the ion-channel-centric physics basis for the fields at the level of a single neuron, Figure 8-2 can be detailed with specific links to the general kinds of adaptation the cues that would be expected to operate in a real tissue/syncytium context. This is documented in Figure 8-4, which shows the AP-axis (connectionist/recurrent loop) feedback system marked in red. Action potential current activity propagates in the membrane-longitudinal direction (simultaneously dromic

and antidromic), and, through that mechanism, involves itself in the neuron's self modification. The antidromic (as shown in Figure 7-2) part of the AP wave delivers AUTO-FEEDBACK. The dromic part of the AP delivers ALLO[1]-FEEDFORWARD via the external neuron syncytium and its tortuous axo-dendritic paths, eventually returning, through the action potentials of recurrent loops, to impact via the external AP ALLO-FEEDBACK loop.

(a)

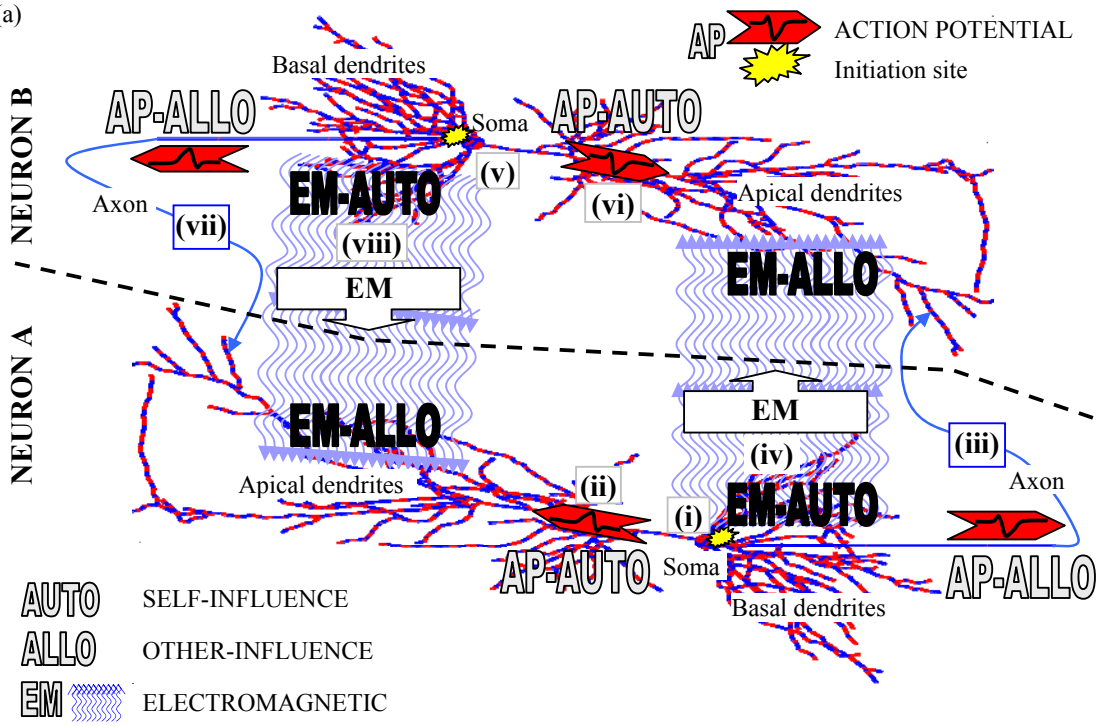

(b)

(i)	AP firing in neuron A.
(ii)	AP anti-dromic progression in neuron A.
(iii)	AP dromic progression in neuron A to neuron B.
(iv)	EM electromagnetic field produced by (ii) and (iii).
(v)	AP firing in neuron B.
(vi)	AP anti-dromic progression in neuron B.
(vii)	AP dromic progression in neuron B to neuron A.
(viii)	EM electromagnetic field produced by (v) and (vi).

(c)

	Predecessor				Successor		
	B AP-ALLO	(vii)					
1	B EM-ALLO	(viii)	⇒	A	AP	(i)	
	A AP-AUTO	(ii)					
				A	AP-AUTO	(ii)	GO TO 1.
2	A AP	(i)	⇒	A	AP-ALLO	(iii)	
				A	EM	(iv)	
	A AP-ALLO	(iii)					

Figure 8-3 (a) A roughly physical equivalent to Figure 8-2 is depicted. Item (b) activities (i) to (viii) are enacted in the (c) sequence.

[1] AUTO is to self as ALLO is to 'other'. For example, auto-poetic systems self construct (e.g. humans) and allo-poetic systems are constructed by others (e.g. cars) (Maturana and Varela 1980).

Figure 8-4 also shows the EM-axis and its novel 'backpropagation' mechanism, in blue. Some of the adaptation mechanisms by which the EM axis may operate are also shown. The EM field is produced by the net impact of the AP and/or subthreshold oscillations. The diagram shows that EM-axis acts by line-of-sight in the membrane-transverse direction. The blue dashed line indicates how the previously functionally inert EM mechanism becomes active, with a functional role acting in quasi-quadrature with the existing (red) feedback mechanism. Note that the dashed line indicates the EM ALLO-FEEDFORWARD impact on the remainder of the syncytium. In contrast, feed*back* from the transverse system is twofold. First we have EM AUTO-FEEDBACK, which is when a neuron's EM field impacts its own structure. Second we have EM ALLO-FEEDBACK, where the neighbourhood EM fields combine with its own EM field feedback. Jointly they determine the final cell behaviour. The *net* EM field will bathe cytosol, membranes and ECS on a line-of-sight basis and modulate the local chemical processes. The modulation can be viewed as the dynamic and rapid alteration of whatever process is under way and is likely to be best characterized as a multiplicative effect on the parameters that might be operating if the fields did nothing. For example, the dynamics of spike-time-dependent plasticity around a particular synapse may be multiplicatively modulated by the impacting EM field.

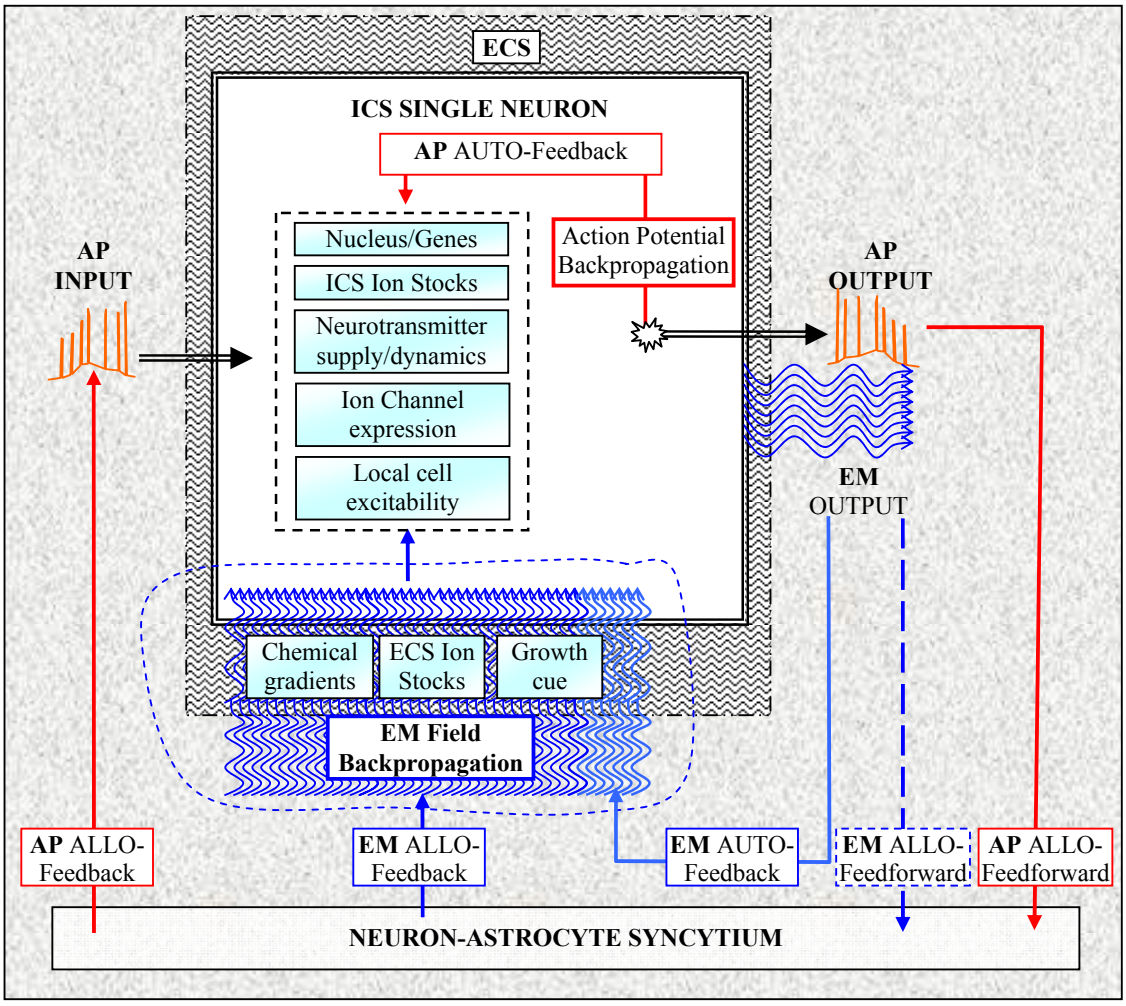

Figure 8-4 EM feedback (blue) joins AP (red/spike propagation) in the 'quasi-quadrature' feedback mechanism for an individual neuron. In the past, the EM fields existed but were not held accountable for an active functional role. Each axis of feedback influences the various mechanisms in light-blue boxes. Only the EM axis influences the extracellular medium.

Finally, as a means of representing the two-axis resonance, Figure 8-5(a) shows a diagrammatic idealization. Based on its now known origins, the traditionally described 'longitudinal' axis acts in quasi-quadrature to the EM 'transverse' axis. Figure 8-5(b) shows how the longitudinal and transverse

axes exist in realistic material. The two axes are not formally, physically orthogonal. They are functionally or operationally orthogonal. Only EM field details will reveal the extent to which the 'transverse' axis operates.

8.5.3 Binding, 'synchrony' & gamma/other coherences

In the neuroscience of consciousness and cognition, the 'binding problem' refers to the search for a clear understanding of how fragmentary perceptual/cognitive constructs (regarded as isolated complex patterns in neural sub-population activity) become appropriately associated and dissociated. The concept dates from the early nineteen eighties (Revonsuo 1999, Singer 2001, Velik 2010). Binding is central to cognition and behaviour. If a mental state cannot be adaptively integrated with an appropriate decision/action and subsequent feedback, we cannot act intelligently in the face of novelty. Binding of neural activity can appear to have two aspects depending on whether an associated conscious experience is included in the binding. The binding problem itself tends to be fragmented into discussions of separate kinds, for example, 'temporal', 'spatial', 'memory', 'attentional', 'feature', 'perceptual', 'cognitive', 'visual', 'auditory', 'cross-modal', 'sensory-motor', 'stimulus-response', 'top-down/bottom-up', 'syntactic/semantic' and so forth. Despite this proliferation, the binding issue can be explained readily under the revised quasi-quadrature model. For example, in a search for a 'red, round thing', the redness is an obvious experiential content but the 'roundness' does not. Yet in the search for it they are unified and in that unity, behaviour ensues. The mechanism of this dynamic, evanescent unity is the solution to the binding problem. Regardless of the experiential content, the basic idea is that otherwise disparate constructs can become dynamically integrated and dissociated as part of the moment to moment operation of the brain.

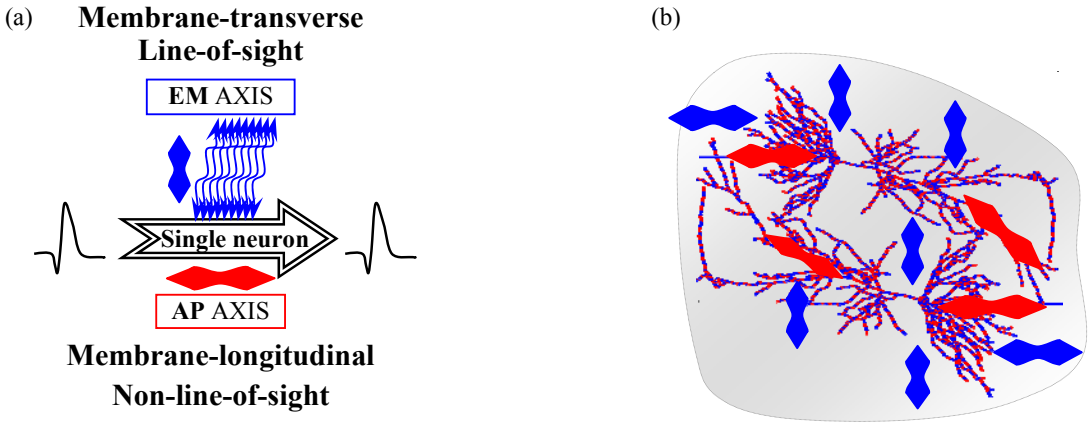

Figure 8-5 In (a) is an abstracted version of the quasi-quadrature resonance intended to highlight the difference in causal impact between membrane-transverse (EM) and membrane-longitudinal (AP) axes. Action potentials operate in the plane of the membrane. In (b) we see a simple syncytium presented to indicate the operation of the two axes.

In this thesis, a link to a novel view of the binding issue comes from the physical coherence idea suggested by the action of the EM axis. With a capacity to describe brain dynamics in terms of a mutual (quasi-orthogonal) interaction between two competing physical phenomena (the AP and EM axes), each with its own relationship to the same material substrate, we inherit a novel perspective on a physical solution to the binding problem. In the literature there is a significant and growing body of work that investigates gamma band (Buzsaki and Draguhn 2004) synchrony. It is in this particular frequency range that the EM axis acquires some precedence in an explanation of binding. In the EM-axis, coherence across multiple scales of neural organization now has a separable (to some extent) 'life-of-its-own'. Because the 'line-of-sight' connectivity happens at the speed of light and has the non-locality built into the general theory of electromagnetism, the dynamic binding issue can be solved by recognition that the binding happens in the EM axis and need not directly involve the physico-chemical tortuous, slow connectivity of the AP-axis. In the greater scheme of a contribution to

the understanding of brain dynamics as it relates to cognition, the 'binding problem' seems to be an easy potential explanandum for the EM-axis.

8.6 Perspectives on scientific description of neural tissue form and function

The elaboration of the EM field origins, along with an understanding of its expected behaviour, has general implications for the science of the excitable cell tissue.

8.6.1 Hierarchy theory and neural tissue

Hierarchy theory is a technically sound way of revealing the transdisciplinary structural nature of the neural EM field. In its most general form, hierarchy theory classifies the organization of the natural world into 'nested' and 'non-nested' kinds. These two kinds may occur inside each other. A nested hierarchy is a container of, in the sense of literally comprised of, its components. Nesting therefore involves self-containment by its own deeper organizational layers. A classically quoted example of the non-nested hierarchy is a social hierarchy such as the military command hierarchy. The commander at the peak of a military structure neither contains, nor is composed of, the subordinates in the structure (Ahl and Allen 1996, Allen and Starr 1982, Beer 1995, Feinberg 2011, Gnoli and Poli 2004, Koestler 1967, Koestler 1970, Margalef 1968, Minati, Pessa *et al.* 2006, Novikoff 1945, Pattee 1973, Poli 2001, Poli 2006a, Poli 2006b, Salthe 1985).

Here, brain tissue is our chosen example of a matter hierarchy and is shown in Figure 8-6, where Figure 8-6(c) line A-A′ represents the 'surgical lineage' of the hierarchical organization of the tissue. In our chosen neural tissue context, formally, the matter hierarchy is a dynamic, dissipative, nested (containment) hierarchy. Each of these aspects will now be outlined in a brain-EM field context. The hierarchical structure of the EM field in brain tissue, previously shown in Figure 1-3(b), is reproduced in Figure 8-6(b) in a more general explanatory context. The previous chapters have revealed that the appropriate way to view the emergence of a unified EM field system in brain tissue is to consider it based on a set of originating charges, but dominated by specific, intricately stationed and *coherently* choreographed ion behaviours within the brain's active electrolyte regions, but is most likely the transmembrane activity that creates and mediates the ECS and ICS ion population activity. The physical/material origins of the Figure 8-6(b) hierarchically structured EM field is shown in terms of the matter hierarchy explored by traditional mono-disciplinary sciences of Figure 8-6(c). In turn, in Figure 8-6(a), we see that the hierarchical system of science activity responsible for creating the material hierarchy is matched by the hierarchy of the traditional science sub-disciplines.

The 'dynamic' term signifies that the members of any organizational layer are in a continual state of renewal on a timescale that is a characteristic of the organisational layer.

> "*It is a basic characteristic of living systems that they are maintained in a continuous exchange of components. This is manifest at all levels: exchange of chemical components in the cell, of cells in the multicellular organism, of individuals in the population, etc*"
>
> Ludwig von Bertalanffy (Bertalanffy 1969, p73).

A good example of this is the population of organisms. Organisms are continually born and die, yet the 'population', comprised entirely and only of organisms, continues. The appropriate way to view the dynamics of a nested hierarchy is to apply it individually to every layer of Figure 8-6(c). 'Dissipative', in the context of hierarchy theory, means that at some level in the hierarchy, an exchange of energy with the overall containing environment is required in order that the structure is maintained. At the level of the containing environment, the matter hierarchy inclusive of a brain can be described as dissipative. Thus applied to brain tissue, this hierarchical, holistic, unified view of the tissue organization is one in which the importance of the EM fields becomes most apparent because the EM field inherits the entire nested organizational structure of the matter that generates it. The field

itself has as much structure within it as that expressed by its originating charges. This was introduced in Chapter 1.

Figure 8-6(c) has also been characterized with two axes of description. The 'appearance' axis alludes to the traditional stratified monodisciplinary view of the tissue. This view is argued as historically appropriate for constructing a reductionist description of the tissue componentry. In neural tissue, however (this will apply to other excitable cell tissues as well), it can be argued that the field system is an additional, physically/functionally unique phenomenon impressed on space. The unified behaviour of the EM field can be characterized as emergent in the collective behaviour of the field's originators. It is the collective behaviour that is (a) expressed at points in space other than its atomic originators and (b) impacts with and feeds back onto the material originators. This emergent behaviour can be seen to be a self-modifying function of the organization of the material evident only if viewed in the direction of the 'structure' axis of Figure 8-6(c).

Interestingly, the computational description of the EM field system revealed in the previous chapters is a 'structure-axis' view. In light of the previous classification of the 'EM-axis' and the 'AP axis', it becomes clear that the 'AP-axis' description is an 'appearance' axis description located at the neuron level in the strata of Figure 8-6(c). In contrast, the computational description created in chapters 1-7 is a transdisciplinary or 'structure' axis description, spanning nanometre to mm scales and from microseconds to milliseconds. This is at least metaphorically suggestive that the EM-axis corresponds to the Figure 8-6(c) structure axis and the AP-axis corresponds to the Figure 8-6(c) 'appearance' axis.

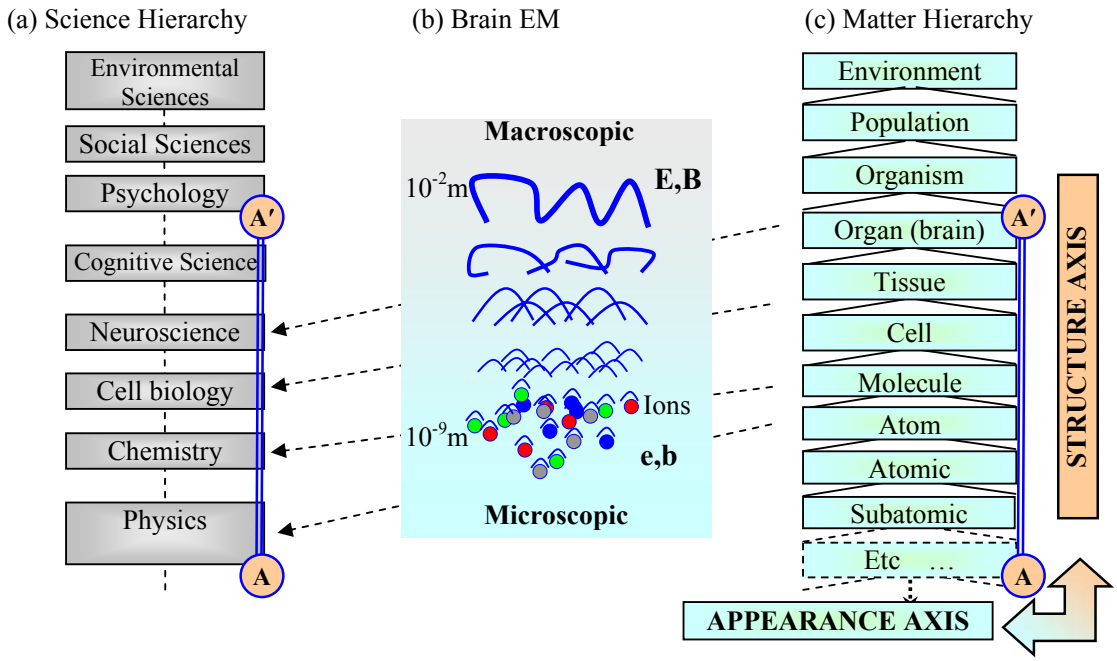

Figure 8-6 The matter nested hierarchy, the sciences of the matter hierarchy strata, the physical structure of the EM field, the 'structure' axis and the 'appearance' axis.

8.6.2 Brain tissue nested/non-nested hierarchy; structure and function

There is a further pairing of attributes that relates to the dual-axis pairings discussed above. It stems from the recent recognition of brain tissue as having properties of both nested and non-nested hierarchies. The brain is physically nested and functionally non-nested (Feinberg 2011). Clearly, the EM field is a nested structure because it is based on the nested physical structure of the material. However, *function* relates to the dynamics of the system. It is in its dynamics that the brain acquires its non-nested structure – where one neuron can control many. The non-nested 'social' structure of brain operation that results from brain interconnectedness, has been recognized in the context of EM field production (Nunez and Srinivasan 2007). In sitting 'on the fence' between these two forms of

hierarchy, being both (to some extent), the EM field therefore has some claim to a special status in the description of the brain. The mutual resonance between the EM axis (the nested hierarchy) and the AP-axis (the non-nested hierarchy) can be seen to embody the mapping between structure and function in the brain.

8.6.3 High performance computing (HPC) and the 'structure' axis: The tyranny of numbers in transdisciplinary science

The structure-axis involves the scientist in the oppression of sheer quantity that was addressed in Chapters 1 and 2. To address this issue, high performance computing (HPC) has been effectively used in this research to overcome the ion channel and cell morphology statistics. In contrast, the appearance-axis characterises, post hoc, the results of emergence – how the emergence appears to an observer. The more accurate sense of the use of HPC is that it is fundamentally necessitated by transdisciplinary science. HPC is, in a world of transdisciplinary science, more than merely a blunt instrument for manipulating structure-axis numbers. The reported behaviour of HPC literally *is* the science outcome. HPC exploration of the structure axis is therefore posited as a qualitatively and quantitatively novel way of viewing the natural world.

8.6.4 The EM field system, its relation to perception and cognition and their relationship with science

Using considerations of EM in the unique context of brain tissue science, it becomes possible to see a link between the EM field as a supplier of brain function, and the brain's function insofar as it is literally enables an act of scientific behaviour. Together, the EM-axis and the AP-axis mutually resonate at multiple nested spatiotemporal scales. As a result of this activity, human perception and cognition is created. Insofar as perception and cognition are necessitated in a scientific act, the scientific characterization of brain tissue is literally the characterization of how scientists do science. Note that this reality, of neuroscience as the scientific study of how scientific behaviour comes about, has many cousins in other areas. For example, the scientific characterization of brain tissue is simultaneously the characterization of how tennis players play tennis. One might be tempted to devalue the usefulness of this kind of idea. Such is not the case for science however. Science is a fundamentally different human behaviour because its target, 'laws of nature' (natural regularity) exists both (i) a-priori (would exist even if humans didn't) and (ii) outside the scientist. This makes scientific behaviour uniquely conclusive insofar as it can be used in its own right as a source of objective evidence in scientifically characterizing brain tissue function (cognition and perception).

Neuroscience, recognized as the implicit study of how scientists can do science, along with the realization that brain tissue EM is intimately involved in tissue function, elevates excitable cell tissue EM to a special place in science. Brain tissue EM, in being recognized as a central causal agent in brain function, directly invokes a series of wider implications that has been the focus of a lot of my research prior to the process of the numerical study of volume conduction. The outcome of the research is a collection of publications that are offered here in support of a claim that it strikes a rich vein of novel possibilities:

- The scientific explanation of scientists is the special circumstance used to construct a clear statement of the paradoxical nature of science of perception/consciousness identified above (that neuroscience is the implicit scientific explanation of scientific behaviour). This was a winner in an ASSC[2] essay contest (Hales 2010a).
- By formulating a 'scientific test for scientific behaviour', I have been able to construct a test which offers the eventual prospect of a scientific test for the presence of (P- or phenomenal) consciousness in an organic/natural or inorganic/artificial general intelligence (Hales 2009b).
- I have also used the functional necessities implicit in scientific behaviour to construct a refutation of computationalism (Hales 2011).

[2] See the Association for the Scientific Study of Consciousness, www.theassc.org.

- I was able to use the special circumstances of the scientific testing for scientific behaviour to contribute an invited commentary on an artificial intelligence proposition by Aaron Sloman (Hales 2010b).
- Using the special circumstances of the empirical scientific study of scientific behaviour, I have been able to construct a revision to our science framework designed to eliminate the well-recognized anomalous and paradoxical relationship that science has with consciousness (Hales 2009a). This idea was also published earlier, in a different form, for an artificial intelligence/technology audience (Hales 2006).

I hasten to add that the results of this research do not directly add support to hypotheses H1 and H2 except insofar as H1/H2 logically lead to a rich new territory of unexplored possibilities that construct quite compelling scientific cases in a variety of areas. The richness of the new territory can be directly traced to the centrality of the role of the EM field in brain tissue by virtue of the fact that the list of the EM-axis and the AP-axis exhausts the list of original natural causes of physical brain material properties involved directly in behaviour, intellect, cognition, perception and consciousness. From there, the EM field can be traced to a role in a raft of well known scientific problems (of the kind addressed in the list above). I look forward to making more contributions in this area.

8.7 Conclusion

Neural tissue organizational complexity has made unambiguous description of the origins of its endogenous electromagnetic field an elusive goal. It has been equally difficult to isolate the origins of a *causal* role for the EM field. However, the period of focussed study behind this thesis (2004-2011) has seen a significant change in the status of the neural EM field as a causal agent. It has been apparent for some time that some neural network population dynamics can be sensitive to electric fields under 1V/m (Francis, Gluckman *et al.* 2003). However, tracing the unequivocal origins of the variability to the single cell level has only happened in recent empirical measurements that have, finally, been able to support, with an acceptable level of certainty, a claim that the endogenous EM fields can have causally active role brain dynamics (Anastassiou, Perin *et al.* 2011, Frohlich and McCormick 2010). With improvement in tools and techniques, further confirming outcomes are likely as more researchers delve into this empirically difficult area. In addition, throughout this past two decades, the LFP has increasingly been found to be an equally effective indicator of the neural activity underlying normal and pathological brain states. Correlation of LFP and cell potential or firing rate is increasingly the norm in the description of neural activity underlying behavioural and cognitive phenomena (Pesaran 2009, Pesaran 2010).

It is in this recent raising the importance of knowledge of the endogenous fields that the lack of an originating cause has become a critical issue. This observation places an observed empirical phenomenon in need of an originating mechanism. This thesis has delivered a potential originating mechanism. This was done through the laws of electromagnetism applied with biological realism made possible by high performance computing applied in a single neuron modelling context. This combination has proved to be a productive route to the exploration of a plausible potential physical origin for the electric field due to an isolated, artificially induced action potential. There are reasons to consider the presented ‘bridging form’ of the volume conduction equations a productive route to the future more accurate and comprehensive modelling of brain electric and magnetic fields. From there, the route to a number of green fields of enquiry have been opened and are highly recommended.

8.8 Chapter bibliography

Ahl, V. and Allen, T. F. H., Hierarchy Theory : A Vision, Vocabulary, and Epistemology, Columbia University Press, New York, 1996, p. 206 p.

Allen, T. F. H. and Starr, T. B., Hierarchy : Perspectives for Ecological Complexity, University of Chicago Press, Chicago, 1982, pp. xvi, 310.

Anastassiou, C. A., Perin, R., Markram, H. and Koch, C. 'Ephaptic Coupling of Cortical Neurons', *Nature Neuroscience* vol. 14, no. 2, 2011. 217-223.

Bedlack, R. S., Wei, M. D. and Loew, L. M. 'Localized Membrane Depolarizations and Localized Calcium Influx During Electric Field-Guided Neurite Growth', *NEURON* vol. 9, no. 3, 1992. 393-403.

Beer, R. D. 'A Dynamical-Systems Perspective on Agent Environment Interaction', *Artificial Intelligence* vol. 72, no. 1-2, 1995. 173-215.

Bennett, M. V. L. and Zukin, R. S. 'Electrical Coupling and Neuronal Synchronization in the Mammalian Brain', *Neuron* vol. 41, no. 4, 2004. 495-511.

Bertalanffy, L. v., Robots, Men and Minds: Psychology in the Modern World, 1969

Bullock, T. H. 'Signals and Signs in the Nervous System: The Dynamic Anatomy of Electrical Activity Is Probably Information-Rich', *Proceedings of the National Academy of Sciences of the United States of America* vol. 94, no. 1, 1997. 1-6.

Buzsaki, G. and Draguhn, A. 'Neuronal Oscillations in Cortical Networks', *Science* vol. 304, no. 5679, 2004. 1926-1929.

Dudek, F. E., Yasumura, T. and Rash, J. E. "Non-Synaptic' Mechanicsms in Seizures and Epileptogenesis', *Cell Biology International* vol. 22, no. 11-12, 1998. 793-805.

Edelman, G. M., Second Nature : Brain Science and Human Knowledge, Yale University Press, New Haven, Conn. ; London, 2006, pp. x, 203 p.

Faber, D. S. and Korn, H. 'Electrical-Field Effects - Their Relevance in Central Neural Networks', *Physiological Reviews* vol. 69, no. 3, 1989. 821-863.

Feinberg, T. E. 'The Nested Neural Hierarchy and the Self', *Consciousness and Cognition* vol. 20, no. 1, 2011. 4-15.

Francis, J. T., Gluckman, B. J. and Schiff, S. J. 'Sensitivity of Neurons to Weak Electric Fields', *Journal of Neuroscience* vol. 23, no. 19, 2003. 7255-7261.

Frohlich, F. and McCormick, D. A. 'Endogenous Electric Fields May Guide Neocortical Network Activity', *Neuron* vol. 67, no. 1, 2010. 129-143.

Furness, J. B., The Enteric Nervous System, Blackwell Publishing, 2005

Gnoli, C. and Poli, R. 'Levels of Reality and Levels of Representation', *Knowledge Organization* vol. 31, no. 3, 2004. 151-160.

Hales, C. 'Ai and Science's Lost Realm', *IEEE Intelligent Systems* vol. 21, no. 3, 2006. 76-81.

Hales, C. 'Dual Aspect Science', *Journal of Consciousness Studies* vol. 16, no. 2-3, 2009a. 30-73.

Hales, C. 'An Empirical Framework for Objective Testing for P-Consciousness in an Artificial Agent', *The Open Artificial Intelligence Journal* vol. 3, no. http://www.bentham.org/open/toaij/, 2009b. 1-15.

Hales, C. 'The Scientific Evidence of Qualia Meets the Qualia That Are Scientific Evidence', *PSYCHE* vol. 16, no. 1, 2010a. 24-29.

Hales, C. 'The Well-Tested Young Scientist. An Invited Review of a Paper by Aaron Sloman.', *International Journal of Machine Consciousness* vol. 2, no. 1, 2010b. 35-39.

Hales, C. 'On the Status of Computationalism as a Law of Nature', *International Journal of Machine Consciousness* vol. 3, no. 1, 2011. 1-35.

Hille, B., Ion Channels of Excitable Membranes, Third ed., Sinauer Associates, Inc., Sunderland, MA., 2001

Hong, K. and Nishiyama, M. 'From Guidance Signals to Movement: Signaling Molecules Governing Growth Cone Turning', *Neuroscientist* vol. 16, no. 1, 2010. 65-78.

Koestler, A., The Ghost in the Machine, Hutchinson, London, 1967, pp. xiv, 384.

Koestler, A. (1970) Beyond Atomism and Holism -the Concept of the Holon. In A. Koestler, and J. R. Smythies (eds.). *Beyond Reductionism; New Perspectives in the Life Sciences*, Macmillan, New York].

Maggio, B., Borioli, G. A., Del Boca, M., De Tullio, L., Fanani, M. L., Oliveira, R. G., Rosetti, C. M. and Wilke, N. 'Composition-Driven Surface Domain Structuring Mediated by Sphingolipids and Membrane-Active Proteins', *Cell Biochemistry and Biophysics* vol. 50, no. 2, 2008. 79-109.

Margalef, R. n., Perspectives in Ecological Theory, University of Chicago Press, Chicago,, 1968, pp. viii, 111.

Maturana, H. R. and Varela, F. J. (1980) Autopoiesis and Cognition: The Organization of the Living. In R. S. Cohen, and M. W. Wartofsky (eds.). *Autopoiesis and Cognition: The Realization of the Living. Boston Studies in the Philosophy of Science*, D. Reidel Pub. Co., Dordrecht, Holland; Boston.

McCaig, C. D., Song, B. and Rajnicek, A. M. 'Electrical Dimensions in Cell Science', *Journal of Cell Science* vol. 122, no. 23, 2009. 4267-4276.

Milstein, J. N. and Koch, C. 'Dynamic Moment Analysis of the Extracellular Electric Field of a Biologically Realistic Spiking Neuron', *Neural Computation* vol. 20, no. 8, 2008. 2070-2084.

Minati, G., Pessa, E. and Abram, M., Eds. (2006). Systemics of Emergence : Research and Development. New York, Springer.

Niedermeyer, E. and da Silva, F. H. L., Electroencephalography : Basic Principles, Clinical Applications, and Related Fields, 5th ed., Lippincott Williams & Wilkins, Philadelphia, 2005, pp. xiii, 1309 p.

Novikoff, A. B. 'The Concept of Integrative Levels and Biology', *Science* vol. 101, no. 2618, 1945. 209-215.

Nunez, P. L. and Srinivasan, R., Electric Fields of the Brain : The Neurophysics of Eeg, 2nd ed., Oxford University Press, Oxford, New York, 2006

Nunez, P. L. and Srinivasan, R. 'Hearts Don't Love and Brains Don't Pump: Neocortical Dynamic Correlates of Conscious Experience', *Journal of Consciousness Studies* vol. 14, no. 8, 2007.

Pattee, H. H., Ed. (1973). Hierarchy Theory : The Challenge of Complex Systems. New York, George Braziller.

Pesaran, B. 'Uncovering the Mysterious Origins of Local Field Potentials', *Neuron* vol. 61, no. 1, 2009. 1-2.

Pesaran, B. 'Neural Correlations, Decisions, and Actions', *Current Opinion in Neurobiology* vol. 20, no. 2, 2010. 166-171.

Poli, R. 'The Basic Problem of the Theory of Levels of Reality', *Axiomathes* vol. 12, no. 3-4, 2001. 261-283.

Poli, R. 'Levels of Reality and the Psychological Stratum (Levels of Reality and Levels of Interpretation)', *Revue Internationale De Philosophie* vol. 61, no. 236, 2006a. 163-180.

Poli, R. (2006b) The Theory of Levels of Reality and the Difference between Simple and Tangled Hierarchies. In G. Minati, E. Pessa, and M. Abram (eds.). *Systemics of Emergence : Research and Development*, Springer, New York.

Revonsuo, A. 'Binding and the Phenomenal Unity of Consciousness', *Consciousness and Cognition* vol. 8, no. 2, 1999. 173-185.

Salthe, S. N., Evolving Hierarchical Systems : Their Structure and Representation, Columbia University Press, New York, 1985, pp. x, 343 p.

Schrödinger, E., What Is Life? : The Physical Aspect of the Living Cell ; with, Mind and Matter ; & Autobiographical Sketches, Cambridge University Press, Cambridge ; New York, 1992, pp. viii, 184 p.

Singer, W. (2001) Consciousness and the Binding Problem. In P. C. Marijuan (ed.). *Cajal and Consciousness - Scientific Approaches to Consciousness on the Centennial of Ramon Y Cajal's Textura*

Velik, R. 'From Single Neuron-Firing to Consciousness-Towards the True Solution of the Binding Problem', *Neuroscience and Biobehavioral Reviews* vol. 34, no. 7, 2010. 993-1001.

Wright, J. J. 'Generation and Control of Cortical Gamma: Findings from Simulation at Two Scales', *Neural Networks* vol. 22, no. 4, 2009. 373-384.

Appendix A

A USEFUL PROOF FOR USE IN BRAIN ELECTRODYNAMICS

This appendix provides a proof that is very useful in the bioelectromagnetism. This result is not simple or obvious. Nor has the proof of this well known identity been found in any useful or obviously accessible form in the literature. It is provided here for life-science electromagnetism researchers can internalize the mathematics without having to wade through the arcane physics literature. It is recommended that the equation be used sparingly, for whilst it produces accurate results, the process tends to hide important nuances which are apparent in a more long-winded treatment.

A.1 The equation

The result in question is the proof of the following general equation (Manby and Knowles 2001, Equation 10):

$$\int_U \frac{\nabla'^2 f(\mathbf{r}')}{|\mathbf{r}-\mathbf{r}'|} d^3 r' = -4\pi f(\mathbf{r}) . \quad \textbf{(A.1)}$$

A.2 The proof

We start by noting Laplace's equation,

$$\nabla \bullet \nabla \phi = \nabla^2 \phi = 0 . \quad \textbf{(A.2)}$$

We also note that Poisson's equation is a driven/sourced version of Laplace's equation satisfying

$$\nabla^2 \phi = f . \quad \textbf{(A.3)}$$

We commence by looking at the mathematics of particular solutions G to the special Poisson equation

$$\nabla^2 G = \delta(\mathbf{r}) , \quad \textbf{(A.4)}$$

or, more generally

$$\nabla^2 G(\mathbf{r},\mathbf{r}') = \delta(\mathbf{r}-\mathbf{r}') . \quad \textbf{(A.5)}$$

This has implications for solutions to Laplace's equation (A.2) which are of great utility in electromagnetism. The particular equation of interest is the Dirac delta function, defined as being a function of the kind

$$\delta(\mathbf{r}) = 0 \forall (\mathbf{r} \neq 0), \delta(\mathbf{r}) \neq 0 (\mathbf{r} = 0), \int_{-\infty}^{\infty} \delta(\mathbf{r}') d^3 r' = 1, \quad \textbf{(A.6)}$$

where, in our three-dimensional case,

$$\delta(\mathbf{r}) = \delta(x)\delta(y)\delta(z). \quad \textbf{(A.7)}$$

It is a fundamental property of δ(.) that

$$\int_{-\infty}^{\infty} f(\mathbf{r}) \delta(\mathbf{r} - \mathbf{r}') d^3 r' = f(\mathbf{r}'). \quad \textbf{(A.8)}$$

Also note that for $f(\mathbf{r}) = 1$,

$$\int_{-\infty}^{\infty} \delta(\mathbf{r} - \mathbf{r}') d^3 r' = f(\mathbf{r}) = 1. \quad \textbf{(A.9)}$$

Applying integral (A.6) to the Poisson equation (A.5) gives

$$\int_{-\infty}^{\infty} \nabla^2 G(\mathbf{r}, \mathbf{r}') d^3 r' = \int_{-\infty}^{\infty} \delta(\mathbf{r} - \mathbf{r}') d^3 r' = 1. \quad \textbf{(A.10)}$$

This puts a constraint on *G* which creates a class of well known functions called Green's functions. Note that the integral is equivalent to a volume integral in the limit thus

$$\lim_{V \to \infty} \left(\iiint_V \nabla^2 G(\mathbf{r}, \mathbf{r}') d^3 r' \right) = \lim_{V \to \infty} \left(\iiint_V \nabla \bullet \nabla G(\mathbf{r}, \mathbf{r}') d^3 r' \right) = 1. \quad \textbf{(A.11)}$$

This is rather convenient to visualise because the delta function is zero everywhere but at **r** = **r`**. We can now use the very general divergence theorem from vector calculus:

$$\iiint_V \nabla \bullet \mathbf{a}(\mathbf{r}') d^3 r' = \oint_S \mathbf{a}(\mathbf{r}') \bullet \mathbf{n}(\mathbf{r}') dS' \quad \textbf{(A.12)}$$

Where S is the surface of volume V and **n**(**r**) is a unit outward normal to S at point **r**. This is the point where we can properly attend to the problem at hand – the derivation of (A.1). With

$$\mathbf{a} = \nabla G, \quad \textbf{(A.13)}$$

we express a volume limited version of (A.11) in divergence-theorem form thus

$$\iiint_V \nabla \bullet \nabla G(\mathbf{r}, \mathbf{r}') d^3 r' = \oint_S \nabla G(\mathbf{r}, \mathbf{r}') \bullet \mathbf{n}(\mathbf{r}, \mathbf{r}') dS' = 1. \quad \textbf{(A.14)}$$

Let us consider our surface S to be a sphere of radius c centred on the point **r`**. The points **r`** are 'source points' and the points **r** are an observation point. The crucial fact about (A.14) is that for the final result to come out to be a constant, the function *G* must be a constant for all points where **r** = **r`**. Another way of viewing it is that the final solution G to Poisson's equation must be invariant to the coordinate system (and therefore invariant to rotation). That is, the function G(**r**,**r`**) can only be a function of the magnitude of the difference |**r**-**r`**|. Therefore, because of the involvement of the δ function, no matter what *G* is whenever |**r**-**r`**| takes on a value, say R, *G* will take on a constant value. Therefore, on the surface S of our sphere of radius c the function G has a constant value k_G and a direction identical to **n**. Consider the function

$$G(R) = \frac{k_G}{R} = \frac{k_G}{|\mathbf{r} - \mathbf{r}'|}. \quad \textbf{(A.15)}$$

Take the GRAD of it,

$$\nabla\left(\frac{k_G}{|\mathbf{r}-\mathbf{r}'|}\right)=\frac{-k_G(\mathbf{r}-\mathbf{r}')}{|\mathbf{r}-\mathbf{r}'|^3}=-\frac{k_G\mathbf{n}}{|\mathbf{r}-\mathbf{r}'|^2}=-\frac{k_G\mathbf{n}}{R^2}, \tag{A.16}$$

If we substitute (A.16) into the right term of (A.14) it becomes

$$\oint_S \frac{-k_G}{|\mathbf{r}-\mathbf{r}'|^2}\mathbf{n}(\mathbf{r},\mathbf{r}')\bullet\mathbf{n}(\mathbf{r},\mathbf{r}')\,dS'=\oint_S\frac{-k_G}{c^2}dS'=-4\pi k_G, \tag{A.17}$$

On the surface S the value of the term 1/|**r**-**r**`| is a constant 1/c. The integration therefore computes the surface area of a sphere of radius c. In order that (A.14) hold, the value of k_G must be

$$k_G=\frac{-1}{4\pi}, \tag{A.18}$$

Which means that

$$G(R)=G(\mathbf{r},\mathbf{r}')=\frac{-1}{4\pi|\mathbf{r}-\mathbf{r}'|} \tag{A.19}$$

is the special Green's function that must be involved. Going back to (A.11) we now have evaluated the integral

$$\lim_{V\to\infty}\left(\iiint_V\nabla^2\left(\frac{-1}{4\pi|\mathbf{r}-\mathbf{r}'|}\right)d^3r'\right)=\lim_{V\to\infty}\left(\iiint_V\nabla\bullet\nabla\left(\frac{-1}{4\pi|\mathbf{r}-\mathbf{r}'|}\right)d^3r'\right)=1, \tag{A.20}$$

From (A.5) we now know that

$$\nabla^2\left(\frac{-1}{4\pi|\mathbf{r}-\mathbf{r}'|}\right)=\delta(\mathbf{r}-\mathbf{r}'), \tag{A.21}$$

or, defining a new Green's function

$$G(\mathbf{r},\mathbf{r}')=\frac{1}{|\mathbf{r}-\mathbf{r}'|}, \tag{A.22}$$

we can construct general form

$$\nabla^2G(\mathbf{r},\mathbf{r}')=\nabla^2\left(\frac{1}{|\mathbf{r}-\mathbf{r}'|}\right)=-4\pi\delta(\mathbf{r}-\mathbf{r}'). \tag{A.23}$$

This is the result we have used elsewhere here. We can now move directly towards the proof of (A.1). Using the now well defined Green function and the standard vector identity

$$\nabla(fg)=f\nabla g+g\nabla f, \tag{A.24}$$

it follows that

$$\nabla\bullet(\phi\nabla\varphi)=\phi\nabla^2\varphi+(\nabla\phi\bullet\nabla\varphi) \tag{A.25}$$

with

$$\phi=f(\mathbf{r}'),\varphi=\frac{1}{|\mathbf{r}-\mathbf{r}'|}, \tag{A.26}$$

Changing to primed variables, substitute (A.26) into (A.25), giving

$$\nabla'\bullet\left(f(\mathbf{r}')\nabla'\left(\frac{1}{|\mathbf{r}-\mathbf{r}'|}\right)\right)=f(\mathbf{r}')\nabla'^2\left(\frac{1}{|\mathbf{r}-\mathbf{r}'|}\right)+\left(\nabla' f(\mathbf{r}')\bullet\nabla'\left(\frac{1}{|\mathbf{r}-\mathbf{r}'|}\right)\right). \tag{A.27}$$

Applying the divergence theorem (A.12) with a vector **a** defined as

$$\mathbf{a}=\phi\nabla\varphi, \tag{A.28}$$

gives the left side volume integral as

$$\begin{aligned}&\iiint_V \nabla'\bullet\left(f(\mathbf{r}')\nabla'\left(\frac{1}{|\mathbf{r}-\mathbf{r}'|}\right)\right)d^3r'\\&\quad=\iiint_V f(\mathbf{r}')\nabla'^2\left(\frac{1}{|\mathbf{r}-\mathbf{r}'|}\right)+\left(\nabla' f(\mathbf{r}')\bullet\nabla'\left(\frac{1}{|\mathbf{r}-\mathbf{r}'|}\right)\right)d^3r'\end{aligned} \tag{A.29}$$

and the right surface integral as

$$\oint_S\left(f(\mathbf{r}')\nabla'\left(\frac{1}{|\mathbf{r}-\mathbf{r}'|}\right)\right)\bullet\mathbf{n}(\mathbf{r}')\,dS'. \tag{A.30}$$

Return to (A.25) and reverse the allocation of scalar functions thus

$$\phi=\frac{1}{|\mathbf{r}-\mathbf{r}'|},\varphi=f(\mathbf{r}'). \tag{A.31}$$

Again, changing to primed variables, substitute(A.31) into (A.25):

$$\nabla'\bullet\left(\frac{1}{|\mathbf{r}-\mathbf{r}'|}\nabla' f(\mathbf{r}')\right)=\left(\frac{1}{|\mathbf{r}-\mathbf{r}'|}\right)\nabla'^2 f(\mathbf{r}')+\left(\nabla'\frac{1}{|\mathbf{r}-\mathbf{r}'|}\bullet\nabla' f(\mathbf{r}')\right). \tag{A.32}$$

Apply the divergence theorem (A.12) with the **a** defined with (A.31), applied via (A.25) to (A.32). The left side volume integral is

$$\begin{aligned}&\iiint_V \nabla'\bullet\left(\frac{1}{|\mathbf{r}-\mathbf{r}'|}\nabla' f(\mathbf{r}')\right)d^3r'=\\&\quad\iiint_V\frac{1}{|\mathbf{r}-\mathbf{r}'|}\nabla'^2 f(\mathbf{r}')\,d^3r'+\iiint_V\nabla' f(\mathbf{r}')\bullet\nabla'\left(\frac{1}{|\mathbf{r}-\mathbf{r}'|}\right)d^3r'\end{aligned} \tag{A.33}$$

The right side surface integral is

$$\oint_S\left(\frac{1}{|\mathbf{r}-\mathbf{r}'|}\nabla f(\mathbf{r}')\right)\bullet\mathbf{n}(\mathbf{r}')\,dS'. \tag{A.34}$$

From (A.29)=(A.30) and (A.33)=(A.34) we now have two divergence theorems based on the same pair of functions and over the same domain:

$$\begin{aligned}&\iiint_V f(\mathbf{r}')\nabla'^2\left(\frac{1}{|\mathbf{r}-\mathbf{r}'|}\right)d^3r'+\iiint_V\nabla' f(\mathbf{r}')\bullet\nabla'\left(\frac{1}{|\mathbf{r}-\mathbf{r}'|}\right)d^3r'\\&\quad=\oint_S\left(f(\mathbf{r}')\nabla'\left(\frac{1}{|\mathbf{r}-\mathbf{r}'|}\right)\right)\bullet\mathbf{n}(\mathbf{r}')\,dS'\end{aligned} \tag{A.35}$$

and

$$\iiint_V \frac{1}{|\mathbf{r}-\mathbf{r}'|}\nabla'^2 f(\mathbf{r}')\,d^3r' + \iiint_V \nabla' f(\mathbf{r}')\bullet\nabla'\left(\frac{1}{|\mathbf{r}-\mathbf{r}'|}\right)d^3r' = \oint_S \left(\frac{1}{|\mathbf{r}-\mathbf{r}'|}\nabla f(\mathbf{r}')\right)\bullet\mathbf{n}(\mathbf{r}')\,dS' \quad \textbf{(A.36)}$$

If we subtract these two equations we get

$$\iiint_V f(\mathbf{r}')\nabla'^2\left(\frac{1}{|\mathbf{r}-\mathbf{r}'|}\right) - \frac{1}{|\mathbf{r}-\mathbf{r}'|}\nabla'^2 f(\mathbf{r}')\,d^3r' = \oint_S \left(f(\mathbf{r}')\nabla'\left(\frac{1}{|\mathbf{r}-\mathbf{r}'|}\right)\right)\bullet\mathbf{n}(\mathbf{r}') - \left(\frac{1}{|\mathbf{r}-\mathbf{r}'|}\nabla f(\mathbf{r}')\right)\bullet\mathbf{n}(\mathbf{r}')\,dS'. \quad \textbf{(A.37)}$$

Applying (A.23) and rearranging, we get

$$f(\mathbf{r}) = -\frac{1}{4\pi}\iiint_V \frac{\nabla'^2 f(\mathbf{r}')}{|\mathbf{r}-\mathbf{r}'|}d^3r' - \frac{1}{4\pi}\oint_S \left(f(\mathbf{r}')\nabla'\left(\frac{1}{|\mathbf{r}-\mathbf{r}'|}\right)\right)\bullet\mathbf{n}(\mathbf{r}') - \left(\frac{1}{|\mathbf{r}-\mathbf{r}'|}\nabla f(\mathbf{r}')\right)\bullet\mathbf{n}(\mathbf{r}')\,dS'. \quad \textbf{(A.38)}$$

The surface integral on a limiting boundary S has captured the essence of the proof of our target equation (A.1). In the limit, as **r`**→∞ and V→U:

$$f(\mathbf{r}) = -\frac{1}{4\pi}\int_U \frac{\nabla'^2 f(\mathbf{r}')}{|\mathbf{r}-\mathbf{r}'|}d^3r'. \quad \textbf{(A.39)}$$

The final proof rests on both terms in the surface integral approaching zero as **r`** approaches ∞. The left term evaluates to

(A.40)

where **R** = (**r**-**r`**) and $\mathbf{R}_u$ is a unit vector in the direction of **R**. As **r`** approaches ∞ the integrand will approach zero provided *f*(**r**) increases in the direction of **n** at a rate less than **R**. The right surface integral is

$$\frac{1}{4\pi}\oint_S \left(\frac{1}{|\mathbf{R}|}\nabla f(\mathbf{r}')\right)\bullet\mathbf{n}(\mathbf{r}')\,dS'. \quad \textbf{(A.41)}$$

This integrand will approach zero as **r`** approaches ∞ provided the *gradient* of *f*(**r**, **r'**) in the direction of **n** *decreases* at a rate greater than 1/**R**. If we restrict ourselves to only those *f*(**r**, **r'**) that fall off at a rate greater than 1/**R**, then both surface integrals can be justified as approaching zero as **r`** approaches ∞. In that circumstance we have demonstrated that equation (A.1) is the result. Fortunately, for the physical electromagnetism processes of interest this restriction on **f**(**r**, **r'**) is viable and (A.1) can be used.

A.3 Discussion

Note that a useful but more specialised version of this proof, indirectly related to the (A.1) proof, can be found in Jackson(Jackson 1999, Page 36/37), who has very revealing advice about the circumstances. Knowledge of the above process is very important for those doing electrodynamics simulations, in which the integration volume and the simulation volume must be finite. In that case it is simply impossible for **r`** to approach infinity and care must be taken to ensure this does not affect the results. In that circumstance equation (A.38) tells us about the effective impact of the simulation

volume boundary. The impact of the boundary is to invoke extra boundary behaviour to manipulate the value of $f(\mathbf{r})$ so that it becomes *zero outside the (uncomputed) volume V*. This means that the region outside the volume *V* has no effect inside *V*. As a result of a finite *V* the boundary *S*, which is invoked to eliminate the effect of the region outside *V*, will therefore impact the *inside* of the volume through the operation of the surface integral. Note that in the case in electromagnetism where the volume V contains no sources, the boundary condition completely defines the fields inside the volume *V* by invoking 'virtual sources' on the boundary *S*. The practical constraint of this situation is therefore that the simulation volume must be larger than its contained contents (a simulated ensemble) to the extent needed to ensure that the impact on the ensemble of the failure to compute/simulate the boundary *S* (and its surrounds!) can be neglected.

A.4 Bibliography

Jackson, J. D., Classical Electrodynamics, 3rd ed., Wiley, New York, 1999

Manby, F. R. and Knowles, P. J. 'Poisson Equation in the Kohn-Sham Coulomb Problem', *Physical Review Letters* vol. 87, no. 16, 2001. art. no.-163001.

Appendix B

A NOVEL INTEGRAL FORM OF THE MICROSCOPIC FIELDS

B.1 Introduction

It may be a surprise to learn that there are different integral forms of the solutions to MmE. The underlying reason for this is the degenerate relationship **e** and **b** have with scalar and vector potentials. This results from the choice of electromagnetic gauge, where solutions vary depending on the gauge choice, yet exactly the same physical **e** and **b** fields are produced by the solution. This particular analysis proceeds directly to equations for the fields, not the potentials. The integral solution to be derived has not been found in the literature inspected thus far. Therefore the process must involve a tacit choice of a particular gauge. In avoiding explicit potentials we also avoid important issues such as 'advanced' and 'retarded' field formulations and the vexing issue of causality which has only relatively recently been comprehensively consolidated. We set aside the symmetric form of Maxwell's equations for the moment and repeat the basic set of differential MmE here for completeness(Craig and Thirunamachandran 1984, Jackson 1999, Nunez and Srinivasan 2006):

$$\nabla \cdot \mathbf{e}(\mathbf{r},t) = \frac{\eta(\mathbf{r},t)}{\varepsilon_0} \tag{B.1}$$

$$\nabla \times \mathbf{e}(\mathbf{r},t) + \frac{\partial \mathbf{b}(\mathbf{r},t)}{\partial t} = 0 \tag{B.2}$$

$$\nabla \cdot \mathbf{b}(\mathbf{r},t) = 0 \tag{B.3}$$

$$\nabla \times \mathbf{b}(\mathbf{r},t) - \frac{1}{c^2}\frac{\partial \mathbf{e}(\mathbf{r},t)}{\partial t} = \mu_0 \mathbf{j}(\mathbf{r},t)\,. \tag{B.4}$$

The first significant feature of MmE are that they are the more fundamental form of Maxwells' equations(Craig and Thirunamachandran 1984), deriving from quantum field theory. With MmE thus established, the material abstractions of MME are then derived (Jackson 1999, Chapter 6) and apply contingent on the applicability of the assumptions made by that abstraction. The second feature is that in the asymmetric form there is only one originating set of charges and these are electric. There is a group of charges (and associated mass) located in space as per the right hand side of (B.1). These are the electrons and nucleons of the atoms involved in the charge density η. The very same set of charges, are also *moving* according to the right hand side of (B.4). This behaviour is entirely responsible for the fields exhibited.

The third significant feature of MmE relates to the practicalities of simulation. Simulation involves identifying a set of charges, η, populating a region of interest (ROI) called a 'computational chemistry reactor'. Charge ensemble η is notionally separated and isolated, in some controlled way, from the rest of the charge in the universe. If constrained to a particular set of charges, the fields produced by equations (B.1) to (B.4) *do not include field ingress from other sources* outside the ROI. Nor do the reactor internal fields computationally egress the ROI bounds. This means that **e** and **b** equations, when applied to one set of charges, *does not compute the total field throughout the ROI*. The implication in the context of a molecular *electro*-dynamics simulation is that the simulation reactor's computational context must be carefully crafted to account for the boundary with rest of the universe outside the reactor if the complete electric and magnetic fields are to be accounted for inside the reactor. Further examination of this issue is carried out later in this chapter.

Returning to the problem at hand, note that (B.1) to (B.4) do not reveal any explicit solution for **e** and **b**. Rather they specify the various coupled vector field component properties. In the literature these (DIV, CURL) component properties are variously named (solenoidal, irrotational) or (transverse, longitudinal) respectively. A reformulation to make **e** and **b** explicit is the integral form which is to be derived. Equations revealing explicit **e** and **b** can be formulated from (B.1) to (B.4) through a rather fearless use of (a) Helmholtz decomposition (see (Arfken and Weber 2001, Page 96-100)) and (b) a convolution with a Newtonian potential in generalised abstract vector field theory in three dimensional space. The full derivation from basic vector field theory is presented here for the record. In the process the nomenclature and methods used throughout this thesis will be established.

B.2 Basic derivation

It can be shown that any vector field $\mathbf{V}(\mathbf{r})$ of spatial position $\mathbf{r}$, which is at least two times continuously differentiable and vanishes sufficiently fast as $\mathbf{r}\to\infty$ can be decomposed into (1) an irrotational part (CURL is zero) as the gradient of a scalar potential, $\mathbf{V}_{\text{irr}}$, and (2) a source-free solenoidal part expressed as the CURL of a vector potential (DIV is zero), $\mathbf{V}_{\text{sol}}$. Thus:

$$\mathbf{V}(\mathbf{r}) = \mathbf{V}_{irr}(\mathbf{r}) + \mathbf{V}_{sol}(\mathbf{r}) \text{ where } \mathbf{V}_{irr}(\mathbf{r}) = -\nabla\varphi(\mathbf{r}) \text{ and } \mathbf{V}_{sol}(\mathbf{r}) = \nabla\times\mathbf{A}(\mathbf{r}) \quad \textbf{(B.5)}$$

or

$$\mathbf{V}(\mathbf{r}) = -\nabla\varphi(\mathbf{r}) + \nabla\times\mathbf{A}(\mathbf{r}). \quad \textbf{(B.6)}$$

The CURL of the (GRAD φ) field is zero. However, the DIV of the **A** field is not necessarily zero and has some arbitrariness to it. This is covered in the later chapters on electromagnetic gauge. Fundamental vector field theory also tells us that the sources of a field **V** are

$$\nabla\cdot\mathbf{V}(\mathbf{r}) = s(\mathbf{r}) \quad \text{Source density} \quad \textbf{(B.7)}$$

and

$$\nabla\times\mathbf{V}(\mathbf{r}) = \mathbf{c}(\mathbf{r}) \quad \text{Circulation density.} \quad \textbf{(B.8)}$$

Using standard vector identities in (B.6), it follows that

$$\nabla\cdot\mathbf{V}(\mathbf{r}) = -\nabla^2\varphi(\mathbf{r}) = s(\mathbf{r}) \quad \textbf{(B.9)}$$

$$\nabla\times\mathbf{V} = \nabla(\nabla.\mathbf{A}) - \nabla^2\mathbf{A} = c(\mathbf{r}). \quad \textbf{(B.10)}$$

Note that (B.9) is a scalar Laplacian (Poisson's equation) and that (B.10) involves the *vector* Laplacian (see equation (B.80) below). We seek to solve for the two potentials in (B.5). To do that in general terms we need housekeeping. Note that convolution in a 3D Euclidean space is defined as follows:

$$(u * v)(\mathbf{r}) = \int_a^b u(\mathbf{r}')v(\mathbf{r}-\mathbf{r}')d^3\mathbf{r}' \quad \textbf{(B.11)}$$

A 'Newtonian potential' on a vector **a** is a singular integral operator defined by convolution with a function having a mathematical singularity at the origin:

$$\mathcal{G}(\mathbf{a}) = \begin{cases} c_1 |\mathbf{a}| & : d = 1 \\ c_2 \log \|\mathbf{a}\| & : d = 2 \\ c_d \|\mathbf{a}\|^{2-d} & : d > 2 \end{cases}. \tag{B.12}$$

Here c_d denotes a normalisation constant which depends on the dimensionality *d*. In our particular case $d = 3$ and therefore, for a vector $\mathbf{r} = (r_x, r_r, r_z)$, in our 'region of interest':

$$\mathcal{G}(\mathbf{r}) = c_d \|\mathbf{r}\|^{-1} \text{ where } \|\mathbf{r}\| = \sqrt{r_x^2 + r_y^2 + r_z^2} = \sqrt{\mathbf{r} \cdot \mathbf{r}}\,. \tag{B.13}$$

Remaining focussed on solving for the two potentials in (B.5), consider solving the general case:

$$\nabla^2 \varphi(\mathbf{r}) = f(\mathbf{r}) \text{ or } \frac{\partial^2 \varphi(r_x, r_y, r_z)}{\partial r_x^2} + \frac{\partial^2 \varphi(r_x, r_y, r_z)}{\partial r_y^2} + \frac{\partial^2 \varphi(r_x, r_y, r_z)}{\partial r_z^2} = f(r_x, r_y, r_z)\,. \tag{B.14}$$

To solve equation (B.9) for the potential $\varphi(\mathbf{r})$ given source field $s(\mathbf{r})$ we make use of the a properties of convolution with a Newtonian potential over a Euclidean space. *By definition* the Newtonian potential applied to a function f satisfies Poisson's equation thus:

$$\mathcal{G} * (-\nabla^2 f) = f\,. \tag{B.15}$$

This convolution with the function defined in (B.12) demands that the function f automatically satisfies Poisson's equation. In other words for an arbitrary decomposed field **F** this means that

$$\mathbf{F} = -\nabla \mathcal{G}(\nabla \cdot \mathbf{F}) + \nabla \times \mathcal{G}(\nabla \times \mathbf{F}), \tag{B.16}$$

where we have defined

$$\mathcal{G}(\bullet) = \mathcal{G} * (\bullet) \tag{B.17}$$

so that (B.16) looks sufficiently like (B.6). Equation (B.16) shows how, through the use of the Newtonian Kernel, its convolution with the field **F** decomposes a field **F** into a DIV and CURL that, appropriately used, expresses the original field. From (B.15) we can see that, as related to equation (B.13), if we convolve the Newtonian Kernel with $s(\mathbf{r})$ then we generate $\varphi(\mathbf{r})$ in the process. To show what such a convolution looks like for the particular Kernel of (B.13):

$$\mathcal{G}(\mathbf{r}) * s(\mathbf{r}) = \int_{-\infty}^{\infty} \mathcal{G}(\mathbf{r}') s(\mathbf{r} - \mathbf{r}')\, d\mathbf{r}' = c_d \int_U \frac{s(\mathbf{r} - \mathbf{r}')}{\|\mathbf{r}'\|} d\mathbf{r}' = \varphi(\mathbf{r}) \tag{B.18}$$

First note that convolution is commutative. Next note that each source point in $s(\mathbf{r})$ is located at, say, $\mathbf{r}_2$ and exerts an influence on the potential at $\mathbf{r}_1$, which is actually the point $\mathbf{r}$ at which φ is calculated in (B.17). This means that the integration (B.18), with $c_d = (1/4\pi)$, becomes:

$$\varphi(\mathbf{r}) = \frac{1}{4\pi} \int_U \frac{s(\mathbf{r}_2)}{\|\mathbf{r} - \mathbf{r}_2\|} d\mathbf{r}_2 \tag{B.19}$$

This equation is equivalent to the assumed potential equation used in the proof of Helmholtz's theorem in Arfken and Weber(Arfken and Weber 2001, Section 1.16). With the general decomposition idea in hand, now we can see how, under the appropriate conditions, an arbitrary field **V** can be expressed as a sum of a scalar and vector potential fields. Let's restate the general situation in one place so we can see it:

$$\mathbf{V}(\mathbf{r}) = -\nabla \varphi(\mathbf{r}) + \nabla \times \mathbf{A}(\mathbf{r}) \tag{B.20}$$

$$\mathbf{V}_{irr}(\mathbf{r}) = \nabla \cdot \mathbf{V}(\mathbf{r}) = s(\mathbf{r}),\ \nabla \times \mathbf{V}_{irr}(\mathbf{r}) = 0 \qquad \text{Irrotational} \tag{B.21}$$

$$\mathbf{V}_{sol}(\mathbf{r}) = \nabla \times \mathbf{V}(\mathbf{r}) = \mathbf{c}(\mathbf{r}),\ \nabla \cdot \mathbf{V}_{sol}(\mathbf{r}) = 0 \qquad \text{Solenoidal} \tag{B.22}$$

$$\mathbf{V}(\mathbf{r}) = \mathbf{V}_{sol}(\mathbf{r}) + \mathbf{V}_{irr}(\mathbf{r}) \qquad \text{Total} \tag{B.23}$$

Equation (B.20) must be consistent with (B.23). This means that when the divergence source s(**r**) and the circulation source **c**(**r**) are known, then the total field becomes, using equations (B.16) and (B.17):

$$\begin{aligned} \mathbf{V}(\mathbf{r}) &= -\nabla\mathcal{G}(\nabla\cdot\mathbf{V}) + \nabla\times\mathcal{G}(\nabla\times\mathbf{V}) \\ &= -\nabla\mathcal{G}(\mathrm{s}(\mathbf{r})) + \nabla\times\mathcal{G}(\mathbf{c}(\mathbf{r})) \\ &= -\nabla\varphi(\mathbf{r}) + \nabla\times\mathbf{A}(\mathbf{r}) \end{aligned} \tag{B.24}$$

Equating terms we get, in general,

$$\mathcal{G}(\mathrm{s}(\mathbf{r})) = \left[\mathcal{G}(\mathbf{r}) * s(\mathbf{r})\right] = \varphi(\mathbf{r}) \tag{B.25}$$

and

$$\mathcal{G}(\mathbf{c}(\mathbf{r})) = \left[\mathcal{G}(\mathbf{r}) * c(\mathbf{r})\right] = \mathbf{A}(\mathbf{r}). \tag{B.26}$$

This means that the universal relationship between the field expression and a potential expressions through the existence of known *s* source (divergence) and **c** circulation (curl), the potentials can be computed by the convolutions:

$$\varphi(\mathbf{r}) = \frac{1}{4\pi}\int_U \frac{\nabla\cdot\mathbf{V}(\mathbf{r}')}{|\mathbf{r}-\mathbf{r}'|}d^3r' = \frac{1}{4\pi}\int_U \frac{s(\mathbf{r}')}{|\mathbf{r}-\mathbf{r}'|}d^3r' \tag{B.27}$$

$$\mathbf{A}(\mathbf{r}) = \frac{1}{4\pi}\int_U \frac{\nabla\times\mathbf{V}(\mathbf{r}')}{|\mathbf{r}-\mathbf{r}'|}d^3r' = \frac{1}{4\pi}\int_U \frac{\mathbf{c}(\mathbf{r}')}{|\mathbf{r}-\mathbf{r}'|}d^3r' \tag{B.28}$$

Note that these are 3D spatial integrals *over the entire universe* U. With this general result in hand we can now apply it to the special case of a three dimensional Euclidean simply connected space (manifold) with our fields of interest expressed in it: **e**(**r**) and **b**(**r**). The MmE present four empirically established statements of the DIV and CURL of **e** and **b** by specifying the source and circulation density of each field. Without having any empirical details, we can formulate our fields in a form suited to the above Helmholtz decomposition by noting that we already know the solenoidal and irrotational components of the two fields and they can be expressed generally as:

$$\mathbf{e}_{irr}(\mathbf{r}) = \nabla\cdot\mathbf{e}(\mathbf{r}) = s_e(\mathbf{r}) \tag{B.29}$$

$$\mathbf{e}_{sol}(\mathbf{r}) = \nabla\times\mathbf{e}(\mathbf{r}) = \mathbf{c}_e(\mathbf{r}) \tag{B.30}$$

$$\mathbf{b}_{irr}(\mathbf{r}) = \nabla\cdot\mathbf{b}(\mathbf{r}) = \mathrm{s}_b(\mathbf{r}) \tag{B.31}$$

$$\mathbf{b}_{sol}(\mathbf{r}) = \nabla\times\mathbf{b}(\mathbf{r}) = \mathbf{c}_b(\mathbf{r}) \tag{B.32}$$

And the covarying/coupled empirical relationships for each of these components is, from the microscopic form of the MmE:

$$\nabla\cdot\mathbf{e}(\mathbf{r}) = \mathrm{s}_\mathrm{e}(\mathbf{r}) = \frac{\eta(\mathbf{r})}{\varepsilon_0} \tag{B.33}$$

$$\nabla\times\mathbf{e}(\mathbf{r}) = \mathbf{c}_e(\mathbf{r}) = -\frac{\partial\mathbf{b}(\mathbf{r})}{\partial t} \tag{B.34}$$

$$\nabla\cdot\mathbf{b}(\mathbf{r}) = s_b(\mathbf{r}) = 0 \tag{B.35}$$

$$\nabla \times \mathbf{b}(\mathbf{r}) = \mathbf{c}_b(\mathbf{r}) = \mu_0 \mathbf{j}(\mathbf{r}) + \frac{1}{c^2}\frac{\partial \mathbf{e}(\mathbf{r})}{\partial t} \tag{B.36}$$

By recognising the appropriate components of the field as per (B.29)-(B.32) and substitution of (B.33)…(B.36) into two pairs of potentials as per (B.27) and (B.28), the four resultant *microscopic* potentials are:

$$\phi_e(\mathbf{r}) = \frac{1}{4\pi}\int_U \frac{\eta(\mathbf{r}')}{\varepsilon_0}\frac{1}{|\mathbf{r}-\mathbf{r}'|}d^3r' \tag{B.37}$$

$$\mathbf{a}_e(\mathbf{r}) = \frac{1}{4\pi}\int_U -\frac{\partial \mathbf{b}(\mathbf{r}')}{\partial t}\frac{1}{|\mathbf{r}-\mathbf{r}'|}d^3r' \tag{B.38}$$

$$\phi_b(\mathbf{r}) = 0 \tag{B.39}$$

$$\mathbf{a}_b(\mathbf{r}) = \frac{1}{4\pi}\int_U \mu_0 \mathbf{j}(\mathbf{r}')\frac{1}{|\mathbf{r}-\mathbf{r}'|}d^3r' + \frac{1}{4\pi}\frac{1}{c^2}\int_U \frac{\partial \mathbf{e}(\mathbf{r}')}{\partial t}\frac{1}{|\mathbf{r}-\mathbf{r}'|}d^3r'. \tag{B.40}$$

Thus, to complete the expressions for the total field we can substitute (B.37)-(B.40) in the appropriate forms of equation (B.6):

$$\mathbf{e}(\mathbf{r}) = -\nabla\phi_e(\mathbf{r}) + \nabla \times \mathbf{a}_e(\mathbf{r}) \tag{B.41}$$

$$\mathbf{b}(\mathbf{r}) = -\nabla\phi_b(\mathbf{r}) + \nabla \times \mathbf{a}_b(\mathbf{r}). \tag{B.42}$$

Substituting (B.37)-(B.40) into (B.41) and (B.42), the total fields **e** and **b** become specified by two rather formidable cross-coupled equations in two unknowns:

$$\mathbf{e}(\mathbf{r}) = \underbrace{-\frac{1}{4\pi}\nabla\int_U\left[\frac{\eta(\mathbf{r}')}{\varepsilon_0}\frac{1}{|\mathbf{r}-\mathbf{r}'|}\right]d^3r'}_{Electrostatic} \underbrace{-\frac{1}{4\pi}\nabla\times\int_U\left[\frac{\partial \mathbf{b}(\mathbf{r}')}{\partial t}\frac{1}{|\mathbf{r}-\mathbf{r}'|}\right]d^3r'}_{Electrodynamic} \tag{B.43}$$

and

$$\mathbf{b}(\mathbf{r}) = \underbrace{\frac{\mu_0}{4\pi}\nabla\times\int_U \mathbf{j}(\mathbf{r}')\frac{1}{|\mathbf{r}-\mathbf{r}'|}d^3r'}_{Magnetostatic} + \underbrace{\frac{1}{4\pi}\frac{1}{c^2}\nabla\times\int_U \frac{\partial \mathbf{e}(\mathbf{r}')}{\partial t}\frac{1}{|\mathbf{r}-\mathbf{r}'|}d^3r'}_{Magnetodynamic} \tag{B.44}$$

Various rearrangements and forms of these equations will now be examined to provide confidence that these equations are compatible with more familiar forms.

B.2.1 e, b: free-space formulation

In a region of space devoid of all matter (charge/current density), equations (B.43) and **Error! Reference source not found.** reduce to:

$$\mathbf{e}(\mathbf{r}) = -\frac{1}{4\pi}\nabla\times\int_U \frac{\partial \mathbf{b}(\mathbf{r}')}{\partial t}\frac{1}{|\mathbf{r}-\mathbf{r}'|}d^3r' \tag{B.45}$$

$$\mathbf{b}(\mathbf{r}) = \frac{1}{4\pi c^2}\nabla\times\int_U \frac{\partial \mathbf{e}(\mathbf{r}')}{\partial t}\frac{1}{|\mathbf{r}-\mathbf{r}'|}d^3r'. \tag{B.46}$$

The Gaussian unit form of these SI unit equations is quoted by physicist Eugene Wigner in his 1969 paper "*Are we machines?*"(Wigner 1969), which considered the 'incompleteness' of Maxwell's equations.

B.2.2 e, b integral form: consistency with Gauss' law

Here we consider how the differential form of Gauss' law results from appropriate assumptions applied to (B.43) and **Error! Reference source not found.**:

$$\nabla\cdot\mathbf{e}=-\frac{1}{4\pi}\nabla\cdot\left[\nabla\int_U\frac{\eta(\mathbf{r}')}{\varepsilon_0}\frac{1}{|\mathbf{r}-\mathbf{r}'|}d^3r'+\nabla\times\int_U\frac{\partial\mathbf{b}(\mathbf{r}')}{\partial t}\frac{1}{|\mathbf{r}-\mathbf{r}'|}d^3r'\right]. \tag{B.47}$$

Because of the vector identity

$$\nabla\cdot(\nabla\times\mathbf{V})=0 \text{ (for an arbitrary field V),} \tag{B.48}$$

equation (B.47) reduces to

$$\nabla\cdot\mathbf{e}=-\frac{1}{4\pi\varepsilon_0}\left[\nabla\cdot\nabla\int_U\frac{\eta(\mathbf{r}')}{|\mathbf{r}-\mathbf{r}'|}d^3r'\right]. \tag{B.49}$$

Using the identity

$$\nabla\cdot f\mathbf{a}=\mathbf{a}\cdot\nabla f+f\nabla\cdot\mathbf{a} \tag{B.50}$$

with f=1/|**r** – **r'**| and, bearing in mind that the ∇ operator operates on **r** not **r**', we can rearrange (B.49) as

$$\nabla\cdot\mathbf{e}(\mathbf{r})=-\frac{1}{4\pi\varepsilon_0}\left[\nabla\cdot\int_U\nabla\left(\frac{\eta(\mathbf{r}')}{|\mathbf{r}-\mathbf{r}'|}\right)d^3r'\right] \tag{B.51}$$

The right side of which becomes:

$$-\frac{1}{4\pi\varepsilon_0}\left[\nabla\cdot\int_U\eta(\mathbf{r}')\nabla\left(\frac{1}{|\mathbf{r}-\mathbf{r}'|}\right)d^3r'\right] \tag{B.52}$$

Using the vector identity(Jackson 1999, page 29):

$$\nabla\left(\frac{1}{|\mathbf{r}-\mathbf{r}'|}\right)=-\frac{\mathbf{r}-\mathbf{r}'}{|\mathbf{r}-\mathbf{r}'|^3}=-\nabla'\left(\frac{1}{|\mathbf{r}-\mathbf{r}'|}\right) \tag{B.53}$$

And (Jackson 1999, page 35):

$$\nabla\cdot\left(-\frac{\mathbf{r}-\mathbf{r}'}{|\mathbf{r}-\mathbf{r}'|^3}\right)=\nabla\cdot\left[\nabla\left(\frac{1}{|\mathbf{r}-\mathbf{r}'|}\right)\right]=\nabla^2\left(\frac{1}{|\mathbf{r}-\mathbf{r}'|}\right)=-4\pi\delta(\mathbf{r}-\mathbf{r}') \tag{B.54}$$

or

$$\nabla\cdot\left(\frac{\mathbf{r}-\mathbf{r}'}{|\mathbf{r}-\mathbf{r}'|^3}\right)=4\pi\delta(\mathbf{r}-\mathbf{r}') \tag{B.55}$$

The divergence of **e** becomes:

$$\nabla\cdot\mathbf{e}(\mathbf{r})=\frac{4\pi}{4\pi\varepsilon_0}\int_U\eta(\mathbf{r}')\delta(\mathbf{r}-\mathbf{r}')d^3r'. \tag{B.56}$$

By virtue of the Dirac delta function the integrand is only defined at **r** = **r**' and the volume integral evaluates to:

$$\nabla \cdot \mathbf{e}(\mathbf{r}) = \frac{\eta(\mathbf{r})}{\varepsilon_0} \tag{B.57}$$

Which is the familiar result from equation (B.1) for the divergence of the microscopic electric field. The equation (B.4) divergence of the magnetic field is immediately obvious from equation (B.48). We thus have some comfort in having a 'complete' specification of **e** and **b**. For more detail of the contrasting behaviours of the macroscopic and microscopic equations and their derivation see Jackson(Jackson 1999), Russakof (Russakof.G 1970), Craig and Thirunamachandran(Craig and Thirunamachandran 1984) and also, more recently, Yan(Yan 1995) and the various references therein.

B.2.3 e,b integral form: expressing the Coulomb field

For completeness, the link between equations (B.43) (**e**) and **Error! Reference source not found.** (**b**) and the standard electrostatics form used in molecular *mechanics* (Coulomb force field) is derived. Most molecular dynamics ensembles outside a biomolecular context assume that the overall ensemble has no net current density **j** and that spatiotemporal variability of charge motion is so minor that the **e** term dominates the forces in the Lorentz equation (effectively the magnetic field is zero and its rate of change is zero, as is the rate of change of **e**). As such equation **Error! Reference source not found.** for **b** is ignored, as is the right hand side of equation (B.43) for **e**. That being the case, equation (B.43) reduces to

$$\mathbf{e}(\mathbf{r}) = -\frac{1}{4\pi}\nabla\int_U \left[\frac{\eta(\mathbf{r}')}{\varepsilon_0}\frac{1}{|\mathbf{r}-\mathbf{r}'|}\right] d^3r' . \tag{B.58}$$

This is the origin of the Coulomb force field found in molecular mechanics formulations. The k^{th} point charge q_k in an ensemble of K charges, each located at position $\mathbf{r}_k(t)$ has a charge density function:

$$\eta_k(\mathbf{r},t) = q_k\delta(\mathbf{r}-\mathbf{r}_k(t)) \tag{B.59}$$

Note that we have not assumed that there is no charge motion, but merely that the motion is slow and changes slowly enough for no electrodynamic or magnetostatic terms to be significant. Thus the position of particle k can change with time. For our ensemble of charges, this becomes the classic Coulomb potential(Sadiku 2001, Page 106):

$$\eta(\mathbf{r},t) = \sum_{k=1}^{K} q_k\delta(\mathbf{r}-\mathbf{r}_k(t)) \tag{B.60}$$

When (B.60) is inserted in the integral term of (B.58), it becomes:

$$\mathbf{e}(\mathbf{r}) = -\frac{1}{4\pi\varepsilon_0}\nabla\int_U \frac{\sum_{k=1}^{K} q_k\delta(\mathbf{r}-\mathbf{r}_k(t))}{|\mathbf{r}-\mathbf{r}'|} d^3r' \tag{B.61}$$

This becomes, rearranging terms:

$$\mathbf{e}(\mathbf{r}) = -\frac{1}{4\pi\varepsilon_0}\sum_{k=1}^{K} q_k\left[\nabla\int_U \frac{\delta(\mathbf{r}-\mathbf{r}_k(t))}{|\mathbf{r}-\mathbf{r}'|} d^3r'\right] \tag{B.62}$$

To construct the total field consider the contribution of particle k alone:

$$\mathbf{e}_k(\mathbf{r}) = -\frac{q_k}{4\pi\varepsilon_0}\nabla\int_U \frac{\delta(\mathbf{r}'-\mathbf{r}_k(t))}{|\mathbf{r}-\mathbf{r}'|} d^3r' \tag{B.63}$$

This integration only has a non-zero integrand when

$$\mathbf{r}' = \mathbf{r}_k(t) \tag{B.64}$$

And the Dirac delta function results in (B.63) taking on the form:

$$\mathbf{e}_k(\mathbf{r}) = -\frac{q_k}{4\pi\varepsilon_0}\nabla\left[\frac{1}{|\mathbf{r}-\mathbf{r}_k(t)|}\right] \tag{B.65}$$

Using the general identity(B.53):

$$\mathbf{e}_k(\mathbf{r}) = \frac{q_k}{4\pi\varepsilon_0}\left[\frac{\mathbf{r}-\mathbf{r}_k(t)}{|\mathbf{r}-\mathbf{r}_k(t)|^3}\right] \tag{B.66}$$

This is the familiar Coulomb potential form for a single charge(Sadiku 2001, Page 106). When inserted into (B.62) we get the total field:

$$\mathbf{e}(\mathbf{r}) = \frac{q_k}{4\pi\varepsilon_0}\sum_{k=1}^{K} q_k \frac{(\mathbf{r}-\mathbf{r}_k(t))}{|\mathbf{r}-\mathbf{r}_k(t)|^3} \tag{B.67}$$

It is this form which is found in the molecular mechanics formulations eg (MacKerell 2001).

B.2.4 e,b integral form: b and the Biot-Savart (magnetic) field

Again, for completeness and confidence in the total field formulation we can show that equation **Error! Reference source not found.** contains the Biot-Savart Law of magnetostatics. Consider the first term of equation **Error! Reference source not found.**, which is the 'magnetostatic' term which is generally left out of MD formulations (see Jackson for the MME version (Jackson 1999, Page 179)):

$$\mathbf{b}(\mathbf{r}) = \frac{\mu_0}{4\pi}\nabla\times\int_U \frac{\mathbf{j}(\mathbf{r}')}{|\mathbf{r}-\mathbf{r}'|}d^3r' \tag{B.68}$$

Bringing the curl operator inside the integral:

$$\mathbf{b}(\mathbf{r}) = \frac{\mu_0}{4\pi}\int_U\left[\nabla\times\frac{\mathbf{j}(\mathbf{r}')}{|\mathbf{r}-\mathbf{r}'|}\right]d^3r' \tag{B.69}$$

Introducing the general vector identity:

$$\nabla\times f\mathbf{a} = (\nabla f\times\mathbf{a}) + (f\nabla\times\mathbf{a}) \tag{B.70}$$

If we assign the role of **a** to **j**(**r**') and f to 1/|**r**-**r'**| then the integrand of (B.69) becomes:

$$\nabla\times\left[\frac{\mathbf{j}(\mathbf{r}')}{|\mathbf{r}-\mathbf{r}'|}\right] = \left(\nabla\left(\frac{1}{|\mathbf{r}-\mathbf{r}'|}\right)\times\mathbf{j}(\mathbf{r}')\right)_a + \left(\frac{1}{|\mathbf{r}-\mathbf{r}'|}\nabla\times\mathbf{j}(\mathbf{r}')\right)_b. \tag{B.71}$$

Note that the curl operates with respect to **r** not **r**', so the *b* term in (B.71) becomes zero.

$$\nabla\times\left[\frac{\mathbf{j}(\mathbf{r}')}{|\mathbf{r}-\mathbf{r}'|}\right] = \nabla\left(\frac{1}{|\mathbf{r}-\mathbf{r}'|}\right)\times\mathbf{j}(\mathbf{r}') \tag{B.72}$$

Using the identity of equation (B.53), equation (B.72) becomes:

$$\nabla\times\left[\frac{\mathbf{j}(\mathbf{r}')}{|\mathbf{r}-\mathbf{r}'|}\right] = -\left(\frac{\mathbf{r}-\mathbf{r}'}{|\mathbf{r}-\mathbf{r}'|^3}\right)\times\mathbf{j}(\mathbf{r}') = \mathbf{j}(\mathbf{r}')\times\left(\frac{\mathbf{r}-\mathbf{r}'}{|\mathbf{r}-\mathbf{r}'|^3}\right) \tag{B.73}$$

Inserting (B.73) in (B.69) reveals that equation (B.68) finally becomes

$$\mathbf{b}(\mathbf{r}) = \frac{\mu_0}{4\pi}\int_U \left[\mathbf{j}(\mathbf{r}') \times \left(\frac{\mathbf{r}-\mathbf{r}'}{|\mathbf{r}-\mathbf{r}'|^3} \right) \right] d^3r' \quad \textbf{(B.74)}$$

which is the microscopic version of the macroscopic result in Jackson(Jackson 1999, Page 178), which is a generalisation of the Biot-Savart law.

B.2.5 e,b integral form: Integral to differential form-preliminaries

The following two sections deliver the one remaining test of the integral form of the MmE equations by showing how they generally lead to the differential forms. To carry this out requires a particularly obscure integration which is done here in generic form. Consider an arbitrary (well behaved in the sense of differentiable) vector function of a vector parameter **f**(**r**). Now consider the integral:

$$\mathbf{I}_{\mathrm{f}}(\mathbf{r}) = \frac{1}{4\pi}\nabla \times \int_U \left[\mathbf{f}(\mathbf{r}') \frac{1}{|\mathbf{r}-\mathbf{r}'|} \right] d^3r' \quad \textbf{(B.75)}$$

For the integral to differential version of this equation we take the CURL of $\mathbf{I}_{\mathrm{f}}(\mathbf{r})$ thus:

$$\nabla \times \mathbf{I}_{\mathrm{f}}(\mathbf{r}) = \frac{1}{4\pi}\nabla \times \nabla \times \int_U \left[\mathbf{f}(\mathbf{r}') \frac{1}{|\mathbf{r}-\mathbf{r}'|} \right] d^3r' \quad \textbf{(B.76)}$$

To evaluate the right side of (B.76) we make use of the vector identity:

$$\nabla \times \nabla \times \mathbf{a} = \nabla(\nabla \bullet \mathbf{a}) - \nabla^2 \mathbf{a} \quad \textbf{(B.77)}$$

Setting **a** in (B.77) as follows:

$$\mathbf{a} = \mathbf{f}(\mathbf{r}') \frac{1}{|\mathbf{r}-\mathbf{r}'|} \quad \textbf{(B.78)}$$

Moving the CURLs inside the integration and inserting **a** gives:

$$\nabla \times \mathbf{I}_{\mathrm{f}}(\mathbf{r}) = \frac{1}{4\pi}\int_U \nabla \left(\nabla \bullet \left[\mathbf{f}(\mathbf{r}') \frac{1}{|\mathbf{r}-\mathbf{r}'|} \right] \right) - \nabla^2 \left[\mathbf{f}(\mathbf{r}') \frac{1}{|\mathbf{r}-\mathbf{r}'|} \right] d^3r' \quad \textbf{(B.79)}$$

For the record, because it is relatively obscure, note that the last term in equation (B.77) is the *vector* Laplacian, which has the form:

$$\begin{aligned} \nabla^2 \mathbf{a} = & \left[\frac{\partial^2 a_x(r_x,r_y,r_z)}{\partial {r_x}^2} + \frac{\partial^2 a_x(r_x,r_y,r_z)}{\partial {r_y}^2} + \frac{\partial^2 a_x(r_x,r_y,r_z)}{\partial {r_z}^2} \right] \mathbf{u}_x \\ & + \left[\frac{\partial^2 a_y(r_x,r_y,r_z)}{\partial {r_x}^2} + \frac{\partial^2 a_y(r_x,r_y,r_z)}{\partial {r_y}^2} + \frac{\partial^2 a_y(r_x,r_y,r_z)}{\partial {r_z}^2} \right] \mathbf{u}_y \\ & + \left[\frac{\partial^2 a_z(r_x,r_y,r_z)}{\partial {r_x}^2} + \frac{\partial^2 a_z(r_x,r_y,r_z)}{\partial {r_y}^2} + \frac{\partial^2 a_z(r_x,r_y,r_z)}{\partial {r_z}^2} \right] \mathbf{u}_z \end{aligned} \quad \textbf{(B.80)}$$

Where $\mathbf{a} = a_x\mathbf{u}_x + a_y\mathbf{u}_y + a_z\mathbf{u}_z$ and the **u** are unit vectors in the three orthogonal axes. Equation (B.80) relates to the scalar laplacian as follows:

$$\nabla^2 \mathbf{a} = \nabla^2 a_x(r_x,r_y,r_z)\mathbf{u}_x + \nabla^2 a_y(r_x,r_y,r_z)\mathbf{u}_y + \nabla^2 a_z(r_x,r_y,r_z)\mathbf{u}_z \quad \textbf{(B.81)}$$

Moving on, we now perform the two separate integrals of (B.79) thus:

$$\nabla\times\mathbf{I}_f(\mathbf{r})=\frac{1}{4\pi}\int_U\nabla\left(\nabla\bullet\left[\mathbf{f}(\mathbf{r}')\frac{1}{|\mathbf{r}-\mathbf{r}'|}\right]\right)d^3r'\Bigg|_{(a)}-\frac{1}{4\pi}\int_U\nabla^2\left[\mathbf{f}(\mathbf{r}')\frac{1}{|\mathbf{r}-\mathbf{r}'|}\right]d^3r'\Bigg|_{(b)}, \tag{B.82}$$

Function **f** operates on primed variables only. Using (B.81) therefore transforms (B.82)(b) into

$$\frac{1}{4\pi}\int_U\mathbf{f}(\mathbf{r}')\nabla^2\left[\frac{1}{|\mathbf{r}-\mathbf{r}'|}\right]d^3r'\Bigg|_{(b)}, \tag{B.83}$$

Using the identity (proven in a later chapter)

$$\nabla^2\left[\frac{1}{|\mathbf{r}-\mathbf{r}'|}\right]=-4\pi\delta(\mathbf{r}-\mathbf{r}'), \tag{B.84}$$

equation (B.82)(b) becomes:

$$\frac{1}{4\pi}\int_U\mathbf{f}(\mathbf{r}')4\pi\delta(\mathbf{r}-\mathbf{r}')d^3r'\Bigg|_{(b)}=\mathbf{f}(\mathbf{r}). \tag{B.85}$$

Equation (B.82)(a) is a little more troublesome. Making use of identity (B.53), identity (B.50) and rearranging (B.82)(a) terms:

$$\frac{1}{4\pi}\nabla\int_U\mathbf{f}(\mathbf{r}')\bullet\nabla'\left[\frac{1}{|\mathbf{r}-\mathbf{r}'|}\right]d^3r'\Bigg|_{(a)} \tag{B.86}$$

Note that **f** has the following form:

$$\mathbf{f}(r_x,r_y,r_z)=f_x(r_x,r_y,r_z)\mathbf{u}_x+f_y(r_x,r_y,r_z)\mathbf{u}_y+f_z(r_x,r_y,r_z)\mathbf{u}_z, \tag{B.87}$$

and the dot product in the (B.86) integrand becomes the scalar quantity

$$\begin{aligned}\mathbf{f}(\mathbf{r}')\bullet\nabla'\left[\frac{1}{|\mathbf{r}-\mathbf{r}'|}\right]=&+f_x(r_x',r_y',r_z')\frac{\partial}{\partial r_x'}\left[\frac{1}{|\mathbf{r}-\mathbf{r}'|}\right]\\&+f_y(r_x',r_y',r_z')\frac{\partial}{\partial r_y'}\left[\frac{1}{|\mathbf{r}-\mathbf{r}'|}\right]\\&+f_z(r_x',r_y',r_z')\frac{\partial}{\partial r_z'}\left[\frac{1}{|\mathbf{r}-\mathbf{r}'|}\right]\end{aligned}, \tag{B.88}$$

This suggests no obvious quick way to evaluate the integral. However, the integration of (B.88) in (B.86) can be done by parts. In consideration of

$$\frac{1}{4\pi}\nabla\int_U\mathbf{f}(\mathbf{r}')\bullet\nabla'\left[\frac{1}{|\mathbf{r}-\mathbf{r}'|}\right]d^3r'\Bigg|_{(a)}, \tag{B.89}$$

we first note that vector integration by parts over a 3-space volume Ω bounded by a surface δΩ with surface normal **n** is as follows:

$$\int_\Omega\nabla u\bullet\mathbf{v}\,d^3r=\int_{\delta\Omega}u\mathbf{v}\bullet\mathbf{n}\,ds-\int_\Omega u\nabla\bullet\mathbf{v}\,d^3r, \tag{B.90}$$

with **v** = **f(r')** and u=1/|**r-r'**|. In our case the volume is U, the entire universe, and the surface integral sums to zero if we assume that **f** is a function of a class that approaches zero at least as fast as 1/|**r-r'**|. The (B.89) integrand thus takes the form of the right term in (B.90) and becomes:

$$-\frac{1}{4\pi}\nabla\int_U\left[\frac{\nabla'\bullet\mathbf{f}(\mathbf{r}')}{|\mathbf{r}-\mathbf{r}'|}\right]d^3r'\Bigg|_{(a)} \tag{B.91}$$

Thus the total volume integral of (B.82) becomes:

$$\nabla\times\mathbf{I}_f(\mathbf{r})=-\frac{1}{4\pi}\nabla\int_U\left[\frac{\nabla'\bullet\mathbf{f}(\mathbf{r}')}{|\mathbf{r}-\mathbf{r}'|}\right]d^3r'+\mathbf{f}(\mathbf{r}) \tag{B.92}$$

The CURL $\mathbf{I}_f$ thus takes on a value depending on the divergence of **f**. The interpretation of a particular application of the equation will lead to a result. In the case of MmE equations the DIV term is zero and represents a conservation law. A MME version of this integral can be found in (Jackson 1999, Page 179). It has been generalised above and is now adapted to MmE.

B.2.6 Integral to differential form: e(r)

Equation (B.92) is now applied with $\mathbf{I}_f = \mathbf{e}(\mathbf{r})$ and applied to (B.43) slightly rearranged:

$$\begin{aligned}\nabla\times\mathbf{e}(\mathbf{r})&=\left[-\frac{1}{4\pi}\nabla\times\nabla\int_U\left[\frac{\eta(\mathbf{r}')}{\varepsilon_0}\frac{1}{|\mathbf{r}-\mathbf{r}'|}\right]d^3r'\right]_{(a)}\\&+\left[-\frac{1}{4\pi}\nabla\times\nabla\times\int_U\left[\frac{\partial\mathbf{b}(\mathbf{r}')}{\partial t}\frac{1}{|\mathbf{r}-\mathbf{r}'|}\right]d^3r'\right]_{(b)}\end{aligned} \tag{B.93}$$

A standard vector identity says that the CURL of the GRAD of any scalar function of a vector is always zero. Therefore (B.93) (a) is zero. We now apply equation (B.92) to (B.93)(b) with:

$$\mathbf{f}(\mathbf{r}')=\frac{\partial\mathbf{b}(\mathbf{r}')}{\partial t}, \tag{B.94}$$

which gives

$$\nabla\times\mathbf{e}(\mathbf{r})=-\left[-\frac{1}{4\pi}\nabla\int_U\frac{\nabla'\bullet\frac{\partial\mathbf{b}(\mathbf{r}')}{\partial t}}{|\mathbf{r}-\mathbf{r}'|}d^3r'+\frac{\partial\mathbf{b}(\mathbf{r})}{\partial t}\right], \tag{B.95}$$

From (B.3) the DIV of the magnetic field **b** is always zero, hence the integrand is zero and equation (B.95) becomes

$$\nabla\times\mathbf{e}(\mathbf{r})=-\frac{\partial\mathbf{b}(\mathbf{r})}{\partial t}, \tag{B.96}$$

which is the differential form above in (B.2).

B.2.7 Integral to differential form: b(r)

Equation (B.92) is now applied with $\mathbf{I}_f = \mathbf{b}(\mathbf{r})$ and applied to **Error! Reference source not found.** slightly rearranged:

$$\nabla\times\mathbf{b}(\mathbf{r})=\left[\frac{1}{4\pi}\nabla\times\nabla\times\int_U\mu_0\mathbf{j}(\mathbf{r}')\frac{1}{|\mathbf{r}-\mathbf{r}'|}d^3r'\right]_{(a)} \tag{B.97}$$

$$+\left[\frac{1}{4\pi}\nabla\times\nabla\times\int_U\frac{1}{c^2}\frac{\partial\mathbf{e}(\mathbf{r}')}{\partial t}\frac{1}{|\mathbf{r}-\mathbf{r}'|}d^3r'\right]\Bigg|_{(b)}$$

Noting that the time dependence is implicit throughout. We now apply (B.92) twice, first to (B.97)(a) with

$$\mathbf{f}(\mathbf{r}')=\mu_0\mathbf{j}(\mathbf{r}'), \tag{B.98}$$

which generates:

$$-\frac{1}{4\pi}\nabla\int_U\left[\frac{\nabla'\bullet\mu_0\mathbf{j}(\mathbf{r}')}{|\mathbf{r}-\mathbf{r}'|}\right]d^3r'+\mu_0\mathbf{j}(\mathbf{r}). \tag{B.99}$$

To see how to interpret the integrand of (B.99) we can take the DIV of equation (B.4):

$$\nabla\bullet\left(\nabla\times\mathbf{b}(\mathbf{r})\right)-\frac{1}{c^2}\nabla\bullet\frac{\partial\mathbf{e}(\mathbf{r})}{\partial t}=\mu_0\nabla\bullet\mathbf{j}(\mathbf{r}). \tag{B.100}$$

The first term of (B.100) is always zero. The remaining terms become, using (B.1) for the **e** term:

$$-\frac{1}{c^2}\frac{\partial}{\partial t}\left[\nabla\bullet\mathbf{e}(\mathbf{r})\right]=-\frac{1}{c^2}\frac{\partial}{\partial t}\left[\frac{\eta(\mathbf{r}')}{\varepsilon_0}\right]=\mu_0\nabla\bullet\mathbf{j}(\mathbf{r}) \tag{B.101}$$

The DIV term in (B.99) will only be non-zero when charge is created (or enters/leaves a given simulated volume). Thus, because charge is conserved (we can enforce containment in a simulation over a limited volume V in a particular experiment) the DIV of the current density is always zero. Note that this does not apply in the macroscopic quasi-magnetostatic formulation, where there is no DIV only in 'steady-state conditions'(Jackson 1999, Page 219). This means that the final result of (B.97)(a) from (B.99) is:

$$\mu_0\mathbf{j}(\mathbf{r}) \tag{B.102}$$

Next we apply equation (B.92) to (B.97)(b) with:

$$\mathbf{f}(\mathbf{r}')=\frac{1}{c^2}\frac{\partial\mathbf{e}(\mathbf{r}')}{\partial t}, \tag{B.103}$$

which generates

$$\nabla\times\mathbf{b}(\mathbf{r})=-\frac{1}{4\pi}\nabla\int_U\left[\frac{\nabla'\bullet\frac{1}{c^2}\frac{\partial\mathbf{e}(\mathbf{r}')}{\partial t}}{|\mathbf{r}-\mathbf{r}'|}\right]d^3r'+\frac{1}{c^2}\frac{\partial\mathbf{e}(\mathbf{r})}{\partial t}. \tag{B.104}$$

The integrand of (B.104) is zero for the reasons already outlined above. This means that the final result of (B.97)(b) term from (B.104) is

$$\frac{1}{c^2}\frac{\partial\mathbf{e}(\mathbf{r}')}{\partial t}. \tag{B.105}$$

Substituting (B.102) and (B.105) into (B.97) gives

$$\nabla\times\mathbf{b}(\mathbf{r})=\mu_0\mathbf{j}(\mathbf{r})+\frac{1}{c^2}\frac{\partial\mathbf{e}(\mathbf{r})}{\partial t}. \tag{B.106}$$

This is the differential form as per (B.4).

B.3 Another road through field decomposition

The above Helmholtz decomposition process that resulted in (B.43) and **Error! Reference source not found.** has another quick route which can be deduced from Jackson(Jackson 1999, Section 6.3). It is generalised here and applied to the microscopic form. As already outlined, fundamental vector calculus tells us that any vector field **F** can be expressed as a sum of a solenoidal (transverse) $\mathbf{F}_t$ and irrotational (longitudinal) $\mathbf{F}_l$ components:

$$\mathbf{F} = \mathbf{F}_l + \mathbf{F}_t \text{ or } \mathbf{F} = \mathbf{F}_{\parallel} + \mathbf{F}_{\perp}, \tag{B.107}$$

where either set of subscript symbols can be found in the literature. For the moment we will use the former. The choice is arbitrary. The components of **F** satisfy

$$\nabla \times \mathbf{F}_l = 0 \tag{B.108}$$

and

$$\nabla \bullet \mathbf{F}_t = 0. \tag{B.109}$$

As the previous Helmholtz decomposition method showed, one route to recovery of $\mathbf{F}_t$ and $\mathbf{F}_l$ from **F** is via:

$$\mathbf{F}_l(\mathbf{r}) = -\frac{1}{4\pi}\nabla \int_U \frac{\nabla \bullet \mathbf{F}(\mathbf{r}')}{|\mathbf{r}-\mathbf{r}'|} d^3 r' \tag{B.110}$$

$$\mathbf{F}_t(\mathbf{r}) = \frac{1}{4\pi}\nabla \times \nabla \times \int_U \frac{\mathbf{F}(\mathbf{r}')}{|\mathbf{r}-\mathbf{r}'|} d^3 r' \tag{B.111}$$

The proof of this can be done by expansion of (B.111) using the standard identity:

$$\nabla \times \nabla \times \mathbf{V} = \nabla(\nabla \bullet \mathbf{V}) - \nabla^2 \mathbf{V} \tag{B.112}$$

with **V** as

$$\mathbf{V}(\mathbf{r}) = \int_U \frac{\frac{\mathbf{F}(\mathbf{r}')}{4\pi}}{|\mathbf{r}-\mathbf{r}'|} d^3 r', \tag{B.113}$$

This makes (B.111) become

$$\mathbf{F}_t(\mathbf{r}) = \frac{1}{4\pi}\left\{\nabla\left[\int_U \nabla \bullet \frac{\mathbf{F}(\mathbf{r}')}{|\mathbf{r}-\mathbf{r}'|} d^3 r'\right] - \nabla^2\left[\int_U \frac{\mathbf{F}(\mathbf{r}')}{|\mathbf{r}-\mathbf{r}'|} d^3 r'\right]\right\} \tag{B.114}$$

which becomes

$$\mathbf{F}_t(\mathbf{r}) = \frac{1}{4\pi}\left\{\nabla\left[\int_U \mathbf{F}(\mathbf{r}') \bullet \nabla\left(\frac{1}{|\mathbf{r}-\mathbf{r}'|}\right) d^3 r'\right] - \nabla^2\left[\int_U \frac{\mathbf{F}(\mathbf{r}')}{|\mathbf{r}-\mathbf{r}'|} d^3 r'\right]\right\} \tag{B.115}$$

$$\mathbf{F}_t(\mathbf{r}) = \frac{1}{4\pi}\left\{\nabla\left[-\int_U \mathbf{F}(\mathbf{r}') \bullet \nabla'\left(\frac{1}{|\mathbf{r}-\mathbf{r}'|}\right) d^3 r'\right] - \left[\int_U \nabla^2\left(\frac{\mathbf{F}(\mathbf{r}')}{|\mathbf{r}-\mathbf{r}'|}\right) d^3 r'\right]\right\} \tag{B.116}$$

$$\mathbf{F}_t(\mathbf{r}) = \frac{1}{4\pi}\left\{\nabla\left[-\int_U \mathbf{F}(\mathbf{r}') \bullet \nabla'\left(\frac{1}{|\mathbf{r}-\mathbf{r}'|}\right) d^3 r'\right] - \left[\int_U \mathbf{F}(\mathbf{r}') \nabla^2\left(\frac{1}{|\mathbf{r}-\mathbf{r}'|}\right) d^3 r'\right]\right\} \tag{B.117}$$

Integration of (B.117) by parts as per (B.90) as well as use of identity (B.54) gives

$$\mathbf{F}_t(\mathbf{r}) = \frac{1}{4\pi}\left\{\nabla\left[-\left(-\nabla\int_U \frac{\nabla'\bullet\mathbf{F}(\mathbf{r}')}{|\mathbf{r}-\mathbf{r}'|}d^3r'\right)\right] + 4\pi\mathbf{F}(\mathbf{r})\right\} \quad \textbf{(B.118)}$$

and

$$\mathbf{F}_t(\mathbf{r}) = \frac{1}{4\pi}\nabla\int_U\left(\frac{\nabla'\bullet\mathbf{F}(\mathbf{r}')}{|\mathbf{r}-\mathbf{r}'|}\right)d^3r' + \mathbf{F}(\mathbf{r}), \quad \textbf{(B.119)}$$

which, applying (B.107), leads to

$$\mathbf{F}(\mathbf{r}) = \mathbf{F}_t(\mathbf{r}) - \frac{1}{4\pi}\nabla\int_U\left(\frac{\nabla'\bullet\mathbf{F}(\mathbf{r}')}{|\mathbf{r}-\mathbf{r}'|}\right)d^3r' \quad \textbf{(B.120)}$$

or

$$\mathbf{F}_l(\mathbf{r}) = -\frac{1}{4\pi}\nabla\int_U\frac{\nabla'\bullet\mathbf{F}(\mathbf{r}')}{|\mathbf{r}-\mathbf{r}'|}d^3r', \quad \textbf{(B.121)}$$

which is (B.110). The process is thus self consistent. By way of example, if we apply (B.110) and (B.111) to current density as a vector field we get:

$$\mathbf{j}_l(\mathbf{r}) = -\frac{1}{4\pi}\nabla\int_U\frac{\nabla'\bullet\mathbf{j}(\mathbf{r}')}{|\mathbf{r}-\mathbf{r}'|}d^3r' \quad \textbf{(B.122)}$$

$$\mathbf{j}_t(\mathbf{r}) = \frac{1}{4\pi}\nabla\times\nabla\times\int_U\frac{\mathbf{j}(\mathbf{r}')}{|\mathbf{r}-\mathbf{r}'|}d^3r', \quad \textbf{(B.123)}$$

This result can be seen in Jackson(Jackson 1999, Page 242).

B.4 Bibliography

Arfken, G. B. and Weber, H. J., Mathematical Methods for Physicists, 5th ed., Harcourt Academic, San Diego, Calif. ; London, 2001, pp. xiv, 1112 p.

Craig, D. P. and Thirunamachandran, T., Molecular Quantum Electrodynamics : An Introduction to Radiation-Molecule Interactions, Academic Press, London ; Orlando, 1984, pp. xi, 324 p.

Jackson, J. D., Classical Electrodynamics, 3rd ed., Wiley, New York, 1999

MacKerell, A. D. (2001) Atomistic Models and Force Fields. In O. M. Becker, A. D. MacKerrel, B. Roux, and M. Watanabe (eds.). *Computational Chemistry and Biophysics*, Marcel Dekker, Inc, New York.

Nunez, P. L. and Srinivasan, R., Electric Fields of the Brain : The Neurophysics of Eeg, 2nd ed., Oxford University Press, Oxford, New York, 2006

Russakof.G. 'A Derivation of Macroscopic Maxwell Equations', *American Journal of Physics* vol. 38, no. 10, 1970. 1188-&.

Sadiku, M. N. O., Elements of Electromagnetics, 3rd ed., Oxford University Press, New York, 2001

Wigner, E. P. 'Are We Machines?', *Proceedings of the American Philosophical Society* vol. 113, no. 2, 1969. 95-101.

Yan, C. C. 'Can the Macroscopic Maxwell Equations Be Obtained from the Microscopic Maxwell-Lorentz Equations by Performing Averages?', *Foundations of Physics* vol. 25, no. 3, 1995. 491-502.

Appendix C

CHAPTER 7, TEST 6 ION CHANNEL ALLOCATION

C.1 General organization of the filaments of the artificial dendrite structure

Frusta 1-7 were retained. Two 46-frustum dendrites were constructed from D151 original dendrites 71…284 as shown in Table C-1. The general nature of the filaments is that a 'stripe' is a straight line of identically directed filaments spaced 'pitch' apart and centred, as a group, equidistant from the frustum ends. All stripes are spaced equidistantly around the circumference of the frustum.

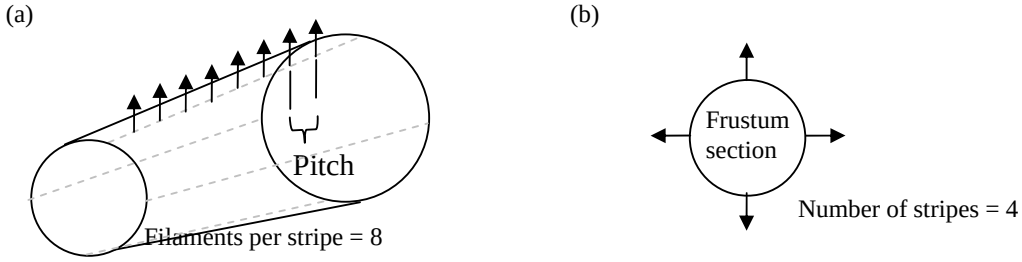

Figure C-1 General arrangement of ion channels on artificial dendrites.

The figure shows that the ion channels are in a grid pattern, but following the slope of the frustum. The transmembrane total current that is applied to the ion channels is the D151 original compartment current. For example, Table C-1 shows that artificial dendrites 17 and 63 (marked with a *) are both based on D151 frustum 165. Both these compartments are therefore driven by the D151 frustum 165 current.

C.2 Filament allocation per compartment.

Final Compartment number	Number of stripes	Filaments per stripe	TOTAL filaments	D151 Original Compartment	Description
1	28	5	140	1	Soma
2	34	4	136	2	Soma

3	36	4	144	3	Soma
4	32	3	96	4	Soma
5	23	4	92	5	Soma
6	6	10	60	6	Hill
7	4	13	52	7	Iseg
8	8	8	64	72	Dendrite1,1
9	7	9	63	118	Dendrite1,2
10	5	6	30	119	Dendrite1,3
11	5	5	25	140	Dendrite1,4
12	5	14	70	141	Dendrite1,5
13	5	27	135	142	Dendrite1,6
14	4	9	36	162	Dendrite1,7
15	4	10	40	163	Dendrite1,8
16	4	8	32	164	Dendrite1,9
*17	4	4	16	165	Dendrite1,10
18	4	6	24	177	Dendrite1,11
19	4	9	36	178	Dendrite1,12
20	4	7	28	179	Dendrite1,13
21	4	6	24	180	Dendrite1,14
22	4	7	28	181	Dendrite1,15
23	4	6	24	182	Dendrite1,16
24	4	7	28	183	Dendrite1,17
25	4	7	28	184	Dendrite1,18
26	4	6	24	185	Dendrite1,19
27	4	4	16	186	Dendrite1,20
28	4	3	12	187	Dendrite1,21
29	4	4	16	188	Dendrite1,22
30	4	6	24	189	Dendrite1,23
31	4	6	24	190	Dendrite1,24
32	4	4	16	191	Dendrite1,25
33	2	5	20	192	Dendrite1,26
34	2	5	20	193	Dendrite1,27
35	6	11	66	194	Dendrite1,28
36	5	5	25	195	Dendrite1,29
37	4	11	44	268	Dendrite1,30
38	4	9	36	269	Dendrite1,31
39	4	10	40	270	Dendrite1,32
40	4	5	20	271	Dendrite1,33
41	4	5	20	272	Dendrite1,34
42	4	8	32	273	Dendrite1,35
43	4	9	36	274	Dendrite1,36
44	4	9	36	275	Dendrite1,37
45	4	9	36	276	Dendrite1,38
46	4	26	104	277	Dendrite1,39
47	4	9	36	278	Dendrite1,40
48	4	10	40	279	Dendrite1,41
49	4	9	36	280	Dendrite1,42
50	4	9	36	281	Dendrite1,43
51	4	9	36	282	Dendrite1,44
52	4	9	36	283	Dendrite1,45
53	4	14	56	284	Dendrite1,46
54	8	8	64	72	Dendrite2,1
55	7	9	63	118	Dendrite2,2

56	5	6	30	119	Dendrite2,3
57	5	5	25	140	Dendrite2,4
58	5	14	70	141	Dendrite2,5
59	5	27	135	142	Dendrite2,6
60	4	9	36	162	Dendrite2,7
61	4	10	40	163	Dendrite2,8
62	4	8	32	164	Dendrite2,9
*63	4	4	16	165	Dendrite2,10
64	4	6	24	177	Dendrite2,11
65	4	9	36	178	Dendrite2,12
66	4	7	28	179	Dendrite2,13
67	4	6	24	180	Dendrite2,14
68	4	7	28	181	Dendrite2,15
69	4	6	24	182	Dendrite2,16
70	4	7	28	183	Dendrite2,17
71	4	7	28	184	Dendrite2,18
72	4	6	24	185	Dendrite2,19
73	4	4	16	186	Dendrite2,20
74	4	3	12	187	Dendrite2,21
75	4	4	16	188	Dendrite2,22
76	4	6	24	189	Dendrite2,23
77	4	6	24	190	Dendrite2,24
78	4	4	16	191	Dendrite2,25
79	4	5	20	192	Dendrite2,26
80	4	5	20	193	Dendrite2,27
81	6	11	66	194	Dendrite2,28
82	5	5	25	195	Dendrite2,29
83	4	11	44	268	Dendrite2,30
84	4	9	36	269	Dendrite2,31
85	4	10	40	270	Dendrite2,32
86	4	5	20	271	Dendrite2,33
87	4	5	20	272	Dendrite2,34
88	4	8	32	273	Dendrite2,35
89	4	9	36	274	Dendrite2,36
90	4	9	36	275	Dendrite2,37
91	4	9	36	276	Dendrite2,38
92	4	26	104	277	Dendrite2,39
93	4	9	36	278	Dendrite2,40
94	4	10	40	279	Dendrite2,41
95	4	9	36	280	Dendrite2,42
96	4	9	36	281	Dendrite2,43
97	4	9	36	282	Dendrite2,44
98	4	9	36	283	Dendrite2,45
99	4	14	56	284	Dendrite2,46
			4068		

Table C-1 Artificial neuron filament disposition.